Imposing Structure on Chaos in Complex Quantum Systems

theoretical predictions to experimental validation

Dissertation
zur Erlangung des akademischen Grades
Doctor rerum naturalium
(Dr. rer. nat.)

vorgelegt von
Lucien Philippe Leonard Suchsland

durchgeführt am
Max-Planck-Institut für Physik komplexer Systeme, Dresden

Wissenschaftlicher Betreuer
Prof. Dr. Roderich Moessner

vorgelegt der
Fakultät Physik
Bereich Mathematik und Naturwissenschaften
Technische Universität Dresden

1. Gutachter Prof. Dr. Roderich Moessner
2. Gutachter Prof. Dr. Benoît Douçot

Eingereicht am 19. August, 2025
Verteidigt am 7. Oktober, 2025

Acknowledgements

First of all I would like to thank my supervisor, Roderich Moessner. Over the past years, he taught me how to structure my chaotic thoughts. Additionally, his guidance has been vital to stay at least on some winding path and to have the confidence to push forward. His ideas, thoughts and perspectives have been essential for making progress on this path. I am very grateful to him for sharing his curiosity about quantum dynamics with me, making me look forward to my future endeavors in this field. I cannot thank you enough for mentoring me. Thank you for your time, patience, support and the philosophical discussions. I hope you may share your perspectives with me also in the future.

I thank Pieter Claeys for many inspiring and fruitful discussions. I very much value his initiative, creativity, methodology and mentoring during my time in Dresden going far beyond anything I may have wished for as a student. He showed me how enthusiasm can lead you further. His thoughtful words shaped my approach to challenging situations. I am looking forward to the next joint exploration.

I am very thankful to Vedika Khemani for the collaboration on information spreading and Subhro Bhattacharjee for working together on entanglement. In particular through them I learned the importance of exploring phenomena from different angles.

I am very grateful for the exciting time at Google Quantum AI with many intriguing and inspiring discussions. I like to thank Vadim Smelyansky, Tom O'Brien, Kostyantyn Kechedzhi, Dmitry Abanin, Hartmut Neven, Sergio Boixo, Ben Villalonga, Xiao Mi, Alexis Morvan, Amir Karamlou, Igor Aleiner, Yuri Lensky, Brayden Ware, Nikita Astrakhantsev, Vlad Kurilovich and the whole Quantum AI team.

There are many people to whom I am thankful for making the past years so enjoyable and who had a significant impact on the creation of this thesis, including Jonathan Hallén, Benoît Douçot, Masud Haque, Benedikt Placke, Adam McRoberts, Michael Rampp, Jiangtian Yao and Michael Sonner.

Furthermore, I like to thank the whole non-academic staff at PKS for taking their time to deal with last-minute requests while maintaining the excellent work conditions at the institute.

Finally, I very much thank my sister and my parents. Without question it has been their continuous support and encouragement throughout the decades and the fruits thereof, which made all of this possible. I still rediscover old memories reflecting on the everlasting impact your support has had. Also looking ahead, the last sentence is dedicated to the amazing person who is enriching my life in many regards. Thank you for everything, Katharina.

Philippe Suchsland

Contents

x

1 Introduction

At the heart of physics lies the human fascination with natural phenomena and the wish to understand the underlying principles. A well-known example is the butterfly effect. It describes how small changes in the initial state can cause significantly different measurement outcomes at later times. Such sensitivity to initial conditions is a key signature of chaotic systems and reflects their instability under small perturbations. The principle underlying this phenomenon is information spreading: with time, information about the perturbation spreads through the system, changing measurement results at distant locations. In quantum systems, information not only spreads but can also scramble, meaning that the precise details about the perturbation are hidden in highly nonlocal correlations. Information scrambling has emerged as a universal feature of quantum chaos and, in combination with other universal features, serves as an organizing principle for quantum systems. This motivates imposing structure like locality on quantum systems in order to probe the capabilities and limits of such organizing principles.

Probing the nuances of these principles has been made possible by significant advances in both theoretical and experimental directions. The advances have been driven by hardware development, enabling turnkey simulations of quantum systems with up to 10^4 states and precise experiments capable of probing specific quantum features in great detail. The flexibility in designing experiments and simulations also inspires the analytical study of quantum systems from the bottom up, where tractable models offer insights into the generic features of quantum mechanics.

The study of minimal chaotic models provides a complementary approach to deducing simplified models from real-world systems. Starting point is ensembles of completely unstructured Hamiltonians, which are obtained by imposing a minimal set of constraints. Then, additional structure is gradually introduced by adding constraints such as symmetries or locality. This research direction is grounded in random matrix theory (RMT), which explores universal emergent features of unstructured Hamiltonians modeled as random matrices. One prominent example is the level spacing distribution, which is in good agreement between random matrices and certain real-world systems. Hence, RMT can be used to classify quantum systems according to their spectral properties. Quantum systems are considered chaotic when

their spectral properties align with those of random matrices. This example demonstrates how bottom-up approaches like random matrix theory can serve to classify real-world systems.

More recently, sparked by hardware developments in spatially extended quantum systems, there has been an increasing interest in adding spatial structure as a constraint and investigating the universal dynamical phenomena generated by local Hamiltonians or quantum circuits composed of local unitaries. Examples of studied phenomena include the spectral form factor, entanglement growth, Krylov complexity growth, and information spreading. Since information spreading is directly tied to spatial geometry, it provides an understanding of the influence of the locality of the Hamiltonian through emergent hydrodynamics.

Having established universal features of generic Hamiltonians in minimal models, a natural next step is to investigate how these features behave in significantly more structured systems. Additional structure can emerge from conservation laws or in the semi-classical limit, but detecting the structure present in a complex quantum system can be challenging. Characterizing the universal features of generic quantum systems with added structure enables their use as a probe of chaos and structure in more complex quantum systems.

In the first part of this thesis, we contribute to the development of probes of quantum chaos, studying entanglement in Chapter 2 and Krylov complexity in Chapter 3. We show how the semi-classical limit and monitoring can stabilize classical behavior and delay chaotic dynamics as probed by entanglement. We extend the framework of Krylov complexity to dynamics generated by unitary circuits and identify its universal behavior. This reveals a thermalization scale beyond which chaotic behavior emerges, as probed by Krylov complexity, and a transition between different complexity regimes in structured systems with an extensive number of conservation laws—specifically, integrable systems. While stable particles prevent thermalization in integrable systems, we show how their spectral properties can become featureless. We discuss the relation of the found thermalization scale to information spreading, which we focus on in the second part.

In Chapter 4, we apply existing probes of quantum chaos to investigate information spreading in proximity to integrable systems with additional structure, specifically through the order present in a quantum phase transition. We reveal a new information spreading phenomenon—relocalization—and examine its stability against breaking the integrability. In turn, we study systems with less structure in Chapter 5. There we discuss information spreading generated by the interplay between chaotic dynamics and conservation laws. We demonstrate how conservation laws stabilize correlation functions with respect to certain forms of noise. We show how a similar

perspective can be applied to fully chaotic systems by measuring the stabilization of information spreading in purely random circuits, as observed in experiments with up to 95 superconducting qubits. The experiments establish the stability of information spreading against local perturbations as a universal feature of generic quantum systems.

Summary of Chapter 2

We begin with a detailed discussion of the behavior of entanglement in chaotic systems. We impose a minimal amount of local structure by separating the system into two parts, each modeled as a single spin. We validate the predicted entanglement for typical states in such systems and show that it saturates the Page limit as the Hilbert space dimension increases. We then study how different initially unentangled product states approach the Page limit under time evolution. We consider three types of product states, each representing a distinct case. Random product states represent generic states only restricted by the absence of entanglement. Random dipole and quadrupolar states represent two distinct types of semi-classical structure. We characterize these states by their on-site entanglement and purity—a measure closely related to complexity. This analysis shows that among the three, random dipole states exhibit the most structure, while random product states are the least structured. Next, we examine how entanglement evolves under dynamics generated by different types of Hamiltonians. The results refine our earlier conclusion, demonstrating that the semi-classical limit can suppress the generation of extensive entanglement when starting from random dipole states. This suppression does not occur for random product or quadrupolar states; the imposed structure is insufficient to significantly reduce entanglement growth in the limit of large spin sizes. We conclude by presenting two protocols that can stabilize the dynamics of random dipole states at finite spin sizes, similar to the semi-classical limit.

Summary of Chapter 3

In the third chapter, we move from measuring the complexity of time-evolved states using entanglement to investigating time-evolved operators through the lens of Krylov complexity. After a short introduction to Krylov complexity for Hamiltonian dynamics, we generalize the framework for discrete time evolution. We present its properties and its relationship to the spectral function. We identify the linear growth of Krylov complexity as a universal feature of generic systems and analyze its behavior as we transition from chaotic to increasingly structured systems. Dual-unitary circuits converge to-

ward this universal behavior at rates that can be as fast as exponential, consistent with their classification as maximally chaotic with respect to spectral correlations. We then approximately restore energy conservation by considering trotterized systems, ranging from unstructured and chaotic to highly structured and integrable ones. We find these systems to thermalize on a scale set by the trotterization step, slowly approaching the universal linear Krylov complexity growth regime. Approaching the linear growth regime is a fundamental property of trotterized systems with an unbounded spectrum, as becomes evident from the properties of the spectral function. However, systems with a bounded energy spectrum, such as free fermionic systems, can evade thermalization as probed by Krylov complexity. Instead, we find a nonanalytic transition as the Trotter step size increases, which we relate to the spectral properties. Our study of Krylov complexity establishes its universal properties for discrete time evolution. The presented results deepen our understanding of the thermalizing behavior of different classes of systems in relation to their spectral properties by introducing an intuitive notion of a bath with chaotic characteristics. We link this thermalization behavior to information spreading, which we explore in the second part of this thesis.

Summary of Chapter 4

Information scrambling, along with the associated spreading, is a key phenomenon in chaotic systems with local structure. In this chapter, we investigate information spreading in proximity to integrable systems exhibiting spontaneous symmetry breaking. Our starting point is the integrable transverse field Ising model (TFIM). As expected, information spreads in the TFIM while the integrability prevents the scrambling of information, meaning time-evolved operators do not spread evenly over the whole operator Hilbert space. At the same time, information spreading probed by quenched out-of-time ordered correlators (OTOCs) exhibits features reminiscent of the quantum phase transition present in the TFIM. We unravel the intricate behavior of these OTOCs by computing them at large times and system sizes, enabling extrapolation to the thermodynamic limit. These results hint at an underlying mechanism that stabilizes the long-time values of OTOCs, which we identify as a dynamical relocalization phenomenon. Through analytical calculations and numerical simulations, we provide a detailed explanation of the relocalization phenomenon. The insights gained from the analytical calculations allow us to relate the non-analytic behavior of the OTOC to spontaneous symmetry breaking. Both can be traced back to the $k = \pi$ momentum subspace. However, we present two variations of the TFIM where the non-analytic behavior of the OTOC is unrelated to the

presence of a quantum phase transition. This shows that no direct, universal relation exists between the two. Finally, we discuss the effects of breaking the integrable structure of the TFIM from three perspectives. By analyzing the effects of adding disorder, comparing to classical analogs, and incorporating interactions. Our results show that for short times, chaotic systems in proximity of integrability can retain signatures of integrability in the form of relocalization. In contrast, we observe significant changes at large times. This suggests that information scrambling, as a universal feature of chaotic systems, is restored at large times—even in systems near integrability that exhibit order.

Summary of Chapter 5

Following the analysis of information spreading close to integrable regimes, we study the stability of information spreading in more generic systems. First, we consider charge-conserving random circuits. In these systems, charge-charge correlators exhibit large fluctuations across different circuit instances with a slow polynomial decay in time. At the same time, they remain stable against fine-tuned perturbations, which can be interpreted as dephasing noise in the eigenbasis of the charge density operators. Equivalently, charge-charge correlators are mostly insensitive to decoherence, with interference effects contributing only subleading corrections. In this sense, the charge information spreading probed by charge-charge correlators is effectively "classical". In a path integral framework, the correlator values are largely determined by paired trajectories. We perform a detailed analysis and quantify the dephasing insensitivity of these correlators. This suggests that circuit-to-circuit fluctuations can be captured by considering small regions where "quantum" effects are included, embedded within otherwise "classical" dynamics. This observation motivates the development of an algorithm to compute charge-charge correlators for individual circuits on classical computers with high accuracy. We quantitatively relate the algorithm's performance to the dephasing analysis. We demonstrate the algorithm's accuracy numerically for charge-charge correlators. Then, we argue that in generic circuits without conservation laws, the information spreading, as probed by out-of-time ordered correlators (OTOCs), follows similar principles. We conclude by comparing OTOC values measured on quantum devices with up to 95 superconducting qubits and 1000 gates to predictions from the approximate algorithm. This cross-validates experimental measurements and theoretical predictions.

Part I

Probes of Quantum Chaos

2 Entanglement in the Semi-Classical Limit

Our journey into the realms of quantum chaos begins with a detailed study of the interplay of chaos and structure emerging in systems that approach classical behavior. In this chapter, we analyze emerging classical dynamics by considering a quantum system composed of two spins of size S and taking the semiclassical limit, where S becomes infinitely large. Considering systems composed of two distinct subsystems also yields a notion of locality and imposes minimal spatial structure. As such, the two-spin system is a representative for quantum systems with locality and a semiclassical limit. Hence, in this chapter, we study two-spin systems to gain a better understanding of the generic behavior of probes of complexity, chaos, and classicality. In particular, we focus on entanglement, out-of-time ordered correlators, purity, and spin length.

For quantum chaotic systems, one expects such probes to take on universal values with small fluctuations. However, In the semiclassical limit, one expects these quantities to exhibit behavior dominated by classical structure. In the following, we characterize the evolution of quantum systems in terms of these quantities when transitioning from quantum systems to classical ones, indicating how the semiclassical limit can stabilize the dynamics of two spins. We show that such stabilization can also be achieved through monitoring the system.

This chapter is structured as follows. In Section 2.1, we discuss possible platforms to realize two spin systems and provide a brief overview of related research and our results. A more detailed outline of our results is given in Section 2.2. In Section 2.3 we introduce briefly the measured quantities, and characterize the different sets of considered initial states. We discuss the properties of various Hamiltonians in Section 2.4 and report on the results for purity and entanglement generation under time evolution in Section 2.5. Finally, we show how the dynamics of observables can be stabilized in the semiclassical limit in Section 2.6 and by monitoring the system's evolution in Section 2.7. We conclude in Section 2.8.

2.1 Overview

The two-spin system studied in this chapter belongs to the larger class of systems of *few* interacting degrees of freedom, but each with effectively a *large* Hilbert space dimension—dubbed deep Hilbert spaces in Ref. [1]. Labeled qudits, such platforms have been developed in quantum information settings [2–5] and argued [6–9] to have distinct advantages over their more conventional qubit counterparts for quantum simulations and computations. A qudit is naturally represented in terms of a spin-S with Hilbert-space dimension of $(2S+1)$ and the simplest interacting setting consists of two such interacting spin-Ss.

There are several contexts where the above situation arises. Beyond the computational platforms where such 2-spin systems have been built [2], there is the field of quantum structured light [9, 10]. Here, the orbital angular momentum and polarization of photons are combined and advanced splitting techniques applied [11] to generate Bloch two-photon states with effectively high angular momentum resembling a two spin-S system. Other experimental platforms are split BEC droplets [12] or weakly coupled BEC droplets in a double-well potential [13]. In these cases, the effective spin-$S(=N/2)$ is made up of many spin-$\frac{1}{2}$s in a totally symmetric state [1] such as the Bloch spin states or squeezed spin states. Somewhat closer to conventional solid-state systems, are the so-called spin-S magnetic insulators where at each site of the lattice, a multiplet of electrons align in parallel (by Hund's rule) to form $(2S+1)$ dimensional Hilbert-space at every site such that there are $(2S+1)^2-1$ observables (spin-operators) at every site. The spins at different sites then interact with each other, typically through short-ranged interactions whose form dictates the nature of the low energy states of the system. Concretely a two spin-S system can arise in such situation in non-magnetic insulators with dilute spin-S impurities as dilute magnetic semiconductors [14, 15].

In context of the coupled BEC droplets, it is important to note that each droplet is often in a Bloch state made up of a totally symmetric state of spin-$\frac{1}{2}$s. As argued in Ref. [1], the manifold of such totally symmetric states is quite atypical and there are an exponentially large number $(2^N-(N+1))$ of states belonging to the *deep Hilbert space* that do not belong to this manifold and whose static and dynamic properties are rather different from the former [1]. In the limit of the large local Hilbert-space dimension (in our case $S\to\infty$), it is known that generic states are highly entangled and violate the generalized Bell's inequalities [16, 17] and are in this sense *nonclassical*.

Even if one starts from product states that are closest to the classical

limit[1], any generic unitary evolution via interacting many-body Hamiltonians always generates some amount of entanglement, thereby corrupting the product structure.

This would seem to be at odds with the general expectation in spin systems that $S \to \infty$ leads to classical limit around which the spin dynamics can be treated semiclassically in systematic $1/S$ expansions. A possible route for such many-body classical physics to emerge in quantum systems is to consider limits where product (quantum) states evolve into other (near-)product states. In this scenario, the resultant states can always be described locally—a hallmark of classical mechanics. Note that this is not sufficient and requires control at the single-particle level via minimizing uncertainty of non-commuting local operators, which is often provided by Bloch states. At the same time, the above evolution within the set of product states necessarily implies that no entanglement is generated. Otherwise a classical description of the many-body system in terms of the local degrees of freedom will surely break down [18].

The above observation raises an interesting question: under what circumstances do product states evolve into (near-) product states, and what is the upper limit to the time-scale—the so-called Ehrenfest time—before uncontrolled growth of entanglement renders the possible classical limit, as defined above, useless?

This question is central to several important issues, both in principle and in practice, in understanding the collective behavior of both statics and dynamics of quantum many-body systems. We approach it for the simplest setting of two coupled spins-S for different values of $S = 1/2 \ldots \infty$. We study their statistical mechanics, and above all their dynamics, by varying the following three ingredients of their joint dynamics. First, their initial states, including observables (dipole/quadrupole expectation values), quantum uncertainty as well as the entanglement between the spins. Second, we consider families of Hamiltonians differing with regard to symmetry and rank (as defined below). Third, the nature of the dynamics: we contrast possible semiclassical limits with fully coherent quantum dynamics, as well as setups involving interactions with an environment.

The rich set of behavioral patterns we observe are summarized in the following section. In a few words, we identify the emergence of classical behavior as contingent upon a weakly entangled initial state, being terminated

[1] Note that this is not sufficient and requires control at the single-particle level via minimizing uncertainty of non-commuting local operators – often provided by Bloch states, but the above evolution within the set of product states necessarily implies no generation of entanglement. Otherwise a classical description of the many-body system in terms of the local degrees of freedom will surely break down [18].

by entanglement growth at later times. Even "mild" departures from an initial coherent spin state can impact this emergence. We also find that a unique semiclassical limit is not always apparent; notably, the emergence of classical behavior in the dynamics of ordered magnets depends not on a limit of large-S, but rather on the emergence of hydrodynamic behavior.

2.2 Outline of Results

We start with a summary of the results presented. The $(2S+1)$-dimensional Hilbert space for a single spin-S admits multipole operators, which are spherical tensors up to rank $k = 2S$. The eigenstates of these operators form a useful basis for preparing the system with large-S in a semiclassical initial state. For instance, Bloch states [Eq. (A.6)] are eigenstates of the dipole operators with dipole moment along an arbitrary direction on the Bloch sphere and minimize the spread in the limit $S \to \infty$. Similarly, it is easy to construct pure eigenstates of the spin-quadrupole operator [Eq. (2.9)]. However, unlike the Bloch states, the fluctuation in the expectation value of various on-site multipole operators measured in the quadrupolar state does not vanish in the limit of $S \to \infty$. This distinction between the two states is due to the difference in the *complexity* of the two classes of states that can be captured via the constitutive entanglement entropy. While the Bloch states have zero constitutive entropy, that of the quadrupolar states is finite. Thus, under Hamiltonian evolution the rate of growth of entanglement entropy of the quadrupolar states is faster than for Bloch states while smaller than for random product states.

2.3 Two Spin-S Systems

The Hilbert-space dimension of a two spin-S system is $(2S+1)^2$ such that a generic state of the system is given by

$$|\Psi\rangle = \sum_{m_1,m_2=1}^{(2S+1)} \Psi_{m_1,m_2} |m_1; m_2\rangle, \tag{2.1}$$

where $\Psi_{m_1,m_2} \in \mathbb{C}$ is a $(2S+1) \times (2S+1)$ matrix that corresponds to the amplitudes in the joint Hilbert space dimension $(2S+1)^2$. The reduced density-matrix corresponding to such a pure state, obtained by integrating out one spin (say the second spin), is then given by

$$\rho_1 = \mathrm{Tr}_2[|\Psi\rangle\langle\Psi|] = \Psi \cdot \Psi^\dagger. \tag{2.2}$$

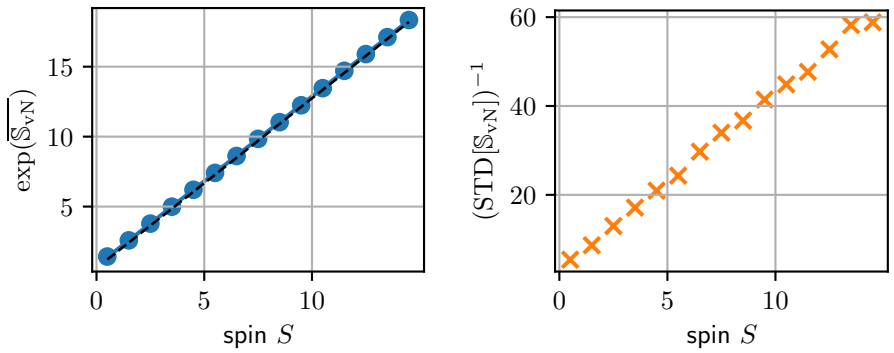

Figure 2.1: *The Page limit: The average bipartite entanglement for $S = 1/2$ to 15 as well as the corresponding standard deviation for 1000 random two-spin-S Haar states chosen from an uniform Haar distribution. On the x-axis the spin size S is varied in half-integer steps. Left and right respectively, the average bipartite von-Neumann entanglement entropy $\overline{\mathbb{S}_{\mathrm{vN}}}$ and the inverse of its standard deviation are plotted. The Haar random states (RS) $|\Psi\rangle$ [Eq. (2.1)] were created by generating $2(2S+1)^2$ random numbers $z_{m_1,m_2;1(2)}$, uniformly distributed between -1 and 1. Then $\Psi_{m_1,m_2} = (z_{m_1,m_2;1}+iz_{m_1,m_2;2})/\sqrt{\sum(z_{m_1,m_2;1})^2 + (z_{m_1,m_2;2})^2}$. This confirms that such states saturate the Page limit [Eq. (2.3)] (black dotted line) on average with a distribution of vanishing spread for $S \to \infty$ [Eq. (2.4)].*

Different classes of two-spin states [19, 20] can now be obtained by choosing Ψ from different ensembles. On choosing Ψ_{m_1,m_2} from the rows of a randomly generated unitary matrix with uniform Haar measure of dimension $(2S+1)^4$ [16, 20], we get random two-spin states (RS), which we denote as $|\Psi_{\mathrm{RS}}\rangle$. For such pure RSs $|\Psi_{\mathrm{RS}}\rangle$ it is well known that the average bipartite von Neumann entropy for the two-spin system is *near* maximal value—the Page limit [21–25], which is for two spins and $S \gg 1$

$$\overline{\mathbb{S}_{\mathrm{vN}}} \approx \ln(2S+1) - 1/2, \tag{2.3}$$

where the overline denotes averaging uniformly over the pure RS. Notably [26],

$$\mathrm{Var}\,[\mathbb{S}_{vN}] \sim \frac{1}{(2S+1)^2} \tag{2.4}$$

such that a typical pure RS in the $S \to \infty$ limit is *near* maximally entangled such that the corresponding reduced density matrix is *almost* uniform, i.e., $\rho_1 = \frac{\mathbb{I}}{2S+1}$. Such uniform density matrices lead to the first term on the RHS of Eq. (2.3). However, random matrix based studies of the distribution of Renyi entropies in large quantum systems show that the weight of such states is actually vanishingly small [26, 27] giving rise to the sub-leading corrections

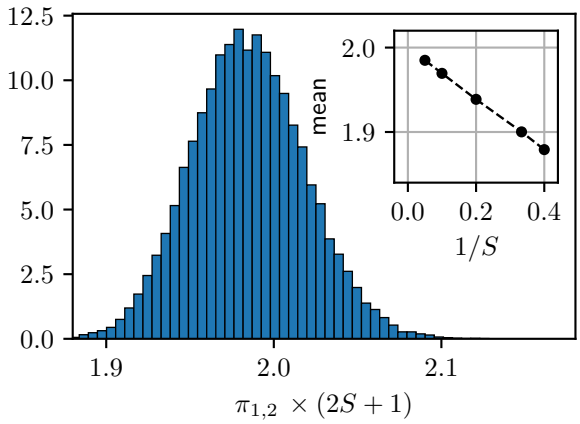

Figure 2.2: *The probability distribution of purity for the reduced density matrix ρ_1 of random states (RS) for 50000 realizations with S=20. The form is consistent with the expectation from the large deviation analysis of Ref. [26, 27]. The mean tends towards 2 as $S \to \infty$ (inset).*

in Eq. (2.3). The validity of the Page limit and its fluctuations are shown in Fig. 2.1.

Further, in Fig. 2.2, we show the distribution of purity

$$\pi_{12} = \mathrm{Tr}[\rho_1^2] = \sum_{i=1}^{2S+1} \lambda_i^2 \tag{2.5}$$

for $S = 20$ where λ_i are eigenvalues of the reduced density matrix ρ_1, see Eq. (2.2). The distribution is in accordance with the large deviation analysis of Refs. [26, 27]. This completes our characterization of the random 2-spin-S Haar states, which indicates that in the limit of $S \to \infty$ typical 2-spin-S Haar states are highly entangled.

Product states The subset of the two-spin states, see Eq. (2.1), for which the amplitudes can be written as a product function $\Psi_{m_1,m_2} = (\psi_1)_{m_1}(\psi_2)_{m_2}$, are referred to as random product states (RPS). The vectors ψ_1 and ψ_2 are now chosen randomly (subject to unit norm) with uniform Haar measure from a single spin-S Hilbert space of dimension $(2S+1)$ such that

$$|\Psi_{\mathrm{RPS}}\rangle = |\psi_1\rangle \otimes |\psi_2\rangle. \tag{2.6}$$

Such pure product states, $|\Psi_{\mathrm{RPS}}\rangle$, have zero bipartite entanglement and, hence, are far from the Page limit of typical RS [Eq. (2.1)] in the $S \to \infty$ limit. This can be reconciled by noting that the product states of the form

in Eq. (2.6) form a measure-zero subset of all random two-spin states of the form in Eq. (2.1) in the limit of $S \to \infty$ [2].

However, such generic product states do not necessarily allow for a classical description as they are not minimum uncertainty states for on-site operators. Indeed, for spin-S there are exactly $(2S+1)^2 - 1$ on-site Hermitian operators (observables) that can be expressed in terms of the k-th moments of the spin with $k = 1, 2, 3$ being dipole, quadrupole, octupole and so on such that $k_{\max} = 2S$. We denote a rank-k spherical tensor operator on the site i as (see Appendix A.1)

$$\mathcal{O}^{(k)}_{i,\alpha} \tag{2.7}$$

where $\alpha = -k, \cdots, k$ are the components of the rank k spherical tensor with $k = 0$ corresponding to the identity operator. We consider a product state to be *semiclassical*, if all *on-site* physical observables can be calculated sharply, i.e., with minimum uncertainty in the limit of $S \to \infty$.

A typical example of such *semiclassical* states are obtained by choosing ψ_1 and ψ_2 uniformly on the Bloch sphere whence we get random Bloch states (RBS)

$$|\Psi_{\text{RBS}}\rangle = |\hat{\Omega}_1\rangle \otimes |\hat{\Omega}_2\rangle, \tag{2.8}$$

where $\hat{\Omega}_1$ and $\hat{\Omega}_2$ are respectively the random direction of quantization on the Bloch spheres of the two spins (see Appendix A.2 and in particular Eq. (A.6)). The RBS maximizes the dipole moments, $\langle S^\alpha \rangle_{\hat{\Omega}} = S\hat{\Omega}$, of the two spins along $\hat{\Omega}_1$ and $\hat{\Omega}_2$ respectively with spread decreasing as $S \to \infty$ and all higher order multipoles are obtained as a product of the expectation value of the dipole operators.

Other types of choices are also possible. For higher spins, the above Bloch states can be generalized such that up to $(k-1)$th rank on-site moments are exactly zero [28]. For example, for quadrupole operators,

$$\mathcal{Q}_i^{\alpha\beta} = \frac{1}{2}\left(S_i^\alpha S_i^\beta + S_i^\beta S_i^\alpha\right) - \frac{S(S+1)}{3}\delta_{\alpha\beta} \tag{2.9}$$

we can construct pure quadrupolar product states of the form

$$|\Psi_{\text{RQS}}\rangle = |\mathcal{Q}_1\rangle \otimes |\mathcal{Q}_2\rangle, \tag{2.10}$$

[2] The two spin RS lives on the generalized Bloch sphere belonging to the manifold of Ref. [16] $U((2S+1)^2)/(U((2S+1)^2 - 1) \times U(1))$, where $U(N)$ is a unitary matrix of dimension N. On the other hand for random product state each state lives on a manifold of $U((2S+1))/(U((2S+1) - 1) \times U(1))$ such that the ratio of the two volumes, namely $\lim_{S\to\infty} vol[RS]/vol[RPS]$ goes to infinity.

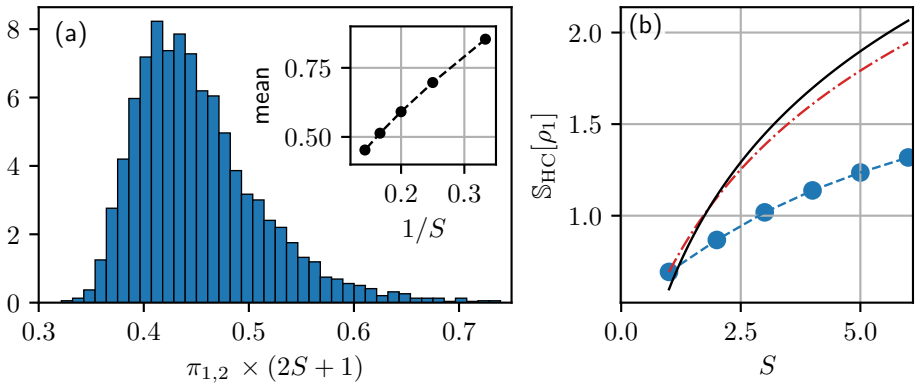

Figure 2.3: *(a) The distribution of half-chain purity (over 5000 realizations for $S = 7$) corresponding to a single spin Haar random product state [Eq. (2.13)] for the constituent spin-$\frac{1}{2}$ chain of length $2S$ corresponding to a single spin-S. Inset shows a different behavior of mean as a function of $1/S$ compared to two-spin Haar random states in Fig. 2.2. The dashed line is the best fit of $y = 0.16 + 2.09x$. (b) Half-chain constitutive entanglement entropy $\mathbb{S}_{\rm HC}[\rho_1]$ for a pure quadrupolar state of spin-S (in blue points and blue dashed line) as a function of spin length. The red dot-dashed line shows $\log(S+1)$ which is the maximal value of such constitutive entanglement while the black solid line denotes the corresponding Page limit for such constitutive entanglement.*

where $\mathcal{Q}$ denote Bloch state representation for a pure random quadrupolar state (RQS) as given by Eq. (A.15) in Appendix A.2. For these states the expectation value of the dipole moments and all time reversal odd higher multipole moments are identically zero while the quadrupole moments and the even higher order moments are nonzero. Centrally, unlike the Bloch states [Eq. (2.8)], the fluctuations in the expectation value of of all on-site quadrupolar operators do not go to zero in the large S limit making such states inherently different from the RBS.

The above product states form a class of *simple* states which provide a natural choice as initial states to study quantum dynamics both theoretically and experimentally [29, 30].

Characterizing complexity of a single spin-state: Constitutive entanglement entropy A useful quantitative difference between a generic RPS and the RBS and RQS even at the level of a single spin stems from considering the spin-S operator at site $i(=1,2)$, S_i^α $(\alpha = x, y, z)$ made up of

$2S$ spin-$\frac{1}{2}$ operators as

$$S_i^\alpha = \sum_{a=1}^{2S} s_{i,a}^\alpha \tag{2.11}$$

such that the $(2S+1)$ basis states for the spin-S are made up of the symmetric states of the constituent spin-$\frac{1}{2}$s with appropriate Clebsch-Gordon coefficients. Then the RBS for the first spin (say) is given by [1, 31]

$$|\Omega_1\rangle = \otimes_{a=1}^{2S} |\Omega_1^{\left(\frac{1}{2}\right)}\rangle, \tag{2.12}$$

where $|\Omega_1^{\left(\frac{1}{2}\right)}\rangle$ denotes that each constituent spin-$\frac{1}{2}$ is pointing in the same direction on their respective Bloch sphere as the spin-S; it is *totally* symmetric [1]. On the other hand a Haar random state for the same spin has a generic form

$$|\psi_1\rangle = \sum_{m_1=-S}^{S} (\psi_1)_{m_1} \mathcal{C}_{S\{s_a\}}^{S,m_1} |\mathcal{S}\{s_a\}\rangle, \tag{2.13}$$

where as before ψ_{m_1} is chosen from an uniform Haar measure for the spin-S and $|\mathcal{S}\{s_a\}\rangle$ is the symmetric state in terms of the underlying constituent spin-$\frac{1}{2}$s with $\mathcal{C}_{S\{s_a\}}^{S,m_1}$ being the corresponding Clebsch-Gordon coefficients.

A quantitative characterization of the on-site complexity of the spin-S state is obtained by considering the *constitutive entanglement* in terms of the underlying spin-$\frac{1}{2}$s characterized by the half-chain entanglement $\mathbb{S}_{\text{HC}}$ of the resultant spin-$\frac{1}{2}$ chain of length $2S$ from Eq. (2.13), for example via their purities. A product state, like the one presented in Eq. (2.12), has a purity of 1. The distribution of half-chain purity for 5000 Haar random states for $S = 5$ is plotted in Fig. 2.3(a). While different from the *totally* symmetric random Bloch state for reasons discussed above, the difference in the distribution compared to Fig. 2.2 is also evident, particularly from the behavior of mean as a function of S. This is because, the state in terms of the constituent spin-$\frac{1}{2}$s are not completely Haar random since they all have to be symmetric to be a valid basis state for the underlying spin-S.

Notably however, for the pure quadrupolar states [Eq. (2.10)] the on-site constitutive entanglement is nonzero since they are obtained from the $S^z = 0$ states (for integer spins as described in Appendix A.2). In fact for $S = 1$ it corresponds to a maximally entangled state and for higher spins the half-chain constitutive entanglement is shown in Fig. 2.3(b).

2.4 Dynamics of Spin Hamiltonians

Fig. 2.1 suggests that typical two spin-states in the limit of $S \to \infty$ saturate the Page limit, i.e., they are maximally entangled. This cannot be reconciled with the expectation of the emergence of a semiclassical limit valid for almost all states. It provides the platform for understanding the circumstances for recovering the semiclassical description in the limit of $S \to \infty$. The question, also depends, in addition to the properties of the Hilbert space, on the nature of the dynamics governed by the Hamiltonian, which we now turn to.

Spin Hamiltonians are naturally written in terms of the on-site multipole operators defined in Eq. (2.7) such that the generic two-spin Hamiltonian is then given by

$$\mathcal{H}_{\text{generic}} = \sum_{k,k'=0}^{2S} \sum_{\alpha=-k}^{k} \sum_{\beta=-k'}^{k'} J_{\alpha\beta}^{(kk')} \mathcal{O}_{1,\alpha}^{(k)} \mathcal{O}_{2,\beta}^{(k')} \tag{2.14}$$

where $J_{\alpha\beta}^{(kk')} \in \mathbb{R}$ are the coupling constants such that the Hamiltonian is Hermitian. Note that the above Hamiltonian includes the identity operator and it allows for on-site terms such as

$$J_{00}^{(00)} + \sum_{k=1}^{2S} \sum_{\alpha=-k}^{k} J_{0\alpha}^{(0k)} \mathcal{O}_{2,\alpha}^{(k)}. \tag{2.15}$$

While the first term is a constant offset, the second set corresponds to generalized Zeeman terms. The Hamiltonian in Eq. (2.14) does not have any symmetry. One can impose further constraints on it by demanding symmetries which are often present in materials via $[\mathcal{S}, \mathcal{H}_{\text{generic}}] = 0$ where $\mathcal{S}$ is a symmetry generator. One example is time reversal symmetry (TRS), for which $J_{\alpha\beta}^{(kk')} = 0$ when $\mathcal{O}_{1,\alpha}^{(k)} \mathcal{O}_{2,\beta}^{(k')}$ is not real. Alternatively, $J_{\alpha\beta}^{(kk')} = 0$ for all operators that do not commute with $\mathcal{S} = e^{-i\pi S_1^y/\hbar} e^{-i\pi S_2^y} K$, where K is the complex conjugation operator [32, Chapter 4.4.4].

Finally, in Mott insulators, when the underlying high energy physics (from which the spin Hamiltonians are derived as effective low energy Hamiltonians for the Mott insulators) is governed by mutually repelling electrons moving on a lattice (such as the multi-orbital Hubbard model), the strong coupling approaches typically lead to low rank operators per site corresponding to $k = 1, 2$. Most of our discussion in this work will be focused on such low rank Hamiltonians.

Heisenberg Hamiltonians: The simplest of the above set of Hamiltonians is obtained when we demand global SU(2) spin rotation symmetry

such that the Hamiltonian fulfills $[S_T^\alpha, \mathcal{H}_{\text{generic}}] = 0$, which gives generalized Heisenberg Hamiltonians of the form

$$\mathcal{H}_{\text{Heisenberg}} = \sum_{k=1}^{2S} \mathcal{J}_k \left(\mathbf{S}_1 \cdot \mathbf{S}_2\right)^k . \tag{2.16}$$

They are manifestly invariant under global SU(2) spin rotations. A particularly high symmetry limit of the above Hamiltonian is obtained by setting $\mathcal{J}_k = \mathcal{J}\ \forall\ k$ whence it is $SU(N = 2S + 1)$ symmetric. As it is well known, such symmetries severely restrict the dynamics by imposing various selection rules.

Random Hamiltonians: On the other extreme from the Heisenberg model we have random Hamiltonians where the coupling constants in Eq. (2.14), $J_{\alpha\beta}^{(k_1k_2)}$ are chosen from a distribution of order one random numbers—e.g. identically distributed Gaussian random variables with zero mean and unit variance $\mathcal{N}(0, 1)$ or uniformly distributed random numbers in the window $[-1, 1]$. Furthermore, while Eq. (2.14) contains operators of all ranks, we can consider situations where only a subset of them are present and this is given by

$$H_K = \sum_{k_1,k_2:k_1+k_2\leq K} \sum_{\alpha\beta} J_{\alpha\beta}^{(k_1k_2)} \mathcal{O}_{1,\alpha}^{(k_1)} \mathcal{O}_{2,\beta}^{(k_2)} . \tag{2.17}$$

The simplest example of random Hamiltonians is when we keep at most the $k_1, k_2 = 0, 1$ operators, i.e.,

$$\mathcal{H}^{(1)} = \sum_{i=1,2} \sum_{\alpha=x,y,z} h_{i,\alpha} S_i^\alpha + \sum_{\alpha,\beta=x,y,z} \mathcal{J}_{\alpha\beta} S_1^\alpha S_2^\beta , \tag{2.18}$$

where $h_{i,\alpha}$ are random Zeeman fields and $\mathcal{J}_{\alpha\beta}$ are random couplings between the spin components on the two sites. On considering $\mathcal{J}_{\alpha\beta} = \mathcal{J}_\alpha \delta_{\alpha\beta}$, the interactions are diagonal in the spin components whence we have a random XYZ Hamiltonian in a site dependent random Zeeman field. For $h_{i,\alpha} = 0$, the system has time reversal symmetry.

2.4.1 Energy of RS vs RPS

The average energy of random states [Eq. (2.1)] is given by

$$\overline{\overline{\mathcal{E}}}_{\text{RS}} = \overline{\overline{\langle \Psi_{\text{RS}} | \mathcal{H} | \Psi_{\text{RS}} \rangle}}, \tag{2.19}$$

where $\overline{\overline{(\cdot)}}$ denotes averaging over a uniform distribution of two-spin RS and $\mathcal{H}$ denotes any of the Hamiltonians discussed above. Using the explicit forms [Eq. (2.1)], we get

$$\overline{\overline{\mathcal{E}}}_{\rm RS} = \sum_{m_1,m_2}\sum_{\tilde{m}_1,\tilde{m}_2} \overline{\overline{\Psi^*_{m_1,m_2}\Psi_{\tilde{m}_1\tilde{m}_2}}}\langle m_1,m_2|\mathcal{H}|\tilde{m}_1\tilde{m}_2\rangle \tag{2.20}$$

For uniform distribution we expect $\overline{\overline{\Psi^*_{m_1,m_2}\Psi_{\tilde{m}_1\tilde{m}_2}}} = \mathcal{W}_{\rm RS}\delta_{m_1,\tilde{m}_1}\delta_{m_2,\tilde{m}_2}$ such that

$$\overline{\overline{\mathcal{E}}}_{\rm RS} = \mathcal{W}_{\rm RS}\sum_{m_1,m_2}\langle m_1,m_2|\mathcal{H}|m_1,m_2\rangle. \tag{2.21}$$

On the other hand for the random product states we have

$$\overline{\mathcal{E}}_{\rm RPS} = \overline{\langle\Psi_{\rm RPS}|\mathcal{H}|\Psi_{\rm RPS}\rangle}, \tag{2.22}$$

where $\overline{(\cdot)}$ now denotes uniform averaging over RPS. This now gives :

$$\overline{\mathcal{E}}_{\rm RPS} = \mathcal{W}_{\rm RPS}\sum_{m_1,m_2}\langle m_1,m_2|\mathcal{H}|m_1,m_2\rangle \tag{2.23}$$

where we now have $\overline{\psi^*_{m_1}\psi^*_{m_2}\psi_{\tilde{m}_1}\psi_{\tilde{m}_2}} = \mathcal{W}_{\rm RPS}\delta_{m_1,\tilde{m}_1}\delta_{m_2,\tilde{m}_2}$. Therefore,

$$\overline{\overline{\mathcal{E}}}_{\rm RS} - \overline{\mathcal{E}}_{\rm RPS} = (\mathcal{W}_{\rm RS} - \mathcal{W}_{\rm RPS})\sum_{m_1,m_2}\langle m_1,m_2|\mathcal{H}|m_1,m_2\rangle. \tag{2.24}$$

For a generic random Hamiltonian, such states have an average energy in the middle of two-spin energy spectrum as shown in Fig. 2.4(left) for random rank-1 Hamiltonian [Eq. (2.18) without the Zeeman field). The standard deviation of the energy distributions for RPS and 2-spin random Haar states (Fig. 2.4(right)) decreases with S in accordance with the expectation of Eq. (2.24). Therefore, the two classes of random states differ, in absence of symmetries, in terms their bipartite entanglement entropy.

2.4.2 Characterization of Random Hamiltonians

At this point we would like to briefly note a few facts about the two-spin random Hamiltonians $\mathcal{H}^{(1)}$, Eq. (2.18), in context of the random matrix theory (RMT) [33]. The random Hamiltonian $\mathcal{H}^{(1)}$ differs from the canonical random matrices (RMs) (of dimension $(2S+1)^2 \times (2S+1)^2$) in two main aspects—(1) In the real-space spin basis, unlike the RMs where all matrix

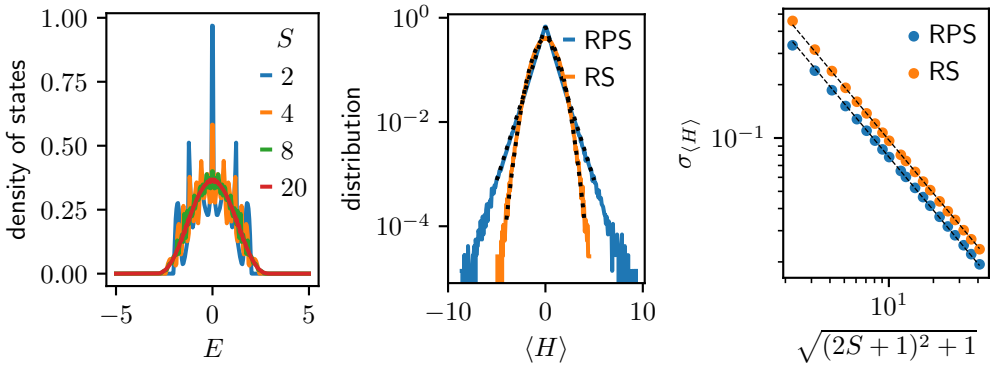

Figure 2.4: *Left: Density of states of 10^6 Hamiltonians [Eq. (2.18)] with $h_{i,\alpha} = 0$ and coupling constants $\mathcal{J}_{\alpha,\beta} \sim \mathcal{N}(0,1)$ normalized as $H/\sqrt{\mathrm{Tr}[H^2]}$. Center: Distribution of energy expectation values for 10^6 Haar random product states (RPS, blue) and 10^6 Haar random states (RS, orange) for a spin $S = 20$ rescaled to have unit variance. The RS follow a Gaussian distribution, the RPS follow an exponential distribution $\propto e^{-1.36|\langle H\rangle|}$ (dotted lines). Right: The standard deviation of the energy distribution, $\sigma_{\langle H\rangle}$ of the energy for RPS and 2-spin random Haar states (RS) on a log-log scale vs $\sqrt{(2S+1)^2+1}$, the prediction from Weingarten calculus [App. D.2].*

elements are typically non-zero and obtained from independent identical distributions (IID), in Hamiltonians $\mathcal{H}^{(1)}$ only a handful of matrix elements are non-zero and hence they represent sparse RMs in the above real-space spin basis. (2) For the coupling constants, $\mathcal{J}_{\alpha\beta}$, being $\mathcal{O}(1)$ random numbers, due to the S dependence of the matrix elements of the spin-operators, the resultant matrix elements of the Hamiltonian are no longer elements of IID since it is a priori not clear if S can be scaled out.

On including higher rank spin-operators, while the sparsity (in the above basis) decreases, the operators need to be normalized appropriately to compare with the results of RMT. However, using un-normalized higher rank spin-operators lead to dominance of the largest rank operator as $S \to \infty$ and hence may deviate from conventional RMT. In Appendix A.5, we summarize these aspects.

2.5 Evolution of Bipartite Entanglement

Having characterized the system and the Hamiltonian, we now turn to the question of evolution of the entanglement in such a system with time, starting from the three classes of product states introduced above, i.e., (1) Bloch states with or without randomness [Eq. (2.8)], (2) random product states

(RPS), $|\Psi_{\rm RPS}\rangle$ [Eq. (2.6)], and, (3) random quadrupolar states (RQS), $|\Psi_{\rm RQS}\rangle$.

For evolving the above three classes of states we choose different types of Hamiltonians introduced in the previous section. We start with the SU(2) symmetric rank-1 Heisenberg Hamiltonian for both ferro- and antiferromagnetic exchanges [Eq. (2.16)] with $\mathcal{J}_k = \pm\delta_{k,1}$. The mid spectrum properties do not depend on the sign of the exchange. The rank-1 Heisenberg model gives way to the rank-1 spin model $\mathcal{H}^{(1)}$ [Eq. (2.18)] on breaking the spin rotation symmetry completely. We consider the case of a random XYZ model with $J_{00} = h_{i\alpha} = 0$ and $\mathcal{J}_{\alpha\beta} = \mathcal{J}_\alpha\delta_{\alpha\beta}$ with $\mathcal{J}_\alpha \in [-1, 1]$, i.e., a uniform distribution.

We consider the evolution of the bipartite entanglement of such states as a function of time obtained via unitary evolution $|\Psi(t)\rangle = e^{-iHt}|\Psi(t=0)\rangle$, where H denotes one of the above Hamiltonians.

2.5.1 Entanglement Dynamics for Bloch States

We start with product Bloch states, Eq. (2.8), where $\Omega_{1,2}$ denote spin directions on the Bloch sphere (Appendix A.2). Without loss of generality we can take Ω_1 to be the north pole such that $\Omega_1 \cdot \Omega_2 = \cos\theta$ with θ being the polar angle (the relative azimuthal angle is taken to be zero). The resultant growth of entanglement for a Heisenberg ferromagnet for $S = 15$ is plotted in Fig. 2.5.

The corresponding matrix elements of the reduced density matrix (after integrating out the second spin, say) are given by

$$\begin{aligned}\langle n_1|\rho_1|n_1'\rangle = \sum_{m_2'=-S}^{S}\sum_{S_T,J_T=0}^{2S}\sum_{m_2,p_2=-S}^{S} {}^{2S}C_{S+m_2}\,{}^{2S}C_{S+p_2} \\ \times (\cos\theta/2)^{2S+m_2+p_2}\,(\sin\theta/2)^{2S-m_2-p_2}\exp\left[-i\mathcal{J}(S_T^2 - J_T^2)t/2\right] \\ \times \mathcal{C}^{S,S;S_T}_{S,m_2;S+m_2}\mathcal{C}^{S,S;S_T}_{n_1,m_2';n_1+m_2'}\mathcal{C}^{S,S;J_T}_{S,p_2;S+p_2}\mathcal{C}^{S,S;J_T}_{n_1',m_2';n_1'+m_2'},\end{aligned} \tag{2.25}$$

where $\mathcal{C}$ are the Clebsch-Gordon coefficients and $\mathcal{J}$ is the ferromagnetic coupling. At $t = 0$, this corresponds to a zero entangled state; it remains so for $\theta = 0$ for all $t > 0$. On the other hand, anti-aligned initial spins corresponding to $\theta = \pi$, receive contributions from all total spin sectors as is easy to see from Eq. (2.25). On evolution, the weights of these sectors change, giving rise to a generically entangled state similar to the case of random product states. Other values of θ interpolate continuously between the two above limits.

For $\theta \neq 0$, the product state generically evolves into an entangled one. Note that for times $\mathcal{J}(S_T^2 - J_T^2)t/2$ being a multiple of 2π, the unentangled

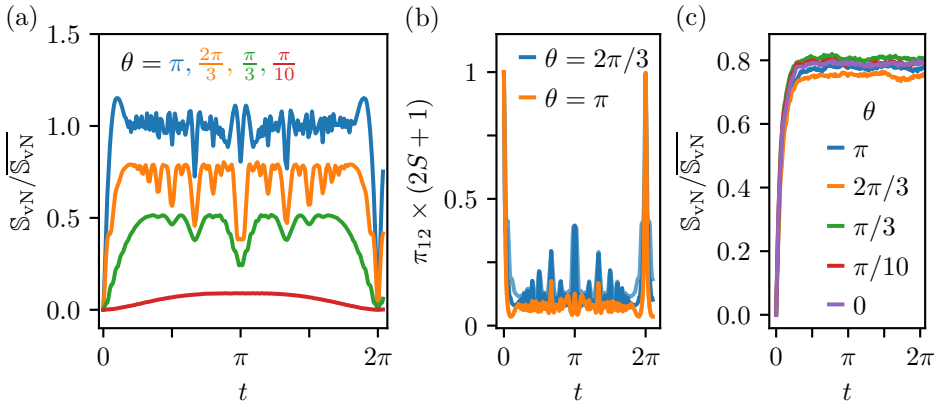

Figure 2.5: *(a) Dynamics of the bipartite von Neumann entropy $\mathbb{S}_{\rm vN}$ for $S = 15$ (normalized to the entanglement entropy for random spins $\overline{\mathbb{S}_{\rm vN}}$) for two spins with different random Bloch states [Eq. (2.8)] with initial values of mutual angle θ. The system is evolved under the ferromagnetic Heisenberg Hamiltonian, see Eq. (2.16) with $\mathcal{J}_k = \delta_{k,1}$. For a pair of antiparallel spins, $\theta = \pi$, the entanglement entropy of completely random states is recovered at certain times. (b) The associated evolution of purity for the product Bloch states where the initial angle between the two spins is $\theta = \pi, \theta = 2\pi/3$. The full recurrences for $t = 2\pi$ are also visible in the purity. (c) The growth of the entanglement $\mathbb{S}_{\rm vN}/\overline{\mathbb{S}_{\rm vN}}$ for Bloch states similar to Fig. 2.5(a), but for $S = 10$ evolved under a random rank-1 Hamiltonian [Eq. (2.18) with $h_{i,\alpha} = 0$ and $\mathcal{J}_{\alpha\beta} \sim \mathcal{N}(0,1)$ averaged over 50 realizations]. Noticeably, the recurrences seen in Fig. 2.5(a) are absent due to reduced symmetry of the Hamiltonian.*

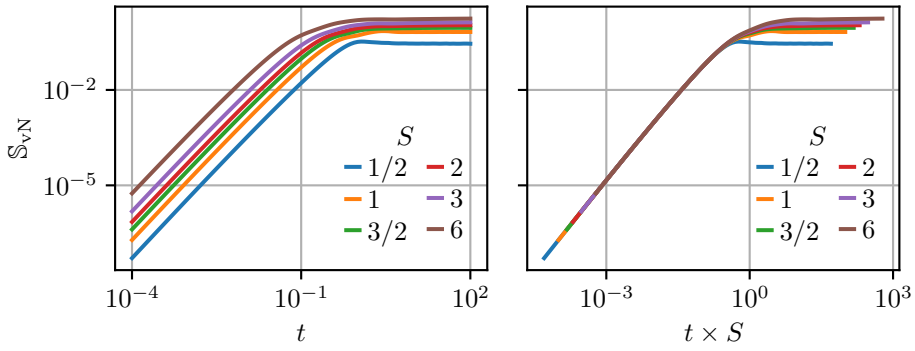

Figure 2.6: *The evolution of the bipartite unnormalized entanglement for two spin-S starting with a random product Bloch states (RBS) and random rank-1 Hamiltonian, Eq. (2.18) with $h_{i,\alpha} = 0$ and $\mathcal{J}_{\alpha\beta} \sim \mathcal{N}(0,1)$, vs time (left) and time scaled by the spin value (right) to show early time collapse. Hence, the entanglement growth is intensive with respect to the Hilbert space dimension for Bloch states.*

state is fully recovered (Fig. 2.5(a) for $\theta = \pi$). However, this recovery is generically not complete at other times and we get many partial recoveries as indicated in Fig. 2.5(a) by dips in the entanglement entropy. Such recurrent recoveries are also seen in the purity (Fig. 2.5(a)) of the first spin $\pi_{12} = \mathrm{Tr}[\rho_1^2]$, where ρ_1 is the reduced density matrix (Eq. (2.2)). The recurrences in purity were also observed in Ref. [34].

These recurrences of lower entangled states are expected to go away for larger number of spins and/or reducing the symmetry of the Hamiltonian. The latter is displayed in Fig. 2.5(c), where a random rank-1 Hamiltonian is used instead of the Heisenberg ferromagnet whence the oscillations in the individual cases average out (averaged over the coupling constants). Noticeably, in Fig. 2.5(c), the entanglement does not reach the Page-limit, but saturates at a value lower than that depending on the details of the RPS such as the angle θ.

At early times ($St \leq 1$), entanglement growth can be scaled as shown in Fig. 2.6. The bipartite entanglement entropy obtained from Eq. (2.25) for short times $\mathcal{J}t < 1$ has the form for $\theta = \pi$:

$$a_S(1 - \log[(St)^2] + b_S)(St)^2 + \mathcal{O}(t^3) \tag{2.26}$$

where all the constants are positive and depend on the spin-size, S. The scaling of time with spin, i.e., $t \to St$ is naturally explained by noticing that the matrix elements of the Hamiltonian that contribute to the entanglement typically scale as S such that for unit coupling constants the time runs faster for larger spins by the same factor [1, 34, 35]. Hence the growth of entanglement can be controlled by appropriately scaling the coupling constant (or distribution of the coupling constant in case of random Hamiltonian).

The above evolution of entanglement vis-a-vis the nature of the wave-function becomes clear by plotting the weight of the wave-function on the Bloch sphere of each spin at different times. This shows (Fig. A.5 of Appendix A.6) a gradual spread of the weight over the Bloch sphere.

2.5.2 Entanglement Dynamics for RPS and RQS

Turning to random product states (RPS), In Fig. 2.7, we plot the average evolution of the bipartite entanglement for random rank-1 Hamiltonians for $S = 1/2 \ldots 5$. Due to the interaction between the two spins, the bipartite entanglement increases as a function of time and saturates to the corresponding Page limit, see Fig. 2.1. Noticeably, the rate of growth of entropy increases with spin-size such that the Page limit is reached faster for larger spins. Further, unlike in the case of the Bloch states, the oscillations are absent for

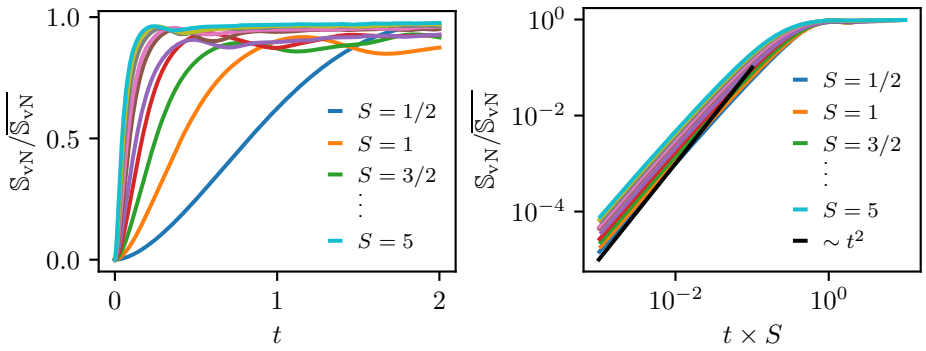

Figure 2.7: *Time evolution of bipartite entanglement starting with RPS under random Hamiltonians [Eq. (2.18) with $h_{i,\alpha} = 0$ and $\mathcal{J}_{\alpha\beta} \in [-1, 1]$ uniform], see Eq. (2.18). The entanglement entropy is averaged over 20 Hamiltonians over 10 different initial states. In the right panel, time is scaled by spin-length (for the same data as the left panel) to reveal the lack of collapse of the entanglement growth compared to the RBS. We also plot the line corresponding to $\sim t^2$ (in black) for comparison. The entropies are renormed using the Page values $\overline{\mathbb{S}_{\mathrm{vN}}}$ from Fig. 2.1.*

RPS in the large S limit even for Heisenberg Hamiltonians for individual configurations (not shown).

The growth of the average entanglement is shown in Fig. 2.7. It is noticeably faster compared to the RBS. Additionally, the growth does not scale with spin length in the same way as the RBS as is evident from Fig. 2.7(b). In absence of the scaling (with S) in the entanglement growth of the RPS, we consider characterizing the growth by considering the time taken to reach a fraction of the Page limit. This is shown for the 50% of the Page limit in Fig. 2.8. Therefore under rescaling of time $t \to St$, while, $t_{50\%}$ goes to infinity for RBS, it vanishes for RPS reiterating the faster entanglement growth for the latter. Indeed, it shows that even under the *natural* rescaling of time, while the classical limit exists for RBS, it does not for RPS. The same observation is made for RQS, for which the entanglement growth appears to be only slightly slower than that for RPS.

2.5.3 The Out-of-Time Ordered Commutators

The above rapid growth of bipartite entanglement leads to scrambling of the quantum state, which is expected to be captured via the temporal evolution of the out-of-time-commutators (OTOCs) defined as

$$\mathrm{OTOC}(\mathcal{O}_{i,\alpha}^{(k_1)}(t), \mathcal{O}_{j,\beta}^{(k_2)}) = \overline{\langle\Psi|[\mathcal{O}_{i,\alpha}^{(k_1)}(t), \mathcal{O}_{j,\beta}^{(k_2)}(0)]^\dagger[\mathcal{O}_{i,\alpha}^{(k_1)}(t), \mathcal{O}_{j,\beta}^{(k_2)}(0)]|\Psi\rangle} \tag{2.27}$$

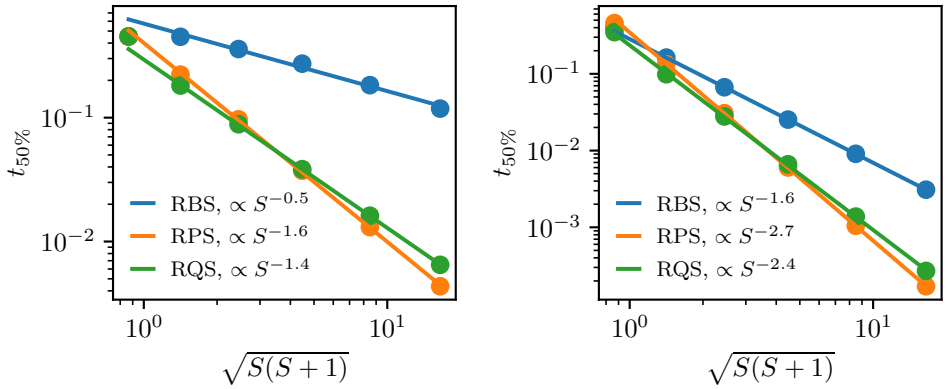

Figure 2.8: *Speed of the averaged entanglement growth. We show time taken to reach 50% of the Page value $\mathbb{S}_{\mathrm{vN}}(t_{50\%}) = \overline{\mathbb{S}_{\mathrm{vN}}}/2 = (\log(2S+1) - 1/2)/2$, where $\mathbb{S}_{\mathrm{vN}}(t)$ is averaged over 10^6 instances. The time $t_{50\%}$ is plotted for RBS, RPS and RQS in dependence of S. The time evolution is generated by a random rank-1 Hamiltonians [Eq. (2.18) with $h_{i,\alpha} = 0$ and $\mathcal{J}_{\alpha\beta} \sim \mathcal{N}(0,1)$] (left) and with a random Hamiltonian as in Eq. (2.17) with $k_1 + k_2 = 3$ and $J_{\alpha\beta}^{(k_1 k_2)} \sim \mathcal{N}(0,1)$ (right). The found exponents vary by about 0.15 when calculating $t_{30\%}$ or $t_{70\%}$. The scaling $\sqrt{S(S+1)}$ is found empirically, $S+1$ would work similarly well but increases the absolute value of the exponents by about 10%.*

where the overline corresponds to averaging over the ensemble of initial states and/or the Hamiltonians. In Fig. 2.9, we plot the OTOC for $\mathcal{O}_1 = S_{1,x}$ and $\mathcal{O}_2 = S_{2,x}$

However starting with Bloch states and evolving with random XYZ Hamiltonians, we find no sign of an exponential growth even for $S = 10$. Instead the growth is power-law and indicates a same scaling as before, i.e., $t \to St$. Further, when compared with Fig. 2.6, it is clear that the saturation of the OTOC at $St \approx 1$ coincides with the entanglement reaching the Page limit in accordance with the notions of quantum scrambling.

2.6 Dynamics of Local Observables

The above entanglement dynamics is intimately connected to that of the local observables. The dynamics of any operator, $\mathcal{O}$ [Eq. (2.7)], is given by the Heisenberg equation of motion such that for a time independent Hamiltonian H, as considered in Sec. 2.4, the expectation value at any subsequent time is given by (we have suppressed various indices for clarity)

$$\langle \mathcal{O}(t) \rangle = \langle \Psi | e^{iHt} \mathcal{O} e^{-iHt} | \Psi \rangle. \tag{2.28}$$

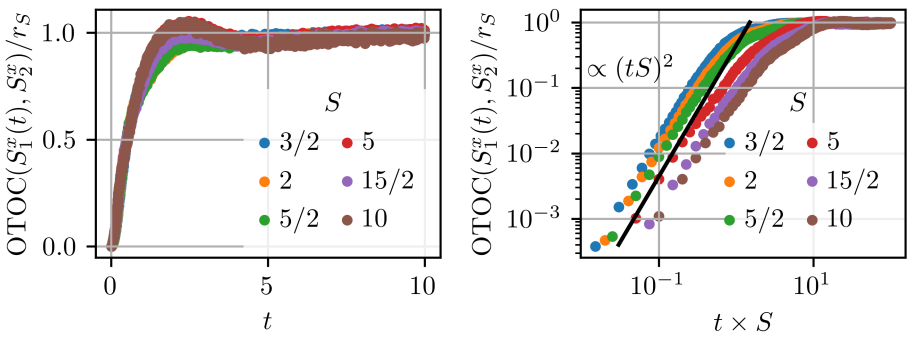

Figure 2.9: *The OTOC for the RBS for random XYZ Hamiltonians on linear scale (left) and log-log scale (right). In both panels, the OTOC is rescaled with* $r_S = \lim_{t\to\infty} \mathrm{OTOC}(S_1^x(t), S_2^x)$*, its long time value, which scales as* $r_S \sim S^2$*. The initial state for both spins is* $|S, m_z = S\rangle$ *and the OTOC results are averaged over 2000 Hamiltonian realizations. The black line indicates* $(tS)^2$*.*

Obtaining the classical equations of motion typically requires decoupling of operator averages to on-site averages as

$$\langle \mathcal{O}_{1,\alpha}^{(k_1)}(t)\mathcal{O}_{2,\beta}^{(k_2)}(t)\rangle \to \langle \mathcal{O}_{1,\alpha}^{(k_1)}(t)\rangle\langle \mathcal{O}_{2,\beta}^{(k_2)}(t)\rangle, \tag{2.29}$$

where the average value corresponds to the classical on-site dynamic variable corresponding to each multipole operator. The corresponding classical "Ehrenfest equations" [Eq. (A.35)] are then obtained from the Heisenberg equations [Eq. (2.16)] as discussed in Appendix A.7.

Now such on-site expectations are given by

$$\langle \mathcal{O}_{1,\alpha}^{(k)}(t)\rangle = \mathrm{Tr}_{12}\left[\hat{\rho}\mathcal{O}_{1,\alpha}^{(k)}(t)\right] = \mathrm{Tr}_1\left[\hat{\rho}_1(t)\mathcal{O}_{1,\alpha}^{(k)}\right], \tag{2.30}$$

where $\hat{\rho} = |\Psi\rangle\langle\Psi|$ is the initial density matrix and $\hat{\rho}_1(t) = \mathrm{Tr}_2\left[\hat{\rho}(t)\right]$ is the reduced density matrix at time t.

The rapid growth of the bipartite entanglement all the way to the Page limit for the classes of states discussed in the previous section, therefore, indicates that the reduced density matrix is very close to identity (or infinite temperature Gibbs form) such that the expectation values of all the local/on-site observables decay to their infinite temperature value in accordance with the expectation from ETH, i.e.,

$$\langle \mathcal{O}_{1,\alpha}^{(k)}(t)\rangle \to \mathrm{Tr}_1\left[\mathcal{O}_{1,\alpha}^{(k)}\right] \to 0 \tag{2.31}$$

for all traceless operators. Thus the rapid growth of entanglement is accompanied by the decay of the on-site expectation values possibly invalidating the local (on-site) description even in the limit of $S \to \infty$.

To understand this, we particularly concentrate on the first two moments, namely the dipole and the quadrupole. For the dipole, we focus on the evolution of the component of the on-site spin operators given by $\langle\Psi|S_i^\alpha(t)|\Psi\rangle$, where $|\Psi\rangle$ can be various two-spin wave functions discussed in Sec. 2.3 and $S_i^\alpha(t)$ is the $\alpha = x, y, z$ component of the spin/dipole operator at site $i = 1, 2$, in the Heisenberg picture at time t. For brevity, we may denote expectation values as $\langle S_i^\alpha(t)\rangle$, omitting the dependence on the initial state Ψ. In addition, we also study the evolution of the on-site quadrupole operators in Eq. (2.9).

For $S > 1/2$, the decoupling in Eq. (2.29) requires further attention since any multipole operator of rank $k > 1$ can be expressed as a function of the three spin operators S_i^α of the respective site, i.e., $\mathcal{O}_{i,\alpha}^{(k_i)} = f_\alpha^{k_i}(S_i)$ where the functional form for the quadrupole (rank-2) is given by Eq. (2.9) and the generic structure is discussed in Appendix A.1. Thus, in presence of higher rank operators differenct choices for decoupling exist.

For now, we focus on the simplest case and do not decouple the $\mathcal{O}_{i,\alpha}^{(k_i)}$ further. The classical equations of motions are obtained by introducing a classical variable $\mathcal{O}_{i,\alpha}^{\mathrm{cl},(k_i)}$ for each operator $\mathcal{O}_{i,\alpha}^{(k_i)}$ and deriving their classical equations of motions. They are obtained by replacing the commutator with the generalized Poisson brackets as explained in Appendix A.7. For dipole operators this procedures corresponds to obtaining the normalized expectation value of the spin operators at the initial time t_0, i.e.,

$$M_i^\alpha(t_0) = \frac{\langle S_i^\alpha(t_0)\rangle}{\sqrt{\sum_\alpha \langle S_i^\alpha(t_0)\rangle^2}}, \tag{2.32}$$

and calculating the time evolved $M_i^\alpha(t)$ using the spin Poisson bracket as $\{f, g\} = -\epsilon_{\alpha\beta\gamma}\frac{\partial f}{\partial M^\alpha}\frac{\partial g}{\partial M^\beta}M^\gamma$ with specified initial conditions. These are then used to calculate the time evolution of $M_i^\alpha(t)$ and, hence, can be considered the *conventional classical limit*.

The deviation from the classical trajectories can be characterized via

$$\Delta\left(S_i^\alpha(t)\right)) = |\langle S_i^\alpha(t\,\mathcal{T})\rangle/\mathcal{S} - M_i^\alpha(t)|, \tag{2.33}$$

where the first (second) term is the quantum (classical/Poisson) evolution for the same initial product state and $\mathcal{T}, \mathcal{S}$ are potentially S dependent rescaling factors which need to be determined.

We study the deviation for a random Hamiltonian with initial states being RPS and Bloch states in Fig. 2.10. To make different spin sizes and RPS comparable, we generate the RPS and then rotate them so that their dipole moment aligns with the z axis. Hence for a given Hamiltonian, all aligned RPS should converge to the same classical equations of motions. However, up to $S = 16$, there is no convergence, Fig. 2.10 (left). Conversely, for

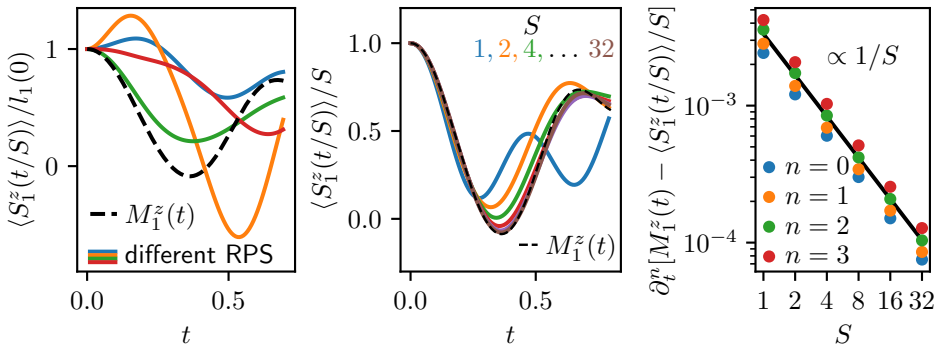

Figure 2.10: *Comparison of the quantum and classical equations of motions (Eq. (2.29)) for RPS (left) and RBS (center, right). We pick one Hamiltonian at random, see Eq. (2.18) with $J_{\alpha\beta} \sim \mathcal{N}(0,1)$ and $h_{i,\alpha} = 0$. We find qualitative similar results for different Hamiltonians. Left: We generate four random product states for $S = 16$ and rotate them to align them with the z-axis. We rescale the expectation values with the initial spin length $l_1^2(t) = \sum_\alpha \langle S_1^\alpha(t)\rangle^2$. Up to $S = 16$, the quantum values $\langle S_1^z(t)\rangle$ do not converge to the classical ones $M_1^z(t)$. Center: For initial product Bloch states $|m_z = S\rangle|m_z = S\rangle$, we find $\langle S_1^z(t/S)\rangle/S \to M_1^z(t)$ with increasing spin size S for the same Hamiltonian. Right: Higher orders in time converge as $\partial_t^n[M_1^z(t) - \langle S_1^z(t/S)\rangle/S] \propto 1/S$ at $t = 10^{-2}$. Note that the derivatives are rescaled to be of the same order of magnitude for visual purposes.*

Bloch states, the expectation values $\langle S_i^\alpha(t)\rangle$ converge to $M_i^\alpha(t)$ up to rescaling time and values as shown in Fig. 2.10 (center). This can be quantified by Taylor expanding $\Delta(S_i^\alpha(t))$. In Fig. 2.10 (right) we show that the first three expansion coefficients decay as $1/S$ in spin length.

More insights can be obtained by calculating the evolution of the spin-length defined as,

$$l_i^2(t) = \sum_\alpha \left(\langle S_i^\alpha(t)\rangle\right)^2 . \tag{2.34}$$

The spin length is compared to the classical spin length $\sum_\alpha (M^\alpha(t))^2 = S^2$, which is constant in time. For Bloch states, the quantum spin length coincides with the classical one $l_i^2(0)/S^2 = 1$. This is plotted in Fig. 2.11 for RBS evolved by random Hamiltonians. The initial quadratic growth in $1 - l_i^2/S^2$ is expected (same reasoning is true for the initial t^2 growth in Fig. 2.10) from the short time expansion of Eq. (2.28), i.e.,

$$\langle \mathcal{O}(t)\rangle = \langle \mathcal{O}\rangle - it\langle [\mathcal{O}, H]\rangle - \frac{t^2}{2}\langle [[\mathcal{O}, H], H]\rangle + \cdots \tag{2.35}$$

The constant of proportionality for growth is $\sim S$ such that under $t \to St$,

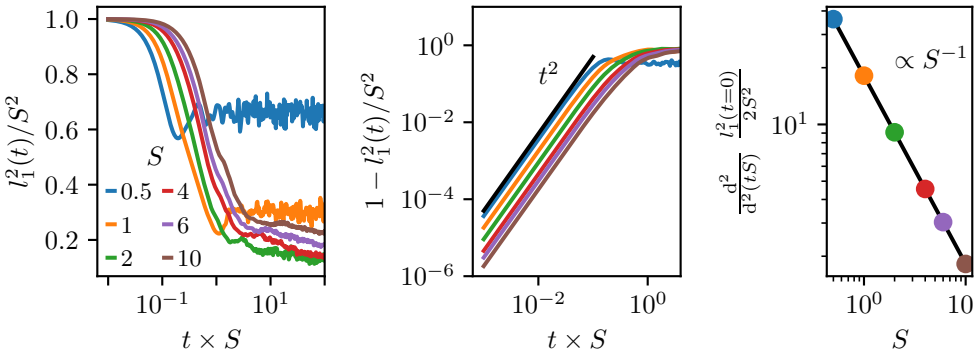

Figure 2.11: *Time evolution for a random Hamiltonian, see Eq. (2.18) with $J_{\alpha\beta} \sim \mathcal{N}(0,1)$ and $h_{i,\alpha} = 0$, and random initial Bloch states averaged over 100 realizations. The decay of the spin length is shown in the first panel, renormed with S^2. In the second panel we plot the renormed decay on a logarithmic scale to show the quadratic scaling at small times and obtain the prefactor, which is shown in the right panel. These results indicate that for Bloch states $1-l^2(t)/S^2 \propto (tS)^2/S$.*

the decay vanishes in the $S \to \infty$ limit, see Fig. 2.11(right). This scaling is consistent with the entanglement growth studied in the previous section.

For RPS, already the initial spin length renormed by S^2 decays to 0. This can be made plausible by noting that the ensemble averaged spin length is proportional to the ensemble variance of the expectation value

$$\overline{\overline{l_1^2(0)}} = \sum_\alpha \overline{\overline{\langle S_1^\alpha \rangle^2}} = 3\overline{\overline{\langle S_1^\alpha \rangle^2}} = 3\mathrm{Var}_{\mathrm{RPS}}[\langle S_1^\alpha \rangle] \tag{2.36}$$

and we expect relative fluctuations to decay with increasing Hilbert space size for Haar random states. This can be confirmed through a random matrix theory calculation, which yields $l_1^2(0) \propto S$, see Appendix D.2 using that $V|0\rangle$ is a Haar random state for V being Haar random. The results for the decay of the spin length in time are shown in Fig. 2.12. For RPS, we find an initial decay of the spin length with time $\propto t^2$, similar to RBS, as expected from our previous analysis, Eq. (2.35). However, this quadratic part decays far slower with S and may even converge to being constant in S, see Fig. 2.12(right). As a result, the decay of the initial spin length does not slow down for RPS like for RBS. This shows that for RPS even with large S, the dynamics does not become as stable as for RBS.

Since quadrupoles have a vanishing spin length, we study the behavior of rank-2 spherical tensor operators such as $\mathcal{O}^{(2)}_{i,xz} = S_1^x S_1^z + S_1^z S_1^x$. We find that for quadrupoles, the quantum expectation values do not converge to the naive classical equations of motion in the limit $S \to \infty$. We illustrate this observation with the following example.

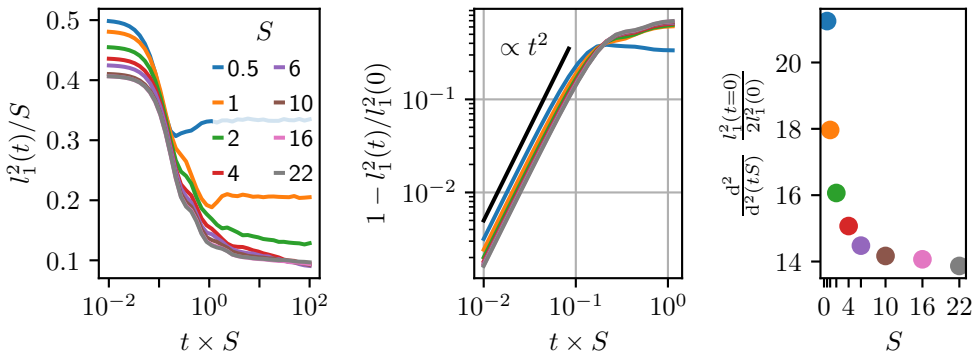

Figure 2.12: *Spin length decay for random product states (RPS) analogous to Fig. 2.11 averaged over 10^4 realizations. The decay of the spin length is shown in the first panel, renormed with the scaling factor S expected from Weingarten calculus (see App. D.2). In the second panel we plot the decay renormed on a logarithmic scale to verify the small times quadratic scaling and obtain the prefactor, which is shown in the right panel. These results indicate that for random states $1 - l_1^2(t)/l_1^2(0) \propto (tS)^2$ and are consistent with $l_1^2(0) \propto S, l_1^2(\infty) \propto S$ for large S.*

Quadrupole illustrative example Next, we discuss a simple example for which the naive classical equations of motion differ from the time dependent quantum expectation values in the limit $S \to \infty$. This reflects the fact that Ehrenfest's equation of motion yield particularly straightforward prescriptions for a quantum-to-classical correspondence of the equations of motion only in simple settings, such as for the harmonic oscillator. For more complex equations of motion and initial states, the fact that expectation values of functions of observables need not be equal to the functions evaluated for the expectation values of the observables leads to the failure of such straightforward prescriptions.

Against the difficulty of deriving semiclassical equations of motion in closed form, our example will illustrate that a well-defined semiclassical limit $S \to \infty$ can nonetheless emerge. The Hamiltonian we consider is

$$H = (S_1^x S_1^z + S_1^z S_1^x) S_2^y. \tag{2.37}$$

We aim to describe the dynamics of $S_2^x S_2^x$ for the initial quadrupole product state $|m_z = 0\rangle_1 |m_z = 0\rangle_2$.

For the classical equations of motion, we use the generalized Ehrenfest equations, Appendix A.7. They correspond to replacing each of the Hermitian operators by scalars $S_i^\alpha S_i^\beta + S_i^\beta S_i^\alpha \to c_i^{\alpha\beta}$ and replacing $\langle \mathcal{O}_{1,\alpha}^{(k_1)} \mathcal{O}_{2,\beta}^{(k_2)} \rangle \to \langle \mathcal{O}_{1,\alpha}^{(k_1)} \rangle \langle \mathcal{O}_{2,\beta}^{(k_2)} \rangle$, as stated in Eq. (2.29).

We can straightforwardly derive the classical, first order equations of mo-

tion

$$\frac{\mathrm{d}\langle S_2^x S_2^x\rangle}{\mathrm{d}t} = i\langle[H, S_2^x S_2^x]\rangle = \langle(S_1^x S_1^z + S_1^z S_1^x)(S_2^x S_2^z + S_2^z S_2^x)\rangle \tag{2.38}$$

$$\to \langle S_1^x S_1^z + S_1^z S_1^x\rangle\langle S_2^x S_2^z + S_2^z S_2^x\rangle. \tag{2.39}$$

To obtain a closed set of equations, we therefore also need to evaluate

$$\frac{\mathrm{d}\langle S_2^x S_2^z + S_2^z S_2^x\rangle}{\mathrm{d}t} = \langle(S_1^x S_1^z + S_1^z S_1^x)(S_2^z S_2^z - S_2^x S_2^x)\rangle \tag{2.40}$$

$$\to \langle S_1^x S_1^z + S_1^z S_1^x\rangle\langle S_2^z S_2^z - S_2^x S_2^x\rangle. \tag{2.41}$$

as well as

$$\frac{\mathrm{d}\langle S_2^z S_2^z\rangle}{\mathrm{d}t} \to -\langle S_1^x S_1^z + S_1^z S_1^x\rangle\langle S_2^x S_2^z + S_2^z S_2^x\rangle. \tag{2.42}$$

Rewriting in terms of the classical scalars yields

$$\frac{\mathrm{d}c_2^{xx}}{\mathrm{d}t} = 2c_1^{xz}c_2^{xz}, \quad \frac{\mathrm{d}c_2^{zz}}{\mathrm{d}t} = -2c_1^{xz}c_2^{xz}, \tag{2.43}$$

$$\frac{\mathrm{d}c_1^{xz}}{\mathrm{d}t} = 0, \quad \frac{\mathrm{d}c_2^{xz}}{\mathrm{d}t} = c_1^{xz}(c_2^{zz} - c_2^{xx})/2. \tag{2.44}$$

We can solve them by noting that the initial values are

$$c_2^{xx}(t=0) = S(S+1), \tag{2.45}$$

$$c_2^{zz}(t=0) = c_2^{xz}(t=0) = c_1^{xz}(t=0) = 0. \tag{2.46}$$

Hence, all time derivatives in Eq. (2.44) vanish, so that the prediction of these naive classical equations of motion are constant values for these observables.

However, this is not the case for the quantum equations of motion. For that, we calculate the second derivative

$$\frac{\mathrm{d}^2\langle S_2^x S_2^x\rangle}{\mathrm{d}t^2} = -\langle[H,[H, S_2^x S_2^x]]\rangle \tag{2.47}$$

$$= 2\langle(S_1^x S_1^z + S_1^z S_1^x)^2(S_2^z S_2^z - S_2^x S_2^x)\rangle = S(S+1)S(S+1)/2\ . \tag{2.48}$$

This is nonvanishing, so that in the quantum system, the expectation value of the Heisenberg evolved operators has a non-trivial time dependence. Furthermore, upon rescaling the operators with $\sqrt{S(S+1)}$ as well as time with $1/\sqrt{S(S+1)}$, we find the equations of motion to converge, as is also evident for the second order derivative from Eq. (2.48). This is shown in the numerical solution for difference values of S in Fig. 2.13.

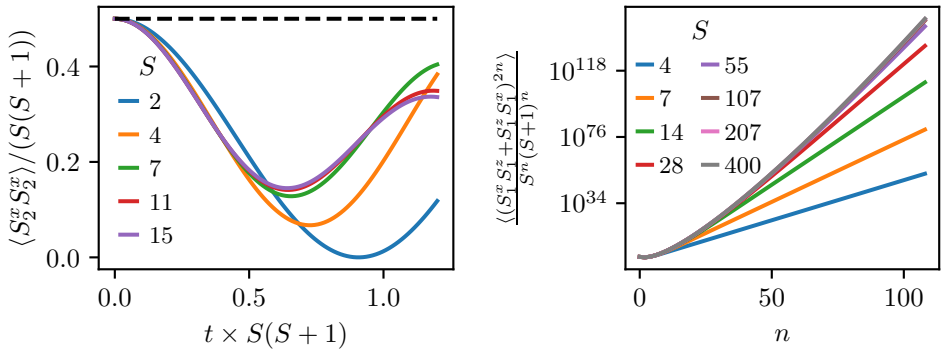

Figure 2.13: *Left: Numerical results for the time evolved expectation value of $S_2^x S_2^x$ with H given by Eq. (2.37). A converged regime emerges for large S. The rescaling factor $S(S+1)$ has been found empirically and is consistent with the expected scaling $S_i^\alpha S_j^\beta \sim S(S+1)$. Right: Numerical results for the derivatives, Eq. (2.48). The derivatives converge for $S \to \infty$ towards a growth faster than exponential.*

Through iteration, one finds the explicit equations for the higher-order correlators

$$\left.\frac{\mathrm{d}^{2n}\langle S_2^x S_2^x(t)\rangle}{\mathrm{d}t^{2n}}\right|_{t=0} = \tag{2.49}$$

$$(-4)^n \langle (S_1^x S_1^z + S_1^z S_1^x)^{2n} (S_2^z S_2^z - S_2^x S_2^x)\rangle/2 \tag{2.50}$$

$$= -(-4)^{n-1} S(S+1) e_n,$$

where $e_n = \langle m_z = 0 | (S_1^x S_1^z + S_1^z S_1^x)^{2n} | m_z = 0 \rangle$. They converge in the limit $S \to \infty$, see Fig. 2.13(right). Since the e_n do not converge to a simple exponential growth, it appears as every higher moment contains more information, not included in any lower moment—a simple reduction of all moments to a product of lower moments in a semiclassical description does not seem possible.

2.7 Monitored Dynamics and Local Observables

The uncontrolled growth of entanglement for generic states and Hamiltonians under unitary quantum dynamics therefore threatens to invalidate the approach to the semiclassical limit as $S \to \infty$. However, most quantum systems do not undergo fully unitary evolution, e.g., due to being in contact with a bath. The effects of such nonunitarity on the dynamics of different observables are rather non-trivial, and are the subject of much recent research such as that under the heading of measurement-induced phase transitions [36].

This particularly can result in the arrest of the entanglement growth well before a Page limit is reached.

To investigate this in the present context, we study two different protocols which involve periodically resetting the entanglement to zero, and which can be implemented in modern quantum simulator platforms. The first we call classical co-moving resetting (Sec. 2.7.1), and, the second projective measurement (Sec. 2.7.2).

2.7.1 Classical Co-Moving Resetting

This periodic classical resetting protocol for our two-spin system involves, after a quantum time evolution of both spins, resetting one of the spins to its *classical* state at regular intervals using the classical equations of motion, Eq. (2.29) and Appendix A.7, as follows:

1. We start with initializing both spins to (a) Bloch states in the first scenario or (b) quadrupolar states in the second scenario yielding the density matrix
$$\rho_0 = |\Psi_1\rangle\langle\Psi_1| \otimes |\Psi_2\rangle\langle\Psi_2|. \tag{2.51}$$
2. This is evolved for time τ with the Hamiltonian H to obtain
$$\rho_0(\tau) = e^{-iH\tau}\rho_0 e^{iH\tau}. \tag{2.52}$$
3. Next, we trace out the first spin, yielding a density matrix for the second spin
$$\rho_2 = \mathrm{Tr}_1\rho_0(\tau). \tag{2.53}$$
4. The first spin is then reset to a Bloch or quadrupolar state $|\vec{\mathcal{O}}_1^{\mathrm{cl}}(\tau)\rangle$ whose expectation values are in agreement with the predictions of the classical equations of motion $\vec{\mathcal{O}}_1^{\mathrm{cl}}(\tau)$ at time τ:
$$\langle\vec{\mathcal{O}}_1^{\mathrm{cl}}(\tau)|\mathcal{O}_{1,\alpha}^{(k_1)}|\vec{\mathcal{O}}_1^{\mathrm{cl}}(\tau)\rangle = \mathcal{O}_{1,\alpha}^{\mathrm{cl},(k_1)}(\tau). \tag{2.54}$$
After resetting, the density matrix of the first spin is
$$\rho_{1,\mathrm{reset}} = |\vec{\mathcal{O}}_1^{\mathrm{cl}}(\tau)\rangle\langle\vec{\mathcal{O}}_1^{\mathrm{cl}}(\tau)|. \tag{2.55}$$
Thus at time $\tau + 0^+$, the density matrix of the system is reset to
$$\rho = \rho_{1,\mathrm{reset}} \otimes \rho_2. \tag{2.56}$$
5. We iterate this procedure at step 2. using ρ at a frequency $1/\tau$ and compare the difference between the classical evolution of the dipole and quadrupole operators for the second spin, $\vec{\mathcal{O}}_2^{\mathrm{cl}}(\tau)$, with the expectation value obtained via the above resetted quantum dynamics.

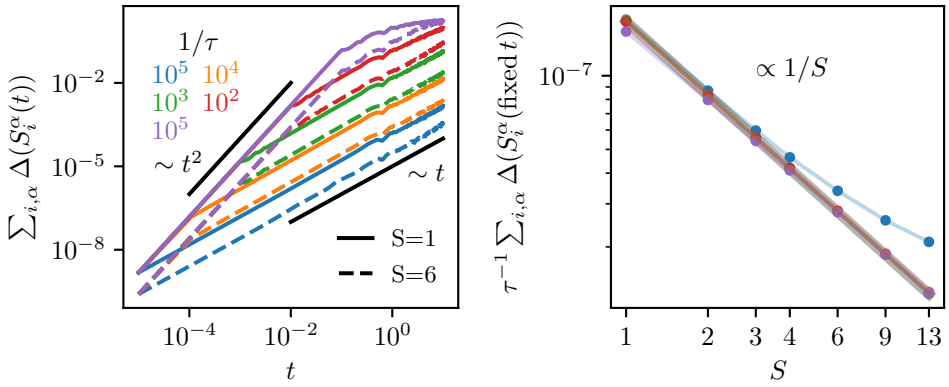

Figure 2.14: *Results for the deviations $\Delta(S_i^\alpha)(t) = |\langle S_i^\alpha(t/S)\rangle/S - M_i^\alpha(t)|$ [Eq. (2.33)] summed over $\alpha \in \{x, y, z\}$ and sites i for the reset protocol with Bloch states. The results are averaged over 10 Hamiltonians, specified in Eq. (2.18), with $h_{i,\alpha} = 0$ and $\mathcal{J}_{\alpha\beta} \sim \mathcal{N}(0, 1)$. Empirically, we find the rescaling factors $\mathcal{S} = 1/\mathcal{T} = S$. We vary the reset frequency $1/\tau$ and the spin length and show the averaged, summed deviations as a function of time (left) and spin length for fixed $t = 0.1$ (right). Upon rescaling with τ, the deviations collapse (left, colors refer to the same frequencies as in the right panel). This yields a scaling of $\Delta(S_i^\alpha(t)) \propto t\tau/S$ for $t > \tau$.*

Bloch States We begin with initializing the spins to Bloch states and resetting the first spin to Bloch states as well. For the time evolution, we consider random Hamiltonians of the form

$$H = \sum_{\alpha,\beta\in\{x,y,z\}} c_{\alpha,\beta} S^\alpha \otimes S^\beta, \tag{2.57}$$

with $c_{\alpha,\beta}$ normal distributed and symmetric $c_{\alpha,\beta} = c_{\beta,\alpha}$.

The results for the deviation of the classical values and quantum expectation values are shown in Fig. 2.14(left). We observe a clear linear growth in time. The deviation scales as $|\mathcal{O}_2^{\text{cl},\alpha}(t) - \langle S_2^\alpha(t/S)\rangle/S| \sim t\tau/S$ as is clear from the combination of the results presented in Fig. 2.14.

Quadrupolar states Next, we turn our attention to quadrupolar states. We initialize both spins to the quadrupolar state $|S, m_z = 0\rangle$ and resetting the first spin to a quadrupolar state following the same co-moving classical resetting protocol as elaborated above. However, for the time evolution, we consider random Hamiltonians of the form

$$H = \sum_{\alpha,\beta,\gamma\in\{x,y,z\}} c_{\alpha,\beta,\gamma} S^\alpha \otimes (S^\beta S^\gamma + S^\gamma S^\beta) + c_{\alpha,\beta,\gamma}(S^\beta S^\gamma + S^\gamma S^\beta) \otimes S^\alpha, \tag{2.58}$$

with $c_{\alpha,\beta,\gamma}$ normal distributed.

These rank-1–rank-2 Hamiltonians generate the simplest non-trivial classical equations of motion using the generalized Ehrenfest equations, see Appendix A.7. For Hamiltonians of the form $S_1^\alpha S_2^\beta$, the time derivatives of the classical variables are zero, so that the classical variables never evolve. Hence, the lowest rank Hamiltonian with non-constant classical dynamics is of the form Eq. (2.58). Note that these Hamiltonians also have the advantage for initial quadrupolar states to never couple the classical variables corresponding to rank-2 operators $\mathcal{O}_{i,\alpha}^{\mathrm{cl},(2)}$ to any variables corresponding to higher rank operators $\mathcal{O}_{i,\alpha}^{\mathrm{cl},(k>2)}$. Hence, the classical equations of motion can be simulated by only considering variables corresponding to rank-2 operators $\mathcal{O}_{i,\alpha}^{\mathrm{cl},(2)}$.

The results are reported in Fig. 2.15. Again, we find a scaling of the deviation as

$$E^{\alpha\alpha}(t) = |\mathcal{O}_{2,\alpha\alpha}^{\mathrm{cl},(2)}(t) - \langle [S_2^\alpha S_2^\alpha](t\mathcal{T})\rangle/\mathcal{S}| \sim \tau t, \tag{2.59}$$

with $\mathcal{T}, \mathcal{S}$ rescaling parameters to be determined. We find similar results for other operators, but focused on these for simplicity. The results are shown in Fig. 2.15. We find that $E^{\alpha\alpha}$ is constant in the spin length for large spins. This is qualitatively different from RBS, where we found the quantum equations of motion to converge to the classical ones for $S \to \infty$. This is in agreement with earlier results discussed in Section 2.6, where we also found the quadrupolar states to not converge to the classical equations of motion with increasing spin size. This behavior is similar to the spin length decay of RPS, which also appeared to be independent of S, see Fig. 2.12. These results appear to be consistent with the entanglement dynamics discussed in Section 2.5, which is similar for RPS and RQS, while the entanglement grows slower for RBS. In conclusion, with the reset protocol, we can stabilize the dynamics for longer times by increasing the reset frequency. In the next section, we present a second approach to stabilize classical dynamics.

2.7.2 Projective Evolution

In the previous section, we reset the first spin to the state expected from the classical equations of motion. In this section, we reset the entire state by projecting it back on the manifold of classical states, i.e., product Bloch states

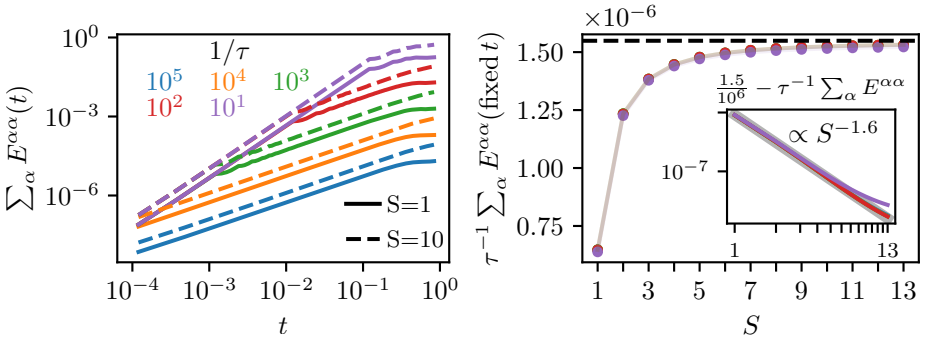

Figure 2.15: *Results for the summed deviations $E^{\alpha\alpha} = |\mathcal{O}^{\mathrm{cl},(2)}_{2,\alpha\alpha} - \langle S^\alpha_2 S^\alpha_2\rangle|$, $\alpha \in \{x, y, z\}$, for the reset protocol with quadrupolar states $|m_z = 0\rangle|m_z = 0\rangle$. The results are averaged over 10 random Hamiltonians, drawn at random as specified in the main text, Eq (2.58). The rescaling factor $1/\mathcal{T} = \mathcal{S} = S(S+1)$ for time is found empirically. We vary the reset frequency $1/\tau$ and the spin length S in the left panel. Similar to the RBS, $E^{\alpha\alpha}(t)$ grows initially with t^2 for $t < \tau$ and with t for $t > \tau$. In the right panel $t = 0.12$ is fixed and we multiply the deviations with τ^{-1}. We find the deviations to converge to a constant value with S. This is probed in the inset by subtracting the deviations from the estimated value 1.5×10^{-6} the results are converging to. The results yield a functional form of $E^{\alpha\alpha} \propto t\tau(1 + O(S^{-1.6}))$. Similar results were obtained for other observables of rank 2.*

or product quadrupolar states. This projective evolution protocol resets the bipartite entanglement to zero and hence can help recover the classical limit. The point on the manifold that we reset the state to is determined by measuring the respective operators. A primary issue in this regard is the observable that is being measured. For a spin S, there are $(2S+1)^2 - 1$ on-site observables of the form given by Eq. (2.7) that do not necessarily commute with each other. In continuation to the previous subsection, we restrict ourselves to measuring only rank 1 and 2, i.e., dipole and quadrupole, operators. Note that generically $[S^\alpha, S^\beta] \neq 0$, $[S^\alpha, \mathcal{Q}^{\beta\gamma}] \neq 0$ as well as $[\mathcal{Q}^{\alpha\beta}, \mathcal{Q}^{\gamma\delta}] \neq 0$ and, hence, the nature of the evolution depends on the details of the protocol used for projection. Below, we elaborate on a protocol to recover classical evolution by choosing to project one set of observables (dipoles or quadrupoles) along their respective classical trajectories at finite intervals.

Bloch states We first consider the evolution with dipolar projection. The protocol is as follows :

1. Start with a two-spin random (product) Bloch state (RBS) of the form in Eq. (2.8).

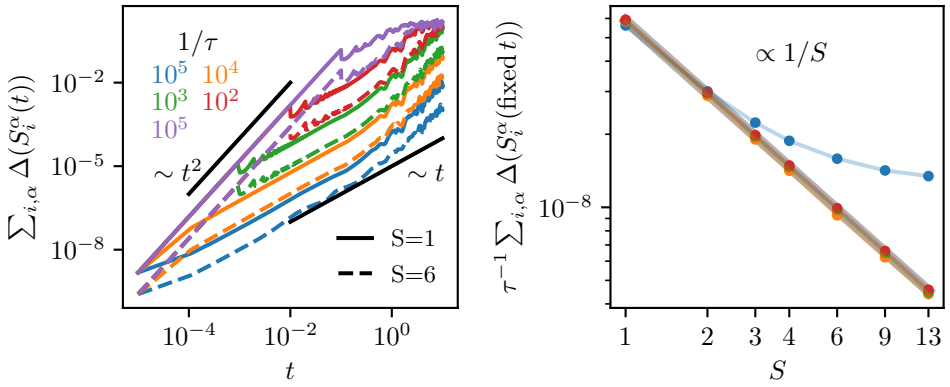

Figure 2.16: *Results for the deviations $\Delta(S_i^\alpha)(t)$ [Eq. (2.33)] summed over $\alpha \in \{x, y, z\}$ and sites i with initial Bloch states as in Fig. 2.14, but with projective measurements instead of resets. Empirically, we find the same rescaling factors like before $\mathcal{S} = 1/\mathcal{T} = S$. In the right panel, we fix $t = 0.1$. Upon rescaling with τ, the deviations collapse (left) to the same scaling like for the reset protocol $\Delta(S_i^\alpha(t)) \propto t\tau/S$ for $t > \tau$.*

2. Perform a time evolution according to some Hamiltonian for a time τ yielding $|\Psi(\tau)\rangle = e^{-iH\tau}|\Psi(\tau)\rangle$. Hence, projections are performed with frequency $1/\tau$.

3. Calculate the expectation of the dipole moments $\langle\Psi(\tau)|S_i^\alpha|\Psi(\tau)\rangle$ for $\alpha \in \{x, y, z\}$ and both sites $i \in \{1, 2\}$ to obtain the expected orientation of the moment at site i. Let these directions be respectively specified by $\tilde{\Omega}_1 \equiv (\theta_1, \phi_1)$ and $\tilde{\Omega}_2 \equiv (\theta_2, \phi_2)$ on the Bloch spheres of the two spins.

4. Project on the classical manifold $|\Psi(\tau)\rangle \to |\tilde{\Omega}_1\rangle \otimes |\tilde{\Omega}_2\rangle$.

5. Continue with this new state as initial state from step 2 on.

The results of this procedure are shown in Fig. 2.16 for an average over random Hamiltonians without Zeeman-field given by Eq. (2.57). We first plot the difference, $\Delta(S_i^\alpha(t))$ as defined in Eq. (2.33), between the projected quantum evolution and classical trajectories of the two spins as a function of time for different spin lengths $S = 1 \ldots 13$ and projection frequencies. The plot indicates that for the same rate of projection, the growth of the difference slows down with increasing S. Further the deviation decreases on increasing the frequency of projection. Overall, we find $\Delta(S_i^\alpha(t)) \propto t\tau/S$, which is the same scaling behavior we also found for the resetting protocol shown in Fig. 2.14. This implies that the average direction on the Bloch sphere agrees

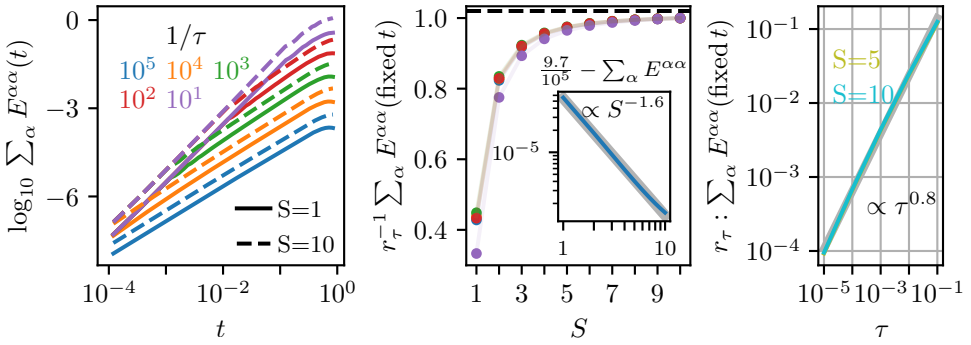

Figure 2.17: *Results for the summed deviations $E^{\alpha\alpha} = |\mathcal{O}^{\mathrm{cl},(2)}_{2,\alpha\alpha} - \langle S_2^\alpha S_2^\alpha\rangle|$ for the projection protocol with quadrupolar states $|m_z = 0\rangle|m_z = 0\rangle$, analogously to Fig. 2.15. The results are shown for a typical Hamiltonian and not averaged due to instabilities of the protocol occurring for all examples at some times, see Appendix A.3. The Hamiltonians are drawn at random as specified in the main text, Eq. (2.58). The rescaling for time $S(S+1)$ is found empirically. We vary the reset frequency $1/\tau$ and the spin length S in the left panel. In the central panel $tS(S+1) = 0.12$ is fixed and we multiply the deviations with a rescaling factor $r_\tau = E^{\alpha\alpha}(t = 0.12, S = 10)$, shown in the right panel. Again, the deviations converge with S as $S^{-1.6}$ (inset for $\tau = 10^{-5}$). This indicates a functional form of $E^{\alpha\alpha} \propto t\tau^{0.8}(1 + O(S^{-1.6}))$. Similar results were obtained for other Hamiltonians and observables of rank 2.*

with the classical equations of motions. The vanishing deviation between classical and quantum values follows from the construction: By resetting the states to product states at time t_i, the first order derivatives of the classical and quantum equations of motion coincide at t_i, see Appendix A.3. The error induced by the second order derivatives disagreeing is suppressed in τ and vanishes with increasing projection frequency, similar to the Zeno effect.

In summary, the dipolar measurements do make the time evolution follow the classical one increasingly closely, stabilizing the classical trajectories. Furthermore we can observe again a manifestation of the Ehrenfest time effect for Bloch states like in the previous sections: for larger spins the quantum evolutions follows the classical evolution closely for a longer time.

Quadrupolar states For the projection of the quadrupole, we replace the 3rd and 4th step of the previous protocols as follows :

3′. Measure the on-site quadrupole moments $\mathcal{O}_i^{\mathrm{meas},\alpha} = \langle\Psi(\tau)|\mathcal{Q}_i^\alpha|\Psi(\tau)\rangle$ for $i = 1, 2$ and $\alpha \in \{xx, xy, xz, yy, yz, zz\}$. It is then possible to construct product pure quadrupolar states $|\vec{\mathcal{O}}_i^{\mathrm{meas}}\rangle$ (outlined in Appendix A.2)

whose expectation values agree with the measured ones

$$\langle \vec{\mathcal{O}}_i^{\text{meas}} | \mathcal{O}_i^{\alpha} | \vec{\mathcal{O}}_i^{\text{meas}} \rangle = \mathcal{O}_i^{\text{meas},\alpha}. \tag{2.60}$$

4′. Project on the classical manifold of product quadrupolar states like before $|\Psi(\tau)\rangle \to |\vec{\mathcal{O}}_1^{\text{meas}}\rangle \otimes |\vec{\mathcal{O}}_2^{\text{meas}}\rangle$.

Like specified in Eq. (2.58) in the previous section, we consider Hamiltonians which generate classical equations of motion that only couple rank 2 operators to other rank 2 operators for initial quadrupolar states. The results are shown in Fig. 2.17. We note that the protocol appears to be numerically unstable, see Appendix A.3. Hence, we focus on the results for a particular instance in Fig. 2.17. The results are the same as for the resetting protocol, except for the scaling with the projection frequency $1/\tau^{0.8}$.

2.8 Conclusions

In the second chapter of this thesis, we provided a detailed characterization and discussion of the behavior of a two spin S system in the limit $S \to \infty$. For product states composed of two random Bloch states and low-rank Hamiltonians, we can confirm the expectation and all studied quantities approach a classical behavior in the limit of large spin size. In these configurations, the relative entanglement growth slows down with increasing spin size, the spin length decay slows down, and the quantum equations of motion approach the classical ones in the limit of large S. In this scenario, the semiclassical limit stabilizes the quantum evolution. Alternatively, it can be stabilized by monitoring the system with increasing frequency, as we have shown for two different protocols.

For random product states and random quadrupolar states, the results are rather different. In both cases, the relative entanglement growth does not vanish in the limit of large spin sizes. Moreover, the spin-length decay appears to approach a constant rate with increasing spin size, rather than slowing down. For quadrupolar states, the quantum equations of motion converge with increasing spin size, but not to the generalized classical equations of motion. Stated differently, monitoring can stabilize the classical equations of motion, but this stabilization is not enhanced by increasing the spin size.

This shows that for a semiclassical limit to exist, all three parts in a quantum system have to possess structure: the initial state, the Hamiltonian and the observable. For random product states, a semiclassical limit does not exist. However, random Bloch states and also random quadrupolar states can follow a classical description.

The detailed description and study in this work leave many open questions for future research. In particular, future work could explore how Hamiltonian complexity (e.g., rank) and state complexity (e.g., higher-order moments) affect the results—generalizing beyond dipolar and quadrupolar states. Regarding the monitoring protocols, a generalization would be desirable to obtain a full understanding of the emergence of classical equations of motion in monitored quantum systems.

On a higher level, the results in this chapter provide a first step towards a more detailed understanding of the application of a semiclassical description of hydrodynamic behavior in quantum systems. In Chapter 5, we take a further step and show that conservation of the z-component S^z can give rise to a semiclassical description. It would be interesting to further explore the connection of the results in this chapter to semiclassical approximations such as spin wave theory.

For now, we shift our focus from state complexity, as measured by entanglement, to operator complexity, as captured by Krylov complexity in the next chapter.

3 Krylov Complexity

The work in this chapter has appeared as part of the following article
Philippe Suchsland, Roderich Moessner, and Pieter W. Claeys.
Krylov complexity and Trotter transitions in unitary circuit dynamics.
In: Phys. Rev. B 111, 014309 (15 January, 2025) [37]

In the previous chapter we discussed entanglement growth as a characteristic feature of time-evolved states in chaotic quantum systems, contrasting it with the suppressed growth observed in the semiclassical limit. We now shift from the state-based to an operator-based perspective. In this chapter, we analyze characteristic features of operator dynamics in chaotic systems in the Heisenberg picture, as well as how these features are evaded in non-chaotic systems.

While the Schödinger picture of quantum mechanics considers the dynamics of states, in the Heisenberg picture all dynamics correspond to a unitary transformation of operators representing physical observables. If this dynamics is chaotic, initially "simple" operators are expected to become increasingly complex as time goes on [38]. This complexity can, e.g., be observed through initially localized operators becoming increasingly delocalized, a process known as operator spreading, which is physically reflected in the growth of entanglement and operator scrambling. One possible probe for this complexity growth is Krylov complexity [39]. In simple terms, Krylov complexity quantifies the minimal number of basis operators needed to capture the time evolved operator. In this way, it serves as a measure of operator complexity in the Heisenberg picture [40]. Crucially, a maximized Krylov complexity growth rate has been conjectured to be a characteristic feature of chaotic systems. Here, we extend the notion of Krylov complexity to unitary circuit dynamics. Correspondingly, we identify 'maximal ergodicity' of operators as a characteristic behavior of Krylov complexity for operator dynamics generated by circuits. Such circuits have become of interest as prototypical quantum systems for quantum dynamics and in their role as the formalization of quantum dynamics on digital quantum hardware.

This chapter is structured as follows. We begin with a detailed overview of the results in Sec. 3.1. The full formalism of Krylov dynamics is presented in Sec. 5.3 and is subsequently applied to dual-unitary circuits in Sec. 3.3, both

as an illustrative example for which analytical calculations are possible, and to illustrate the existence of maximally ergodic operators as attractors in the Krylov subspace. In Sec. 3.4 the formalism is applied to Trotterized circuits and numerical results are presented for chaotic, interacting integrable, and noninteracting integrable circuits. The nonanalytic Trotter transition in the latter case is subsequently discussed in more detail in Sec. 3.5, where we present analytic results in a representative example. The growth of Krylov complexity in these different classes of circuits is illustrated in Sec. 3.6.

Operator growth and information scrambling are shown to be closely linked to Krylov complexity growth. We therefore turn our focus to information spreading in the second part of this thesis.

3.1 Overview

In this chapter, we focus on one way of quantifying the complexity of operator dynamics through the so-called "Krylov complexity". Here, the dynamics of an initial operator is described in a Krylov subspace [41]: the initial operator spreads out in a basis of operators obtained through a Gram-Schmidt orthonormalization procedure. Roughly speaking, the Krylov basis consists of orthonormal operators with increasing support and increasing complexity, acting as an effective bath for the initial operator. This notion of complexity has been studied first for Hamiltonian dynamics, since it was conjectured that chaotic quantum dynamics results in a maximal growth of the Krylov complexity [39]. The Krylov dynamics was also conjectured to satisfy a 'universal operator growth hypothesis' and it was shown that Krylov complexity bounds a large class of physical complexity measures, including out-of-time-order correlators. It was subsequently realized that quantum chaos corresponds to delocalization in this Krylov subspace [42–44]. There has been an increasing interest to go beyond the dynamics generated by a static local Hamiltonian and study unitary dynamics like in driven systems [45] or in unitary circuit models [46]. In turn, Krylov complexity has been used in systems with unitary dynamics to study weak and strong zero modes in Floquet spin chains in Refs. [47, 48].

In the following, we present a different approach and make extensive use of the unitarity to restrict our theoretical framework, such that we will not need to consider the full unitary superoperator, and focus on unitary circuits, which allows us to make statements about the locality of Krylov operators and make the connection with Hamiltonian dynamics [39]. This approach is an extension of the framework of Krylov subspaces and the universal operator growth hypothesis from static Hamiltonians to unitary dynamics without an underlying local Hamiltonian, with a focus on the dynamics described by

unitary circuits. As one major motivation, this framework also allows us to study 'Trotterized' circuits. These unitary circuits arise as the decomposition of Hamiltonian dynamics in discrete time steps [49, 50], and have both fundamental and practical applications: Trotterization is a key element in numerical algorithms for quantum many-body dynamics such as time-evolving block decimation (TEBD) [51–54], and in the digital quantum simulation of quantum many-body dynamics [55]. This approach is more generally motivated by the enormous success that unitary circuits have had in the study of operator growth [46, 56–72]. On the simplest level, unitary circuits provide minimally structured models mimicking local Hamiltonian dynamics, where the locality is directly encoded in the construction of the unitary evolution operator. Such circuits can either be purely random, where random unitary circuits have been highly successful in reproducing generic aspects of operator spreading [46, 56–61], or structured, where e.g., dual-unitary circuits have allowed for exact results on many-body dynamics and spectral measures of quantum chaos [62–72]. Remarkably, various Trotterized circuits arising from integrable Hamiltonians remain integrable at any Trotter step, and both noninteracting and interacting integrable circuit models exist [73–83].

We first argue that, a universal, characteristic feature of operator dynamics for generic, chaotic unitary dynamics is the maximal growth of the Krylov complexity. This maximal growth is accompanied by the convergence of the Krylov basis operators to 'maximally ergodic operators': operators for which the autocorrelation function vanishes instantaneously. In this way these Krylov basis operators act as a memoryless bath. For these operators the usual description of many-body dynamics in terms of the eigenstate thermalization hypothesis (ETH) reduces to a purely random matrix theory (RMT) prediction, highlighting the effect of the Trotterization and the deviation from Hamiltonian dynamics. These operators act as attractive points in the Krylov subspace and are reminiscent of classical Bernoulli systems [84], which are similarly maximally ergodic. These maximally ergodic operators present an intuition for the relaxation to equilibrium in unitary many-body dynamics. Here, dual unitary circuits serve as an exemplary system exhibiting a maximally chaotic behavior [38, 62, 65, 85, 86], also in terms of Krylov complexity.

Then, we study the transition between time evolution generated by static Hamiltonians and unitary circuit models in trotterized systems. For chaotic systems, we argue that with increasing Trotter step there is a crossover in the Krylov dynamics from the Hamiltonian regime, where the dynamics satisfy the universal operator growth hypothesis, to the maximally ergodic regime, where the Krylov operators converge to maximally ergodic operators. In the latter regime the dynamics can no longer be accurately described using

a local Hamiltonian. The fundamental implication is that, for any nonzero Trotter step, it is possible to construct large but local operators for which the dynamics reduces to the purely random matrix prediction and the autocorrelation function trivializes, no matter how close the circuit appears to be to Hamiltonian dynamics.

Last, we compare the behavior of Krylov complexity in chaotic systems to integrable systems, which no chaotic dynamics. In noninteracting integrable circuits we observe a nonanalytic Trotter transition rather than a crossover between different regimes as the Trotter step is varied. For sufficiently small Trotter step no maximally ergodic operators exist and no maximal Krylov complexity growth is possible, indicating that the possible dynamics remains highly constrained by the conservation laws, as in the Hamiltonian case, but at a critical Trotter step maximally ergodic operators appear as attractors in the Krylov subspace and the Krylov dynamics approaches this universal regime. Remarkably, in this regime the autocorrelation function can appear maximally ergodic despite the highly nonergodic nature of the underlying circuit.

We present an explanation for transition from ergodic to nonergodic through the spectral function of the Krylov operators, i.e., the Fourier transform of their autocorrelation function, which determines their response to external perturbations. The Gram-Schmidt procedure used to construct the Krylov basis results in basis operators whose spectral function is increasingly flattened and the correlation functions increasingly featureless, indicating that the dynamics converges to operators with a flat spectral function and a corresponding instantaneous decay of correlation functions. Crucially, the spectral functions of the Krylov operators are proportional to the spectral function of the initial operator, explaining the nonanalytical transition in free systems: for sufficiently small Trotter steps the spectral function has a finite support, scaling linearly with the Trotter step, and a resulting gap in the excitation spectrum (around the π-mode of the Floquet Brillouin zone), but at the critical Trotter step this gap closes. A closed gap is necessary in order to have a flat spectrum for the Krylov operators, whereas in the presence of a gap no maximally ergodic operators can appear, since this gap is inherited by the spectral functions of all Krylov operators.

While this effect might seem surprising, there is a class of circuits for which it already has been shown that maximally ergodic operators exist: dual-unitary circuits, characterized by an underlying space-time duality [63, 66, 87]. This space-time duality effectively enforces the Trotter step to be large, and dual-unitary circuits can be either integrable or chaotic while still supporting maximally ergodic dynamics. For the Trotterized circuits considered here, dual-unitary gates appear deep in the maximally ergodic

regime.

3.2 Formalism

In this work we consider unitary evolution described by so-called 'brickwall' circuits, with the added restriction that we require the dynamics to be periodic in time (leading to Floquet dynamics [45]). Such brickwall circuits describe the dynamics of an infinite one-dimensional lattice in a discrete time, and are constructed from a local two-site unitary gate. Taking $U_{j,j+1}$ to be a two-site unitary matrix acting on sites j and $j+1$, we consider a unitary evolution operator for a single discrete time step as

$$U = U_{\text{odd}} U_{\text{even}}, \tag{3.1}$$

with

$$U_{\text{odd}} = \prod_{j\in\mathbb{Z}} U_{2j-1,2j}, \quad U_{\text{even}} = \prod_{j\in\mathbb{Z}} U_{2j,2j+1}\,. \tag{3.2}$$

The resulting unitary dynamics can be graphically represented in tensor network language as

$U^t =$ 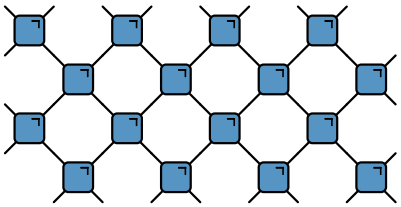 (3.3)

here illustrated for two time steps, $t = 2$, and eight lattice sites, and where every blue square represents a unitary gate acting on two sites. For convenience we take all unitary gates to be identical, although this is not a necessary assumption for our framework. Note that a single time step corresponds to two rows of unitary gates, such that the dynamics is periodic with period one.

The main focus of this chapter is on describing the operator dynamics generated by such a unitary circuit in a Krylov subspace. While the developed formalism will be applicable to more general unitary dynamics, we focus on unitary circuits because they allow for a direct connection with previous results on Krylov dynamics. As the space of all operators is a Hilbert space itself, we use the Dirac notation for the operator space and write $|O) \equiv O$ to represent the operator O. Here we use round brackets to refer to the operator Hilbert space, in contrast to the commonly used

angle brackets denoting the Hilbert space of states. The scalar product is defined as $(O_1|O_2) = \mathrm{Tr}[O_1^\dagger O_2]/\mathcal{D}$, where $\mathcal{D}$ is the dimension of the (state) Hilbert space. In the remainder of this chapter we will typically work in the thermodynamic limit of an infinite system size.

Any operator O evolves in discrete time under the repeated application of the unitary transformation U, corresponding to, e.g., a Floquet unitary or a single time step in a unitary brickwall circuit. We define the unitary superoperator $\mathcal{U}$ to act as $\mathcal{U}|O) = |U^\dagger O U)$ and consider an initial operator O_0 which we take to be Hermitian, traceless, and normalized as $(O_0|O_0) = 1$. The full dynamics is encoded in the sequence of operators

$$|O_t) = \mathcal{U}^t\,|O_0)\,, \quad t \in \mathbb{N}_0\,, \tag{3.4}$$

giving the time-evolved operator at every discrete time t. The autocorrelation function for O_0 follows directly as

$$(O_0|O_t) = (O_0|\mathcal{U}^t|O_0) = \mathrm{Tr}\left[O_0^\dagger U^{\dagger t} O_0 U^t\right]/\mathcal{D}\,. \tag{3.5}$$

The Krylov subspace of an initial operator O_0 is spanned by basis elements obtained from an appropriate orthonormalization of the sequence $\{|O_0), |O_1), |O_2) \dots\}$.

If the initial operator O_0 is initially localized, e.g., on a single site, the support of the operator $|O_t)$ grows linearly with t due to the unitarity and the brickwall geometry [59, 65]. Using the unitarity of the individual gates, a single-site operator can be directly shown to evolve as

$|O_0) =$ 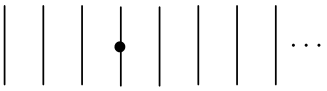 (3.6)

$|O_1) =$ 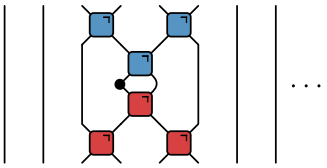 (3.7)

$|O_2) =$ 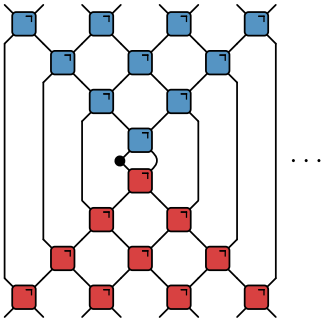 (3.8)

where the black circle denotes the initial operator and the red squares represent the Hermitian conjugate of the unitary gates. This linear growth then bounds the support of the Krylov operators.

Written in this way, the operator dynamics has been extensively analyzed in, e.g., random unitary circuits [46, 56–61]. Here, we take a different approach and consider the operator dynamics in an orthonormal basis, obtained through a Gram-Schmidt orthonormalization of the set of operators $|O_t)$. This approach is also known as the Arnoldi iteration [88].

3.2.1 Hermitian Superoperator

The Krylov approach has been instructive when considering Hamiltonian dynamics, where the operator dynamics is governed by a Liouvillian $\mathcal{L}(O) = [H, O]$ for a given Hamiltonian H. In this case, the orthonormalization is done on a set of operators $|O_n) = \mathcal{L}^n|O_0)$. We briefly review the main formalism from Ref. [39].

Identifying $|\mathcal{O}_0) = |O_0)$ and $|\mathcal{O}_1) = \mathcal{L}|\mathcal{O}_0)/\tilde{b}_1$ with $\tilde{b}_1 = (\mathcal{L}\mathcal{O}_0|\mathcal{L}\mathcal{O}_0)^{1/2}$, it is possible to inductively define

$$|A_n) = \mathcal{L}|\mathcal{O}_{n-1}) - \tilde{b}_{n-1}|\mathcal{O}_{n-2}), \tag{3.9}$$

$$\tilde{b}_n = (A_n|A_n)^{1/2}, \quad |\mathcal{O}_n) = |A_n)/\tilde{b}_n\,. \tag{3.10}$$

These operators form an orthonormal basis for the operator dynamics, $(\mathcal{O}_m|\mathcal{O}_n) = \delta_{mn}$, and arise as a Gram-Schmidt orthonormalization of the sequence $\{\mathcal{L}^n|O_0)\}$. The Liouvillian is tridiagonal in this basis,

$$\mathcal{L}_{mn} = (\mathcal{O}_m|\mathcal{L}|\mathcal{O}_n) = \begin{pmatrix} 0 & \tilde{b}_1 & 0 & 0 & \dots \\ \tilde{b}_1 & 0 & \tilde{b}_2 & 0 & \dots \\ 0 & \tilde{b}_2 & 0 & \tilde{b}_3 & \dots \\ 0 & 0 & \tilde{b}_3 & 0 & \dots \\ \vdots & \vdots & \vdots & \vdots & \ddots \end{pmatrix}. \tag{3.11}$$

The tridiagonal form is direct consequence of the Hermiticity of the superoperator $i\mathcal{L}$, and the diagonal elements vanish because of the commutator structure of $\mathcal{L}$. The Lanczos coefficients $\{\tilde{b}_n\}$ fully encode the Liouvillian in this basis. A review of this recursion approach can be found in Ref. [41], and the Lanczos coefficients were argued to exhibit universal behavior in Ref. [39]. Specifically, for a nonintegrable lattice Hamiltonian the Lanczos coefficients were argued to asymptotically grow linearly with n, $\tilde{b}_n \propto n$, up to a logarithmic correction in one-dimensional systems. This constitutes the "universal operator growth hypothesis" of Ref. [39]. This linear growth was

contrasted with the boundedness of the Lanczos coefficients in noninteracting integrable systems, $\tilde{b}_n \propto \text{Cst.}$, and the sublinear growth observed in interacting integrable systems, where for the integrable XXZ Hamiltonian a growth $\tilde{b}_n \propto \sqrt{n}$ was observed.

There have subsequently been a large number of recent studies on Krylov dynamics ranging from spin models [89–94], models with restricted symmetry group [95–99], quantum scars [100–102], and quantum networks [103], to (holographic) field theories [104–111]. Noteworthy are also studies in chaotic open systems [112] and of chaotic single particle dynamics [113], in which no linear growth of the Lanczos coefficients $\{\tilde{b}_n\}$ have been found, refining the original conjecture [39]. The associated notion of Krylov complexity has also been shown to be intimately related to various notions of entanglement and complexity [114–118] as well as physical observables [119, 120] and satisfies a quantum speed limit [121]. Krylov methods have also found natural applications in counterdiabatic driving [122–124].

3.2.2 Unitary Superoperator

For the unitary superoperator $\mathcal{U}$ relevant for this chapter both the orthonormalization procedure and the resulting matrix representation of the superoperator are slightly more involved. A detailed derivation can be found in Appendix B.2, and we here only quote the final result. The Krylov operators $\{|\mathcal{O}_0), |\mathcal{O}_1), |\mathcal{O}_2), \dots\}$ are obtained through a Gram-Schmidt orthonormalization of the operators $\{|O_0), |O_1), |O_2), \dots\}$, satisfying $(\mathcal{O}_m|\mathcal{O}_n) = \delta_{mn}$. The Krylov basis can be expanded as

$$|\mathcal{O}_n) = \sum_{t=0}^{n} \alpha_{n,t} |O_t), \tag{3.12}$$

which can be inverted as

$$|O_t) = \sum_{n=0}^{t} \beta_{t,n} |\mathcal{O}_n). \tag{3.13}$$

If the initial operator $|O_0)$ is local, the operators $|\mathcal{O}_n)$ are similarly local, with a support that grows linearly in n [59, 65]. In this basis $\mathcal{U}$ has the structure of an upper Hessenberg form, whose matrix elements $\mathcal{U}_{mn}$ vanish for $m > n+1$, as opposed to the tridiagonal matrix observed in the Hermitian case (as also observed in Ref. [47] and for open systems in Ref. [125]). Furthermore, the

unitary superoperator can be fully parametrized by three functions:

$$\mathcal{U}_{mn} = (\mathcal{O}_m|\mathcal{U}|\mathcal{O}_n) = \begin{cases} 0 & \text{if} \quad m > n+1\,, \\ b_m & \text{if} \quad m = n+1\,, \\ a_m\, c_n/c_m & \text{if} \quad m < n+1\,, \end{cases} \tag{3.14}$$

leading to an upper Hessenberg matrix of the form

$$\mathcal{U}_{mn} = \begin{pmatrix} a_0 & a_0c_1/c_0 & a_0c_2/c_0 & a_0c_3/c_0 & \dots \\ b_1 & a_1 & a_1c_2/c_1 & a_1c_3/c_1 & \dots \\ 0 & b_2 & a_2 & a_2c_3/c_2 & \dots \\ 0 & 0 & b_3 & a_3 & \dots \\ 0 & 0 & 0 & b_4 & \dots \\ \vdots & \vdots & \vdots & \vdots & \ddots \end{pmatrix}. \tag{3.15}$$

The three sequences correspond to specific matrix elements

$$a_n = (\mathcal{O}_n|\mathcal{U}|\mathcal{O}_n), \tag{3.16}$$
$$b_n = (\mathcal{O}_n|\mathcal{U}|\mathcal{O}_{n-1}), \tag{3.17}$$
$$c_n = (\mathcal{O}_0|\mathcal{U}|\mathcal{O}_n). \tag{3.18}$$

Note that $a_0 = c_0$. The unitarity further constrains these matrix elements in various ways, e.g., $|\mathcal{U}_{mn}| \leq 1, \forall m, n$, which already indicates that the unbounded growth of the Lanczos coefficients observed in Hamiltonian dynamics should not be possible in unitary circuit dynamics. In general we observe c_n to be a decaying sequence, such that the matrix is dominated by the diagonal elements. The structure of b_n and a_n appears to be universal for different classes of systems, in a way that will be made explicit later, with $b_n \to 1$ and $a_n \to 0$ for sufficiently large n.

The matrix representations (3.11) and (3.15) allow for an interpretation of the operator dynamics as dynamics in a semi-infinite one-dimensional chain where each lattice site n represents a Krylov operator $\mathcal{O}_n$ and the initial operator is initially localized at site $n = 0$. The different hopping models for Hamiltonian and unitary dynamics are illustrated in Fig. 3.1.

Recasting the dynamics in a Krylov subspace allows for the evaluation of the so-called Krylov complexity, also known as K-complexity, which measures the spreading of an operator in Krylov space. Following Eq. (3.13), we define the Krylov complexity for unitary circuit dynamics as

$$K(t) = \sum_{n=0}^{t} n|\beta_{t,n}|^2\,. \tag{3.19}$$

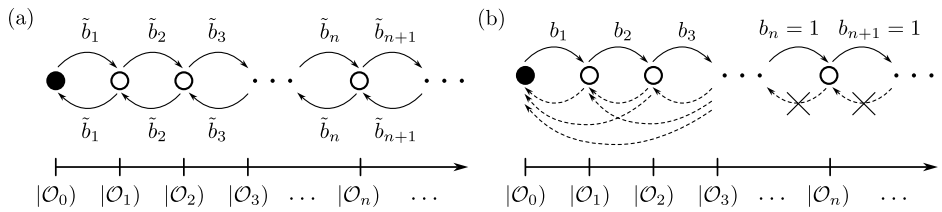

Figure 3.1: *Representation of operator growth as dynamics on a semi-infinite one-dimensional chain in the Krylov subspace. (a) For Hamiltonian dynamics the Krylov dynamics reduces to a nearest-neighbor hopping model with hopping coefficients $\tilde{b}_n$. (b) For unitary circuit dynamics the hopping is asymmetric, with nearest-neighbor hopping to the right with coefficients b_n and long-range hopping terms to the left set by the coefficients a_n and c_n. However, for sufficiently large n the hopping to the right generally dominates and the hopping strength approaches $b_n = 1$, whereas the hopping terms to the left vanish.*

The Krylov complexity was originally proposed as a measure of chaos for continuous time evolution [39]. In this chapter we extend this approach to Floquet evolution and study its universal properties.

3.2.3 Spectral Functions

In this subsection we present an alternative interpretation of the orthonormalization procedure, which will be important in understanding the autocorrelation functions of Krylov operators and Trotter transitions. Readers mainly interested in the application of the developed framework to specific unitary circuits can directly skip to the next section. The action of the orthonormalization procedure can be reinterpreted on the level of the spectral function, also known as the structure function,

$$|f_O(\omega)|^2 = \frac{1}{\mathcal{D}} \sum_{p,q=1}^{\mathcal{D}} |\langle p|O|q\rangle|^2 \, \delta(\theta_q - \theta_p - \omega) \,, \tag{3.20}$$

where $U|p\rangle = e^{i\theta_p}|p\rangle$. The spectral function is the Fourier transform of the autocorrelation function

$$\frac{1}{\mathcal{D}} \mathrm{Tr}\left[O^\dagger U^{\dagger t} O U^t\right] = \frac{1}{\mathcal{D}} \sum_{p,q=1}^{\mathcal{D}} |\langle p|O|q\rangle|^2 \, e^{i(\theta_q - \theta_p)t} \,. \tag{3.21}$$

As such, it encodes information about both the short- and long-time dynamics of the initial operator and hence the level of ergodicity. Within ETH, the spectral function naturally appears as the (averaged over eigenstates)

envelope for the off-diagonal matrix elements [126]. For unitary dynamics where energy is no longer conserved, ETH predicts a universal form for the off-diagonal elements of an observable O as

$$\langle p|O|q\rangle = \mathcal{D}^{-1/2} f_O(\theta_q - \theta_p) R_{pq}, \tag{3.22}$$

where R_{pq} is a random variable with zero mean and unit variance [127, 128]. The operator dynamics is encoded here in the spectral function appearing as an envelope for off-diagonal matrix elements, distinguishing structured dynamics from those generated by a purely random matrix. However, the spectral function remains well-defined through the autocorrelation function even when ETH is not expected to hold and can be used as a sensitive probe of integrability and chaos [129–131].

The orthonormality of the Krylov operators can be directly translated to statements about the orthonormality of polynomials on the unit circle, which can in turn be used to make exact statements about the action of the repeated orthonormalization. Such a connection was already made for Hamiltonian dynamics in Ref. [132], but is simpler for unitary dynamics and allows us to make use of exact statements for orthonormal polynomials on the unit circle that do not apply for orthonormal polynomials on the real line (as in the Hamiltonian case). Expanding the Krylov operators in the original basis as in Eq. (3.12),

$$|\mathcal{O}_n) = \sum_{t=0}^{n} \alpha_{n,t} \, |O_t) \ , \tag{3.23}$$

we define corresponding functions on the unit circle as

$$p_n(\omega) = \sum_{t=0}^{n} \alpha_{n,t} \, e^{it\omega} \, . \tag{3.24}$$

These functions now behave as orthonormal functions provided we use the spectral function as weight function,

$$\int_0^{2\pi} \mathrm{d}\omega \, |f_O(\omega)|^2 p_n(\omega) p_m^*(\omega) = \delta_{mn} \, . \tag{3.25}$$

This orthonormality directly follows from a spectral expansion of the or-

thonormality of the Krylov operators, since

$$\begin{aligned}\mathrm{Tr}\left[\mathcal{O}_m^\dagger \mathcal{O}_n\right]/\mathcal{D} &= \sum_{t=0}^{m}\sum_{s=0}^{n} \alpha_{m,t}^* \alpha_{n,s} \mathrm{Tr}\left[O_t^\dagger O_s\right]/\mathcal{D} \\ &= \sum_{t=0}^{m}\sum_{s=0}^{n} \alpha_{m,t}^* \alpha_{n,s} \int_0^{2\pi} \mathrm{d}\omega\, |f_O(\omega)|^2 e^{i\omega(s-t)} \\ &= \int_0^{2\pi} \mathrm{d}\omega\, |f_O(\omega)|^2 p_n(\omega) p_m^*(\omega)\,. \end{aligned} \tag{3.26}$$

These orthonormal functions are not just a mathematical curiosity. Rather, they fully determine the autocorrelation functions and associated spectral functions of the Krylov operators themselves. The corresponding spectral function can be directly calculated as

$$\begin{aligned}|f_{\mathcal{O}_n}(\omega)|^2 &= \frac{1}{\mathcal{D}} \sum_{p,q=1}^{\mathcal{D}} |\langle p|\mathcal{O}_n|q\rangle|^2\, \delta(\theta_q - \theta_p - \omega) \\ &= \frac{1}{\mathcal{D}} \sum_{p,q=1}^{\mathcal{D}} |\langle p|\mathcal{O}_0|q\rangle|^2 |p_n(\theta_q - \theta_p)|^2\, \delta(\theta_q - \theta_p - \omega) \\ &= |f_O(\omega)|^2 |p_n(\omega)|^2\,. \end{aligned} \tag{3.27}$$

Here we have used that

$$\langle p|\mathcal{O}_n|q\rangle = \langle p|\mathcal{O}_0|q\rangle p_n(\theta_q - \theta_p), \tag{3.28}$$

as follows directly from the definition of $p_n(\omega)$ and Eq. (3.23):

$$\begin{aligned}\langle p|\mathcal{O}_n|q\rangle &= \sum_{t=0}^{n} \alpha_{n,t} \langle p|O_t|q\rangle = \sum_{t=0}^{n} \alpha_{n,t} \langle p|U^{\dagger t} O_0 U^t|q\rangle \\ &= \sum_{t=0}^{n} \alpha_{n,t} e^{it(\theta_q - \theta_p)} \langle p|O_0|q\rangle = p_n(\theta_q - \theta_p) \langle p|O_0|q\rangle\,. \end{aligned} \tag{3.29}$$

We can now use these orthonormal polynomials to derive a result on the spectral function of Krylov operators. As shown in Refs. [133, 134], such orthonormal polynomials have the property that the first n Fourier modes of $|p_n(\omega)|^{-2}$ agree with the first n Fourier modes of $|f_O(\omega)|^2$, i.e.,

$$\int_0^{2\pi} \mathrm{d}\omega\, e^{im\omega} |p_n(\omega)|^{-2} = \int_0^{2\pi} \mathrm{d}\omega\, e^{im\omega} |f_O(\omega)|^2, \quad \text{if} \quad |m| \leq n\,. \tag{3.30}$$

These polynomials hence satisfy

$$\lim_{n\to\infty} |p_n(\omega)|^{-2} = \frac{1}{2\pi}|f_O(\omega)|^2\,, \tag{3.31}$$

provided $\log(|f_O(\omega)|^2)$ is Lebesgue integrable [133, 134]. This convergence will be important when considering the large-n limit of Krylov operators, since it implies that their spectral function generally converges to a constant. Additional properties of such orthonormal polynomials on the unit circle and their relation to the Fourier modes of the spectral function are reviewed in Appendix B.3.

3.3 Dual-Unitary Circuits

Let us illustrate the theoretical framework from the previous section for the specific case of dual-unitary circuits. These circuits are characterized by an underlying space-time duality, allowing their (auto-)correlation functions to be calculated exactly, and support both chaotic and integrable dynamics [63, 66, 87]. As such, they also provide a tractable case for studying Krylov complexity in Floquet circuits, that will be instructive when considering more complicated circuit dynamics. In the following we will consider a random dual-unitary circuit, taking all gates $U_{2j-1,2j}$ and $U_{2j,2j+1}$ in Eq. (3.1) to be identical dual-unitary gates constructed using the parametrization from Refs. [63, 80] with a random choice of parameters, see Appendix B.1.

3.3.1 Local Operators

In dual-unitary circuits all correlation functions for single-site operators vanish everywhere except on the edge of the causal light cone [63, 66]. As one immediate consequence, the autocorrelation vanishes at all times except for $t = 0$ in dual-unitary circuit dynamics, i.e.,

$$(O_0|O_t) = \delta_{t,0}, \tag{3.32}$$

provided we choose O_0 as an single-site operator, e.g., $O_0 = \sigma_j$ only acting nontrivially on a fixed site j. Combining this result with $(O_s|O_t) = (O_0|O_{t-s})$, we find that the Krylov operators can be identified with the (normalized) time-evolved operators $|\mathcal{O}_n) = |O_n)$. The unitary superoperator takes a

particularly simple form since $\mathcal{U}|\mathcal{O}_n) = |\mathcal{O}_{n+1})$ and we can write

$$\mathcal{U} = \begin{pmatrix} 0 & 0 & 0 & 0 & \dots \\ 1 & 0 & 0 & 0 & \dots \\ 0 & 1 & 0 & 0 & \dots \\ 0 & 0 & 1 & 0 & \dots \\ \vdots & \vdots & \vdots & \vdots & \ddots \end{pmatrix} . \tag{3.33}$$

In the language of Eq. (3.14), we find that $b_n = 1, \forall n$ and $a_n = 0, \forall n$. Every operator generated by the unitary superoperator is orthogonal to all previous ones. The Krylov complexity grows linearly in time, and we find that $K(t) = t$ since $\alpha_{n,t} = \beta_{t,n} = \delta_{t,n}$ for $|\mathcal{O}_n) = |O_n)$. Such a growth is in fact the maximal possible growth due to the unitarity of the superoperator. The unitarity restricts $|b_n| \leq 1$, and these coefficients determine the rate of hopping to the right, such that the growth of $K(t)$ is maximal for $|b_n| = 1$ taking its maximal value and correspondingly $|a_n| = 0$ its minimal value, see also Appendix B.2.

Furthermore, since the autocorrelation function is a delta function, the spectral function is a constant,

$$|f_{O_t}(\omega)|^2 = \frac{1}{2\pi} . \tag{3.34}$$

3.3.2 Sums of Local Operators

A less trivial example can be found by considering an initial operator that is a linear combination of local operators, $O_0 \propto \sum_{j\in\mathbb{Z}} \sigma_{2j}$ with σ_{2j} a single site operator. This setup is similar to the one considered in Ref. [135], probing the spectral function in dual-unitary circuits. As detailed in Refs. [63, 135], the autocorrelation functions now take the form

$$(O_0|O_t) = \mathrm{Tr}\left[\sigma \mathcal{M}^{2t}(\sigma)\right] , \tag{3.35}$$

where $\mathcal{M}$ is a quantum channel acting as

$$\mathcal{M}(\sigma) = \frac{1}{q}\mathrm{Tr}_1\left[\tilde{U}^\dagger(\sigma \otimes \mathbb{1})\tilde{U}\right] . \tag{3.36}$$

Here $\tilde{U} \equiv U_{j,j+1}, \forall j$ corresponds to the choice of dual-unitary gate and q is the dimension of the local Hilbert space, which we take to be $q = 2$ in this chapter. Both $\tilde{U}$ and $\sigma \otimes \mathbb{1}$ act on two copies of the local Hilbert space and

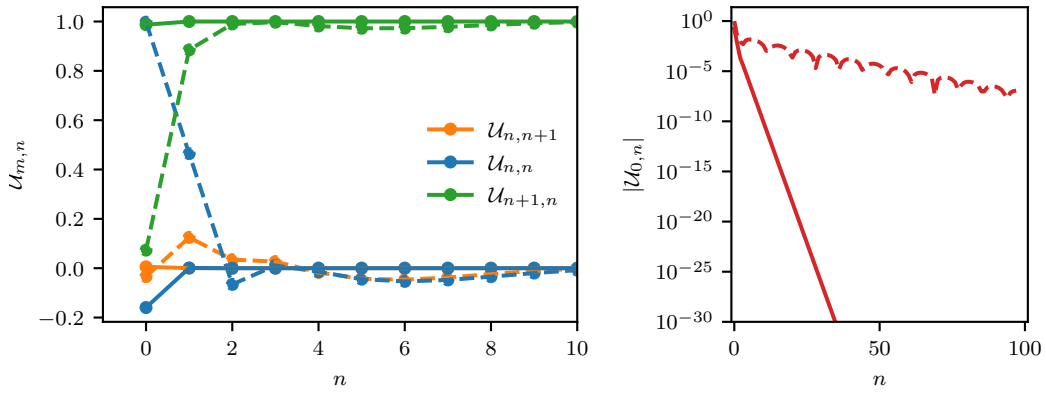

Figure 3.2: *The unitary superoperator $\mathcal{U}$ [Eq. (3.14)] describing the evolution of the initial operator $|O_0) \propto \sum_{j\in\mathbb{Z}} \sigma^z_{2j}$ under dual-unitary dynamics. Here $\mathcal{U}$ is given in the Krylov basis, which is generated by orthonormalization of $\{\mathcal{U}^t|O_0)\}$ with $t \in \mathbb{N}_0$. The unitary superoperator $\mathcal{U}$ is fully described by its tridiagonal matrix elements (top) and its decay away from the diagonal $\mathcal{U}_{n,n+l} = \mathcal{U}_{n,n+1}\mathcal{U}_{0,n+l}/\mathcal{U}_{0,n+1}$ (bottom). We consider two exemplary realizations of the dual-unitary gate: a typical one (solid) and one with slow convergence (dashed). After an initial transient behavior the coefficients $a_n = \mathcal{U}_{n,n}$ and $b_n = \mathcal{U}_{n+1,n}$ approach 0 and 1 respectively (left) and the coefficients $c_n = \mathcal{U}_{0,n}$ decay exponentially (right), indicating that the unitary superoperator becomes dominated by the tridiagonal elements.*

Tr_1 indicates that we are tracing out the first copy. The autocorrelation function can be directly found through an exact diagonalization of the quantum channel $\mathcal{M}$. Introducing an eigenvalue decomposition of $\mathcal{M}$ as

$$\mathcal{M} = \sum_{a=1}^{q^2} \lambda_a \, |r_a)(l_a|, \tag{3.37}$$

the autocorrelation function follows as

$$(O_0|O_t) = \sum_{a=1}^{q^2} \lambda_a^{2t} \, (\sigma|r_a)(l_a|\sigma), \tag{3.38}$$

from which the Krylov operators can be directly calculated since all necessary overlaps in the orthonormalization procedure are of the form $(O_s|O_t) = (O_t|O_s)^* = (O_0|O_{t-s})$ for $t \geq s$. The resulting matrix elements are illustrated in Fig. 3.2 for two generic choices of dual-unitary circuit and with $\sigma = \sigma_z$ a Pauli matrix for $q = 2$. After an initial transient behavior for small n, the matrix elements approach the same form for large n as previously observed, where only $b_n = 1$ is nonzero. We now find that the Krylov complexity grows linearly after some time, with $K(t) = t + \mathrm{Cst}$.

This behavior can be understood by considering the case where our initial operator is an eigenoperator of the quantum channel (3.36), yielding $(O_{n+k}|O_n) = \lambda^{2k}$ [3]. Alternatively, this expression for the autocorrelation function can be understood as an approximation for the late-time dynamics if these are dominated by a single eigenmode of the quantum channel. The Krylov operators can then be analytically calculated as

$$|\mathcal{O}_0) = |O_0), \qquad |\mathcal{O}_n) = \frac{|O_n) - \lambda^2 |O_{n-1})}{\sqrt{1-\lambda^4}}\,. \tag{3.39}$$

We find that the only nonvanishing Krylov matrix elements are now given by $a_0 = \lambda^2$ and $b_1 = \sqrt{1-\lambda^4}, b_n = 1, \forall n > 1$, resulting in

$$\mathcal{U} = \begin{pmatrix} \lambda^2 & 0 & 0 & 0 & \dots \\ \sqrt{1-\lambda^4} & 0 & 0 & 0 & \dots \\ 0 & 1 & 0 & 0 & \dots \\ 0 & 0 & 1 & 0 & \dots \\ \vdots & \vdots & \vdots & \vdots & \ddots \end{pmatrix}. \tag{3.40}$$

After a single time step, the new operators generated by the unitary transformation are always linearly independent from all previously generated operators in the Krylov subspace. This suggests an interpretation of the set of $|\mathcal{O}_{n>0})$ as structureless, maximally ergodic bath states: The initial operator 'leaks' into the bath states during the dynamics, since we can decompose the time-evolved operator as

$$|O_t) = \lambda^{2t}|\mathcal{O}_0) + \sqrt{1-\lambda^4}\sum_{s=1}^{t} \lambda^{2(t-s)}|\mathcal{O}_s), \tag{3.41}$$

where the bath states do not contribute to the autocorrelation function for O_0, since $(O_0|\mathcal{O}_s) = \delta_{s,0}$, and have vanishing autocorrelation functions, $(\mathcal{O}_n|\mathcal{U}^t|\mathcal{O}_n) = \delta_{t,0}$.

The expression (3.41) can be used to directly calculate the Krylov complexity as

$$K(t) = t - \frac{\lambda^4}{\lambda^4 - 1}(\lambda^{4t} - 1)\,, \tag{3.42}$$

returning linear growth after a time scale $t \propto -1/\log|\lambda|$. While this time scale can be arbitrarily large, in Krylov space the maximal complexity growth is observed after a single step.

[3] We here assume that λ is real, which is necessary if the corresponding eigenoperator is Hermitian.

These results can also be understood on the level of the spectral function. Writing $\lambda^2 = e^{-\gamma}$, the spectral function follows as (see also Ref. [135]),

$$|f_O(\omega)|^2 = \frac{1}{2\pi}\frac{\sinh(\gamma)}{\cosh(\gamma) - \cos(\omega)}. \tag{3.43}$$

For large γ the autocorrelation function decays rapidly and the spectral function is nearly flat, whereas for small γ the autocorrelation functions decays slowly and the spectral function is peaked near $\omega = 0$.

Considering the orthonormal polynomials from Eq. (3.24), we immediately find that the polynomials associated with the basis transformation to Krylov operators (3.39) are given by

$$p_0 = 1, \qquad p_n(\omega) = e^{i\omega n}\frac{e^{i\omega} - \lambda^2}{\sqrt{1-\lambda^4}}. \tag{3.44}$$

Furthermore, it is easy to check that $|p_1(\omega)|^{-2} = 2\pi|f_O(\omega)|^2$, and hence

$$|f_O(\omega)|^2|p_1(\omega)|^2 = \frac{1}{2\pi}, \tag{3.45}$$

such that $\mathcal{O}_1$ has a flat spectral function. Even though the autocorrelation function for $\mathcal{O}_0$ is nontrivial at all times, the autocorrelation function for $\mathcal{O}_1$ is now a delta function and after a single time step all operators generated by the unitary superoperator are linearly independent from $\mathcal{O}_0$ and $\mathcal{O}_1$. We term this regime to be *maximally ergodic Krylov dynamics*.

3.3.3 Maximally Ergodic Krylov Dynamics

We can identify three equivalent signifiers of this maximally ergodic regime, where every discrete time step generates an operator that is orthogonal to the previous operators:

1. The unitary superoperator becomes purely lower diagonal with $b_n = 1$ and $a_n = 0$ for n sufficiently large, indicating that $\mathcal{U}|\mathcal{O}_n) = |\mathcal{O}_{n+1})$.

2. The Krylov operators $|\mathcal{O}_n)$ for sufficiently large n have a vanishing autocorrelation function, i.e., all autocorrelations decay instantaneously: $(\mathcal{O}_n|\mathcal{U}^t|\mathcal{O}_n) = \delta_{t,0}$.

3. For sufficiently large n the orthonormal polynomials satisfy $|f_O(\omega)|^2|p_n(\omega)|^2 = \text{Constant}$, i.e., the spectral functions for $\mathcal{O}_n$ flatten.

We will refer to the Krylov operators in this regime as *maximally ergodic*. It is not surprising that such operators can be found in dual-unitary circuits and that they act as attractive fixed points for the Krylov orthonormalization procedure, but we will show in the next section that this behavior is universal in chaotic systems and that the existence of such maximally ergodic operators can serve as a sharp diagnostic for Trotter transitions in integrable systems. The dynamics of these maximally ergodic operators is reminiscent of Bernoulli systems, similarly characterized by instantaneously vanishing correlations [67, 84]. Similar exactly solvable Krylov dynamics is observed in Clifford circuits, as shown in Appendix B.4.

While all these statements hold exactly in dual-unitary circuits and Clifford circuits, in more general circuit dynamics we need to allow for some finite error. In this case we will take maximally ergodic Krylov dynamics as the regime where the autocorrelation function for the Krylov operators $\mathcal{O}_n$ falls below some small but nonzero threshold, and the matrix elements a_n and b_n in the unitary superoperator reproduce those of the maximally ergodic regime up to this error. The precise value of this error only has a small effect on the value of n at which the maximally ergodic regime sets in. In this regime we observe that the autocorrelation functions for Krylov operators $\mathcal{O}_n$ after a single time step decay exponentially with increasing n, i.e., $(\mathcal{O}_n|\mathcal{U}|\mathcal{O}_n) \sim e^{-\nu n}$. Reducing the error leads to a logarithmic growth in the value of n at which this regime sets in, but any nonzero error should lead to a finite n.

Before continuing, we note that the Krylov dynamics does not just probe properties of the unitary evolution, but also of the initial operator O_0. In this respect it is similar to probes of quantum chaos through the spectral function and related measures such as the fidelity susceptibility [136] and the scaling of the adiabatic gauge potential [129, 137]. Even when restricting to local operators, different choices of initial operator can lead to qualitatively different behavior, e.g., integrability-breaking vs. integrability-preserving operators [129, 138]. Rather than probing the dynamics in the full operator space, the dependence on the initial operator is made explicit by working within the Krylov subspace particular to this operator [41].

3.4 Tuning Trotterized Circuits

In this section we apply the developed framework to a specific class of unitary brickwall circuits, namely, those corresponding to Trotter decompositions of local Hamiltonians [49, 50]. Considering the dynamics governed by a local Hamiltonian $H = \sum_j H_{j,j+1}$, the unitary evolution operator can be

approximated as

$$e^{-iHt} \approx (U_{\text{odd}}(\Delta t)U_{\text{even}}(\Delta t))^{t/\Delta t} \,, \tag{3.46}$$

with

$$U_{\text{odd}}(\Delta t) = \prod_{j\in 2\mathbb{Z}+1} \left(e^{-iH_{j,j+1}\Delta t}\right), \tag{3.47}$$

$$U_{\text{even}}(\Delta t) = \prod_{j\in 2\mathbb{Z}} \left(e^{-iH_{j,j+1}\Delta t}\right) \,, \tag{3.48}$$

for sufficiently small time step Δt. This expression reproduces the brickwall structure of Eq. (3.3), with the local unitary gates given by

$$U_{j,j+1} = \exp[-iH_{j,j+1}\Delta t], \tag{3.49}$$

This decomposition underlies the numerical time-evolving block decimation algorithm [51, 52]. However, with the advent of gate-based quantum computation and quantum simulation these circuits can also be realized for larger Δt, and there has been increasing interest in understanding how the dynamics depends on the choice of Trotter step Δt [82, 139–147].

For small Δt, the Krylov framework for unitary circuits should reproduce the known results for Liouvillian dynamics with $\mathcal{L}(O) = [H, O]$. In this limit the superoperators are related as

$$\mathcal{U}(O) = U^\dagger O U \approx e^{iH\Delta t} O e^{-iH\Delta t} \tag{3.50}$$

$$\approx O + i\Delta t[H, O] = (\mathbb{1} + i\Delta t\mathcal{L})O \,, \tag{3.51}$$

up to corrections scaling as Δt^2. As such, we expect the initial Krylov operators $|\mathcal{O}_n)$ to be approximately equal for small Δt. However, the orthonormalization procedure can be sensitive to small perturbations, and in general the Krylov operators for large n for the unitary superoperator will differ significantly from the Krylov operators for the Liouvillian. As such, we only expect the matrix representations of $\mathcal{U}$ and $\mathcal{L}$ to agree (up to perturbative corrections) for sufficiently small n.

In the following, we consider three different classes of Hamiltonians and investigate the corresponding Krylov dynamics. For chaotic systems we first show how the Liouvillian structure is recovered at small Trotter step and transforms to the behavior of maximally ergodic Krylov dynamics, as observed in dual-unitary circuits, with increasing Trotter step. Next, we turn our attention to interacting integrable circuits with the Trotterized XXZ Hamiltonian as an example. Last we report the results for free-fermionic integrable systems using the XX Hamiltonian as an example.

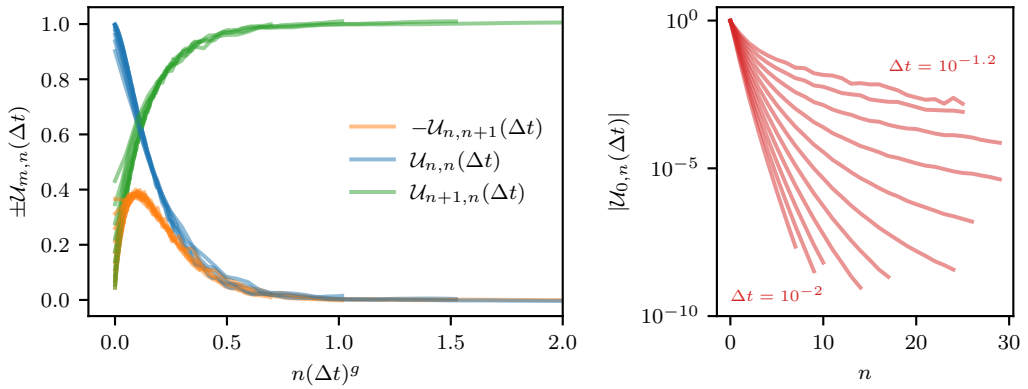

Figure 3.3: *The unitary superoperator $\mathcal{U}$ [Eq. (3.14)] describing the evolution of the initial operator $|O_0) = \sigma_0^z$ when the two-site gate is a Trotterized gate $U_{j,j+1} = \exp(-iH\Delta t)$, where H is drawn from the GUE. We represent the defining components of $\mathcal{U}$ in the Krylov basis as in Fig. 3.2. For small $n(\Delta t)^g$, the matrix elements $\mathcal{U}_{n\pm1,n}$ coincide with the results obtained for continuous evolution. With increasing $n(\Delta t)^g$, $\mathcal{U}_{n,n} = a_n$ and $\mathcal{U}_{n+1,n} = b_n$ approach 0 and 1 respectively (left) and the coefficients $\mathcal{U}_{0,n} = c_n$ decay (right), indicating that the unitary superoperator becomes dominated by the tridiagonal elements. The results were obtained for a representative example using a system of size 70 and TEBD with an MPS bond dimension of 1024 while varying Δt from 10^{-2} to $10^{-1.2}$ equidistant on a logarithmic scale. For this range of parameter values $g \approx 1.4$.*

3.4.1 Chaotic Hamiltonians

We consider a minimal model for chaotic Hamiltonians by drawing $H_{i,i+1}$ from the Gaussian unitary ensemble (GUE) and writing $U_{i,i+1} = \exp(-iH_{i,i+1}\Delta t)$. For different values of Δt we numerically perform the orthonormalization procedure using a tensor network approach, representing all operators as matrix product operators (see, e.g., Ref. [148]).

The results for the matrix elements of $\mathcal{U}$ are shown in Fig. 3.3 for different Trotter steps. We here present the matrix elements $\mathcal{U}_{n,n}$ and $\mathcal{U}_{n,n\pm1}$ for increasing n and different values of Δt, and we observe a collapse of the results for different Trotter steps if we plot the matrix elements as a function of $n(\Delta t)^g$, with $g \approx 1.4$. Before discussing the origin of this scaling collapse, we first observe that two different regimes with an intermediate crossover can be distinguished.

Hamiltonian dynamics. The first regime appears at small values of $n(\Delta t)^g$ and reproduces the expected results from Hamiltonian evolution: up to $n \propto 1/\Delta t$, the matrix elements of $\mathcal{U}$ reproduce those of the Liouvillian $\mathcal{L}$

as discussed in Ref. [39]. To be more precise, we find that

$$|a_n - 1| \propto n^{1.4}\Delta t^2\,, \tag{3.52}$$

$$|\tilde{b}_n + b_n/\Delta t| \propto (n\Delta t)^2\,, \tag{3.53}$$

for $n\Delta t \lesssim 1$. Note that in this regime the unitary superoperator is close to being tridiagonal. The diagonal elements being close to one reflects the appearance of the identity in Eq. (3.50), whereas the off-diagonal elements b_n reproduce the off-diagonal elements $\tilde{b}_n$ from the Liouvillian dynamics up to a rescaling by Δt. In this regime, the operator dynamics of the Trotterized circuit can hence be expected to remain close to the operator dynamics of the original Hamiltonian.

However, this regime cannot persist for arbitrarily large values of n. In chaotic systems the off-diagonal elements $\tilde{b}_n$ in the Liouvillian are expected to grow with the maximal possible rate as n increases, corresponding to growth in the off-diagonal element of $\mathcal{U}$ since $b_n \approx -\tilde{b}_n\Delta t$. However, unitarity restricts the matrix elements of $\mathcal{U}$ to satisfy $|\mathcal{U}_{mn}| \leq 1$, such that the growth of b_n is necessarily bounded.

Maximally ergodic dynamics. The second regime appears at larger values of n. Here $b_n = \mathcal{U}_{n+1,n} \approx 1$ and all other matrix elements $\mathcal{U}_{m,n} \approx 0$ for $m \neq n+1$, with the errors decreasing exponentially with increasing n (see also Appendix B.6). This structure of the Krylov matrix is identical to the structure previously observed in dual-unitary circuits in Eq. (3.33), indicating that in each step the Heisenberg evolution with U creates a new operator that is linearly independent from all previously generated operators in the Krylov subspace. In this regime the operator dynamics in the unitary circuit is qualitatively different from that of the Hamiltonian system. As one example, we can again consider the autocorrelation function for a Krylov operator $|\mathcal{O}_n)$. In the circuit case, the autocorrelation identically vanishes after a single discrete time step (up to exponentially small corrections), same as in dual-unitary circuits, which is prohibited in the Hamiltonian case. Here we can also contrast the long-time behavior of the autocorrelation function, since in the Hamiltonian case the autocorrelation function is expected to reach a nonzero thermal value constrained by conservation of energy, again to be contrasted with the vanishing autocorrelation function in the unitary circuit.

Crossover regime. The remaining question is about the origin of the transition scale and the collapse observed when rescaling n with Δt^g. As it turns out, this scale is very closely related to the size of the operator and operator spreading. Expanding $\mathcal{U}|\mathcal{O}_n)$ in Δt, the first order term is of magnitude $\ell\Delta t$, where ℓ is the number of sites $\mathcal{O}_n$ has support on. Hence, we expect a transition in the behavior of the circuit once an operator $|\mathcal{O}_n)$

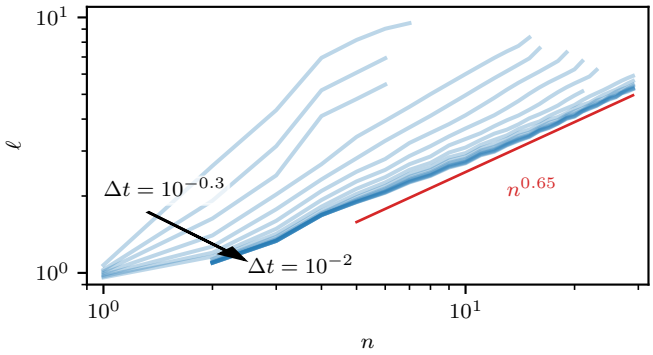

Figure 3.4: *Spatial extent ℓ of the Krylov operators $|\mathcal{O}_n)$ with increasing n. The extent is measured by fitting the error function to the OTOC calculated for each $|\mathcal{O}_n)$ for different Δt. Here ℓ is estimated by the point where the error function takes half its maximum value. For small Δt, the extent of the operator grows roughly as $\ell \propto n^{0.65}$. The same $\mathcal{U}$ and simulation setting was used as in Fig. 3.3. For details see Appendix B.7.*

acts non-trivially on around $\ell \sim 1/\Delta t$ sites. While the full support of both $|O_n)$ and $|\mathcal{O}_n)$ grows linearly in n, the bulk of the operator typically acts on a smaller number of sites, as quantified in, e.g., out-of-time-order correlators (OTOCs) and operator spreading [56–58]. While the support of $|O_n)$ is by now well understood through studies in, e.g., random unitary circuits, these results do not directly translate to the support of $|\mathcal{O}_n)$. We quantify the operator growth in the usual way, considering

$$\mathrm{OTOC}(n, j) = \mathrm{Tr}\left[\mathcal{O}_n^\dagger \sigma_j^\gamma \mathcal{O}_n \sigma_j^\gamma\right] / \mathcal{D}\,, \tag{3.54}$$

with $\gamma \in \{x, y, z\}$. We observe that this profile resembles an error function, as also expected for $|O_n)$, and define ℓ as the value of n where the error function equals $1/2$. The results are shown in Fig. 3.4. For the considered range of Δt, we have that $\ell \propto n^{0.65}$. In combination with $\ell \sim 1/\Delta t$ this roughly yields the observed transition on a scale $n \sim \Delta t^{-1.5}$. However, we note that this exponent is not universal since it crucially depends on Δt, which is apparent when considering different limits.

For large Δt we expect the operator spreading for $|\mathcal{O}_n)$ and $|O_n)$ to coincide and exhibit the biased diffusive growth previously observed [56–58], corresponding to an operator growth $\ell \propto n$. For very small Δt, we can approximate the unitary superoperator by the Liouvillian. In this limit the operator growth is subballistic, as most of the local operators in the Hamiltonian act on the bulk of the operator $|\mathcal{O}_n)$. We hence expect the operator growth to increase from subballistic growth in the limit $\Delta t \to 0$ to ballistic

growth for large Δt, with an intermediate superdiffusive but nonuniversal regime corresponding to the scaling observed in Fig. 3.3.

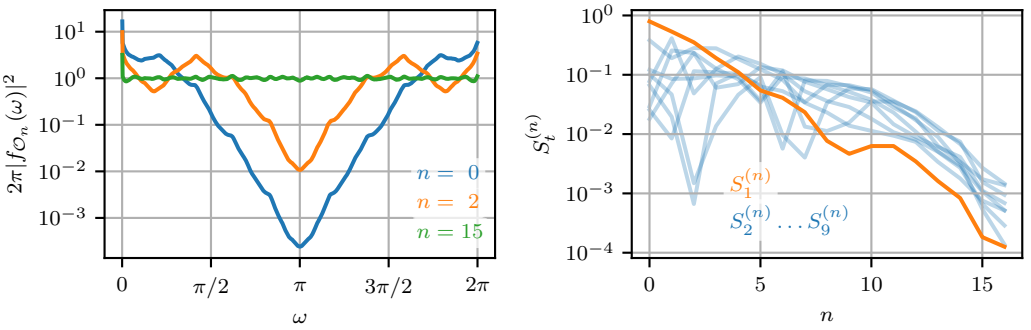

Figure 3.5: *Spectral function* $|f_O(\omega)|^2 = \sum_{p,q} |\langle p|O|q\rangle|^2 \, \delta(\theta_q - \theta_p - \omega)/\mathcal{D}$ *(left) and its Fourier transform (right), i.e., the autocorrelation functions or Fourier modes* $S_t^{(n)} = \mathrm{Tr}[\mathcal{O}_n^\dagger U^{\dagger t} \mathcal{O}_n U^t]/\mathcal{D}$*, for the Krylov operators* $\mathcal{O}_n$ *for the GUE system defined in Eq. (3.20). For* $n \to \infty$*, the spectral function approaches a constant. This approach is quantified through the Fourier modes of the spectral function of* $\mathcal{O}_n$*, where all Fourier modes* $S_t^{(n)}$ *of the spectral function appear to decay exponentially with* n*. This decay implies the exponential decay with* n *of the autocorrelation function of* $\mathcal{O}_n$ *for all times. The first Fourier mode* $S_1^{(n)}$ *is highlighted in orange as it is directly related to the unitary superoperator via* $S_1^{(n)} = \mathcal{U}_{nn} = a_n$ *[Eq. (3.56)]. These results were obtained by exact diagonalization of a system of size 14 with open boundary conditions using the same circuit structure and Hamiltonian parameters as in Fig. 3.3. Here we choose* $\Delta t = 10^{-0.8}$*, but the results are qualitatively similar for different* Δt*. To mitigate finite size effects,* $|f_{\mathcal{O}_n}|^2$ *is averaged over* $\Delta\omega = 2\pi/1000$*.*

Spectral function. The results from the previous section can be understood on the level of the spectral function, which yields a sufficient condition for the existence of the maximally ergodic regime as a stable attractor for the orthonormalization procedure. On the level of the spectral function, maximally chaotic dynamics corresponds to the spectral function of the Krylov operators being a flat function. These spectral functions are plotted in the left panel of Fig. 3.5 for different values of n, and we indeed observe that the spectral function flattens with increasing n.

Following Eq. (3.27), these spectral functions are related to the spectral function of the initial operator as

$$|f_{\mathcal{O}_n}(\omega)|^2 = |f_O(\omega)|^2 |p_n(\omega)|^2 \,, \tag{3.55}$$

where $p_n(\omega)$ are the polynomials representing the Krylov operators, which are orthonormal polynomials with $|f_O(\omega)|^2$ as weight functions. Stating that

the Krylov operators flow to the maximally chaotic regime is equivalent to the convergence of the polynomials stated in Eq. (3.31). As mentioned in Sec. 3.2.3, such a (uniform) convergence has in fact already been established in the theory of orthonormal polynomials on the unit circle provided the weight function/spectral function satisfies certain properties [133, 134]. However, this convergence crucially depends on the original spectral function $\log(|f_O(\omega)|^2)$ being Lebesgue integrable. This Lebesgue integrability is guaranteed if this spectral function is nonvanishing on the entire interval $[0, 2\pi)$, in which case the logarithm of the spectral function is well-defined and finite, yielding a sufficient condition for the existence of the maximally chaotic regime. This condition is expected to be fulfilled on physical grounds for chaotic systems: A vanishing spectral function would imply the existence of either selection rules or a spectrum that is not dense on the unit circle, both prohibited in chaotic dynamics [127, 128]. More specifically, these orthonormal polynomials have the property that the first n Fourier modes of $|p_n(\omega)|^{-2}$ agree with the first n Fourier modes of $|f_O(\omega)|^2$. For $n \to \infty$ all moments agree, indicating that Eq. (3.31) indeed applies (up to pathological exceptions, see also Section 3.5).

The diagonal of the unitary superoperator, $a_n = \mathcal{U}_{nn}$, is directly related to the spectral properties via

$$\mathcal{U}_{nn} = (\mathcal{O}_n|\mathcal{U}|\mathcal{O}_n) = \int_0^{2\pi} \mathrm{d}\omega\, e^{i\omega} |f_{\mathcal{O}_n}(\omega)|^2 \equiv S_1^{(n)}\,. \tag{3.56}$$

This expression relates the exponential decay of the diagonal of the unitary superoperator to the exponential decay of the first Fourier component $S_1^{(n)}$ of the spectral function of $\mathcal{O}_n$. We can more generally consider the decay of arbitrary Fourier modes

$$S_t^{(n)} = \int_0^{2\pi} \mathrm{d}\omega\, |f_{\mathcal{O}_n}(\omega)|^2 e^{i\omega t} \tag{3.57}$$

with $t \in \mathbb{N}_0$ as illustrated in the right panel of Fig. 3.5. All Fourier modes $S_t^{(n)}$ appear to decay similarly with increasing n, as also expected by the uniform convergence in Eq. (3.31). Hence, we expect in general a uniform convergence of the spectral function $|f_{\mathcal{O}_n}|^2$ towards $1/2\pi$, agreeing with the convergence of the unitary superoperator towards its maximally Krylov ergodic form.

We note that this convergence is particular to orthonormal polynomials on the unit circle and hence to unitary circuit dynamics. Conversely, the universal operator growth hypothesis for Hamiltonian dynamics translates to statements about the large-frequency asymptotics of the spectral function [39].

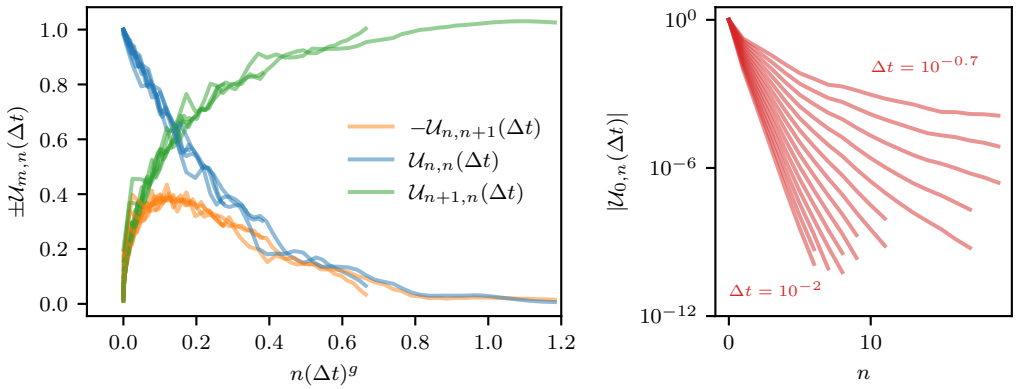

Figure 3.6: *The unitary superoperator $\mathcal{U}$ [Eq. (3.14)] describing the evolution of the initial operator $|O_0) = \sigma_0^z$ when the two-site gate is a Trotterized gate $U_{j,j+1} = \exp(-iH\Delta t)$, where H is the XXZ Hamiltonian with $\Delta = 3$. We represent the defining components of $\mathcal{U}$ in the Krylov basis as in Fig 3.2. The results are qualitatively similar to the GUE case, see Fig. 3.3. For small $n(\Delta t)^g$, the matrix elements $\mathcal{U}_{n\pm1,n}$ coincide with the results obtained for continuous evolution. With increasing $n(\Delta t)^g$, $\mathcal{U}_{n,n} = a_n$ and $\mathcal{U}_{n+1,n} = b_n$ approach 0 and 1 respectively (left) and the coefficients $\mathcal{U}_{0,n} = c_n$ decay (right), indicating that the unitary superoperator becomes dominated by the tridiagonal elements. The results were obtained using a system of size 70 and TEBD with an MPS bond dimension of 1024 while varying Δt from 10^{-2} to $10^{-0.7}$. For this range of parameter values $g \approx 2.1$.*

3.4.2 Interacting Integrable Hamiltonians

Let us now consider the integrable XXZ Hamiltonian,

$$H_{j,j+1} = \sigma_j^x \sigma_{j+1}^x + \sigma_j^y \sigma_{j+1}^y + \Delta \sigma_j^z \sigma_{j+1}^z. \tag{3.58}$$

For small Δt the matrix elements converge towards those of the Liouvillian for the Hamiltonian case, where $\mathcal{L}_{n+1,n} \propto \sqrt{n}$, see Fig. 3.6. However, for larger n the qualitative difference between the integrable and chaotic dynamics disappears and we recover the maximally ergodic form with only ones on the lower diagonal and zeros everywhere else, on the same scales as for the chaotic model. This convergence is not unexpected, since the arguments presented in the previous subsection for the convergence of the spectral function directly carry over to the integrable model, as the spectral function for generic operators is expected to be nonvanishing on the entire interval $[0, 2\pi]$ (which is not guaranteed for noninteracting systems).

The difference in Krylov dynamics for chaotic and interacting integrable remains a topic of active research. Let us briefly discuss some recent results for the Krylov dynamics for interacting integrable systems under Hamiltonian

evolution (see Refs. [43, 44]) and relate these to the observed phenomenology. For finite systems, the Krylov complexity saturates at Heisenberg time scales $t_H \propto \mathcal{D}$. In chaotic systems, this saturation value was argued to be approximately $\mathcal{D}^2/2$, whereas in interacting integrable systems the Krylov complexity saturates at a smaller value (for which no analytic prediction exists). These saturation values can be linked to localization in Krylov space: delocalization in Krylov space results in the chaotic saturation value, whereas a certain degree of localization in Krylov space leads to a saturation value below the chaotic one. Crucially, within interacting integrable systems this localization is induced by disorder in the Lanczos coefficients, where the Lanczos coefficients in interacting integrable system are more disordered than these in chaotic systems. The same behavior can be observed in the unitary superoperator (Fig. 3.6), where the coefficients are noisier compared to the GUE results (Fig. 3.3).

An additional difference between chaotic and interacting integrable can be observed here: while both chaotic and interacting integrable systems converge to the maximally ergodic regime, the number of discrete time steps required to reach this regime appears to be (parametrically) larger in interacting integrable systems. As discussed in the GUE example, the unitary dynamics can be expected to reproduce the Hamiltonian dynamics for sufficiently small n provided the matrix elements of $\mathcal{U}$ reproduce those of the Liouvillian $\mathcal{L}$. For chaotic systems, we already observed that this regime holds up to $n \sim 1/\Delta t$. Conversely, in interacting integrable systems this regime holds up to $n \sim 1/\Delta t^{1.3}$ (with an exponent that we do not expect to be universal) using

$$|a_n - 1| \propto n^{1.5}\Delta t^2\,, \tag{3.59}$$

$$|\tilde{b}_n + b_n/\Delta t| \propto n^{1.5}\Delta t^2 \tag{3.60}$$

as numerically shown in Appendix B.8. As such, it takes parametrically longer to reach the maximally ergodic regime in interacting integrable circuits as compared to the chaotic case. The larger values of n required to reach this regime can also be understood from the slower growth of b_n for small n as compared to chaotic systems, since the maximally ergodic regime is characterized by a saturation of b_n. However, the difference between chaotic and interacting integrable Krylov dynamics remains largely quantitative rather than qualitative (as for Hamiltonian dynamics).

3.4.3 Noninteracting Integrable Hamiltonians

We now consider integrable systems that can be mapped to free fermions. We will first restrict ourselves to numerical results, and analytical arguments

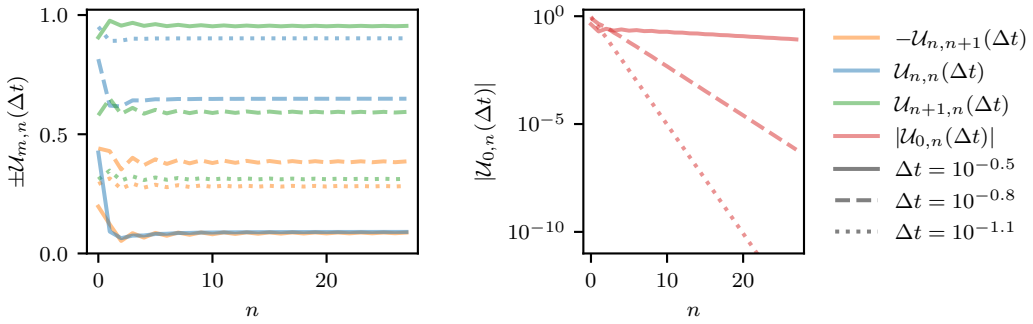

Figure 3.7: *The unitary superoperator $\mathcal{U}$ [Eq. (3.14)] describing the evolution of the initial operator $|O_0) = \sigma_0^z$ when the two-site gate is a Trotterized gate $U_{j,j+1} = \exp(-iH\Delta t)$, where H is the XX Hamiltonian. We represent the defining components of $\mathcal{U}$ in the Krylov basis as in Fig 3.2. After an initial transient behavior the diagonals approach constant values; the dependence of those values on Δt is shown in Fig. 3.8. These results were obtained using the analytical expressions [Eq. (3.67)].*

will be presented in Sec. 3.5. As a representative example, we focus on

$$H_{j,j+1} = \sigma_j^x \sigma_{j+1}^x + \sigma_j^y \sigma_{j+1}^y \,, \tag{3.61}$$

and consider a local initial operator σ_0^z.

For these circuits we again find the diagonal part of the Krylov matrix $\mathcal{L}$ to be dominant, see Fig. 3.7. However, the noticeable difference in comparison to the chaotic and interacting integrable circuits is the large n limit. We observe that for large n, $b_n = \mathcal{U}_{n+1,n}$ approaches a constant value which is lower than 1 for $\Delta t < \pi/8$ and 1 for $\Delta t \geq \pi/8$, see Fig. 3.8. As such, for free-fermionic integrable models the existence of the maximally chaotic regime crucially depends on the choice of Trotter step: for a small Trotter step $\mathcal{U}$ never approaches the maximally ergodic Krylov dynamics. This transition can be understood analytically, as will be made apparent in the next section.

3.5 Trotter Transition in Noninteracting Circuits

We here detail the dynamics of the integrable non-interacting system, presenting exact results for the autocorrelation functions and corresponding spectral functions, and relate these to the nonanalytic Trotter transitions observed in the previous section. A defining feature of noninteracting models is that their dynamics can be decomposed in the dynamics of decoupled single-particle sectors. Trotter decompositions of noninteracting models have the property that the corresponding unitary circuit remains noninteracting

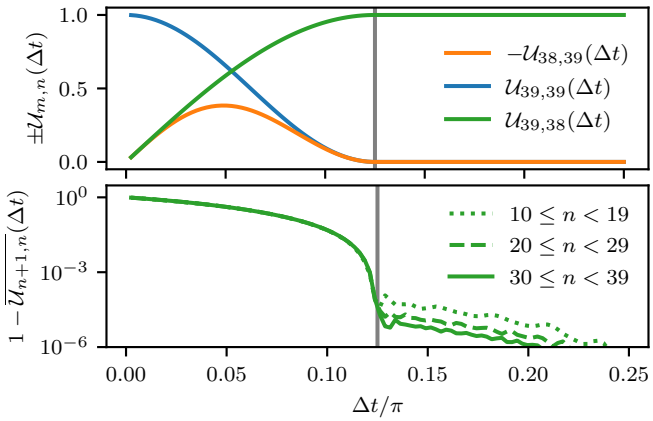

Figure 3.8: *Constant values approached by the tridiagonal part of $\mathcal{U}$ for large n, see Fig. 3.7, as function of Δt. A transition is visible at $\Delta t = \pi/8$, where the value of the lower diagonal $\overline{U}_{n+1,n}$ approaches 1 nonanalytically for $n \to \infty$ (lower panel). The results were obtained by numerical diagonalization of a system of size 200 with open boundary conditions. Data points for the lower diagonal are averaged over the ten indicated values of n for ease of visualization.*

since such a decoupling in single-particle sectors remains possible. This can be understood as a specific case of a Floquet drive of noninteracting models that does not couple different particle sectors, preserving the noninteracting structure and leading to a noninteracting Floquet Hamiltonian [149]. These Trotter transitions can also be seen as transitions in the Floquet Hamiltonian as the driving frequency, as set by Δt, is varied.

The two-site unitary gate underlying this circuit is given by

$$U_{12} = \exp\left[-i\Delta t(\sigma_1^x\sigma_2^x + \sigma_1^y\sigma_2^y)\right] . \tag{3.62}$$

We first note that at $\Delta t = \pi/4$ this gate reduces to the iSWAP gate, i.e.,

$$U = \begin{pmatrix} 1 & 0 & 0 & 0 \\ 0 & 0 & i & 0 \\ 0 & i & 0 & 0 \\ 0 & 0 & 0 & 1 \end{pmatrix} , \tag{3.63}$$

which is a particular case of a dual-unitary gate.

The dynamics of the full circuit can be exactly solved through a Jordan-Wigner transformation followed by a decomposition in Fourier modes with fixed momentum. A detailed derivation is given in Appendix B.9, and we here only outline the final results. The Jordan-Wigner transformation maps the spin operators to fermionic operators, and we consider fermionic single-

particle operators with fixed momentum acting on even and odd sites respectively,

$$c_{k+} = \frac{1}{\sqrt{N}} \sum_{j=0}^{N-1} e^{ikj} c_{2j}, \tag{3.64}$$

$$c_{k-} = \frac{1}{\sqrt{N}} \sum_{j=0}^{N-1} e^{ikj} c_{2j+1}, \tag{3.65}$$

where c_j acts on site j and satisfies the fermionic anticommutation relation $\{c_i^\dagger, c_j\} = \delta_{ij}$. We consider a system consisting of $2N$ sites, and k can take the values $2\pi n/N, n = 0, 1, \ldots, N-1$. Denoting $|c_{k\pm})$ as $|k_\pm)$, we find that the unitary superoperator acting on fermionic annihilation operators can be decomposed as

$$\mathcal{U} = \sum_k \begin{pmatrix} |k_+) & |k_-) \end{pmatrix} \mathcal{U}_k \begin{pmatrix} (k_+| \\ (k_-| \end{pmatrix}, \tag{3.66}$$

where $\mathcal{U}_k$ are 2×2 matrices parametrized as

$$\begin{aligned} \mathcal{U}_k = \mathbb{1} &- \sin(2\Delta t) \\ &\times \begin{pmatrix} \sin(2\Delta t)(1+e^{ik}) & i\cos(2\Delta t)(1+e^{ik}) \\ i\cos(2\Delta t)(1+e^{-ik}) & \sin(2\Delta t)(1+e^{-ik}) \end{pmatrix}. \end{aligned} \tag{3.67}$$

For fermionic creation operators the Hermitian conjugate of this matrix should be used.

Equation (3.66) can be directly diagonalized to obtain two complex-conjugate eigenvalues $e^{\pm i\omega_k}$, where the dispersion relation follows as

$$\cos(\omega_k) = 1 - 2\sin^2(2\Delta t)\cos^2(k/2). \tag{3.68}$$

In the limit $\Delta t \to 0$, we recover the dispersion relation for the original Hamiltonian dynamics, with

$$\omega_k = 4\Delta t \cos(k/2)\,, \tag{3.69}$$

up to corrections scaling as Δt^2. At $\Delta t = \pi/4$ the corresponding brickwall circuit is dual unitary, and we find that

$$\omega_k = k \pm \pi\,. \tag{3.70}$$

Here the linear dispersion indicates that all excitations spread ballistically with a fixed velocity ± 1, as readily apparent for iSWAP gates and more

generally expected for integrable dual-unitary gates, where conservation laws correspond to solitons with maximal velocity ± 1 [150]. The appearance of the factor π indicates a sign change after every time step, which is a consequence of applying the iSWAP gate twice.

The Krylov dynamics is fully determined by the autocorrelation function. For, e.g., $O_0 = \sigma_0^z$, the autocorrelation follows as

$$\frac{1}{2}\mathrm{Tr}\left[\sigma_0^z(t)\sigma_0^z\right] = \left|\mathrm{Tr}\left[c_0^\dagger(t)c_0\right]\right|^2, \tag{3.71}$$

where we used $\sigma_0^z = 1 - 2c_0^\dagger c_0$ and the fermionic commutation relations. We can use the decomposition in eigenmodes to obtain (see Appendix B.9)

$$\mathrm{Tr}\left[c_0^\dagger(t)c_0\right] = \frac{1}{2\pi}\int_0^{2\pi} \mathrm{d}k \cos(\omega_k t), \tag{3.72}$$

where we have taken the thermodynamic limit of an infinite system size, $N \to \infty$, in the previous expressions.

From this expression it follows that the spin autocorrelation function (3.71) will contain oscillations with frequencies $\omega_k \pm \omega_{k'}$. For small Δt these are bounded by $2\omega_{k=0}$, where the dispersion relation takes a particularly simple form,

$$\omega_{k=0} = 4\Delta t\,. \tag{3.73}$$

As such, the spectral function has support in $[-2{\times}4\Delta t, 2{\times}4\Delta t]$, as illustrated in Fig. 3.9. We hence find that the spectral function is gapped around the π-mode where $\omega_k = \pi$ for $0 \leq \Delta t < \pi/8$, the gap at the π-mode closes at $\Delta t = \pi/8$, and then the system remains gapless for $\pi/8 \leq \Delta t \leq 3\pi/8$. In the gapped phase the spectral function has a gap, whereas the spectral function is fully supported on $[0, 2\pi]$ in the gapless phase. The unitary gate is periodic in Δt, so a further increase of Δt would lead to alternating gapped and gapless phases.

The spectral function for S_0^z can be analytically obtained from Eq. (3.72). Focusing on the case $0 \leq \Delta t < \pi/8$ and performing a change of integration variable in Eq. (3.72) from k to ω_k, we find

$$\mathrm{Tr}\left[c_0^\dagger(t)c_0\right] = \int_{-4\Delta t}^{4\Delta t} \mathrm{d}\omega_k \frac{\cos(\omega_k/2)\cos(\omega_k t)}{\sqrt{\cos^2(\omega_k/2) - \cos^2(2\Delta t)}}, \tag{3.74}$$

such that the spectral function for $c_0^\dagger$ can be read off as

$$|f_{c_0}(\omega)|^2 = \frac{\cos(\omega/2)}{\sqrt{\cos^2(\omega/2) - \cos^2(2\Delta t)}}\,. \tag{3.75}$$

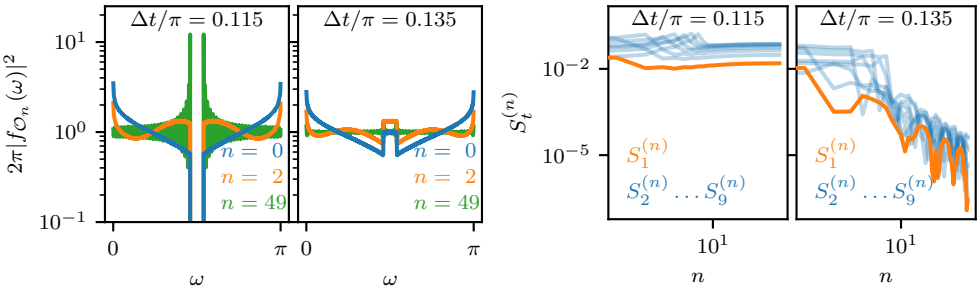

Figure 3.9: *Spectral function* $|f_O(\omega)|^2 = \sum_{p,q} |\langle p|O|q\rangle|^2 \, \delta(\theta_q - \theta_p - \omega)/\mathcal{D}$ *(left two panels) and its Fourier transform (right two panels), i.e., the autocorrelation function or Fourier modes* $S_t^{(n)} = \mathrm{Tr}[\mathcal{O}_n^\dagger U^{\dagger t} \mathcal{O}_n U^t]/\mathcal{D}$*, for the Krylov operators* $\mathcal{O}_n$ *for the non-interacting integrable system based on the Trotterized XX model. Here* $|O_0) = \sigma_0^z$*. For* $\Delta t < \pi/8$*, the spectral function is gapped and the autocorrelation, i.e., Fourier modes* $S_t^{(n)}$*, does not decay with* n*, while the gap is closed for* $\Delta t \geq \pi/8$ *yielding a decaying autocorrelation. The results were obtained by numerical diagonalization of a system of size* 200 *with open boundary conditions. To mitigate finite size effects,* $|f_{\mathcal{O}_n}|^2$ *is averaged over* $\Delta\omega = 2\pi/1000$*.*

for $|\omega| < 4\Delta t$ and zero otherwise. The spectral function for the spin operator σ_0^z then follows from the convolution theorem as

$$|f_O(\omega)|^2 = \frac{1}{2\pi} \int_{-4\Delta t}^{4\Delta t} \mathrm{d}\mu \, |f_{c_0}(\mu)|^2 |f_{c_0}(\omega - \mu)|^2 \,. \tag{3.76}$$

This expression corresponds to the spectral function from Fig. 3.9 in the gapped phase.

The action of the Krylov orthonormalization procedure can again be understood as a flattening of the spectral function, as illustrated in Fig. 3.9. However, if $|f_O(\omega)|^2 = 0$ for some values of ω, then at these values we also have that $|f_{\mathcal{O}_n}(\omega)|^2 = |f_O(\omega)|^2 |p_n(\omega)|^2 = 0$, i.e., the spectral function of $|\mathcal{O}_n)$ also vanishes. As such, for a gapless phase and a spectral function that is fully supported on $[0, 2\pi]$ we can repeat the arguments from Sect. 3.4.1 to argue that the Krylov operators approach the maximally ergodic form where $b_n = 1$ and $(\mathcal{O}_n|\mathcal{U}|\mathcal{O}_n) = 0$ for large n. However, this is impossible in the gapped phase, since the existence of such maximally ergodic operators requires a constant spectral function, which is precluded by the gap in $|f_{\mathcal{O}_n}(\omega)|^2$. The nonanalytic transition in the Krylov dynamics can hence be directly related to the presence of a gap at the π-mode in the spectral function.

The previous analysis depended on the fact that the initial spin operator could be recast as a fermion bilinear. This analysis can be directly extended to operators of increasing size. If an initial operator O_0 can be decomposed in

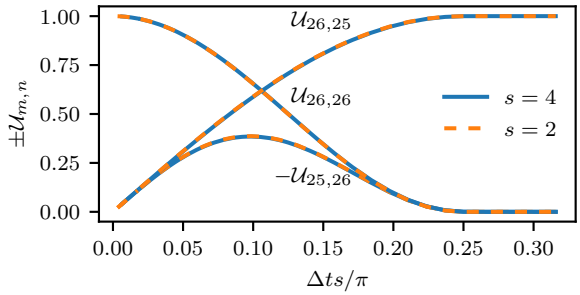

Figure 3.10: *Tridiagonal matrix elements of the unitary superoperator $\mathcal{U}$ for the noninteracting dynamics and initial operators with varying fermionic sizes s. The results were obtained using the autocorrelation function $|\mathrm{Tr}[c_0^\dagger(t)c_0]|^s$, Eq. (3.77). Rescaling Δt with s yields a collapse. The results were obtained using a system of size 2000 with periodic boundary conditions and an increased numerical precision of 100 digits.*

s fermionic operators, the frequencies appearing in the Fourier transform of its autocorrelation will be of the form $\pm\omega_{k_1}\pm\omega_{k_2}\cdots\pm\omega_{k_s}$. Hence, if the single-particle spectrum ω_k has support $[-4\Delta t, 4\Delta t]$, the spectrum of the s-particle operator has extend $[-4s\Delta t, 4s\Delta t]$. Indeed, we find for general operators that the transition appears at $\Delta t = \pi/(4s)$, as illustrated in Fig. 3.10 for an operator with autocorrelation function

$$\left|\mathrm{Tr}\left[c_0^\dagger(t)c_0\right]\right|^s. \tag{3.77}$$

This autocorrelation function corresponds to that of operators $|O_0) = c_0$ ($s = 1$), $|O_0) = \sigma_0^z$ ($s = 2$), and more generally $\sigma_0^z\sigma_m^z\ldots\sigma_{(m-2)s/2}^z$ (arbitrary s) for spatially separated σ^z operators with a sufficiently large spacing m such that the autocorrelation function factorizes. This result highlights the dependence of the chaotic nature of the operator dynamics on the initial operator. The larger the operator, the larger the regime where it is maximally Krylov ergodic. A similar effect was observed in Hamiltonian evolution, where the Krylov dynamics of a nonlocal operator in a noninteracting systems resembles the Krylov dynamics of an operator in an interacting systems [39].

To conclude this section, we briefly contrast the Trotter transition observed in this chapter with the Trotter transitions discussed in Refs. [140, 144]. These works consider integrable Hamiltonians for which the Trotterization breaks integrability for all nonzero Trotter steps. As the Trotter step is increased the integrability-breaking effects become more important and lead to a sharp transition to chaotic dynamics. In this chapter, conversely,

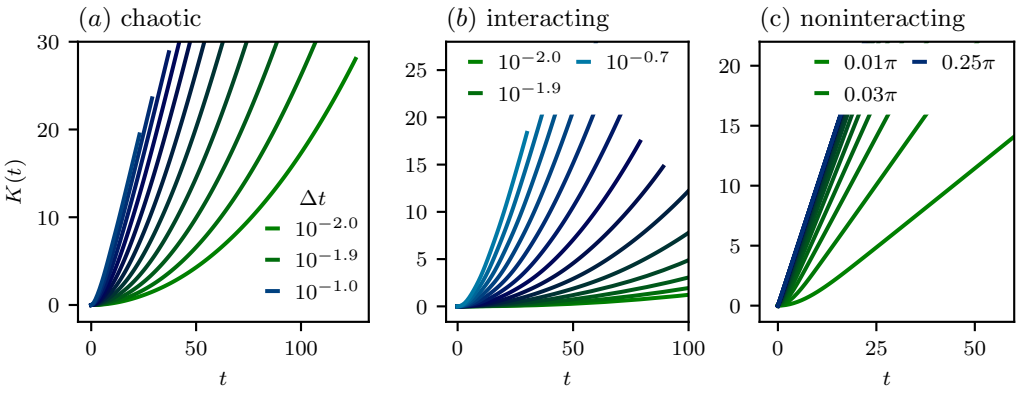

Figure 3.11: *Krylov complexity $K(t)$ [Eq. (3.19)] for the chaotic, interacting integrable, and noninteracting integrable at different values of the Trotter step Δt. In all cases we observe linear growth of the Krylov complexity for sufficiently large t. In chaotic and interacting integrable systems this linear growth has slope 1, whereas for noninteracting integrable systems this slope depends on the Trotter step and transitions to 1 at $\Delta t = \pi/8$.*

we consider Trotterizations that do not break integrability, and these transitions happen while the full circuit remains (noninteracting) integrable. In this sense these transitions are comparable to heating transitions in periodically driven noninteracting system as the driving frequency is varied, which similarly happen without breaking integrability [151–153].

3.6 Krylov Complexity

In this section we illustrate the growth of the Krylov complexity $K(t)$ for the three examples of circuits discussed in the previous section for completeness. Figure 3.11 shows the growth of the Krylov complexity for different choices of Trotter step in (a) chaotic systems drawn from the GUE, (b) the interacting integrable XXZ model, and (c) the noninteracting integrable XX model. As we could already deduce from the analysis of the tridiagonal structure of the unitary superoperator $\mathcal{U}$, the Krylov complexity approaches a linear growth for large t for the chaotic and interacting integrable systems. While there is no qualitative difference between the two, we observe that the Krylov complexity initially grows parametrically significantly slower in the integrable model, as also observed for Hamiltonian dynamics [39, 43, 44]. Note that for small Trotter step many (discrete) time steps are necessary in order to approach this maximally ergodic regime, such that the crossover to the ergodic regime falls outside the considered range of time steps. This effect is especially pronounced in the integrable model due to the slower initial growth of

Krylov complexity.

For the noninteracting integrable system we observe that, after some initial transient dynamics, the Krylov complexity also exhibits a linear growth. The slope of this growth now increases with increasing Trotter step and saturates for $\Delta t > \pi/8$. This behavior agrees with our analysis of the unitary superoperator and the discussed Trotter transition.

3.7 Conclusions and Outlook

In this chapter we extended the notion of Krylov complexity to unitary circuit dynamics and applied this framework to study the effect of Trotterization, contrasting the Hamiltonian dynamics with the circuit dynamics. During the unitary dynamics, an initial operator O_0 will spread out in a corresponding Krylov basis $\{\mathcal{O}_0, \mathcal{O}_1, \mathcal{O}_2, \dots\}$ obtained through a Gram-Schmidt orthonormalization procedure of the set of operators $\{O_0, U^\dagger O_0 U, U^{\dagger 2} O_0 U^2, \dots\}$. The autocorrelation function for O_0 only depends on its weight on $\mathcal{O}_0$ at any given time, giving the Krylov operators $\mathcal{O}_{n>0}$ the interpretation of 'bath operators' that do not contribute to the autocorrelation dynamics. In this basis the unitary evolution superoperator exhibits an upper Hessenberg matrix form that can be characterized with a limited number of parameters. We argued that for generic (chaotic) dynamics this superoperator attains a universal form after sufficiently many steps in the Krylov basis.

Physically, for generic dynamics the orthonormalization procedure underlying the Krylov approach converges to a set of operators that are here denoted 'maximally ergodic Krylov operators'. These maximally ergodic operators present operators for which the unitary circuit dynamics is particularly simple: They are characterized by their instantaneously vanishing autocorrelation function, flat spectral function, and a maximal growth of Krylov complexity. For these operators the correlation function is hence indistinguishable from the random matrix prediction. In this sense the Gram-Schmidt orthonormalization procedure generically converges to maximally random bath operators.

In the specific case of unitary circuits obtained as a Suzuki-Trotter decomposition of local Hamiltonian dynamics, we observed that the approach to the maximally ergodic regime scales with the Trotter step: for smaller Trotter step the maximally ergodic operators, while still local, will have a larger support. For these operators the effect of Trotterization is most severe since the dynamics of their autocorrelation function is indistinguishable from purely random matrix dynamics.

For integrable systems two different behaviors were observed. While interacting integrable systems also converged to the maximally ergodic regime,

they did so on a (parametrically) longer scale and with the Lanczos coefficients exhibiting a noisier structure, as also observed in Hamiltonian dynamics. In noninteracting integrable systems the Krylov dynamics exhibited a nonanalytic transition as the Trotter step was varied. For sufficiently short Trotter step the maximally ergodic regime is never reached, whereas after a critical Trotter step the Krylov dynamics again converges to the maximally ergodic regime.

This transition can be interpreted as a transition in the conservation laws underlying integrability. For short Trotter steps these conservation laws remain sufficiently restrictive that they prevent maximally ergodic dynamics, as expected for integrable Hamiltonian dynamics, whereas at the critical Trotter step the effect of Trotterization becomes apparent and maximally ergodic Krylov dynamics is allowed. These nonanalytic Trotter transitions can be understood through an analytic calculation of the spectral function of the initial operator. For sufficiently short Trotter step this spectral function has a gap at the π-mode of the Floquet Brillouin zone, whereas this gap closes at the critical Trotter step. The orthonormalization procedure for operators translates to an orthonormalization procedure on the spectral function, which generally converges to a flat spectral function. However, the presence of a gap precludes the convergence to a flat spectral function and hence the convergence to maximally ergodic operators.

The work presented in this chapter opens up various directions: Krylov complexity has been widely used in the recent study of Hamiltonian dynamics, and the presented framework can be directly applied to study unitary dynamics in the absence of any underlying static Hamiltonian, e.g., Floquet models. The correspondence between the spectral function and the Krylov dynamics strengthens the deep connection of spectral functions with quantum chaos. In Hamiltonian dynamics the spectral functions can exhibit different behavior for $\omega \to 0$ for chaotic and integrability-breaking vs. integrability-preserving dynamics [129–131], inviting similar studies using the Krylov approach. Here, the difference should be apparent in different limiting behaviors of the Krylov complexity. The connection between quantum chaos and delocalization in Krylov space should similarly still hold, and can be studied for more general unitary dynamics [42–44]. Analytical progress has recently been made for ETH by directly focusing on operator dynamics [154], and a natural direction for future work would be to relate these results to Krylov dynamics. While we focused on one-dimensional systems in this chapter, the developed framework also directly applies to higher-dimensional systems.

Furthermore, it would be interesting to relate the notion of a bath in Krylov dynamics to similar notions of a bath in unitary circuit dynam-

ics, such as in the influence matrix approach [79, 155]. In a similar vein, Refs. [156, 157] proposed a classical simulation of operator dynamics by applying an artificial dissipation acting on long operators, allowing transport coefficients to be efficiently obtained. Backflow corrections from these long operators were argued to be exponentially small, similar to the corrections from the maximally ergodic operators in this chapter – which also encode long operators –, presenting a further justification for this approximation. Exploring this connection would be useful for better understanding both the applicability of this classical approach and the emergence of hydrodynamics from operator dynamics.

The proposed approach may find applications in current Trotter-based methods to study quantum dynamics, both theoretical and analytical, since it highlights which operators are most sensitive to the effect of the Trotterization. The observed transition in noninteracting systems as the Trotter step is varied resembles the heating transition in periodically driven noninteracting systems [151–153, 158], but crucially depends on the operator being studied, as apparent in the dependence of the critical Trotter step on the operator size. In this way unitary Krylov dynamics present a new probe to study Floquet transitions and unitary circuit dynamics.

Part II

Information Scrambling

4 Information Relocalization

The work in this chapter has appeared as part of the following article

Philippe Suchsland, Benoît Douçot, Vedika Khemani, Roderich Moessner. *Dynamical correlations and domain wall relocalization in transverse field Ising chains.*
In: Phys. Rev. B 112, 014311 (21 July, 2025) [159]

The second part of this thesis is dedicated to information scrambling, one of the most studied dynamical aspects of quantum chaos. With recent experimental progress on coherently evolving quantum matter, quantum dynamics has become a focal point of modern physics research [160–176]. In quantum dynamics, information scrambling refers to the delocalization of initially localized information in quantum chaotic systems [177, 178]. This resolves the apparent conflict between the reversibility of quantum evolution and the observation that systems approach thermal states, as formulated in the eigenstate thermalization hypothesis [179]. This strong connection of many-body quantum chaos to information scrambling has made information scrambling a widely studied phenomenon in continuous time, Floquet systems [180, 181], circuit settings [56, 182], maximally chaotic and integrable systems [183–186], with and without conservation laws [187–189], in settings with diffusive as well as ballistic dynamics [190] and in the presence of phase transitions [191–198]. In these studies, out-of-time ordered correlators (OTOCs) emerged as an insightful probe of information spreading and scrambling. Proposed by Larkin *et al.* [199–209], OTOCs measure how a perturbation influences the final measurement, thereby probing the spreading and scrambling of information. Beyond their role in quantum chaos and information scrambling, they have been studied in relation to a variety of phenomena, including black hole physics [210–212].

One research direction considers the properties of OTOCs in the presence of phase transitions. Numerical results suggest that OTOCs can serve as dynamical probes of phase transitions. In this chapter, we explore this idea further by employing numerical and analytical calculations in integrable and chaotic systems. We provide an explanation for the previously found numerical results and present a detailed analysis of the stability of OTOCs in ordered phases under integrability breaking. We discuss the relation to in-

formation spreading and the phase transition in integrable systems, showing that in OTOCs, in general, cannot probe phase transitions reliably.

This chapter is structured as follows. First, we provide a more detailed overview of the results presented in this chapter and the related research in Section 4.1. We introduce the model and observed phenomenology in Section 4.2. We discuss the phenomenology heuristically and introduce the relocalization mechanism in Section 4.3. The explanation and the relocalization mechanism are substantiated in Section 4.4 by interpreting analytical calculations which become exact in the long-time limit. Its relation to the quantum phase transition is discussed in Section 4.6 and its connection to information spreading is covered in Section 4.5. Last, in Section 4.7, we demonstrate the instability of the observed OTOC behavior in an instructive classical setting, with disorder and in systems with broken integrability. We conclude this work in Section 4.8.

4.1 Overview

One recent line of inquiry concerns the possible capacity of OTOCs to act as diagnostics for zero-temperature phases in quench experiments in a way which is not accessible to traditional time-ordered correlators [191–197]. A case in point is the one-dimensional transverse field Ising model (TFIM), where recent work provided numerical evidence that the nonvanishing OTOC of an order parameter (concretely, the local magnetization) evaluated at late times detects the presence of ground state ordering, even starting from an initially fully polarized state [191, 192, 196, 197]. The numerics indicated this behavior for both the TFIM, which is integrable, and a perturbed (interacting/generic) nonintegrable model. These results were surprising because the polarized state is a finite temperature state for any nonzero transverse field, and clean one-dimensional systems do not order at finite temperature. Indeed, in contrast with the OTOC, standard temporal correlators of the magnetization decay to zero, as expected from thermalization to a paramagnetic finite temperature equilibrium state. This raises the theoretical question of how the OTOC might manage to evade thermalization to detect the order present in the ground state of the Hamiltonian, but absent in equilibrium at the energy density corresponding to the initial state of the quench.

In our work, we resolve this and other questions, providing a detailed and comprehensive study of OTOCs for a variety of Ising chains. We first study the integrable $S = \frac{1}{2}$ TFIM and provide an explicit and exact computation of the OTOC starting from the fully polarized state. We show that this does have a nonzero asymptote everywhere in the ferromagnetic phase, even as the time-ordered autocorrelator of the magnetization vanishes. We uncover

a strikingly rich phenomenology in this model summarized in Table 4.1. We provide an intuitive physical picture for these results, identifying the physical processes underpinning the dynamics of domain walls. A central, one is what we term dynamical relocalization. This is linked to the absence of chaos, and it explains the observed signal in the OTOC. We further find that the state underpinning the OTOC signal resembles a rotated state with low entanglement.

Intriguingly, in the analogous classical Ising chain, we find that both the OTOC and autocorrelator of the magnetization exhibit a nonvanishing late-time signal. This can be transparently traced to a failure of the magnetization to thermalize fully. Here, we find that thermalization is promoted by adding disorder to the couplings, thereby removing translational invariance from the Hamiltonian (but not from the initial state of the quench): Now the magnetization at long times vanishes classically.

Analogously, the OTOC in the quantum setting is strongly degraded by disorder. Indeed, the main effect of disorder is to reduce what we refer to as dynamical constraints on the time evolution: These are the integrals of motion which arise due to symmetry and integrability of the Hamiltonian, which render it block diagonal. The sense in which the constraints are degraded is that the blocks of the disordered Hamiltonian have sizes of $O(N)$, the size of the system, rather than $O(1)$ in the clean case.

This in turn suggests that the nonvanishing late-time OTOC is predicated on the nonergodicity arising from the integrability of the TFIM. Indeed, a perturbed nonintegrable Ising magnet, initialized with a fully polarized state at weak transverse field, is doubly proximate to integrability: first, on account of the weakness of the perturbation and, second, as a result of hosting a small density of—and hence weakly interacting—domain walls. The apparently nonvanishing OTOC thus is likely only a prethermal signal, visible on the short to intermediate times to which present day numerical tools are limited.

4.2 The Transverse Field Ising Model

In this section, we introduce the transverse field Ising model and domain walls, which will be used in Section 4.3 to explain the observations. Then, we diagonalize the transverse field Ising model, allowing for an analytical treatment of the observed phenomena in Section 4.4.

4.2.1 Model and Observables

We study the TFIM, a chain of N spins-$\frac{1}{2}$ (represented by Pauli matrices $\sigma_j^{x/y/z}$)

$$H_{\mathrm{TFI}} = -J \sum_{j=-N/2}^{N/2-1} \sigma_j^z \sigma_{j+1}^z + g \sum_{j=-N/2}^{N/2-1} \sigma_j^x \tag{4.1}$$

by mapping it to a noninteracting model of fermions corresponding to a p-wave superconductor [213, 214]. The model has Ising symmetry (generated by $\mathcal{S} = \prod_{i=1}^{N} \sigma_i^x$), spontaneously broken for $J > g$ via a quantum phase transition at $J = g$. We monitor the magnetization dynamics starting from an initial state $|\Psi\rangle$

$$M_\Psi(t) = \langle \Psi | e^{iHt} \sigma_0^z e^{-iHt} | \Psi \rangle \ . \tag{4.2}$$

In the thermodynamic limit (TDL), symmetry breaking in the ground state $|0\rangle$ is diagnosed by nonzero $M_0(t)$.

In addition, for a quench starting with the fully polarized state, a simple OTOC consisting only of tensor product operators $O_{\mathrm{m}}, O_{\mathrm{p}}$ of Pauli matrices σ^z has been proposed as a diagnostic of the phase of the ground state of Eq. (4.1) [191, 192]:

$$C_{O_{\mathrm{m}},O_{\mathrm{p}}}(t) = \langle \uparrow^N | [O_{\mathrm{m}}, O_{\mathrm{p}}(t)]^2 | \uparrow^N \rangle, \tag{4.3}$$

with $O_{\mathrm{p}}(t) = e^{iHt} O_{\mathrm{p}} e^{-iHt}$. Note that $\sigma_j^\alpha(t)$ being Hermitian and unitary implies

$$C_{O_{\mathrm{m}},O_{\mathrm{p}}}(t) = 2\langle \uparrow^N | O_{\mathrm{m}} O_{\mathrm{p}}(t) O_{\mathrm{m}} O_{\mathrm{p}}(t) | \uparrow^N \rangle - 2, \tag{4.4}$$

where in our notation only the operator immediately preceding the (t) is time-evolved in the Heisenberg picture. The considered OTOC is the nontrivial part $\mathcal{F}(t) = \langle \uparrow^N | O_{\mathrm{m}} O_{\mathrm{p}}(t) O_{\mathrm{m}} O_{\mathrm{p}}(t) | \uparrow^N \rangle$ of $C_{O_{\mathrm{m}},O_{\mathrm{p}}}(t)$. We refer to O_{m} as the measured operator, following the action of a perturbing O_{p}.

4.2.2 Domain Wall Description and Diagonalization

For our purposes an insightful description can be obtained by formulating the dynamics in terms of domain walls: The absence (presence) of a domain wall between two neighboring spins corresponds to them being (anti-) aligned [215]. The presence of a domain wall can be measured with $\sigma_i^z \sigma_{i+1}^z$. A $+1$ (-1) measurement result corresponds to the absence (presence) of

a domain wall. A formulation in terms of domain walls is complete, allowing us to map the system with an even number N of spins on sites $j \in \{-N/2, -N/2+1, \ldots, N/2-1\}$ to a system consisting of N domain walls, i.e., two level systems on the dual lattice with sites $j' \in \{-N/2-1/2, -N/2+1/2, \ldots, N/2-3/2\}$. We denote sites on the dual lattice via an apostrophe $j' = j - 1/2$. A domain wall absent (present) on site j' encodes that the two spins on sites $j'-1/2$ and $j'+1/2$ are (anti-)aligned. A domain wall absent (present) on the first site $j' = -N/2 - 1/2$ encodes the spin $j = -N/2$ to be the $+1$ (-1) eigenstate of $\sigma^z_{-N/2}$. We describe the absence (presence) of a domain wall on site j' as the $+1$ (-1) eigenstate of $\tau^x_{j'}$.

In this formulation, the Hamiltonian of Eq. (4.1) reads

$$H_{\mathrm{TFI}'} = -J \sum_{j'=-N/2+1/2}^{N/2-3/2} \tau^x_{j'} + g \sum_{j'=-N/2-1/2}^{N/2-5/2} \tau^z_{j'}\tau^z_{j'+1} + g\tau^z_{N/2-3/2} \tag{4.5}$$

using that $\sigma^z_j\sigma^z_{j+1} \to \tau^x_{j+1/2}$ and $\sigma^x_j \to \tau^z_{j-1/2}\tau^z_{j+1/2}$ except for the last spin where $\sigma^x_N \to \tau^z_{N/2-3/2}$. Note that the two Hamiltonians Eqs. (4.5) and (4.1) describe the same matrix. For completeness, σ^z_j, which will become of interest later, transforms under the duality transformation to

$$\sigma^z_j = \prod_{j'=-N/2-1/2}^{j-1/2} \tau^x_{j'}. \tag{4.6}$$

The Hamiltonian Eq. (4.5) cannot be transformed into a local fermionic Hamiltonian due to the last operator $\tau^z_{N/2-3/2}$. However, if we only intend to measure bulk properties, we can restrict our calculations to sufficiently small timescales where boundary effects are absent.

A Jordan-Wigner transformation [216]

$$\tau^x_{j'} = (1 - 2c^\dagger_{j'}c_{j'}), \qquad \tau^x_{-N/2-1/2}\cdots\tau^x_{j'-1}\tau^z_{j'} = (c^\dagger_{j'} + c_{j'}) \tag{4.7}$$

yields

$$H_{\mathrm{TFI}'} = -J \sum_{j'=-N/2+1/2}^{N/2-3/2} (1 - 2c^\dagger_{j'}c_{j'}) + g \sum_{j'=-N/2-1/2}^{N/2-5/2} (c^\dagger_{j'} - c_{j'})(c^\dagger_{j'+1} + c_{j'+1}). \tag{4.8}$$

This Hamiltonian can be diagonalized, as discussed in Ref. [217, 218] for open boundary conditions and in Refs. [186, 219] for periodic boundary conditions. In order to allow the reader to follow the results presented in the

following sections, we will provide a short summary of the steps required for the case of periodic boundary conditions in the remainder of this section. For introducing periodic boundary conditions, we have to restrict the number of domain walls to be even. In order to fully specify a state, we further switch to a basis in which the symmetry operator $\mathcal{S} = \prod \sigma_j^x$ is diagonal and the position of domain walls is well defined, i.e., $(1 \pm \mathcal{S})|\uparrow_{-N/2} s^z_{-N/2+1} \dots s^z_{-N/2-1}\rangle$. Then, the two types of boundary conditions Ramond (periodic) and Neveu-Schwarz (antiperiodic) correspond to the two symmetry sectors, respectively, and $c^{(\dagger)}_{-N/2-1/2} \equiv \pm c^{(\dagger)}_{N/2-3/2}$. Since we are always taking the limit $N \to \infty$ first, the choice of the boundary conditions does not matter. Performing the Fourier transformation $c_{j'} = \sqrt{N}^{-1} \sum_k e^{-ikj} c_k$ and diagonalizing the Hamiltonian via a Bogoliubov rotation [220] yields for periodic boundary conditions

$$H_{\mathrm{TFI}'} = \sum_{k\neq 0, k\neq \pi} \left(2\epsilon_k \gamma_k^\dagger \gamma_k - \epsilon_k\right) + 2(J+g)c_0^\dagger c_0 + 2(J-g)c_\pi^\dagger c_\pi - 2J, \tag{4.9}$$

$$\epsilon_k = \sqrt{g^2 + J^2 + 2Jg\cos(k)} \tag{4.10}$$

where we used

$$\begin{aligned} \gamma_k &= \cos(\theta_k/2)c_k + i\sin(\theta_k/2)c_{-k}^\dagger \\ \cos(\theta_k) &= (J + g\cos(k))/\epsilon_k, \\ \sin(\theta_k) &= -g\sin(k)/\epsilon_k. \end{aligned} \tag{4.11}$$

As a remark, the Hamiltonian for antiperiodic boundary conditions yields just the first part of Eq. (4.9), i.e., the sum of $2\epsilon_k\gamma_k^\dagger\gamma_k - \epsilon_k$ over momenta k fulfilling $e^{iNk} = -1$.

4.3 Long Time Stability of OTOCs

In this section, we report the observed long-time stability of the OTOC and provide a heuristic explanation based on the analytical calculation presented in Section 4.4.

4.3.1 Phenomenology in the TFIM

Our first key result concerns the time-dependent expectation values of the magnetization and various OTOCs in the thermodynamic limit (TDL); see Fig. 4.1. These results are obtained using the analytical solution of the TFIM combined with Wick's theorem, following the methods of Refs. [186, 217, 219, 220]. The corresponding late-time OTOC values are summarized in Table 4.1.

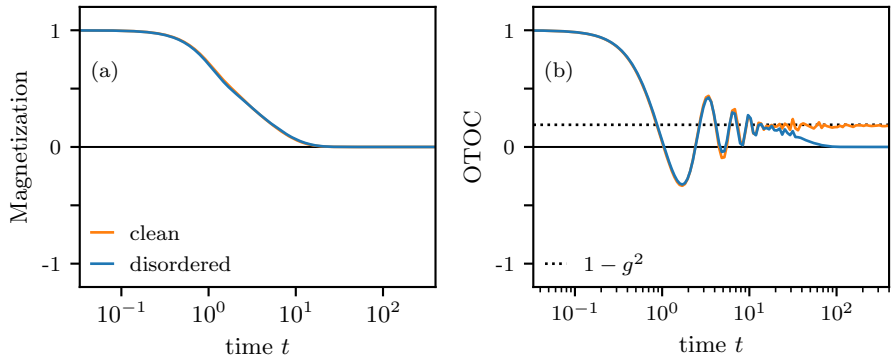

Figure 4.1: *Magnetization $\langle\uparrow^N|\sigma_0^z(t)|\uparrow^N\rangle$ (left) and OTOC $\langle\uparrow^N|\sigma_0^z(t)\sigma_0^z\sigma_0^z(t)|\uparrow^N\rangle$ (right) for the quantum Ising chain given in Eq. (4.1). We use $N = 500$ spins, $J = 1$, coupling strength $g = 0.9$, open boundary conditions, and $O_\mathrm{m} = O_\mathrm{p} = \sigma_0^z$. Static spatial disorder is added to the transverse field (Gaussian with standard deviation $W = 0.04$).*

n_p	n_m	Reloc. part	Deloc. part	OTOC signal
Even	Even	1	1	1
Even	Odd	1	$\sqrt{1-g^2}^{\,n_p}$	$\sqrt{1-g^2}^{\,n_p}$
Odd	Even	$\sqrt{1-g^2}^{\,n_m}$	1	$\sqrt{1-g^2}^{\,n_m}$
Odd	Odd	$\sqrt{1-g^2}^{\,n_m}$	$\sqrt{1-g^2}^{\,n_p}$	$\sqrt{1-g^2}^{\,n_p+n_m}$

Table 4.1: *Late-time signals for the different OTOCs in the TDL for the quantum TFIM with $|g| \leq 1$ (for $g > 1$, the OTOC signal equals 1 for even/even, and 0 otherwise): $\langle\uparrow^N|O_p(t)O_mO_p(t)|\uparrow^N\rangle$, with O_p (O_m) consisting of a product of n_p (n_m) Pauli operators, for concreteness $\sigma_0^z\sigma_{10}^z\sigma_{20}^z\cdots$. Note that an odd value of n_p leads to a dependence of the OTOC on n_m, and vice versa. A heuristic real-space picture of the corresponding time evolution is given in Fig. 4.2.*

While $M_0(t) \simeq [1 - \min(g, 1)]^{1/8}$ [213], $M_{\uparrow^N}(t) = 0$ at late times, see Fig. 4.1, as expected for a state with finite energy density [219–223]. In contrast to, and as noted in Ref. [191], the OTOCs mimic an order parameter: They are nonzero for $g < J$ and vanish otherwise. However, note that these are evidently nonthermal: OTOCs which are Ising even, such as those of the bond energy, do not vanish in thermal equilibrium even for $g > J$, but they do after the quench. In the remainder of the paper, we elucidate the physical processes underpinning this nonthermal behavior.

4.3.2 A Domain Wall Perspective

The above results can be made physically transparent by appealing to the time evolution of domain walls in the Ising chain; for the following heuristic discussion, we refer to the sketch in Fig. 4.2. A complementary and detailed formal treatment of relocalization and delocalization is given in Appendix C.

Essentially, the exact solution of the Ising chain proceeds via fermionization, in terms of the domain wall annihilation (creation) operators $c_{i'}^{(\dagger)}$ acting on the dual lattice sites at $i' = i - \frac{1}{2}$ [186, 216, 223, 224]. We find that the dynamics of these operators exhibits two phenomena, which we call domain wall delocalization and relocalization, through which the behavior of the OTOC (and standard observables) can be straightforwardly understood via the following heuristic account.

The treatment uses the fact that the Pauli matrices are unitary operators, so that the solution can be formulated as if studying a time evolution induced by unitary matrices $\sigma_0^z(t)$. We are thus led to study the time evolution of the single fermion operator

$$d_{j'}(t) = \sigma_0^z(t) c_{j'} \sigma_0^z(t) = \sum_{l'} A_{j'l'} c_{l'} + B_{j'l'} c_{l'}^\dagger, \tag{4.12}$$

where the second equality follows from H_{TFI} being quadratic [186, 222, 223] and $\sigma_0^z c_{i'}^{(\dagger)} \sigma_0^z = \mathrm{sign}(i') c_{i'}^{(\dagger)}$.

4.3.3 Relocalization and Delocalization

Relocalization dominates the structure of $d_{j'}(t)$ in Eq. (4.12). It refers to the part of the overlap $\mathrm{Tr}[d_{j'}(t) c_{l'}^{(\dagger)}]$ that is time independent and decaying algebraically with $|j' - l'|$, see green and red dashed line in Fig. 4.2. Delocalization is subleading and yields a perturbation of the relocalized part of order $O(1/t)$ spread over a region of size $2vt$, with v the maximal group velocity (Fig. 4.2, orange line).

The origin of these two phenomena is sketched in Fig. 4.2 by dividing the evolution of $d_{0'}(t)$ into three steps: (1) the evolution of the initial operator $c_{0'}$ with negative time $c_{0'}(-t)$, (2) the perturbation with σ_0^z creating $\sigma_0^z c_{0'}(-t) \sigma_0^z$ and (3) a final time evolution $[\sigma_0^z c_{0'}(-t) \sigma_0^z](t) = d_{0'}(t)$. During the first step, $c_{0'}$ separates in left- and right-moving wave packets. The two wave packets spread ballistically with the maximum group velocity of the domain walls v, see red and green lines in Fig. 4.2.

Relocalization arises because, in the second step, σ_0^z shifts the phase of the left-moving wave packet by π. The reverse time evolution in the third step then cancels with the time evolution of the first, so that both wave packets

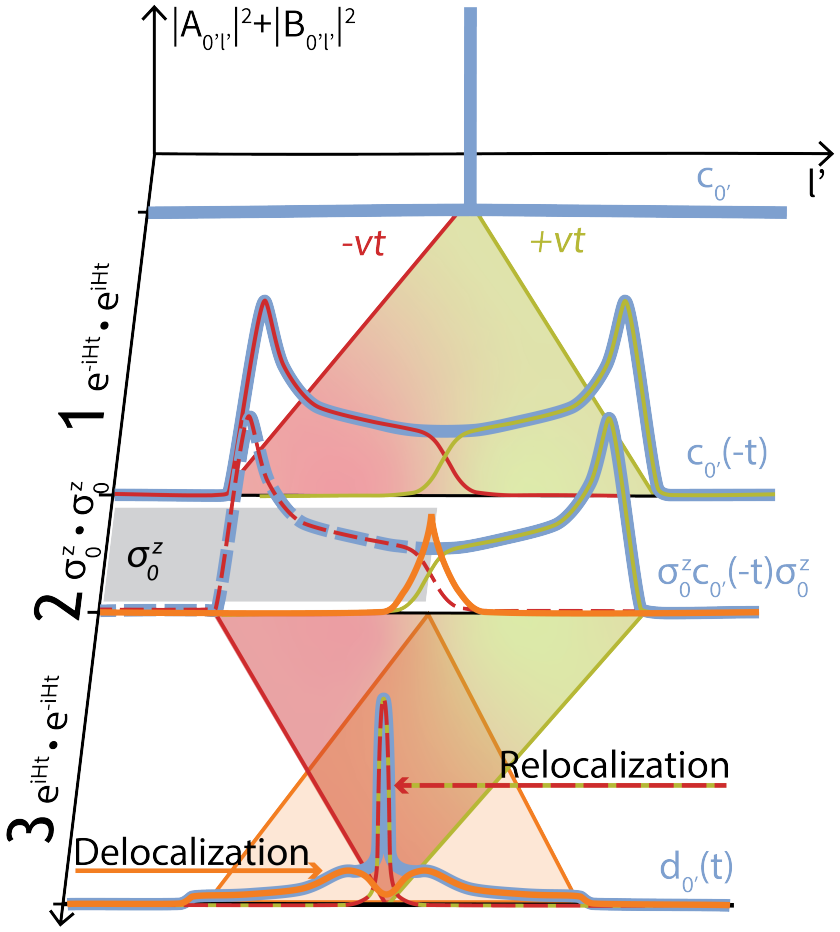

Figure 4.2: *The schematic creation of* $d_{0'}(t) = \sum_{l'} A_{0'l'}c_{l'} + B_{0'l'}c_{l'}^\dagger$*, Eq. (4.12), with relocalization (red, green) and delocalization (orange) in three steps. The blue lines indicate the envelopes of the prefactors* $A_{0'l'}, B_{0'l'}$ *in space when expressing the intermediate stages* $c_{0'}$*,* $c_{0'}(-t)$*,* $\sigma_0^z c_{0'}(-t)\sigma_0^z$ *as a sum* $A_{0'l'}c_{l'} + B_{0'l'}c_{l'}^\dagger$*, respectively. First step: The operator* $c_{0'}(-t)$ *splits into two wavepackets with positive (green) and negative (red) front velocity* v*. Second step: Applying* σ_0^z *yields a global perturbation by shifting the phase of the left half by* π*, indicated by the dashed lines. This decomposes into a phase shift of the left-moving wavepacket and a local perturbation shown in orange. Third step: The two wavepackets (green, red) are relocalized, and the orange perturbation delocalizes. Their sum is* $d_{0'}(t)$*.*

move back to the origin. Due to the relative phase shift, they no longer add up to $c_{0'}$ but to the relocalized part of $d_{0'}(t)$, green and red dashed line in Fig. 4.2.

The origin of the delocalization also lies in the perturbation with σ_0^z. For finite times, the wavepackets are not perfectly separated at $l' = 0$. As a result σ_0^z yields a local perturbation, orange part in Fig. 4.2. In the third step, this locally perturbed part spreads ballistically over a region of size $2vt$. Being delocalized, it is not picked up by a fermionic local operator O_m such as $\sigma_0^z\sigma_1^z = 1 - c_{1'}^\dagger c_{1'}$. Using purely combinatorial arguments, relocalization and delocalization suffice to explain the structure found in Table 4.1 as we will explain in the next section.

4.3.4 Phenomenological Implications of Domain Wall Relocalization

Before presenting the detailed analytical calculation in the next sections, in this section we explain how relocalization and delocalization give rise to the structure observed in Table 4.1. Numerical results supporting this picture are presented in Appendix C.1.2.

The relocalization mechanism accounts for the results in Table 4.1 as follows. As the left- and right-moving wavefront separate with time, for large times, every perturbation operator $\sigma_0^z\sigma_{10}^z\cdots$ yields a phase shift of the left-moving wavefront by π independent of its position, see Fig. 4.2. Hence, with an even number of perturbation operators, the relocalization effect is absent: without the phase shift, the forward and backward time evolution cancel up to delocalization. For an odd number n_p, the left-moving wavepacket obtains an overall phase shift of π. With the phase shift present and neglecting delocalization, we show in Appendix C.1.4 that for $J = 1$, $g < 1$

$$O_p(t)|\uparrow^N\rangle \approx (\sqrt{1-g^2}|\uparrow\rangle + g|\downarrow\rangle)^{\otimes N} \tag{4.13}$$

is just a product state of rotated spins. Hence, in the presence of relocalization, each site on which we measure σ^z contributes a factor of $\sqrt{1-g^2}$ (for $J = 1$). They multiply to $(\sqrt{1-g^2})^{n_m}$, explaining the numerical results in Table 4.1.

Delocalization can be understood as the correction to the relocalization mechanism, for which we assumed well-separated wavepackets. Each of the perturbation operators yields such a correction separately, as shown for one perturbation operator in Fig. 4.2. Each correction term corresponds to a wavefront delocalizing during the backevolution in the third step and reducing the final expectation value of fermionic odd operators by $(\sqrt{1-g^2})^{n_p}$

in total, as reported in Table 4.1. Local fermionic even operators are insensitive to delocalization at large times, as they only probe local domain wall densities. However, the delocalized part spreads out, see Fig. C.3, yielding a vanishing domain wall density. Thus, for an odd number n_m of σ^z in O_m, the delocalization effect cancels out, so that effectively only one of the n_m operators picks up the delocalized part. As a result, the delocalization contribution only depends on the parity of n_m and the total number n_p, as also found numerically and summarized in Table 4.1.

4.4 Analytical Calculation

In preparation for the discussion of the long-time limit of OTOCs in the TFIM and their connection to the quantum and topological insulator phase transition, we begin by presenting the details of the analytical calculation and necessary approximation. In the subsequent parts, we discuss the analytical results for OTOCs in quenched settings as well as at finite temperatures.

4.4.1 Domain Wall Relocalization

The basis of all analytical results in the following sections is calculating the expression $\sigma_0^z(t)c_{j'}\sigma_0^z(t)$, see Eq. (4.12) and Fig. 4.2. We use Eqs. (4.9), (4.11) to write

$$\sigma_0^z[c_{j'}](-t)\sigma_0^z = \frac{1}{N}\sum_{k,l'} e^{-ikj'}\mathrm{sign}(l')\left[\frac{i\sin\theta_k}{2}(e^{2i\epsilon_k t+ikl'} - e^{-2i\epsilon_k t+ikl'})c_{l'}^\dagger \right.$$
$$\left. +(\cos^2(\theta_k/2)e^{2i\epsilon_k t+ikl'} + \sin^2(\theta_k/2)e^{-2i\epsilon_k t+ikl'})c_{l'}\right], \qquad (4.14)$$

where we used $\epsilon_k = \epsilon_{-k}$ and, as stated before, $\sigma_0^z c_{l'}^{(\dagger)}\sigma_0^z = \mathrm{sign}(l')c_{l'}^{(\dagger)}$.

We can make progress by noting that $[c_{j'}](-t)$ spreads in the form of two wavepackets, one left-moving and the other one right-moving. This is evident from the sign of the group velocity $\mathrm{sign}(v_g(k)) = \mathrm{sign}(\partial_k\epsilon_k) = -\mathrm{sign}(k)$ and the factors $e^{\pm 2i\epsilon_k t+ikl'}$ in Eq. (4.14).

Hence, we approximate for large times $\mathrm{sign}(l') \approx \pm\mathrm{sign}(k)$ in Eq. (4.14), which uses that for the first term in Eq. (4.14) the left part of the right-moving wavepacket vanishes

$$\lim_{t\to\infty}\sum_{l'<0}\left|\frac{1}{N}\sum_{k>0}\frac{\sin\theta_k}{2}e^{2i\epsilon_k t+ikl'}\right|^2 \to 0. \qquad (4.15)$$

Similarly, the right part of the left-moving wavepacket vanishes. The same approximation can be made for all other terms in Eq. (4.14), the approximation error as a function of time is shown numerically for all four terms in

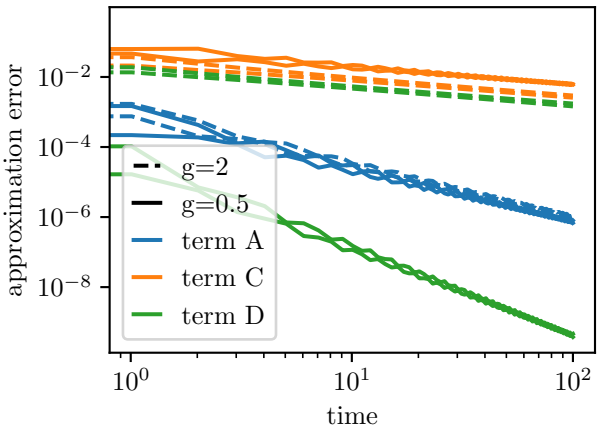

Figure 4.3: *We show the approximation error* $\mathrm{sign}(l') \approx \pm\mathrm{sign}(k)$ *in Eq. (4.14) as a function of time for the four exponential functions appearing in Eq. (4.14) for* $J = 1$*. The results of the second are not shown as they coincide with the first. The approximation error is evalutated as given in Eq. (4.15) for one half of the first term, i.e., exponential in Eq. (4.14), and analogously for all other terms. This shows that the approximation error vanishes for large times as* $1/\sqrt{t}, 1/\sqrt{t}^3$ *or* $1/\sqrt{t}^5$*. The system size is* $N = 1000$*.*

Fig. 4.3. It decays at least as $1/\sqrt{t}$ with time, making the approximation exact in the long-time limit. This yields

$$\begin{aligned}\sigma_0^z(t)c_{j'}\sigma_0^z(t) \approx \frac{1}{N}\sum_{k,l'} e^{-ikj'}\mathrm{sign}(k)\Bigg[&\frac{i\sin\theta_k}{2}(e^{2i\epsilon_k t+ikl'} + e^{-2i\epsilon_k t+ikl'})c_{l'}^\dagger(t) \\ &(\cos^2(\theta_k/2)e^{2i\epsilon_k t+ikl'} - \sin^2(\theta_k/2)e^{-2i\epsilon_k t+ikl'})c_{l'}(t)\Bigg], \\ = \frac{1}{\sqrt{N}}\sum_k e^{-ikj'}\mathrm{sign}(k)&\left[i\sin(\theta_k)c_{-k}^\dagger + \cos(\theta_k)c_k\right]. \qquad (4.16)\end{aligned}$$

This expression enables the calculation of the long-time limit of various OTOCs. Based on the analytical calculation, we gain the following insights. First, the expression is time independent. This is because the approximation assumes the perfect separation of left- and right-moving wavepackets. Hence, the perturbation with σ_0^z only flips the relative sign of the two wavepackets. Since the structure of the wavepacket is otherwise untouched, the back time evolution perfectly cancels with the forward time evolution. This phenomenon, referred to as relocalization, is illustrated in Fig. 4.2. Second, the correction to this approximation comes from the imperfect separation of the wavepackets at the origin and spreads under the backevolution. Hence, we re-

fer to the correction as the delocalized part. For fermionic even operators, this correction vanishes in the long-time limit. For fermionic odd operators, being many-body operators, this correction can still have a contribution in the long-time limit due to the accumulation of individual contributions from each fermionic operator. Third, the relative sign flip between the two wavepackets yields a double rotation as can be seen by comparing Eq. (4.16) to Eq. (4.11). This directly links the $\sigma_0^z(t)$-evolved annihilation operator to the structure of the Hamiltonian via the angle θ_k. In the following section, we will use this result to calculate various infinite and finite temperature OTOCs.

4.4.2 Quenched OTOCs

We gain a better understanding of the nonanalytic behavior of the two phenomena, domain wall relocalization and delocalization, by calculating two OTOCs analytically in this section. First, using Eq. (4.16), we calculate the long-time limit OTOC

$$\mathcal{F}_R = \lim_{t\to\infty} \langle\uparrow^N|\sigma_0^z(t)\,\sigma_0^z\sigma_1^z\,\sigma_0^z(t)|\uparrow^N\rangle = 1 - \frac{2}{N}\sum_k \sin^2\theta_k = \begin{cases} 1-(\frac{g}{J})^2 & g < J \\ 0 & g \geq 0 \end{cases}, \tag{4.17}$$

which only measures relocalization due to $\sigma_0^z\sigma_1^z$ being fermionic even so that the approximation made in Eq. (4.16) becomes exact in the long-time limit. The integral can be solved using a Weierstrass-substitution and symbolic algebra sygtem.

Second, to only probe delocalization, we calculate the total amount of domain walls created by $\sigma_0^z\sigma_1^z$

$$\mathcal{F}_D = \lim_{t\to\infty} \sum_{j'} \langle\uparrow^N|[\sigma_0^z\sigma_1^z](t)\,c_{j'}^\dagger c_{j'}\,[\sigma_0^z\sigma_1^z](t)|\uparrow^N\rangle = 2t(g,J) - t(g,J)^2/2 \tag{4.18}$$

$$t(g,J) = \frac{2}{N}\sum_k \sin^2\theta_k = \begin{cases} (g/J)^2 & g < J \\ 1 & g \geq J \end{cases}. \tag{4.19}$$

For this OTOC, the relocalization prediction would be a signal with a value of 1, so any deviation can be traced back to delocalization.

This shows that the nonanalytic behavior can be traced back to the nonanalytic behavior of $\sin(\theta_k)$ for both, an OTOC just subject to relocalization and an OTOC just subject to delocalization. It suggests that the results reported in Table 4.1 are closely related to the behavior of $\sin(\theta_k)$. In the next section, we show that a similar observation can be made for examples of finite-temperature OTOCs.

4.4.3 Thermal OTOCs

In this section, we present the results for thermal OTOCs at finite and infinite temperature. This shows the interplay between the Hamiltonian generating the dynamics and the thermal ensemble. One simple, insightful, nonvanishing thermal OTOC is

$$\mathcal{F}_\beta = \lim_{t\to\infty} \langle \sigma_0^z(t)\, \sigma_0^z \sigma_1^z\, \sigma_0^z(t)\, \sigma_0^z \sigma_1^z \rangle_\beta, \tag{4.20}$$

where we denote the thermal expectation value at temperature β with $\langle \bullet \rangle_\beta = \mathrm{Tr}\left[\bullet e^{-\beta H}\right] / \mathrm{Tr}\left[e^{-\beta H}\right]$. Using Eq. (4.16) we find

$$\mathcal{F}_\beta = \langle \sigma_0^z \sigma_1^z \rangle_\beta^2 + \mathcal{F}_{\beta=0}, \tag{4.21}$$

$$\mathcal{F}_{\beta=0} = -\left(\frac{1}{N}\sum_k \mathrm{sign}(k) \sin\theta_k\right)^2 = -\left(\frac{2(\epsilon_\pi - \epsilon_0)}{J\pi}\right)^2 = \begin{cases} -\frac{4}{\pi^2}\frac{g^2}{J^2} & J > g \\ -\frac{4}{\pi^2} & J \leq g \end{cases}. \tag{4.22}$$

We find the thermal expectation value consists of two parts. The first one $\langle \sigma_0^z \sigma_1^z \rangle_\beta^2$ stems from separating the two $\sigma_0^z \sigma_1^z$ in Eq. (4.20) in the trace during a calculation using Wick's theorem, yielding the time-evolved operators $\sigma_0^z(t)$ to cancel out. The second part comes from contractions between the two $\sigma_0^z \sigma_1^z$. It is temperature independent and has a functional form similar to those found for other OTOCs, see Table 4.1. The independence of temperature is a reflection of the two Hamiltonians being identical: the one generating the time evolution and the one generating the ensemble; it is a signature of the interplay between dynamics and thermodynamics. This decomposition into a dynamics-independent and a temperature-independent part is not expected to hold in general and may be a peculiarity of the free fermionic TFI model.

Note that another thermal OTOC $\langle \sigma_0^z(t)\, \sigma_0^x\, \sigma_0^z(t)\, \sigma_0^x \rangle_\beta$ yields the same results but with $J \leftrightarrow g$, as also follows from the duality of the TFI model.

We delve further into the peculiarities of the TFI model in the next sections, discussing the relation to information spreading and the connection between the found nonanalyticity for $\mathcal{F}_{\beta=0}$ in this section and phase transitions.

4.5 Operator Spreading and Information Scrambling

In the previous Section 4.4.3, we reported on the results for thermal OTOCs. In this section we discuss the relation to and implications for information scrambling and operator spreading.

To this end, we focus on the dynamics of $\sigma_1^x(t)$ as a feasible example. It can be mapped to the dynamics of $[\sigma_{1'}^z\sigma_{2'}^z](t)$ via the duality transformation, see Section 4.2.2.

For $\sigma_1^x(t)$, the dynamics is in particularly simple as it is restricted to the subspace of Pauli strings indexed through their endpoints i and j

$$\sigma_1^x(t) = \sum_{i,j}(w_{zz,ij}(t)\sigma_i^z\sigma_j^z + w_{zy,ij}(t)\sigma_i^z\sigma_j^y + w_{yy,ij}(t)\sigma_i^y\sigma_j^y)\prod_{i<l<j}\sigma_l^x, \quad (4.23)$$

with $w_{yy,ij} = w_{zz,ij} = 0$ for $i \geq j$. This reduction of complexity for the operator $\sigma_1^x(t)$ reflects the fact that it is a two body operator in terms of fermions and under Jordan-Wigner transformation each operator in Eq. (4.23) is mapped to two fermions located at the endpoints of the Pauli string.

In Sections 4.4.3 and 4.6, we probe the dynamics by measuring the OTOC $\mathrm{Tr}[\sigma_0^z(t)\sigma_0^x\sigma_0^z(t)\sigma_0^x]$. The results can now be reinterpreted in terms of the operator dynamics: The OTOC measures the probability of the two ends of a Pauli string in Eq. (4.23) to be on the same site of σ_0^z

$$\mathrm{Tr}[\sigma_0^z(t)\sigma_0^x\sigma_0^z(t)\sigma_0^x]/\mathcal{D} = \underbrace{\sum_{0 \text{ not in } [i,j]}|w_{ab,ij}(t)|^2}_{p_{\notin}(t)} - \underbrace{\sum_{0 \text{ in } [i,j]}|w_{ab,ij}(t)|^2}_{p_{\in}(t)} + R(t), \quad (4.24)$$

with a correction term $R(t)$ accounting for cases where $i = 0$ or $j = 0$. It is vanishingly small in the long-time limit and neglected in the following discussion of the long-time limit. Note that due to the unitarity of the operator evolution $p_{\notin}(t) + p_{\in}(t) = 1$, neglecting $R(t)$.

Hence, in the long-time limit, the previously calculated OTOC can be understood as the weight difference $p_{\notin} - p_{\in}$ between Pauli strings having spread away from the origin and Pauli strings having overlap with the origin. In Section 4.4.3 we calculated $\mathrm{Tr}[\sigma_0^z(t)\sigma_0^x\sigma_0^z(t)\sigma_0^x]$ in the long-time limit yielding

$$p_{\notin} - p_{\in} \overset{t\to\infty}{\to} \begin{cases} \frac{-4}{\pi^2} & J/g > 1 \\ \frac{-4J^2}{g^2\pi^2} & J/g \leq 1 \end{cases}. \quad (4.25)$$

This implies that in the ferromagnetic phase, the operator is biased towards spreading over Pauli strings that overlap with the origin. This bias is insensitive in variations of the parameter J/g within the phase. When crossing the phase boundary, the bias diminishes: For $g \gg J$, the Pauli string is equally likely to have overlap with the origin or to avoid it.

Having related the operator spreading to the behavior of the OTOC, we can study the bias in the information spreading in more detail by further separating the Pauli strings according to their length as well. To do this, we calculate the distribution of lengths

$$p_{\in,L}(t) = \sum_{|i-j|=L, 0\in[i,j]} |w_{ab,ij}(t)|^2, \tag{4.26}$$

and correspondingly $p_{\notin,L}(t)$. The results are shown in Fig. 4.4 for different g/J for large times. This reveals that not only is the difference $p_{\notin} - p_{\in}$ stable in the ferromagnetic phase, but also the Pauli string length distribution is independent of g/J within the ferromagnetic phase. At $g/J = 1$, a nonanalytic transition occurs and the distribution shifts with increasing g/J towards shorter Pauli strings being entirely located on one site of the origin.

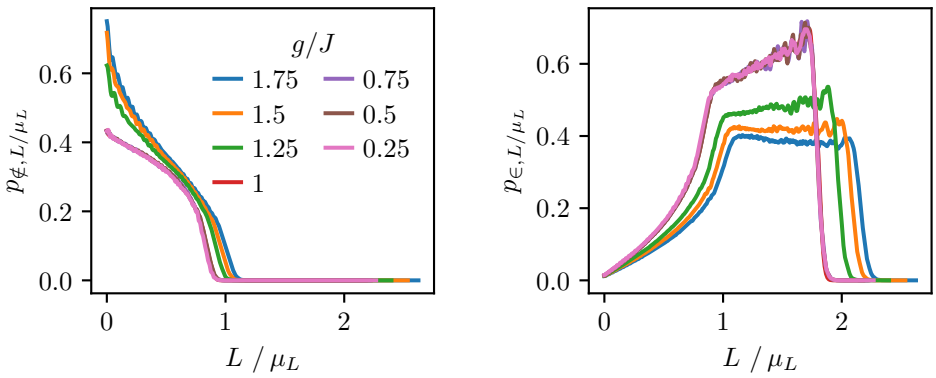

Figure 4.4: *Distribution of normalized Pauli stringlengths in the time-evolved operator $\sigma_0^x(t)$ split up into Pauli strings crossing the origin $p_{\in,L}(t)$ and Pauli strings fully located on one side of the origin $p_{\notin,L}$. The length is renormalized according to the expectation value of the length $\mu_L = \int \mathrm{d}L(p_{\in,L} + p_{\notin,L})$ to cancel out the time dependence in the long-time limit. We used different g/J, a system size of 200 and evolved to the maximal time before finite size effects become visible. The distributions are averaged over a range of about $L/\mu_L = 2$. The distributions are converged with time.*

The bias is not unique to $\sigma_0^x(t)$. As noted earlier, we can obtain the same results for $[\sigma_0^z\sigma_1^z](t)$ by replacing g/J with J/g, consistent with the duality transformation.

This bias towards Pauli strings spanning across the origin arises as an interference effect in the fermionic formulation. This can be seen by using the Jordan-Wigner transformation and writing $\sigma_0^x(t) = 1 - 2c_i^\dagger(t)c_i(t)$, so

that $\sigma_0^x(t)$ is the product of two time-evolved fermionic operators. As the transverse field Ising model is a noninteracting fermionic model, the two parts evolve independently and in particular both $c_i^\dagger(t)$ and $c_i(t)$ spread equally in both directions. However, when taking their product, interference effects occur. As a result, the distribution of $c_i^\dagger(t)c_i(t)$ over sites is not just the product of the individual distributions of $c_i^\dagger(t)$ and $c_i(t)$: the two fermions within $\sigma_0^x(t)$ are more likely to spread in opposite directions. It shows that also for free fermionic systems, more can be different, and relates the phase dependent-operator spreading to interference phenomena in the fermionic basis.

In order to better understand how "more can be different", after discussing the relation of the different phase transitions in Section 4.6, in the following Section 4.7 we will approach the behavior of interacting systems, starting with analyzing the implications of dynamical constraints in a comparable classical system.

In summary, we can observe two different operator spreading behaviors depending on the phase: one, where the information needed to back-evolve the state has more weight on larger operators and one where it has more weight on smaller operators compared to the size of the butterfly cone. It would be interesting to develop a similar picture for the operator spreading within $\sigma_0^z(t)$, which is more challenging as it involves the time evolution of many fermions as opposed to the two in $\sigma_0^x(t)$.

4.6 Connection to the Quantum Phase Transition

For the TFIM, the dynamical transition discussed in the previous sections at $g = J$ coincides with the quantum phase transition and a topological insulator phase transition as we will explain briefly in this section. While the coincidence is suggestive, we will provide arguments in the following sections that such coincidence is not expected to hold in general.

The nature of the quantum phase transition becomes apparent from studying Eq. (4.9). The energies of the lowest eigenstate in each of the two symmetry sectors, i.e., the two types of boundary conditions, are

$$E_0^{\text{pbc}} = -2J - \sum_{k:e^{ikN}=1, k\neq 0, k\neq\pi} \epsilon_k, \qquad E_0^{\text{apbc}} = -\sum_{k:e^{ikN}=-1} \epsilon_k. \tag{4.27}$$

Note that only eigenstates with an even number of domain walls are physical and others are projected out or disregarded. This means that the $k = \pi$ mode is not occupied in the ground state for $g > J$. By performing a Taylor

expansion in N^{-1}, one can calculate the difference between the two energies

$$\begin{aligned}\Delta E_0 &= E_0^{\text{pbc}} - E_0^{\text{apbc}} = -2J + \epsilon_{k=0} + \epsilon_{k=\pi} + \mathcal{O}(N^{-1}) \\ &= -2J + |J+g| + |J-g| + \mathcal{O}(N^{-1}).\end{aligned} \tag{4.28}$$

Apart from the two missing momenta, the difference of the two sums in Eq. (4.27) is subleading. Hence, the quantum phase transition, manifested by the nonanalytic behavior of the energy difference at $|J| = |g|$ can be traced back to the nonanalytic behavior of ϵ_k at $k = \pi$ with $\epsilon_{k=\pi} = |J - g|$ for the anti-ferromagnet with $J, g > 0$.

Another perspective on the phase transition is provided by the concept of a topological insulator phase transition. The perspective is based on the discussion of the paradigmatic model for topological insulators, the Su–Schrieffer–Heeger (SSH) chain [225, 226]. The single particle dynamics of the TFIM follows that of an SSH chain. This can be seen by defining Majorana fermions $a_{j'} = c_{j'}^\dagger + c_{j'}$ and $b_{j'} = i(c_{j'}^\dagger - c_{j'})$ so that the Hamiltonian from Eq. (4.8) becomes

$$H_{\text{TFI}'} = iJ \sum_{j'} a_{j'} b_{j'} - ig \sum_{j'} b_{j'} a_{j'+1}. \tag{4.29}$$

The dynamics of the single particle operators follows

$$\partial_t a_{j'}(t) = i[H_{\text{TFI}'}, a_{j'}(t)] = 2Jb_{j'}(t) + 2gb_{j'-1}(t). \tag{4.30}$$

Hence, the single particle dynamics is governed by alternating nearest neighbor hoppings, commonly referred to as the SSH chain [225]. Following the concepts of topological insulators, we can define the winding number as the number of times the vector describing the Hamiltonian in momentum space $h_k = (-J - g\cos(k), g\sin(k))$ winds around the origin. The winding number is a topological invariant. It only changes value at the "band touching point" $||h_k||_2 = \epsilon_k = 0$ at $g = J$, where it becomes ill-defined. For $|g| < |J|$ the winding number is 0, while it is 1 for $|g| > |J|$. Like for the quantum phase transition, the "band touching point" is located at $k = \pi$ and, conversely, this is the momentum subspace where the origin enters the circle described by h_k and the winding number changes. See also Fig. 4.5 for a visualization. For a detailed discussion see chapter 1 of [226].

This topological phase transition and the quantum phase transition can then be related to the nonanalytic behavior of different OTOCs as follows. The nonanalytic behavior of the different quantities can be traced back to nonanalyticities in momentum space around $k = \pi$ at $J = g$. The winding number changes as the origin enters the circle at $k = \pi$, which is reflected in $\epsilon_{k=\pi} = 0$. The nonanalytic behavior of the ground state degeneracy can be traced back to the nonanalytic behavior of ϵ_k around $k = \pi$, see

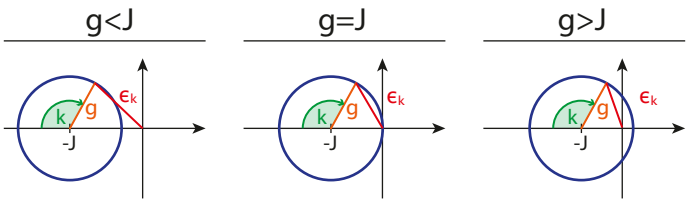

Figure 4.5: *Visualization of the topological insulator phase transition. The Hamiltonian Eq. (4.8) can be written in momentum space as* $(c_k \quad c^\dagger_{-k})h_k(c^\dagger_k \quad c_{-k})^T$ *with* $h_k = -(J + g\cos(k))\sigma_z + g\sin(k)\sigma_y$*. The representation of* h_k *as a two dimensional vector is shown in this figure for the different phases. For the antiferromagnet with* $g < J$*, the circle described by* h_k *does not wind around the origin. It transitions to winding once around the origin for* $g > J$ *through a band touching point appearing at* $k = \pi$*, where* $\epsilon_k = ||h_k|| = 0$ *for* $g = J$*.*

Eq. (4.28). For the OTOCs, it is $\sin(\theta_k) = g\sin(k)/\epsilon_k$, which becomes nonanalytic around $k = \pi$ at $g = J$. It leads to the nonanalytic behavior of the OTOCs, since they are expressed as integrals over $\sin(\theta_k)$ in different forms, see Eqs. (4.17), (4.18) and (4.22). It shows that the nonanalytic behavior of the OTOC can arise due to a nonanalytic structure of the eigenbasis of the Hamiltonian, which in turn can manifest as a topological insulator phase transition or a ground state degeneracy. For two point correlators, this relation has been pointed out before in [227]. We explicitly show the similarity between two point and four point correlators for quenched states in Appendix C.2.

However, as we will see next, nonanalyticities in the OTOC can also have a second origin, namely they could come from nonanalyticities in the group velocity, which are not necessarily linked to topological phase transitions or ground state degeneracies. This arises when a $\sigma^y_i\sigma^y_{i+1}$ term is added to the Hamiltonian

$$H_{\text{TFI+yy}} = -J\sum_{j=-N/2}^{N/2-1}\sigma^z_j\sigma^z_{j+1} + g\sum_{j=-N/2}^{N/2-1}\sigma^x_j - J^{yy}\sum_{j=-N/2}^{N/2-1}\sigma^y_j\sigma^y_{j+1}. \tag{4.31}$$

This Hamiltonian can be diagonalized with the same steps outlined before, yielding

$$\epsilon_k = \sqrt{(J + g\cos(k) + J^{yy}\cos(2k))^2 + (g\sin(k) + J^{yy}\sin(2k))^2} \tag{4.32}$$

with

$$\begin{aligned}\gamma_k &= \cos(\theta_k/2)c_k + i\sin(\theta_k/2)c^\dagger_{-k} \\ \cos(\theta_k) &= (J + g\cos(k) + J^{yy}\cos(2k))/\epsilon_k, \\ \sin(\theta_k) &= (-g\sin(k) - J^{yy}\sin(2k))/\epsilon_k.\end{aligned} \tag{4.33}$$

Hence, we can apply the same arguments to derive the expressions for the thermal OTOC

$$\mathrm{Tr}\left[\sigma_0^z(t)\,\sigma_0^z\sigma_1^z\,\sigma_0^z(t)\,\sigma_0^z\sigma_1^z\right]/\mathcal{D} = -\left(\sum_k \mathrm{sign}(v_g)\sin(\theta_k)\right)^2, \tag{4.34}$$

where $\mathcal{D}$ is the Hilbert space dimension. This shows that nonanalyticities in the OTOC may have two different origins: a nonanalytic structure of the Hamiltonian in k-space through $\sin(\theta_k)$, as well as a nonanalytic behavior of $\mathrm{sign}(v_g)$ where the number of zero-crossings of v_g changes. This is supported by the numerical results shown in Fig. 4.6. Whenever an OTOC is nonanalytic, visible in the left and central panel, there is a band gap closing or a change in the number of zero-crossings of v_g, shown in the right panel.

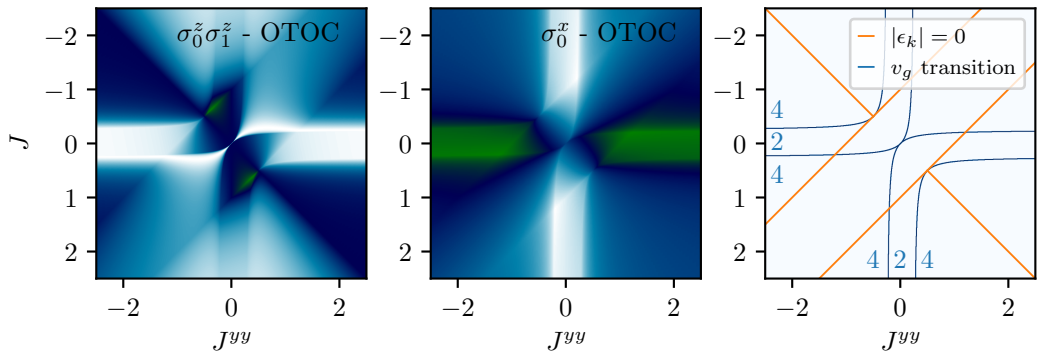

Figure 4.6: *Nonanalytic long-time behavior of the thermal OTOCs* $\mathrm{Tr}\left[\sigma_0^z(t)\,\sigma_0^z\sigma_1^z\,\sigma_0^z(t)\,\sigma_0^z\sigma_1^z\right]$ *(left) and* $\mathrm{Tr}\left[\sigma_0^z(t)\,\sigma_0^x\,\sigma_0^z(t)\,\sigma_0^x\right]$ *(center) for the Hamiltonian Eq. (4.31). Band-gap closings as well as changes in the number of zero-crossings of the group velocity* $v_g(k) = \partial_k\epsilon_k$ *(blue numbers) are depicted by lines in the right panel. This confirms the expectation from Eq. (4.34) that a nonanalytic behavior in the OTOC can be induced by band gap closings as well as changes in the number of zero-crossings of the group velocity.*

In summary, in this section we discussed the relation between the nonanalytic behavior of several OTOCs and phase transitions. Furthermore, we showed that changes in the number of zero-crossings of the group velocity can also cause a nonanalytic behavior of the OTOC. In the next section, we will provide an example of a quantum phase transition, for which the discussed OTOCs are analytic and, hence, cannot be used as an indicator for the phase transition.

4.7 Scattering Through Disorder and Interactions

In this section we discuss the impact of scattering on the observed stability of the OTOCs. In particular, we consider the effects of disorder and interactions that break integrability. This shows that, in general, long-time stability of the OTOC cannot be expected.

4.7.1 Classical Ising Chain

We have found that $\sigma^z(t)|\uparrow^N\rangle$ represents effectively a low-entangled, rotated state (Appendix C.1.4). It is then natural to consider an entirely classical version of the Ising chain. Here, the role of constraints imposed by integrability and symmetry on the observables appears particularly transparent. To obtain the classical version, the vector of Pauli matrices is replaced by unit vectors $\vec{S}_j$ undergoing precessional dynamics in their net (exchange + applied) field [228, 229]

$$H = -J \sum_j S_j^z S_{j+1}^z + g \sum_j S_j^x. \tag{4.35}$$

In analogy to the quantum setup, the initial state is set to all spins being aligned with the positive z-axis. We time evolve the spins according to the equations of motion $\dot{S}_j^\alpha = -\{H, S_j^\alpha\}$, where the Poisson brackets are defined by the Lie-algebra structure $\{S_j^\alpha, S_l^\beta\} = -\delta_{jl}\epsilon^{\alpha\beta\gamma}S^\gamma$. To compute the classical version of the OTOC, we first evolve the system forward in time, then rotate the central spin by an angle of π around the z-axis, and finally evolve the system backward in time.

Due to translational invariance of the initial (fully polarized) state, the equation of motion of $M(t)$—i.e., the zero-wavevector component of the magnetization—decouples from the other momentum modes and effectively yields a single-spin problem. The resulting time evolution of M is fully periodic, Fig. 4.7(a). Numerically, we find the amplitude of the periodic motion of the S^z component to be $1 - \sqrt{1-(g/J)^2}$.

The classical version of the OTOC forward evolves the fully polarized state, then rotates the spin at site j by π around the z axis, and finally back-evolves the state. By contrast with $M(t)$, this operation is not spatially uniform, but the state remains polarized with a similar value to $M(t)$, at least for a long initial time, see Fig. 4.7(b).

4.7.2 Role of Disorder

The stability of even $M(t)$ for the classical case suggests that constraints on the dynamics—in this case the decoupling of the uniform $k = 0$ mode of

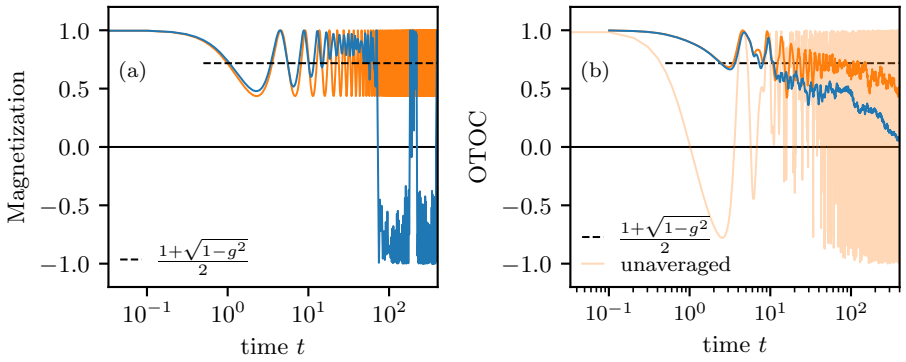

Figure 4.7: *Magnetization (left) and OTOC (right) for the classical Ising chain given in Eq. (4.35). We use $N = 500$ spins, $J = 1$, coupling strength $g = 0.9$, open boundary conditions, and measure the magnetization of the central spin in the z direction. Static spatial disorder is added to the transverse field (Gaussian with standard deviation $W = 0.04$). (b) shows results averaged over a time window of $\sim 0.03t$ and over the nine sites closest to the perturbation to reduce fluctuations. For times $t \gtrsim 50$, the time evolution of the OTOC appears chaotic.*

the spin density—play a central role in the appearance of nonthermal late-time expectation values. To test this for the classical case, we remove this decoupling by adding Gaussian white disorder with standard deviation W to the transverse field. This preserves the Ising symmetry of the system, while the uniformly polarized starting state also remains unchanged. The result is that, already in the presence of only a small amount of disorder, the classical late-time signal in both $M(t)$ and the OTOC vanishes, see Fig. 4.7.

In the quantum system, it is the integrability of the TFIM which yields the (nongeneric) conserved quantities, which follow from the decomposition of the system into 2×2 blocks labeled by the momentum. However, adding disorder to the transverse field keeps the single-particle nature of the problem intact while removing the constraints imposed by translational symmetry and the concomitant momentum conservation. Indeed, doing so immediately degrades the signal of the OTOC, Fig. 4.1(b), indicating that the dynamical constraints underpin the late-time signal [4]. Similarly, as we argue next, the apparent long-time stability of the quantum OTOC signal in the non-integrable case appears to be a finite-time remnant of the integrability of the TFIM and, as such, has the same origin as the relocalization described above.

[4] We note that, while the disorder reduces the dynamical relocalization of domain walls, it instead leads to their Anderson localization, so that for stronger disorder with a short localization length, the OTOC remains visibly nonzero.

4.7.3 Fate of the OTOC Beyond Integrability

The notion of thermalization states that, in an ergodic system, observables at a late time after a quench take on the values characteristic of the energy density of the fully polarized state from which the quench started. In the TFIM, this is patently not the case. Concretely, even a local observable such as the exchange energy of neighboring spins $J\,\sigma_j^z\sigma_{j+1}^z$ takes on a nonthermal value: It vanishes for $g/J > 1$, whereas it is in fact nonzero in any thermal state.

What changes when the constraints imposed by integrability are removed and hence thermalization should occur? The answer in finite-size attainable-time numerics is not much, see Fig. 4.8 and Appendix C.4. The correlators and OTOCs of the ANNNI model described in the next paragraph are very close to those of the integrable TFIM, up to a rescaling of the scale of the effective transverse field.

This rather suggests that thermalization has simply not taken place in the regime accessible to numerics. In fact, we note that the ANNNI model studied in Refs. [191, 220, 230], where a second-neighbor interaction is added that breaks integrability $H_{\mathrm{ANNNI}} = H_{\mathrm{TFI}} - \Delta \sum_j \sigma_j^z\sigma_{j+2}^z$, is close to integrable in two ways: first, due to the smallness of Δ, the integrability-breaking perturbation itself and, second, a four-fermion term of the form

$$H_{\mathrm{int}} \sim -4\Delta \sum_j c_{j'}^\dagger c_{j'} c_{j'+1}^\dagger c_{j'+1}. \tag{4.36}$$

appears. This is separately small in the quasiparticle (domain wall) density $c_{j'}^\dagger c_{j'} \sim (g/J)^2/4$.

The difficulty in confirming definitively that the nonvanishing OTOC is due to a failure to access the actual long-time behavior lies in the fact that adding a generic perturbation removes integrability and hence makes the problem intractable beyond small finite sizes. However, note that even an Ising even quantity like the domain wall energy density at long times behaves in essentially the same way as the OTOC in the numerics, see Fig. 4.8. This would seem to be consistent with the idea that neither quantity has reached its long-time value. As a consequence, either (or perhaps most likely neither) quantity could be used as a ground state phase diagnostic in the spirit of Ref. [191]: The scattering processes between domain walls are too weak to degrade the signal before finite-size effects mask the behavior of the thermodynamic system. We note, however, that the capacity of various observables to pin down the phase transition point [227] is not affected by these considerations.

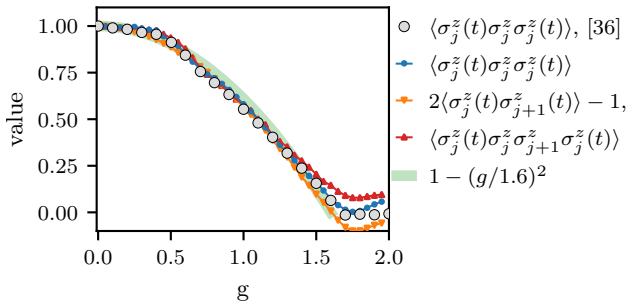

Figure 4.8: *Time-averaged correlators in the nonintegrable ANNNI model at $\Delta = 1/2, J = 1$: OTOC (circles, from Ref. [191] and our own numerics) compared with domain wall density observables (triangles) evaluated in $|\uparrow^N\rangle$ and $\sigma_j^z(t)|\uparrow^N\rangle$. The window for time averaging was chosen after initial transients (by eye), up to the time where boundary effects (determined by comparing $N = 22$ and $N = 24$ results) become visible, see Appendix C.4.1. The data are most reliable for intermediate values of $g \approx 1$: for small g, no clear plateau in the OTOC appears up to $t = 120$, while for large g, boundary effects set in early.*

4.8 Conclusions

In this chapter, we provided a detailed analysis of information spreading, as probed by OTOCs, in both integrable systems undergoing a phase transition and systems with scattering. Through exact analytical calculations in the thermodynamic limit and the interpretation thereof we have found an intuitive explanation for the stability of the quenched OTOC in the ferromagnetic phase. We have shown that the quantum phase transition, the topological insulator phase transition, and the nonanalytic behavior of the OTOC can all be traced back to the $k = \pi$ momentum subspace. We also demonstrated how transitions in the group velocity, even in the absence of a phase transitions, can lead to nonanalytic behavior of the OTOC. This highlights that while nonanalyticities in the OTOC may be related to phase transitions, they are not necessarily signatures of one. Lastly, we showed that in the presence of scattering, OTOCs decay and thereby exhibit the expected thermal behavior. Much work remains to fully understand the behavior of generic many-body systems, here and in higher dimensions.

5 Dephasing and Information Scrambling

The work in this chapter has appeared as part of the following article

Dmitry A. Abanin *et al.*
Constructive interference at the edge of quantum ergodic dynamics.
arXiv:2506.10191 [231]

Having studied the spreading of information in systems close to integrability, in this chapter we study the role of interference effects for information spreading in integrable and chaotic systems. As interference effects can be suppressed via dephasing noise, we will base our analysis on the dephasing noise sensitivity of information spreading, focusing on charge transport and out-of-time ordered correlators. This can also be interpreted as a study of decoherence effects or a benchmark of classical approximation accuracy.

For the in-depth analysis provided in this chapter, we consider two probes of quantum dynamics: two-point correlators and OTOCs, which measure different types of information spreading. Haar random circuits are ideal for this study as they are minimal models resembling generic features of unitary quantum dynamics governed by local interactions [232–239]. Surprisingly, we find the role of interference to be relatively small. An incoherent approximation to the dynamics that takes the form of a classical Markov process captures the average behavior of the observables and a large constant fraction of the circuit-to-circuit fluctuations—even in large circuits, as we demonstrate by comparing to experimental results obtained on quantum computers.

This chapter is structured as follows. First, we analyze the part of the signal that is fully insensitive to dephasing noise, has no interference effects, and can be computed using the simplest form of the Monte Carlo sampling algorithm in Section 5.2. Then, we introduce the formalism and concept of Hamming distance in Section 5.3. We discuss the relation of Hamming distance to dephasing noise and the approximation accuracy. In Section 5.4, we provide an in-depth study of the Hamming distance resolved signal for charge-charge correlators in random circuits with charge conservation and discuss the implications for the dynamics. Then in Section 5.5, we present the algorithm that systematically includes parts with increasing dephasing sensitivity and report in Section 5.6 the experimental results for OTOCs in large circuits. We conclude in Section 5.7.

5.1 Overview

Most general are random circuits without symmetries or structure in space and time, representing unconstrained quantum systems. Being unconstrained, these circuits produce ergodic dynamics that lead to rapid information scrambling — information about the system's initial state quickly disperses throughout the Hilbert space [240]. Consequently, the time-evolved state quickly becomes featureless [236, 241], with two-point correlators that decay exponentially in circuit depth [237, 242, 243]. The spreading of information can be probed using out-of-time ordered correlators (OTOCs), revealing a ballistic spreading of information with a diffusive broadening front, which is expected to be universal for unconstrained quantum systems [199, 237, 244–246].

A notable subclass are random circuits with symmetries, which replicate quantum dynamics constrained by conservation laws. In the case of a U(1) symmetry, i.e., a conservation of particle number, charge or a single component of total spin, the symmetry slows down the equilibration of charge imbalances [189, 246, 247]. In particular, charges are found to spread diffusively yielding charge-charge two-point correlators that decay algebraically with circuit depth, which for the 1D circuits considered in this paper

$$C(t) = \mathrm{Tr}(\sigma_0^z(t)\sigma_0^z) \sim t^{-\frac{1}{2}}. \tag{5.1}$$

While the algebraic decay is universal and can be observed for any typical circuit realization, the value of the charge-charge two-point correlator is nonuniversal and varies between different particular circuit instances. These circuit-to-circuit fluctuations are also found to decay algebraically [248]; thus, the correlator is an interesting object to probe for individual circuits, with significant variations among circuits at large circuit depths. Similarly, OTOC fluctuations are found to decay algebraically at the propagation front [231, 249]. As a consequence of this algebraic rather than exponential decay, a sufficiently accurate quantum computer can efficiently distinguish typical circuit instances from these random ensembles by their correlators or OTOCs, respectively, raising the question of whether a quantum computer is necessary or whether efficient classical algorithms exist for the same task.

To address this question, we study the nature of the correlators and the dynamical processes stabilizing their value and preventing an exponential decay. As we will elucidate, the dominant processes are the dynamics of Markovian random walkers spreading diffusively and enhancing circuit-to-circuit signal fluctuations [237, 248, 250]. Being Markovian, they can be described through a Markov chain and have no relative phases, so their dynamics can be efficiently computed via Monte Carlo sampling. Being phase-insensitive also means that there are no quantum interference effects and their dynam-

ics is insensitive to variation of phases within a quantum circuit. Hence, the dynamics of the walkers provides for the rigidity of the observables but also makes these observables relatively insensitive to the quantum circuit variations. Specifically, the charge correlation functions are relatively insensitive to the insertion of symmetry-respecting dephasing noise, whereas OTOC circuits, which require an identical forward and backward time-evolution, are relatively insensitive to Pauli noise that affects the forward and backward evolutions identically. With a detailed theoretical analysis of how these decoherence affects the observables in the random circuit ensembles, we motivate new classical methods to predict the value of correlators and OTOCs for specific circuit instances with high relative accuracy.

The analysis refines the common understanding of quantum systems and their properties. Widely studied perspectives involve entanglement [54, 251–254] and magic [255–261]. From these perspectives, deep Haar-random circuits involving many sites fulfill the expectations of complex quantum systems; they generate volume-law entangled states via many non-Clifford gates. This makes correlators intractable with out-of-the box methods. In this work, we focus on interference effects in Haar-random circuits, and show that they only yield subleading corrections to the mostly interference-free dynamics. Here, the key insight is that chaotic dynamics generated by random circuits suppresses interference effects by decoherence in the form of dephasing through strong phase fluctuations. In this sense, the dynamics generated in these chaotic systems becomes classical. We base a classical algorithm on this dephasing property, which systematically incorporates interference effects, allowing for the calculation of algebraically decaying correlators with high relative accuracy.

This approach provides a very direct understanding of the interplay of coherence, interference and dephasing for Haar-random systems and establishes coherence alongside entanglement and magic as a key property of chaotic quantum systems. The formalism paves the way to combining the many different perspectives on coherence, noise and quantum corrections already developed in the past. Coherence has been studied within the influence matrix in the form of sojourns [262, 263], as a measure and resource [264–267], in the form of a decoherence functional [268], open systems [269, 270], in connection to entanglement [271, 272], thermalization [273, 274], the spectral form factor [275], and the impact of noise in the realm of matrix-product states [248, 276, 277], Pauli string expansion [278, 279], on entanglement [280], while quantum corrections to classical processes were studied as bubbles in [250].

In particular, we study three types of signals C. We investigate local charge densities with respect to a time-evolved computational basis state

$|a_0(t)\rangle$ with a charge imbalance, charge-charge correlators $\mathrm{Tr}[O(t)O(0)]$ of Heisenberg time-evolved local charge density operators $O(t)$ and OTOCs $\mathrm{Tr}[O_j(t)O_0(0)O_j(t)O_0(0)]$. We start by analyzing the dephasing sensitivity of these quantities when introducing a dephasing noise of strength δ. For that, we decompose the fluctuations of the signal as measured by the variance $\mathrm{Var}\, C(\delta)$ according to its dephasing sensitivity

$$\frac{[\mathrm{Var}\, C](t,\delta)}{[\mathrm{Var}\, C](t,\delta=0)} = \sum_{d=0} r_d(t) e^{-\delta d}, \tag{5.2}$$

so that the fraction of the variance r_d decays exponentially in d and δ. Hence, d may be thought of as a measure for the space-time volume sensitive to noise.

The first key result is that for all cases considered of algebraically decaying $\mathrm{Var}\, C(t)$ in random circuits in the long-time-limit, r_d becomes independent of time, i.e., the value C does not become more noise-sensitive with increasing circuit depth. The noise insensitive term r_0 dominates, and r_d decays rapidly with d. In particular, for charge-charge correlators in Haar-random circuits with charge conservation we find $r_d \sim e^{-\sqrt{d}}$. A parallel result appears for the signal C of OTOCs in Haar-random circuits. In this case, we reformulate OTOCs as correlation functions in a system of two independent copies of the Hilbert space, undergoing the joint evolution $U(t) \otimes U(t)$. The OTOC is then shown to be insensitive to a depolarizing noise channel that acts identically on both copies. We find that in the vicinity of the operator front, $x \sim v_B t \pm \mathcal{O}(\sqrt{t})$, r_d decays exponentially and is asymptotically independent of time. In contrast, far behind the front $x \ll v_B t$, we see that the signal is highly sensitive to global interference effects, but at the same time, the signal is exponentially small. This manifests as a r_d that increases with the space-time volume of the OTOC circuit; for the 1D geometries considered in this paper, r_d is maximal at $d \propto t^2$.

Our second key result is a direct relation between the noise insensitivity and the performance of a classical Monte Carlo sampling algorithm. In its simplest form for the calculation of expectation values, it is based on sampling from the paths $|\Psi(T)\rangle$ an initial computation basis state Ψ takes across computational basis states $|a_t\rangle$ at time steps t. It uses the approximation

$$C \approx \sum_{\{a_t\}} \langle a_T|O|a_T\rangle p(a_T|a_{T-1}) \cdots p(a_2|a_1) p(a_1|a_0) \tag{5.3}$$

with transition probabilities between computational basis steps $p(a_{t+1}|a_t)$. The sum can be efficiently evaluated through Monte Carlo sampling as the sampling complexity of $p(a_{t+1}|a_t)$ is constant in time and space, and $\langle a_T|O|a_T\rangle$ is bounded. A very similar algorithm can be constructed for correlators and

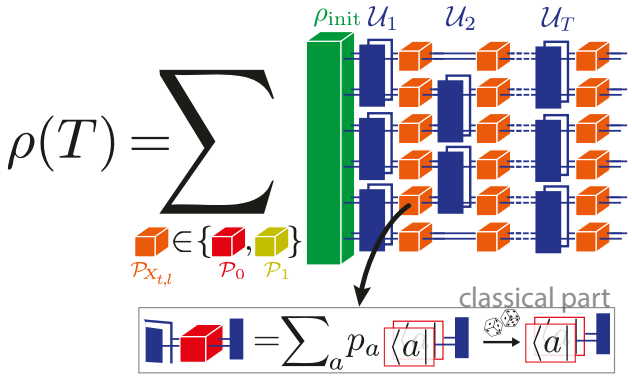

Figure 5.1: *The time evolved density matrix $\rho(T)$ is decomposed into a sum over projection configurations. The initial density matrix ρ_{init} (green) is evolved with a brickwall circuit composed of two-qubit gates (blue). At every site in every timestep we insert a projector $\mathcal{P}_{X_{t,l}}$ (orange), its index $X_{t,l}$ is summed over $0, 1$. The projector $\mathcal{P}_0$ projects locally on the diagonal of the density matrix, see Section 5.3 and $\mathcal{P}_1 = \mathcal{I} - \mathcal{P}_0$. We refer to $X_{t,l} = 0$ for all t, l as the classical part as it corresponds to ρ being projected onto its diagonal at all time steps.*

OTOCs, where for OTOCs we use paths over Pauli strings instead. This algorithm can be shown to capture fluctuations up to the lowest order in $e^{-\delta}$ and, therefore, has a mean square error of $\epsilon^2 = \sum_{d \geq 1} r_d$ when estimating C for individual circuit instances.

The third key result is a systematic extension of this algorithm, capturing all fluctuations up to $d < D$ and yielding a mean squared approximation error of $\epsilon^2 = \sum_{d \geq D} c_d$. It is achieved by sampling after several time steps rather than every time step and by combining different sampling patterns. This algorithm can be shown to be quite efficient, with polynomial to sub-exponential scaling in accuracy.

5.2 Motivation

We begin with a more detailed discussion of the dephasing insensitive part of OTOCs in Haar-random circuits and, in the presence of charge conservation, charge-charge correlators. In particular, we consider brickwall circuits with T layers composed of Haar-random two-qubit gates with and without charge conservation acting on an initial state ρ_{init} with L qubits, as shown in Fig. 5.1. We then measure the OTOC $\text{Tr}[\sigma_2^z(T)\sigma_{L-1}^x(0)\sigma_2^z(T)\sigma_{L-1}^x(0)]/2^L$, where σ^z is a Pauli matrix, and the correlator $\text{Tr}[\sigma_{L/2}^z(T)\sigma_{L/2}^z(0)]/2^L$. The construction of the charge-conserving circuits is detailed in Section 5.3.1.

For the correlator, we consider dephasing noise in the computational ba-

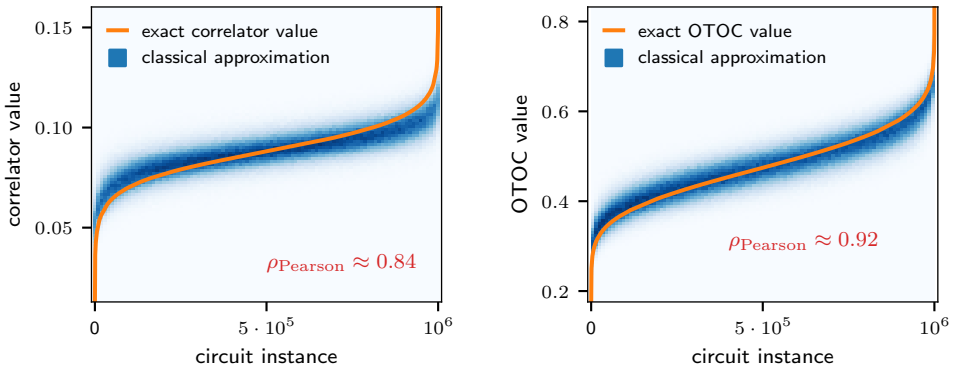

Figure 5.2: *Correlation between the classical and quantum signals for every random circuit. The classical part is obtained by projecting the density matrix at every step onto its diagonal, see Fig. 5.1. Left: Classical signal as an approximation to the exact signal for correlators* $\mathrm{Tr}[\sigma^z_{L/2}(t)\sigma^z_{L/2}]/2^L$ *in Haar-random circuits with* $U(1)$*, i.e., charge, conservation for* $T = 20$ *and* $L = 18$*. Right: Same comparison for the OTOC* $\mathrm{Tr}[\sigma^z_2(t)\sigma^x_{L-1}\sigma^z_2(t)\sigma^x_{L-1}]/2^L$ *for Haar-random circuits with depth* $T = 34$ *and* $L = 24$*.*

sis, i.e., the σ^z basis. The time-evolved operator $\sigma^z_{L/2}(T)$, when reduced to its diagonal after every two-qubit gate, is insensitive to such dephasing noise in between two-qubit gates. This motivates calling it "classical". The reduction can be achieved by inserting projectors $\mathcal{P}_0$ projecting to the diagonal part everywhere in the circuit, see red boxes in Fig. 5.1. The projector $\mathcal{P}_0$ is a superoperator acting on operators, which we indicate in this work by using a curly letter. For now, we sketch this idea as a motivation, a detailed discussion follows in the next chapter.

The reduction to the diagonal part can be understood as pairing trajectories. For this, we use $\rho_{\text{init}} = \sigma^z_{L/2}$ for the correlator and write $\sigma^z_{L/2}(T) = \sum_a s_a |a(T)\rangle\langle a(T)|$ in terms of the computational basis states $|a\rangle$. Then, reducing $\sigma^z_0(T)$ to its diagonal in every step is equivalent to reducing $|a(T)\rangle\langle a(T)|$ to its diagonal, which means that the bra and ket are in the same computational basis state after every two-qubit gate. Thinking of the time-evolved $|a(T)\rangle$ in terms of the trajectories across computational basis states, this reduction to the diagonal is equivalent to pairing the trajectory of the bra and ket.

The same picture holds for the OTOC $\mathrm{Tr}[\sigma^z_2(T)\sigma^x_{L-1}(0)\sigma^z_2(T)\sigma^x_{L-1}(0)]/2^L$, where the reduction to the diagonal corresponds to requiring the two time-evolved operators $\sigma^z_1(T)$ to be in the same state in the Pauli string basis after every step during the Heisenberg evolution. This way, for the OTOC, we pair the two Heisenberg evolved operators via pairing their trajectories

across Pauli strings. Similarly, one can define projectors $\mathcal{P}_0$ achieving such a pairing, so that the diagonal part of the OTOC can also be obtained by inserting $\mathcal{P}_0$ everywhere.

In both cases, we can introduce the $\mathcal{P}_0$s complement $\mathcal{P}_1 = \mathcal{I} - \mathcal{P}_0$, where $\mathcal{I}$ is the identity acting on operators. Then, we can insert identities $\mathcal{I} = \mathcal{P}_0 + \mathcal{P}_1$ everywhere in the quantum circuit, yielding a decomposition one part of which is the diagonal or paired part with $\mathcal{P}_0$s everywhere. This is shown in Fig. 5.1.

The diagonal part can be computed efficiently via Monte Carlo sampling because it effectively encodes a Markov chain process. The pairing yields the prefactors p_a of the paired trajectories to be positive and the unitarity preserves the norm so that all prefactors p_a add up to one. Hence, in every step, we can use the p_a as probabilities to sample the next state, which are either computational basis states for the simulation of charge-charge correlators or Pauli strings for OTOCs. We iterate this procedure, yielding a Markov chain Monte Carlo estimate for the diagonal part.

This estimate also provides a classical (i.e., phase-insensitive) approximation to the full signal, as shown in Fig. 5.2 for 10^6 instances of random circuits. Comparing the diagonal part to the full signal for the two examples, we find a Pearson correlation coefficient of 0.84 for the charge-charge correlator at circuit depth $T = 20$ and system size $L = 18$ and 0.92 for OTOCs at circuit depth $T = 34$ and system size $L = 24$. This indicates that in both cases the diagonal part in the form of a Markov chain process constitutes the dominant contribution to the signal.

Given the dominance of the Markov chain process, we explore in the next chapters the significance of corrections to this process and how to systematically include them in a Monte Carlo sampling algorithm. For that, we start with the introduction of the formalism underlying the systematic expansion in the next chapter.

5.3 Hamming Distance

Since expectation values decay exponentially in Haar-random circuits and thus become unobservable in experimental setups at large times, we study OTOCs in random circuits and correlators in random circuits with charge conservation with L sites. Charge conservation refers to the circuit preserving the total charge $Q^z = \sum_j \sigma_j^z$ where σ_j^z is the Pauli matrix acting on site j. The generation procedure for the two-site unitary with charge conservation is provided in Section 5.3.1. For completeness results for expectation values are provided in Appendix D.4.4, and for correlators in Haar-random circuits in Appendix D.2. In this chapter we focus on correlators for clarity; the

formalism can be generalized to different settings like out-of-time ordered correlators, see Section 5.6.

5.3.1 Charge-Conserving Circuit Construction

The charge conserving two-qubit unitaries used in this section are generated as follows. Requiring the two-qubit unitary $V_{j,j+1}$ to preserve the total charge $\sigma_j^z + \sigma_{j+1}^z$ restricts the matrix elements to be

$$V_{j,j+1} = e^{i\alpha} \begin{pmatrix} 1 & 0 & 0 & 0 \\ 0 & v_{1,1} & v_{1,2} & 0 \\ 0 & v_{2,1} & v_{2,2} & 0 \\ 0 & 0 & 0 & e^{i\beta} \end{pmatrix}, \tag{5.4}$$

where we ordered the states as $|\uparrow\uparrow\rangle, |\uparrow\downarrow\rangle, |\downarrow\uparrow\rangle, |\downarrow\downarrow\rangle$. Here, α and β are real numbers and the subblock $\begin{pmatrix} v_{1,1} & v_{1,2} \\ v_{2,1} & v_{2,2} \end{pmatrix}$ is a Haar-random 2x2 unitary [281]. Haar-random refers to the measure μ_{Haar} on unitary matrices that is invariant under multiplication with any unitary $\tilde{U}$

$$\int_U f(U) \mathrm{d}\mu_{\text{Haar}}(U) = \int_U f(U\tilde{U}) \mathrm{d}\mu_{\text{Haar}}(U) = \int_U f(\tilde{U}U) \mathrm{d}\mu_{\text{Haar}}(U). \tag{5.5}$$

For generating these two-qubit matrices, we omit $e^{i\alpha}$ as a global phase, sample the 2x2 random sub-matrix from the Haar-random ensemble and β uniformly from $[0, 2\pi)$. This measure is invariant under conjugation with any charge-conserving unitary.

5.3.2 Definition and Relation to Decoherence

In this chapter we discuss assigning a Hamming distance to elements of a density matrix or more general an operator. We show in subsequent chapters that correlators are dominated by the parts with small Hamming distance. Hence, the correlators are largely insensitive to decoherence, as defined below. We use this observation to propose an algorithm for the efficient simulation of the correlator measurements.

Similar to the phase flip channel [282], Hamming distance depends on the system and in particular, the basis. For the U(1)-conserving circuits, a suitable basis is the eigenbasis $\{|a\rangle\}$ of the local charge operator σ^z. We define the Hamming distance of the matrix element $|a\rangle\langle b|$ as $||a-b||_1$, where $||a-b||_1$ denotes the Hamming distance between the bitstrings a and b. In

this basis, we can obtain single-qubit projectors on the Hamming distance $\alpha = 0, 1$ subspace:

$$\mathcal{P}_\alpha[\rho] = \rho/2 + (-1)^\alpha \sigma^z \rho \sigma^z/2. \tag{5.6}$$

Using the projectors $\mathcal{P}_\alpha[\rho]$, the phase flip channel with rate γ [5] can be written as

$$\begin{aligned}\mathcal{E}[\rho] &= (1-\gamma)\rho + \gamma\sigma^z\rho\sigma^z \\ &= \mathcal{P}_0[\rho] + (1-2\gamma)\mathcal{P}_1[\rho].\end{aligned} \tag{5.7}$$

For multiple qubits, we can analyze the dephasing sensitivity of a multi-qubit-state by creating multiqubit projectors $\mathcal{P}_{\vec{\alpha}}^{\otimes L} = \mathcal{P}_{\alpha_1} \otimes \mathcal{P}_{\alpha_2} \ldots \otimes \mathcal{P}_{\alpha_L}$ and using that the projectors are a resolution of the identity $\mathcal{P}_0 + \mathcal{P}_1 = \mathcal{I}$, which implies $\sum_{\vec{\alpha}} \mathcal{P}_{\vec{\alpha}}^{\otimes L} = \mathcal{I}^{\otimes L}$.

This enables a decomposition of density matrices ρ using these projectors. For instance, at the single-qubit level, we decompose the single qubit density matrix $\rho = I/2 + \sum_\nu \rho_\nu \sigma^\nu$ with Pauli matrices σ^ν into the diagonal and off-diagonal part $\rho \equiv \mathcal{P}_0[\rho] + \mathcal{P}_1[\rho]$. The diagonal part $\rho_0 = \mathcal{P}_0[\rho] = I/2 + \rho_z\sigma^z$ has Hamming distance 0, is invariant under the phase flip channel $\mathcal{E}[\rho_0] = \rho_0$, and has no coherence in that sense. Analogously, the off-diagonal part $\mathcal{P}_1[\rho] = \rho_x\sigma^x + \rho_y\sigma^y$ has Hamming distance 1, is maximally sensitive in terms of its trace norm [6], and thus can be regarded as maximally coherent. This establishes a direct relation between the Hamming distance and sensitivity to decoherence induced by phase flip noise. Similarly, we can decompose multi-qubit density matrices using $\mathcal{P}_{\vec{\alpha}}^{\otimes L}$. In the following, we use this interpretation of Hamming distance as coherence to gain an intuitive understanding of the systems studied.

5.3.3 Decomposition into Parts

We apply this perspective to expectation values, two-point and out-of-time-ordered correlators for random brickwall circuits acting on L sites. Each circuit U consists of T layers of gates

$$U = U_T \ldots U_2 U_1, \tag{5.8}$$

where each layer U_t is composed of two-site gates $V_{j,j+1}$ as

$$U_t = \begin{cases} \prod_j V_{2j,2j+1} & t \text{ even} \\ \prod_j V_{2j+1,2j+2} & t \text{ odd} \end{cases}. \tag{5.9}$$

[5] The noise rate relates to the noise strength δ in the introduction as $\gamma = 1/2 - e^{-\delta}/2$.

[6] For $\gamma \leq 1/2$, given any $O = o_I I + o_x\sigma^x + o_y\sigma^y + o_z\sigma^z$ with $|O|^2 = 1$, then $\Gamma = |\mathcal{E}[O]|^2 = o_x^2 + o_z^2 + (1-2\gamma)[o_x^2 + o_y^2] \geq (1-2\gamma) = |\mathcal{E}[\mathcal{P}_1[O]]|^2/|\mathcal{P}_1[O]|^2 = \Gamma_{\text{off-diagonal}}$

All two-site gates are independently drawn at each time and location from the group of Haar-random two-qubit gates with $U(1)$ conservation, see Section 5.3.1. The overall circuit structure is shown in Fig. 5.1. The evolution of the density matrix with the layer U_t is described by the superoperator $\mathcal{U}_t$

$$\rho(t) = \mathcal{U}_t[\rho(t-1)] = U_t \rho(t-1) U_t^\dagger \tag{5.10}$$

so that the whole time evolution of the initial density matrix ρ_{init} can be written as

$$\rho(T) = (\mathcal{U}_T \circ \cdots \circ \mathcal{U}_1)[\rho_{\text{init}}]. \tag{5.11}$$

We can now decompose $\rho(T)$ into *parts* ρ_X, labeled by the matrix $X \in \{0,1\}^{T\times L}$, using the resolution of the identity $\mathcal{I} = \mathcal{P}_0 + \mathcal{P}_1$ as follows

$$\begin{aligned}\rho(T) &= (\cdots \circ (\mathcal{P}_0 + \mathcal{P}_1)^{\otimes L} \circ \mathcal{U}_2 \circ (\mathcal{P}_0 + \mathcal{P}_1)^{\otimes L} \circ \mathcal{U}_1)[\rho_{\text{init}}], \\ &= \sum_{X_{t,l}\in\{0,1\}} \rho_X(T),\end{aligned} \tag{5.12}$$

where we use the definition

$$\rho_X(T) = (\mathcal{P}^L_{X_T} \circ \mathcal{U}_T \circ \cdots \circ \mathcal{P}^L_{X_2} \circ \mathcal{U}_2 \circ \mathcal{P}^L_{X_1} \circ \mathcal{U}_1)[\rho_{\text{init}}]$$

and the L-site projectors $\mathcal{P}^L_{X_t} = \mathcal{P}_{X_{t,1}} \otimes \ldots \otimes \mathcal{P}_{X_{t,L}}$. The resulting projected density matrix or part ρ_X is either diagonal $X_{t,l} = 0$ or off-diagonal $X_{t,l} = 1$ at every site l at every time step t

Hence, we define the (summed) Hamming distance d as the total number of off-diagonal projectors $\mathcal{P}_1$ in the part ρ_X

$$d(X) = \sum_{t,l} X_{t,l}, \tag{5.13}$$

which can be understood as a measure of the phase flip sensitivity of a part, see Eq. (5.2). This motivates grouping the parts by d and obtain a decomposition of the density matrix according to Hamming distance d

$$\rho(T) = \sum_d \rho_d(T), \quad \rho_d(T) = \sum_{X \text{ with } d(X)=d} \rho_X(T), \tag{5.14}$$

The density matrix $\rho_0(T)$ corresponds to the part $X_{t,l} = 0$ at all times t and sites l; the density matrix is projected at every step onto its diagonal. It is insensitive to decoherence in the form of phase flips anywhere at any time and, in that sense, classical. As expected for classical dynamics, it is also efficiently computable on a classical computer, as we explain in Section 5.5.

Note that decomposing the density matrix in terms of Pauli strings, $\mathcal{P}_0$ on a site projects onto all Pauli strings with either Pauli matrices I or σ^z at that site, while $\mathcal{P}_1$ projects onto σ^y or σ^x.

5.3.4 Stochastic Independence of Parts

In order to evaluate the decoherence (i.e., phase flip) sensitivity for a measurement $\langle O\rangle_{\rho(T)} = \mathrm{Tr}[\rho(T)O]/2^L$ with observable O, we truncate the sum in Eq. (5.14) to $d \leq D$ yielding an approximation to the density matrix

$$\rho(T) \approx \rho_D(T) = \sum_{d=0}^{D} \rho_d(T). \tag{5.15}$$

We quantify the quality of the approximation by computing the difference between $\langle O\rangle_{\rho_D(T)}$ and the exact result $\langle O\rangle_{\rho(T)}$. Squaring and averaging this difference by integrating the unitaries V over the random ensemble they are selected from (denoted by an overline) yields the mean squared error (MSE), which quantifies the overall approximation quality. In Appendix D.1, we show that if the Kraus operators of the projectors $\mathcal{P}_\alpha$ form a subgroup of the group over which the two-qubit gates are averaged, then the parts ρ_X are stochastically independent

$$\overline{\rho_{X_1} \otimes \rho_{X_2}} = \delta_{X_1,X_2} \overline{\rho_{X_1} \otimes \rho_{X_1}}. \tag{5.16}$$

Consequently, the MSE reduces to a sum over the second moments with Hamming distance d

$$\mathrm{MSE}(T) = \overline{\left|\langle O\rangle_{\rho(T)} - \langle O\rangle_{\rho_D(T)}\right|^2} = \sum_{d=D+1} \overline{\langle O\rangle^2_{\rho_d(T)}}. \tag{5.17}$$

As every part ρ_X of the density matrix provides an independent correction to the classical part ρ_0, including any additional part just reduces the MSE monotonically by the respective second moment of that part $\overline{\langle O\rangle^2_{\rho_X(T)}}$. Intuitively, this monotonic behavior can be understood by noting that every insertion of a projector $\mathcal{P}_0$ yields an additional average: it does not change the circuit mean, but reduces the variance. The stochastic independence of the different parts motivates the analysis of the density matrix in terms of its individual parts, as in Eq. (5.12).

Similarly, the Hamming distance resolved density matrices $\rho_d(T)$, see Eq. (5.14), are stochastically independent, allowing us to analyze the decoherence sensitivity of $\rho(T)$ by decomposing it into $\rho_d(T)$. Most importantly, this makes the approximation $\rho(T) \approx \rho_D(T)$ controlled in the sense that the MSE decreases monotonically in D, motivating including corrections to $\rho_0(T)$ based on their Hamming-distance d, as will be discussed in Section 5.5.3.

We proceed with a systematic study of the decoherence sensitivity by resolving the variance $\mathrm{Var}\langle O\rangle_{\rho_d} = \overline{\langle O\rangle^2_{\rho_d}} - \delta_{d,0}\overline{\langle O\rangle_{\rho_0}}^2$ in terms of the Hamming

distance. We study the variances rather than the second moments as all variances $\mathrm{Var}\langle O\rangle_{\rho_d}$ follow the same scaling with time, namely $T^{-5/2}$ and coincide with the second moments except for $d = 0$, where the second moment decays more slowly: $\overline{\langle O\rangle^2_{\rho_0}} \sim T^{-1}$.

5.4 Dephasing Noise Stability of Correlators

Here, we study correlation functions $C = \mathrm{Tr}[\sigma^z_{L/2}(T)\sigma^z_{L/2}]/2^L$ with $O = \rho_{\mathrm{init}} = \sigma^z_0$. Results for expectation values can be found in Appendix D.4.4. While the initial operator σ^z_0 is not formally a density matrix, this does not affect any previous or following statements. We use that σ^z_0 can be written as a sum of density matrices $\sigma^z_0 = \sum_a s^a |a\rangle\langle a|$ in terms of computational basis states $|a\rangle$ and a sign $s^a = \pm 1$.

The charge conservation causes correlations to decay polynomially in time: The circuit averaged correlation function $\overline{\mathrm{Tr}[\sigma^z_0(T)\sigma^z_0]}$ decays as $T^{-1/2}$ and the circuit-to-circuit variance decays as $T^{-5/2}$ for large times, see Section 5.4.2 and D.4.5.

As discussed before, the charge conservation provides a natural basis to study decoherence in, so that phase flip noise commutes with the charge operator Q^z. Note that both the initial state $\rho(T = 0) = \sigma^z_0$ and the final σ^z_0-probe are diagonal and therefore invariant under phase flip noise. Hence, parts $\rho_X(T)$ with off-diagonal projectors $\mathcal{P}_1$ outside the light cone vanish $\rho_X(T) = 0$.

5.4.1 Numerical Results

We analyze numerically the behavior of the variance $\mathrm{Var}\langle O\rangle_{\rho_d} = \overline{\langle O\rangle^2_{\rho_d}} - \delta_{d,0}\overline{\langle O\rangle_{\rho_0}}^2$ generated by the parts of the density matrix with Hamming distance d, Eq. (5.14).

The results are shown in Fig. 5.3 (top). As a function of time, we find $\mathrm{Var}\langle O\rangle_{\rho_d}$ to first increase and approach its maximum at around $T_{\max} \sim d^{0.6}$, Appendix D.4. After assuming its maximum value, the variance decreases initially faster but converges to a decay of $T^{-2.5}$ for large times.

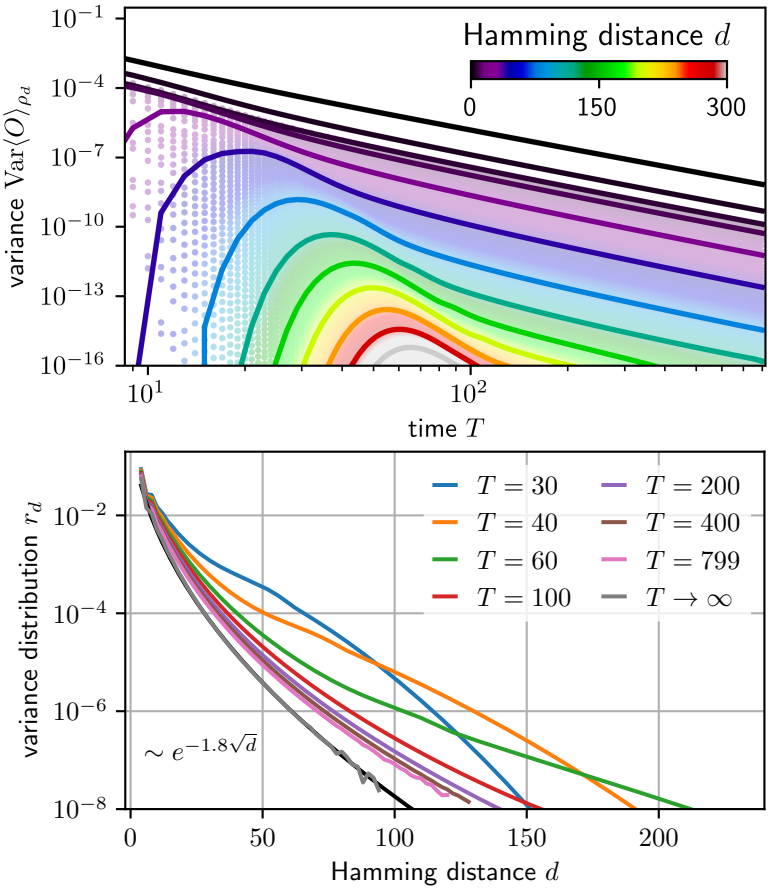

Figure 5.3: *Hamming distance resolved variance* $\mathrm{Var}\langle O\rangle_{\rho_d(T)}$ *with* $O = \rho_{\mathrm{init}} = \sigma_0^z$ *for Haar-random circuits with charge conservation acting on qubits shown in two different ways. (a) Variance* $\mathrm{Var}\langle O\rangle_{\rho_d}$ *as a function of time for different* d*. (b) Variance distribution* $\mathrm{Var}\langle O\rangle_{\rho_d}/\mathrm{Var}\langle O\rangle_{\rho}$ *as a function of total coherence at different times and the extrapolation to the long-time-limit. The results were obtained simulating the action of the averaged gates* $\mathcal{U}_t$*, inserting* $\mathcal{P}_0 + e^{i\omega}\mathcal{P}_1$ *everywhere and Fourier-transformation in* ω*, see also Appendix D.4.4 and D.4.5. We use itensor [54] and TEBD with a cutoff of* 10^{-20} *and system size* $L = 200$*.*

This behavior suggests the following intuitive picture, which is supported further by analytical considerations in Section 5.4.2 and numerical studies in Section 5.5.5.

For a given d, at small times, there are not enough space-time points to insert d projectors $\mathcal{P}_1$, the butterfly cone is too small to accommodate that Hamming distance d so that the variance $\mathrm{Var}\langle O\rangle_{\rho_d}$ vanishes.

For intermediate times, there appear to be two competing mechanisms. With increasing time, the size of the butterfly cone increases, increasing the

number of parts which can have Hamming distance d, which in turn increases the variance $\mathrm{Var}\langle O\rangle_{\rho_d}$. However, there appears to be an optimal density of off-diagonal projectors $\mathcal{P}_1$: when increasing the time further, the variance decays faster than in the long-time-limit. Hence, when increasing the time and also the space between projectors $\mathcal{P}_1$, it suppresses the variance stronger than the increasing number of parts increases it. We hypothesize this to be a "quantum" effect—the enhancement of the variance at short times above the long-time decay $cT^{-2.5}$ with some constant c. The large time variance decay of $T^{-2.5}$ is the same as for the classical variance $\overline{\langle O\rangle_{\rho_0}^2} - \overline{\langle O\rangle_{\rho_0}}^2$. This suggests that it is mostly classical effects governing the decay of the variance at late times: the Hamming distance d occurs only in one space-time region of duration $\mathcal{O}(1)$, while for most of the evolution of the order $\mathcal{O}(T)$ classical dynamics dominate yielding the long-time scaling as $T^{-2.5}$.

The same conclusions can be made when taking a slightly different perspective on the same results. We analyze how the total variance is distributed across different Hamming distances d for different times by calculating the ratios $r_d = \mathrm{Var}\langle O\rangle_{\rho_d}/\mathrm{Var}\langle O\rangle_{\rho}$. Note that $\sum_n r_n = 1$. The results are shown in Fig. 5.3 (bottom).

The variance $\mathrm{Var}\langle O\rangle_{\rho_d}$ decays sub-exponential in d up to a transition point, which increases with time, after which the contributions decay over-exponential. This over-exponential decay again reflects that the Hamming distance is upper bounded by the light cone volume and unlikely to exceed the smaller butterfly cone, strongly suppressing parts ρ_X with Hamming distance $d(X)$ larger than the size of the butterfly cone. For large times, we find $\mathrm{Var}\langle O\rangle_{\rho_d}$ to converge to a stretched exponential distribution over d with

$$r_d = \frac{\mathrm{Var}\langle O\rangle_{\rho_d}}{\mathrm{Var}\langle O\rangle_{\rho}} \overset{T\to\infty}{\to} \mathrm{const}\, e^{-1.8\sqrt{d}} + \mathcal{O}(T^{-0.5}) \tag{5.18}$$

via extrapolation. This is striking: The Hamming distance distribution is independent of time and the size of the butterfly-cone. For a fixed rate of phase flip errors, the relative error ϵ_r approaches a constant

$$\epsilon_\mathrm{r}^2 = \mathrm{MSE}_\gamma(\mathrm{T})/\mathrm{Var}\langle O\rangle_{\rho(T)} \overset{T\to\infty}{\to} \mathrm{const}, \tag{5.19}$$

where MSE_γ refers to the mean squared error obtained for noisy correlation values with phase flip channels at every site in every time step, Eq. (5.7). Stated differently, despite more and more phase flip errors occurring with time, the relative error does not increase. This observation may again be explained with the Hamming distance occurring within a single region in the light cone in every part rather being uniformly distributed. It encourages

the development of a classical algorithm truncating the Hamming distance and in that sense, coherence and is presented in Sec. 5.5.

Here, we can already evaluate the approximation error of the truncation and evaluate the significance of the large Hamming-distance parts with strong decoherence sensitivity. We calculate the relative approximation error for $\rho \approx \rho_D$, Eq. (5.15), using the long-time extrapolation results Eq. (5.18)

$$\epsilon_{\mathrm{r}}^2 = \frac{\mathrm{MSE}(T)}{\mathrm{Var}\langle O\rangle_{\rho(T)}} \overset{T\to\infty}{\to} (0.6\sqrt{D}+1.1)e^{-1.8\sqrt{D}}, \tag{5.20}$$

and, hence, expect a scaling of $D \sim \log(1/\epsilon_{\mathrm{r}})^2$.

Already the classical part ρ_0 yields about 90% of the full variance in the long-time-limit, i.e., the approximation $\rho(T) \approx \rho_0(T)$ yields a high relative accuracy, see Appendix D.4.3.

We conclude that on large scales, the hydrodynamics governing $\langle O\rangle_{\rho(T)}$ in a typical Haar-random quantum circuit with a U(1) conservation law is dominated by the classical dynamics.

5.4.2 Analytical Dynamics and Calculation

We continue by analyzing the structure of the variance in random U(1) circuits analytically. It yields an argument for the variance being created within small space-time regions. Here, we sketch the results; the details of the calculations can be found in Appendix D.4.5.

In order to calculate the MSE, Eq. (5.17), we calculate the circuit-to-circuit average and variance of $\mathrm{Tr}[U\sigma_0^z U^\dagger \sigma_0^z]$ in the continuous space and time limit for infinitely large systems. The average is found to be

$$\mathrm{Tr}[\overline{U(T)\sigma_i^z U(T)^\dagger}\sigma_j^z]/2^L = G(T, i-j) \tag{5.21}$$

where the propagator

$$G(T, i-j) = \frac{e^{\frac{-(i-j)^2}{2T}}}{\sqrt{2\pi T}} \tag{5.22}$$

follows from the σ_i^z performing a random walk under the circuit average as $\overline{V_{i,i+1}\sigma_i^z V_{i,i+1}^\dagger} = \sigma_i^z/2 + \sigma_{i+1}^z/2$. Hence, the circuit averaged correlation function decays as $\mathrm{Tr}[\overline{U(T)\sigma_0^z U(T)^\dagger}\sigma_0^z] = (2\pi T)^{-1/2}$. Next, we calculate the second moment of the correlation function over the circuit ensemble as

$$\overline{\mathrm{Tr}\,[U\sigma_0^z U^\dagger\sigma_0^z]\,\mathrm{Tr}\,[U\sigma_0^z U^\dagger\sigma_0^z]}, \tag{5.23}$$

which can be rewritten in terms of a single trace over a doubled Hilbert space

$$\mathrm{Tr}\left[\overline{(U\sigma_0^z U^\dagger \otimes U\sigma_0^z U^\dagger)}\sigma_0^z \otimes \sigma_0^z\right]. \tag{5.24}$$

In this doubled Hilbert space, the two σ^z perform random walks independently and "interact" when they are in the same location, yielding variance contributions. These contributions may be classical or quantum, where the latter are projected out by applying $\mathcal{P}_0$. As an approximation, we can calculate the variance from a single classical interaction summed over the interaction location x and time t

$$\begin{aligned}\mathrm{Var}\langle O\rangle_{\rho_0} &\approx \frac{1}{12}\sum_t\sum_x [\partial_x G(t,x)]^2[\partial_x G(T-t,x)]^2 \\ &\propto \frac{1}{T^{5/2}},\end{aligned} \tag{5.25}$$

the scaling then follows from dimensional analysis, Appendix D.4.5.

Now, we consider the random walkers interacting classically a second time which we separate into two cases. First, if the second interaction process does not occur close to the first one (i.e. $\mathcal{O}(T)$ away), these processes yield a contribution to the variance scaling as $1/T^4$. Second, if the additional interaction process occurs close (i.e. $\mathcal{O}(1)$) to the existing one, the structure of Eq. (5.25) still applies. Hence, the two interactions within a small region yield a variance contribution $\propto T^{-5/2}$, which is however smaller than the single interaction contribution due to a small interaction strength of $1/12$. Adding more processes within a small region of order $\mathcal{O}(1)$ yields a correction exponentially small in the number of interactions, see Appendix D.4.5. In summary, only processes where the interactions happen in vicinity of each other yield a contribution $\propto T^{-5/2}$ to the classical variance with $d = 0$.

The same applies to processes with a finite $d > 0$. These now involve terms, where the two walkers $\sigma_j^z \otimes \sigma_{j+1}^z$ interact, resulting in terms like $\sigma_j^+\sigma_{j+1}^- \otimes \sigma_j^-\sigma_{j+1}^+$, with $\sigma_j^\pm = \sigma_j^x \pm i\sigma_j^y$. The $\sigma_j^+\sigma_{j+1}^- \otimes \sigma_j^-\sigma_{j+1}^+$ then yield a finite Hamming distance d and are projected out by $\mathcal{P}_0$, giving rise to their interpretation as being quantum. Similar to the classical processes, these interactions are subleading as they have a small prefactor, require the walkers to meet, and effectively couple to the gradients of the distributions $\partial_x G$, like in Eq. (5.25). The interaction structure being analogous to the classical case yields the $T^{-5/2}$ decay also for terms with $d > 0$ in Fig. 5.3: The processes where all of the quantum interactions occur in the vicinity to each other are dominant, processes with quantum interactions distributed over the whole light cone are subleading in time. The parts in which the quantum interactions happen within vicinity to each other then yield variance contributions

decaying as $T^{-2.5}$ similar to a single classical interaction. We speculate that there may be further cancellation effects, so that the variance contribution for a given d decay initially faster than $T^{-2.5}$ after having approached its maximum.

This perspective also suggests a smaller variance contribution from terms with large Hamming distance d, also discussed as operator backflow from the perspective of Pauli string expansion [248]. Large Hamming distances d correspond to long lived or many quantum walkers $\sigma_j^q = \sigma_j^+ \otimes \sigma_j^-$. As σ_j^q performs both, a random walk as well as three-body interactions by creating or annihilating further σ^z-random walkers, the larger d the more likely is the creation of further particles. To contribute to the variance, all of them have to be annihilated again and reduced to $\sigma_0^z \otimes \sigma_0^z$ in order to not vanish with the final trace probe in Eq. (5.24). This may be the competing process yielding a decrease of the variance contribution with time despite the number of possible processes given d growing.

In Section 5.5, we devise an algorithm exploiting this insight: the quantum corrections are dominated by those where the quantum processes occur in the vicinity of each other.

5.5 Algorithm

Based on the insights in the previous chapters, we explore possible classical algorithms in three steps. First, we discuss an algorithm for calculating the classical part of the variance. Second, we propose an extended algorithm to systematically include the quantum corrections. Third, we analyze a more efficient, heuristic version based on the intuition that the quantum interactions typically occur within a single region, i.e., the most relevant parts ρ_X are those where all $\mathcal{P}_1$ occur within one region.

5.5.1 Markov Chain Monte Carlo Algorithm

We start with the states in the computational basis that is formed by the eigenstates $|a\rangle$ of $(\sigma^z)^{\otimes L}$. They can be used to form all eigenoperators of $(\mathcal{P}_0)^{\otimes L}$ with eigenvalue 1. This allows to write

$$\mathcal{P}_0^{\otimes L}[\rho] = \sum_a |a\rangle\langle a|\mathrm{Tr}[\rho|a\rangle\langle a|]. \tag{5.26}$$

For all cases studied in this work ρ_{init} is diagonal. Hence, we can write

$$\begin{aligned}\rho_0(T) &= (\mathcal{P}_0^{\otimes L} \circ \mathcal{U}_T \circ \cdots \circ \mathcal{P}_0^{\otimes L} \circ \mathcal{U}_2 \circ \mathcal{P}_0^{\otimes L} \circ \mathcal{U}_1)[\rho_{\text{init}}] \\ &= \sum_{a_0,a_1,a_2,\ldots} |a_T\rangle\langle a_T|\langle a_0|\rho_{\text{init}}|a_0\rangle \prod_{t=1}^{T} |\langle a_t|U_t|a_{t-1}\rangle|^2. \end{aligned} \tag{5.27}$$

Now we can use that

$$\sum_{a_t} |\langle a_t|U_t|a_{t-1}\rangle|^2 = 1 \tag{5.28}$$

since $|a_t\rangle$ is a complete basis and U_t is unitary together with

$$|\langle a_t|U_t|a_{t-1}\rangle|^2 \geq 0, \tag{5.29}$$

to get valid conditional probabilities

$$p(a_t|a_{t-1}) = |\langle a_t|U_t|a_{t-1}\rangle|^2. \tag{5.30}$$

Similarly, we define

$$p(a_0) = |\langle a_0|\rho_{\text{init}}|a_0\rangle| \tag{5.31}$$

$$s(a_0) = \langle a_0|\rho_{\text{init}}|a_0\rangle / p(a_0). \tag{5.32}$$

We arrive at

$$\begin{aligned}&\langle O\rangle_{\rho_0(T)} = \\ &\sum_{a_0,a_1,\ldots} \langle a_T|O|a_T\rangle s(a_0) \left(\prod_{t=1}^{T} p(a_t|a_{t-1})\right) p(a_0). \end{aligned} \tag{5.33}$$

This expression represents a weighted sum over trajectories in the computational basis. It can be evaluated with a Markov chain Monte Carlo sampling algorithm to accuracy ϵ using $1/\epsilon^2$ samples. The complexity is determined by the computational cost of sampling from the probability distributions $p(a_t|a_{t-1})$ and $p(a_0)$ and the maximum value of $|s(a_0)|$. For the cases studied in this paper, we have $\max_{a_0}|s(a_0)| = 1$.

5.5.2 Forming Partitions by Grouping Gates

A simple way to improve the accuracy is to merge several gates into a bigger one and thereby apply the diagonal projection less often. We refer to this as a *partition* of the circuit. In Appendix D.5.2, we provide a detailed

explanation of the sampling algorithm for partitions. Forming partitions allows a trade-off between accuracy and computational complexity: Merging gates increases the computational complexity for sampling from $p(a_t|a_{t-1})$, and it increases the accuracy because it corresponds to including more parts. All these parts ρ_X, with $\mathcal{P}_0$ or $\mathcal{P}_1$ at the legs connecting merged gates, are stochastically independent, see Appendix D.1. This yields a monotonic accuracy improvement thus merging provides a controlled level of approximation.

5.5.3 Combining Partitions

Next, we combine R partitions to obtain a better approximation reliably. We label a partition by Y with $Y_{t,l} \in \{0, 2\}$ and define $\mathcal{P}_2 = \mathcal{I}$ in analogy to parts labeled through X. As $\mathcal{P}_2 = \mathcal{P}_0 + \mathcal{P}_1$, ρ_Y is a sum of several ρ_X. We have shown in Section 5.3.4 that parts ρ_X are stochastically independent; each additional part included decreases the MSE. Therefore, the strategy for combining several partitions $Y_1, Y_2, \cdots, Y_R$ is to decompose them into parts ρ_X. Then, we iteratively only add those parts in Y_r that are not yet included in $Y_1, \cdots, Y_{r-1}$, ensuring that the MSE decreases monotonically with every additional partition.

This can be formalized as follows: given two partitions Y_1 and $Y_2 \neq Y_1$, the density matrices ρ_{Y_1} and ρ_{Y_2} are not stochastically independent. This can be corrected by subtracting $\rho_{Y_1 \odot Y_2}$, with the partition $(Y_1 \odot Y_2)_{t,l} = (Y_1)_{t,l}(Y_2)_{t,l}/2 \in \{0, 2\}$. Hence, $Y_1 \odot Y_2$ contains all projectors $\mathcal{P}_0$ of Y_1 and Y_2. This way, ρ_{Y_1} and $\rho_{Y_2} - \rho_{Y_1 \odot Y_2}$ are stochastically independent and no part ρ_X is included twice. Hence, the MSE of

$$\rho_{Y_1 \cup Y_2} = \rho_{Y_1} + \rho_{Y_2} - \rho_{Y_1 \odot Y_2} \tag{5.34}$$

is just the sum over all parts that are not included in either Y_1 or Y_2. As a result, $\rho_{Y_1 \cup Y_2}$ yields an MSE less than or equal to the one obtained from using ρ_{Y_1} or ρ_{Y_2} alone. Note that evaluating $\rho_{Y_1 \odot Y_2}$ is expected to be no more difficult than evaluating ρ_{Y_1} or ρ_{Y_2} via Monte Carlo sampling since $\rho_{Y_1 \odot Y_2}$ contains additional projectors $\mathcal{P}_0$ compared to ρ_{Y_1} or ρ_{Y_2}.

The procedure Eq. (5.34) can be iterated to obtain $\rho_{Y_1 \cup Y_2 \cup \cdots \cup Y_R}$ at the cost of applying the sampling algorithm for all $2^R - 1$ partitions summing up to $\rho_{Y_1 \cup Y_2 \cup \cdots \cup Y_R}$.

5.5.4 Upper Bound on the Computational Cost of Combined Partitions

In this section, we discuss one possible partitioning scheme for the addition algorithm. This scheme allows us to make precise statements about the

scaling of the computational cost with accuracy based on the findings in Fig. 5.3.

One possibility for partitions capturing all parts with Hamming distance $d(X)$ up to $d(X) = \tau$ is a diamond pattern like Y_1 in Fig. 5.4 for one-dimensional systems. We generate $\tau/2$ partitions $\{Y'_r\}_{r=1}^{\tau/2}$, where Y'_r is generated by shifting Y_1 in time by $2(r-1)$, e.g., $Y'_3 = Y_2$ in Fig. 5.4. Note that this construction can also be generalized to any spatial dimension.

We proceed with showing that we capture all parts with $d(X) < \tau$. Combining all $\tau/2$ partitions, we miss all parts that are not fully contained in any of the partitions, i.e., a part X is missed if for all partitions Y'_r there is a t, l so that $X_{t,l} = 1$ and $(Y'_r)_{t,l} = 2$. Since at all t, l there are maximally two partitions with $(Y'_r)_{t,l} = 2$, a part is only missed if it has $X_{t,l} = 1$ in at least $\tau/4$ spacetime locations (t, l) (namely those (t, l) where two Y'_r have $(Y'_r)_{t,l} = 2$). As these locations are separated in spacetime, and $X_{t,l} = 1$ requires at least three neighbors to be $X_{t',l'} = 1$, one occurrence of $X_{t,l} = 1$ implies a Hamming distance of at least 4, see Appendix D.4.5. Hence, we have $X_{t,l} = 1$ in at least τ spacetime locations (t, l). Therefore, any missed part has a Hamming distance of $d(X) \geq \tau$.

The computational cost to calculate $p(a_t|a_{t-1})$ scales as $e^{\lambda\tau}$ with some λ. In total, we have to perform the sampling procedure for $2^{\tau/2} - 1$ partitions, so the total computational cost scales as

$$N_{\text{samples}}\, T\, L e^{(\lambda+\log(2)/2)\tau}. \tag{5.35}$$

We have $\tau \sim D$ and $D \sim \log(\epsilon_{\text{r}})^2$ from Eq. (5.20).

Hence, the scaling of the computational cost in the relative accuracy ϵ_{r} is upper bounded by a non-optimized combination of partitions

$$N_{\text{samples}} T L e^{(\lambda+\log(2)/2)\log(\epsilon_{\text{r}})^2}. \tag{5.36}$$

Note that from the analytical calculation we expect the decoherence sensitivity to be further suppressed in higher dimensions, so that we expect this algorithm to work better for higher dimensions. It captures the essence of the quantum corrections: small regions with decoherence sensitivity. We exploit the nature of these small regions in the following section by introducing a heuristic, far more efficient partitioning.

5.5.5 Numerical Results

We can be more efficient compared to the approach in the previous section, which required us to apply the Monte Carlo sampling procedure for $2^{\tau/2} - 1$

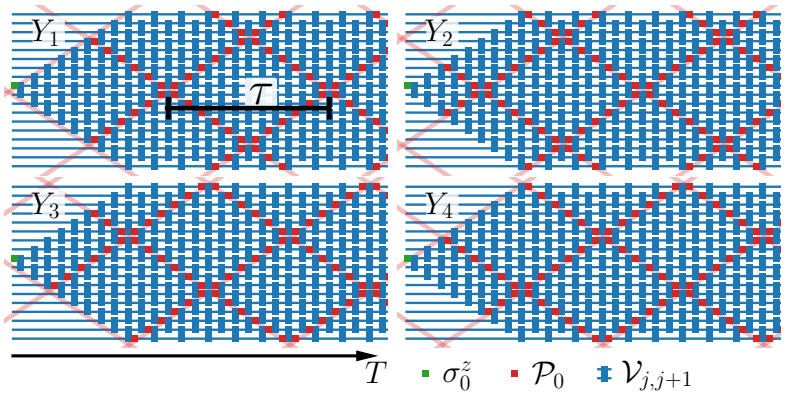

Figure 5.4: *One possibility for circuit partitions in 1+1D depicted similar to Fig. 5.1. The initial density matrix $\rho_{\text{init}} = \sigma_0^z$ (green) is evolved with the superoperators $\mathcal{V}_{j,j+1}$ (blue) consisting of the two-qubit gates $V_{j,j+1}$. We insert projections $\mathcal{P}_0$ (red) along a diamond pattern with periodicity τ and shift the pattern in time and space. Partition Y_2 is created by shifting Y_1 in time by $\tau/2$, and Y_3 and Y_4 in time by $3\tau/4$ and space by $\pm\tau/4$. These four collections are then combined via iterating Eq. (5.34).*

partitions. Here, we focus on just combining four different partitions, shown in Fig. 5.4, so that sampling has to be applied to a total of 15 partitions. Hence, we do not capture low Hamming distance parts where at least two quantum interactions in the form of a $\mathcal{P}_1$ occur on at least two lines with the same orientation, see Fig. 5.5. However, based on the analytical insights, we expect their MSE contribution to be small, the MSE is dominated by contributions with a single region of $\mathcal{P}_1$s as shown in the left panel of Fig. 5.5. This expectation is verified numerically in the following.

The performance of the algorithm in terms of the relative error ϵ_{r} is shown in Fig. 5.6. For large times, we find the relative error of the algorithm to scale roughly as $\epsilon_{\text{r}}^2 \propto e^{-0.5\tau^{0.77}}$, yielding a scaling of the computational cost in terms of the accuracy as

$$N_{\text{samples}} L T e^{\lambda' \log(\epsilon_{\text{r}})^{1.3}}, \tag{5.37}$$

which is significantly better than Eq. (5.36). For large $\tau \gtrsim 50$, four partitions appear insufficient; adding a fifth partition improves the results, Fig. 5.6 (orange dots). It appears that for $\tau \gtrsim 50$, parts with small total Hamming distance generated in multiple locations, Fig. 5.5 (right) dominate the error again rather than parts with a large Hamming distance generated by a single interaction location, Fig. 5.5 (left). These parts with distributed $\mathcal{P}_1$ can be more efficiently captured by increasing the number of partitions R

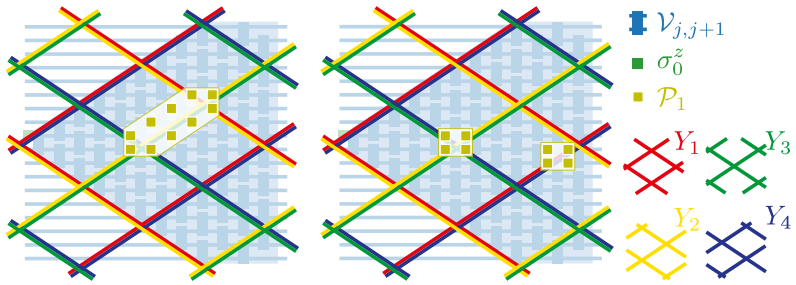

Figure 5.5: *Two examples for parts ρ_X, Eq. (5.12), which are not captured when combining the partitions shown in Fig. 5.4 via Eq. (5.34). Left: parts with one large region of off-diagonal projections $\mathcal{P}_1$ having overlap with $\mathcal{P}_0$s in all four $Y_1, \ldots, Y_4$, so that the part is not captured. Right: parts which have two separate regions of $\mathcal{P}_1$s with overlap with $\mathcal{P}_0$s in all four $Y_1, \ldots, Y_4$. We find the large regions to be the dominant contributions up to $\tau \sim 50$, Fig. 5.6 and Appendix D.5.3. Hence, the four partitions $Y_1, \ldots, Y_4$ are sufficient up to $\tau \sim 50$.*

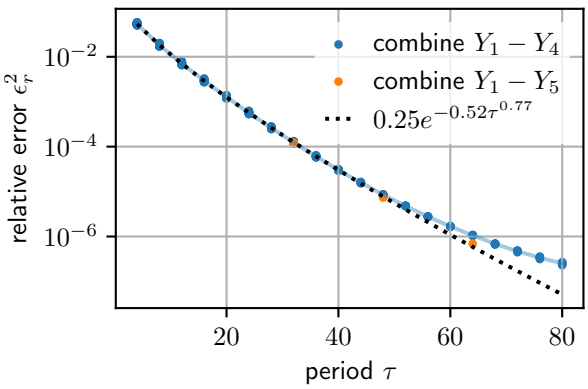

Figure 5.6: *Relative error (squared) ϵ_r^2, Eq. (5.20), for the addition algorithm with the diamond shaped partitions for different τ in the long-time-limit $T \to \infty$, restricted to T being a multiple of τ. Results for four partitions $Y_1, \ldots, Y_4$, Fig. 5.4, (blue) and an additional fifth partition Y_5 (orange), which has the diamond pattern with period $\tau/2$ and is shifted in space and time by $\tau/4$ with respect to Y_1. Fit to 4 partition data including only $\tau \leq 40$ (dotted line).*

combined, so that in practice, the number of partitions used may be adapted heuristically to τ. Further details are provided in Appendix D.5.3.

The performance of this variation of the algorithm as a function of τ confirms the picture suggested by the analytical calculation. Given a part with Hamming distance $d(X)$, the most likely parts or dominant parts in terms of the variance are indeed those where the decoherence sensitivity or $\mathcal{P}_1$s accumulate in space and time rather than dispersing, Fig. 5.5.

Note that all results presented here are calculated using an ensemble average. In practice, for individual circuits, the algorithm proposed here may only be feasible to run on current classical computers up to $\tau \approx 60$ without any further approximations.

5.6 Large Scale Experimental Results

The diagonal approximation approach is not only useful for computing correlation functions—it can also be generalized to out-of-time-ordered correlators (OTOCs), which are used to study global properties of quantum dynamics such as scrambling and chaos. Many classical approaches for computing local correlation functions do not work for OTOCs. In this section, we show that, as with correlation functions in the previous section, OTOCs in random circuits can be well approximated by a "classical" diagonal approximation that neglects interference terms and allows for efficient sampling. Unlike the correlation function case, for approximating the OTOC we sample in operator space, which is based on pairing trajectories of Heisenberg evolved opperators within the classical approximation. In the first part of this section, we argue that OTOCs can be treated similarly to correlators and generalize the formalism to OTOCs, redefining the Hamming distance counting the total number of deviations of trajectories in operator space. In the second part of this section, we provide experimental results showing that a Hamming-distance-based approximation also works for OTOCs in two dimensions and that the dephasing sensitivity is lowest in the middle of the circuit.

5.6.1 Similarity to charge transport

Probing information spreading with OTOCs is conceptually similar to probing dynamics via charge-charge correlators in charge-conserving circuits. In the case of OTOCs, we probe how Pauli strings expand under time evolution, with the identity string remaining invariant. This is similar to probing how charges spread through the system in the presence of charge conservation, with the fully polarized state being invariant. As we will show in the chapter, the OTOC can be reformulated as an expectation value with respect to time

evolved states in an operator Hilbert space, i.e., Heisenberg evolved Pauli strings.

On a more rigorous level, the dynamics probed by OTOCs have been shown to admit a description in terms of random walkers [190, 245, 246], similar to the random walker description of charge transport discussed in Section 5.4.2.

Based on the similarity to charge transport, it is natural to expect that the diagonal approximation remains effective also in this context, as we will validate experimentally in the next section.

5.6.2 Formalism

For simplicity, we consider two-dimensional circuits composed of two-qubit gates. We define

$$\mathrm{OTOC}(j,l,T) = \mathrm{Tr}[\sigma_j^z U^\dagger \sigma_l^z U \sigma_j^z U^\dagger \sigma_l^z U], \tag{5.38}$$

where $U = U(T)$ is a circuit of depth T.

Now, we can apply the Hamming distance formalism by reinterpreting operators O as states $|O)$ in an operator Hilbert space and introducing the superoperators $A\tilde{\otimes}B$ acting as

$$A\tilde{\otimes}B|O) \equiv AOB. \tag{5.39}$$

Hence, the two-site unitaries V evolving an operator is given by $V_{j,l} = W_{j,l}^\dagger \tilde{\otimes} W_{j,l}$, where $W_{j,l}$ is a random two-qubit gate. Then we can write

$$\mathrm{OTOC}(T) = (\sigma_l^z(T)|\sigma_j^z \tilde{\otimes} \sigma_j^z|\sigma_l^z(T)), \tag{5.40}$$

where the time evolution is now generated by a sequence of folded gates $V_{j,l}$ in operator space. The coherence perspective then follows by introducing operator density matrices as $|O_1)(O_2|$.

Since both the initial and final operators in the OTOC are Pauli operators, a natural basis for defining the Hamming distance is the set of Pauli strings

$$P = \prod_{j=1}^{N} \sigma_j^{\alpha_j}. \tag{5.41}$$

With this choice of basis, the single site projector onto the diagonal part of the operator-density matrix is

$$\mathcal{P}_0\left[|\sigma^\alpha)(\sigma^\beta|\right] = \frac{1}{4}\sum_{\gamma\in\{0,x,y,z\}} |\sigma^\gamma\sigma^\alpha\sigma^\gamma)(\sigma^\gamma\sigma^\beta\sigma^\gamma| = \delta_{\alpha,\beta}|\sigma^\alpha)(\sigma^\alpha|. \tag{5.42}$$

Correspondingly $\mathcal{P}_1[\rho] = \rho - \mathcal{P}_0[\rho]$ projects onto the part of the operator-density matrix with Hamming distance 1. With operators recast as states in operator Hilbert space and superoperators defined accordingly, all previous statements from the correlation function case continue to apply. In particular, the time-evolved operator density matrix can be expressed as a sum over parts, each of them contributing stochastically independently to the circuit-to-circuit variance of the OTOC. As a result, the algorithms introduced in the previous section can be directly applied.

5.6.3 Experimental Results

Finally, we evaluate the approximation accuracy of the Markov chain Monte Carlo algorithm (Section 5.5.1) for OTOCs for large, deep circuits. We compare the approximation to measurements on quantum devices with up to 95 superconducting qubits arranged in a square grid and circuits with up to 1000 gates. The gates used are of the form

$$V_{j,l} = e^{i\alpha(\cos(\beta)\sigma_j^x + \sin(\beta)\sigma_j^y)} e^{i\gamma(\cos(\delta)\sigma_l^x + \sin(\delta)\sigma_l^y)} e^{\frac{i\pi}{4}\left(\sigma_j^x\sigma_l^x + i\sigma_j^y\sigma_l^y\right) + i\vartheta\sigma_j^z\sigma_l^z}, \tag{5.43}$$

where α, γ are multiples of $\pi/8$, β and δ are uniformly distributed from 0 to 2π, and ϑ is about $\pi/10$. The two-qubit gates are applied in a repeating pattern with period four. For a given qubit, during the first iteration the two-qubit gate connects the qubit with its top neighbor, in the second with the right neighbor, in the third with the bottom neighbor, and during the fourth with its left neighbor. The same sequence of gates is applied simultaneously to all next-nearest-neighboring qubits. The results are shown in Fig. 5.7.

We find good agreement between the experimental results and the Markov chain Monte Carlo approximation. Even for such large circuits in two dimensions the purely classical approximation works quite well, see Fig. 5.7 (left). When evaluating the OTOC with respect to the fully polarized initial state of the form $\langle 0|\sigma_j^x(T)\sigma_l^z\sigma_j^x(T)|0\rangle$, we observe reduced agreement, Fig. 5.7 (center). The reason is that the OTOC with the initial state imposes weaker constraints. It only requires the two Pauli strings generated by the two $\sigma_j^x(T)$ to multiply to a Pauli string consisting of I and σ^z. The trace OTOC used before enforced the product to be the identity. This weaker condition imposed by the initial state yields additional contributions where the final two Pauli strings are not the same, and hence, are not part of the diagonal of the Pauli string operator density matrix. These contributions are sufficient to cause significant deviations between the approximation and the true result, Fig. 5.7 (center). These contributions can be more accurately accounted for by applying the partitioning algorithm, see Fig. 5.7 (right). There, we partition the circuit into two parts and apply the projection onto the diagonal on

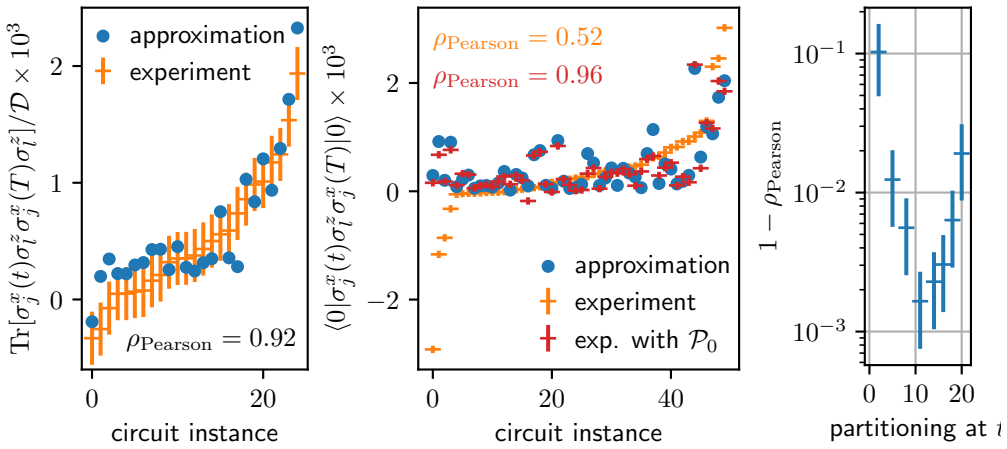

Figure 5.7: *Comparison of experimental measurement results to results of the algorithm in two spatial dimensions, left and center sorted according to the experimental measurement result. Left: Trace OTOC* $\text{Tr}[\sigma_j^z(T)\sigma_l^z\sigma_j^z(T)\sigma_l^z]/\mathcal{D}$ *measurement on* 66 *qubits with* 698 *two-qubit gates applied, i.e.,* 349 *gates per unitary, by averaging over* 900 *initial states. For this dataset,* $\alpha = \gamma = \pi/2$*. Experimental results are in good agreement with the approximate results obtained through the Markov chain Monte Carlo algorithm and sampling after every two-qubit gate. The correlation is mostly limited by the experimental statistical error. Center: State OTOC* $\langle 0|\sigma_j^z(T)\sigma_l^z\sigma_j^z(T)|0\rangle$ *measurement on* 95 *qubits with* 1000 *two-qubit gates (*500 *per unitary). Note that for this experiment* σ_j^z *consists of four* σ^z *acting on four different qubits to fit more gates into the light cone. For the state OTOC, the experimental results differ significantly from the theoretical prediction. To validate the experimental procedure, we add the projectors* $\mathcal{P}_0$ *to the circuit everywhere and measure again on the quantum device. This yields good agreement with the Monte Carlo results with* $\rho_{\text{Pearson}} = 0.96$*. Right: Correlation of state OTOC measurements and approximate results obtained by inserting projectors* $\mathcal{P}_0$ *on all sites at time step* t*, corresponding to a Monte Carlo algorithm where we only sample once at* t*. The measurements are performed on circuits with* 40 *qubits of depth* $T = 22$*. Data taken from [231].*

all sites only once at time step t. Again, we find a strong correlation between the approximation and the exact result. This confirms the effectiveness of the approximation. It works best for $t \sim T/2$, indicating that the OTOC is insensitive to dephasing in particular in the center of the circuit. This is in agreement with the expectation, as for small t, the operator $\sigma_j^x(t)$ is less scrambled, while for large t, off-diagonal contributions due to the initial state become relevant, as discussed before.

5.7 Conclusions and Outlook

We introduced a new perspective decomposing expectation values and OTOCs in terms of their classicalness as measured by the phase flip sensitivity. This is quantified with the Hamming-distance measure, which also forms the basis of a new sampling algorithm we proposed. We discussed how the noise-sensitivity reflects the system's decoherence sensitivity or the relevance of interference effects through off-diagonal density matrix elements. In that sense, we provided an analysis of the classical character of the measured quantities.

For OTOCs in Haar-random circuits or the charge-charge correlator in U(1) conserving Haar-random circuits we showed that the approximation in terms of the Hamming distance is controlled and verified the effectiveness of the classical algorithm. This demonstrates that the OTOC and two-point correlator can be predicted with high accuracy for individual instances of random circuits.

This raises important questions about quantumness of expectation values and the role of decoherence for computational complexity, highlighting the interplay between classical transport and quantum corrections. This elevates decoherence to a key concept for future studies evaluating the power of quantum computers, alongside other indicators such as entanglement and magic.

We note that the results presented in this work were built upon in Reference [231], which introduces further adaptations and variations of the Monte Carlo sampling algorithm.

Interesting future directions of research involve the extension to other observables, continuous-time evolution, non-abelian conservation laws, higher dimensional systems, the role of randomness and correlations, and the development of different variants of the presented algorithm.

Appendices

A Entanglement in the Semi-Classical Limit

A.1 Rank-K On-Site Operators

For a spin-S, one can obtain all the higher rank-$k(=0,1,\cdots,2S)$ operators using the spherical tensor decomposition. A rank-k spherical tensor, $\mathcal{O}_a^{(k)}$ has $2k+1$ components given by $a=-k,\cdots,k$ which obey the following algebra

$$\begin{aligned}[S^z,\mathcal{O}_a^{(k)}] &= a\ \mathcal{O}_a^{(k)}\\ [S^\pm,\mathcal{O}_a^{(k)}] &= \sqrt{(k\mp a)(k\pm a+1)}\ \mathcal{O}_{a\pm1}^{(k)}\end{aligned} \tag{A.1}$$

where $S^\pm=(S^x+iS^y)$ and for brevity we have suppressed the site index. Taking the highest weight of a rank-k operator as

$$\mathcal{O}_{+k}^{(k)} = \left(S^+\right)^k \tag{A.2}$$

and using the above algebra, we can get the explicit expression for the different operators.

A.1.1 $k=1$: Dipole Operators

$$\mathcal{O}_{\pm1}^{(1)} = S^x \pm iS^y, \qquad \mathcal{Q}_0^{(1)} = S^z \tag{A.3}$$

A.1.2 $k=2$: Quadrupole Operators

$$\begin{aligned}\mathcal{O}_{\pm2}^{(2)} &= \mathcal{Q}^{xx}-\mathcal{Q}^{yy}\pm i2\mathcal{Q}^{xy}\\ \mathcal{O}_{\pm1}^{(2)} &= \mp2(\mathcal{Q}^{xz}\pm i\mathcal{Q}^{yz})\\ \mathcal{O}_0^{(2)} &= \sqrt{6}\mathcal{Q}^{zz}\end{aligned} \tag{A.4}$$

where $\mathcal{Q}^{\alpha\beta}$ is given by Eq. 2.9. Higher rank operators can be obtained similarly.

Noticeably, the matrix elements of the multipole operators generically have an explicit dependence on the value of S. If different rank operators are present in the Hamiltonian (such as Eq. (2.17)) then the elements of the two-spin Hamiltonian $(2S+1)^2\times(2S+1)^2$ matrix (in the product Ising basis $|m_1;m_2\rangle$) are of dissimilar magnitudes due to difference is scaling with S. Thus in the limit of $S\to\infty$, high rank operators can dominate due to their faster scaling with S.

A possible alternative Large-S limit is obtained by normalizing the above operators such that

$$\mathrm{Tr}\left[\left(\mathcal{O}_a^{(k)}\right)^\dagger \cdot \mathcal{O}_a^{(k)}\right] = 1 \tag{A.5}$$

whence the elements of the Hamiltonian matrix are normalized and adding higher moment (normalized) operators lead to increasing density (i.e. decreasing sparsity) of non-zero elements of the Hamiltonian matrix.

A.2 The Bloch States

The Bloch basis [283] is defined by the states $|\hat{\Omega}\rangle$ with $\hat{\Omega} = (\theta, \varphi)$

$$|\hat{\Omega}_S\rangle = \sum_M \sqrt{{}^{2S}C_{M+S}} \left[\cos\frac{\theta}{2}\right]^{S+M} \left[\sin\frac{\theta}{2}\right]^{S-M} e^{i(S-M)\varphi}|M\rangle \tag{A.6}$$

which is obtained by starting with the maximally polarized state $|S, m = +S\rangle$ and rotating it on the Bloch sphere to the direction

$$\hat{\mathbf{n}} = [\sin\theta\cos\phi, \sin\theta\sin\phi, \cos\theta]. \tag{A.7}$$

They form an over-complete basis. For such coherent/Bloch states the fractional fluctuation in the length of each spin-component :

$$\frac{\langle\hat{\Omega}|S_\alpha^2|\hat{\Omega}\rangle - \langle\hat{\Omega}|S_\alpha|\hat{\Omega}\rangle^2}{S^2} \tag{A.8}$$

goes to zero as $S \to \infty$ as $\sim 1/S$ for $\alpha = x, y, z$ (irrespective of the commutation relations) such that $\langle f(S_\alpha)\rangle = f(\langle S_\alpha\rangle)$. These give rise to states with maximal dipole moment, i.e.,

$$\langle\hat{\Omega}|\mathbf{S}\cdot\hat{\mathbf{n}}|\hat{\Omega}\rangle = S \tag{A.9}$$

For these states, the higher rank operators are given by moments of the dipole, i.e., the quadrupole operators (Eq. 2.9) for $S = 1$ are

$$\begin{aligned}\langle\Omega|\mathcal{Q}^{\alpha\alpha}|\Omega\rangle &= \frac{1}{6}\left(3m_\alpha^2 - 1\right) \qquad \alpha = x, y, z \\ \langle\Omega|\mathcal{Q}^{\alpha\beta}|\Omega\rangle &= \frac{1}{2}m_\alpha m_\beta \qquad \alpha \neq \beta = x, y, z\end{aligned} \tag{A.10}$$

where $m_\alpha = \langle\Omega|S^\alpha|\Omega\rangle$. Similar expressions can be obtained for $S > 1$ as well as higher rank operators. Thus, the expectation value of the higher rank operators are constrained by that of the dipole (rank-1) operator.

For higher spins, we can then construct states where the first $(k-1)$th moments are identically equal to zero while the kth moment onwards are non-zero (note that if the kth moment is non-zero then all $m(>k)$th moments are generically non-zero). To this end, for the quadrupolar states of spin $S=1$, we have [284]

$$|\mathbf{d}\rangle = \sum_{a=1,2,3} d_a |d_a\rangle, \tag{A.11}$$

where $d_a = u_a + iv_a$ with $u_a, v_a \in \mathbb{R}$, $\mathbf{u}\cdot\mathbf{u} + \mathbf{v}\cdot\mathbf{v} = 1$ for normalization and $\mathbf{u}\cdot\mathbf{v} = 0$ for the global phase, while

$$|d_1\rangle = i\frac{|1\rangle - |-1\rangle}{\sqrt{2}}, \quad |d_2\rangle = \frac{|1\rangle + |-1\rangle}{\sqrt{2}}, \quad |d_3\rangle = -i|0\rangle. \tag{A.12}$$

The pure quadrupolar state is obtained [284] by having (1) $\mathbf{u}=0$, (2) $\mathbf{v}=0$, or (3) $\mathbf{u}=\mathbf{v}$ whence the dipole operator vanishes identically while

$$\langle \mathbf{u},\mathbf{v}|\mathcal{Q}^{ab}|\mathbf{u},\mathbf{v}\rangle = \frac{2}{3}\delta_{ab} - (u_a u_b + v_a v_b). \tag{A.13}$$

A more systematic way to generate the pure quadrupolar states for the integer spins is using the Bloch state representation similar to that of the dipolar states (Eq. A.6), but starting with $|S, m=0\rangle$, i.e.,

$$|S, m=0\rangle = \frac{(2S+1)}{2^S S!}\sqrt{(2S)!}\int d\hat{\mathbf{\Omega}}\ (\sin\theta)^S\ |\hat{\mathbf{\Omega}}_S\rangle \tag{A.14}$$

On rotation, the generic quadrupolar state for integer spins is obtained as

$$|\mathcal{Q}_S\rangle = \sum_{q=0}^{S}\sum_{m=-q|+2}^{q} \frac{(-1)^{(q+m)/2}}{2^q}(\cos\theta)^{S-q}(\sin\theta)^q\ e^{im\phi} \times \frac{\sqrt{(S+m)!(S-m)!}}{(S-q)!(q+m)/2!(q-m)/2!}|S,m\rangle. \tag{A.15}$$

These states generically have $\langle\mathcal{Q}_S|S^\alpha|\mathcal{Q}_S\rangle = 0$ and reduces to

$$|\mathcal{Q}_1\rangle = -\cos\theta|d_3\rangle - \sin\theta\cos\phi|d_1\rangle + \sin\theta\sin\phi|d_2\rangle \tag{A.16}$$

for $S=1$ and

$$\begin{aligned}|\mathcal{Q}_2\rangle = &\left(1-\frac{3}{2}\sin^2\theta\right)|0\rangle \\ &+\sqrt{\frac{3}{4}}\sin(2\theta)\left\{\cos\phi\left(\frac{|-1\rangle-|1\rangle}{\sqrt{2}}\right)+\sin\phi\left(-i\frac{|-1\rangle+|1\rangle}{\sqrt{2}}\right)\right\} \\ &+\sqrt{\frac{3}{4}}\sin^2\theta\left\{\cos(2\phi)\left(\frac{|-2\rangle+|2\rangle}{\sqrt{2}}\right)+\sin(2\phi)\left(-i\frac{|-2\rangle-|2\rangle}{\sqrt{2}}\right)\right\}\end{aligned} \tag{A.17}$$

for $S = 2$. For generic spin-S, the expectation value of various components of the quadrupolar tensor is given by

$$\langle \mathcal{Q}^{xx} \rangle = \frac{S(S+1)}{2} \left(\frac{1}{4} \left\{ 3 + \cos(2\theta) - 2\cos(2\phi)\sin^2\theta \right\} - 2/3 \right) \tag{A.18}$$

$$\langle \mathcal{Q}^{yy} \rangle = \frac{S(S+1)}{2} \left(\frac{1}{4} \left\{ 3 + \cos(2\theta) + 2\cos(2\phi)\sin^2\theta \right\} - 2/3 \right) \tag{A.19}$$

$$\langle \mathcal{Q}^{zz} \rangle = \frac{S(S+1)}{2} \left(\sin^2\theta - 2/3 \right) \tag{A.20}$$

$$\langle \mathcal{Q}^{xy} \rangle = \frac{S(S+1)}{2} \sin^2\theta \sin(2\phi) \tag{A.21}$$

$$\langle \mathcal{Q}^{xz} \rangle = -\frac{S(S+1)}{2} \cos\phi \sin(2\theta) \tag{A.22}$$

$$\langle \mathcal{Q}^{yz} \rangle = \frac{S(S+1)}{2} \sin\phi \sin(2\theta) \tag{A.23}$$

which shows that the expectation values scale as $\sim S^2$. However unlike the Bloch states,

$$\frac{\langle (\mathcal{Q}^{\alpha\beta})^2 \rangle - (\langle \mathcal{Q}^{\alpha\beta} \rangle)^2}{S^4} \neq 0 \tag{A.24}$$

for all $\alpha, \beta = x, y, z$ even in the large S limit which can be explicitly checked easily for the $\theta = 0$ in Eq. A.15. Thus finite fluctuations in expectation value of on-site operators can survive even in the $S \to \infty$ limit for such quadrupolar states.

A.3 Projection Protocol

A.3.1 Convergence for Bloch States

The projection protocol works as follows. We start with an initial Bloch state $|\Omega_1\rangle|\Omega_2\rangle$. Then, we time evolve this state for time τ and measure S_i^α, which yields

$$\langle S_i^\alpha(\tau) \rangle = \langle S_i^\alpha \rangle + i\langle [\mathcal{H}^{(1)}, S_i^\alpha] \rangle \tau + O(\tau^2). \tag{A.25}$$

We use

$$\begin{aligned} \langle [\mathcal{H}^{(1)}, S_1^\alpha] \rangle &= \sum_\beta h_{1,\beta} \langle [S_1^\beta, S_1^\alpha] \rangle + \sum_{\beta,\gamma} \mathcal{J}_{\beta\gamma} \langle [S_1^\beta, S_1^\alpha] S_2^\gamma \rangle \\ &= \sum_{\beta,\delta} h_{1,\beta} i\epsilon^{\beta\alpha\delta} \langle S_1^\delta \rangle + \sum_{\beta,\gamma,\delta} \mathcal{J}_{\beta\gamma} i\epsilon^{\beta\alpha\delta} \langle S_1^\delta S_2^\gamma \rangle \\ &= \sum_{\beta,\delta} h_{1,\beta} i\epsilon^{\beta\alpha\delta} \langle S_1^\delta \rangle + \sum_{\beta,\gamma,\delta} \mathcal{J}_{\beta\gamma} i\epsilon^{\beta\alpha\delta} \langle S_1^\delta \rangle \langle S_2^\gamma \rangle, \end{aligned} \tag{A.26}$$

where we used in the last step that the expectation value $\langle\cdot\rangle$ is taken with respect to a product state. Now we use that $\langle S_\alpha^i\rangle = M_i^\alpha(0)$ so that

$$\langle[\mathcal{H}^{(1)}, S_1^\alpha]\rangle = \sum_{\beta,\delta} h_{1,\beta} i\epsilon^{\beta\alpha\delta} M_1^\delta(0) + \sum_{\beta,\gamma,\delta} \mathcal{J}_{\beta\gamma} i\epsilon^{\beta\alpha\delta} M_1^\delta(0) M_2^\gamma(0) \tag{A.27}$$

$$= -i \frac{\mathrm{d}}{\mathrm{d}t} M_1^\alpha(t)\Big|_{t=0}, \tag{A.28}$$

where we used that $M_i^\alpha(t)$ follows the classical equations of motion Eq. (A.36) in the last step. Hence, the quantum observables follow the classical values up to $O(\tau^2)$

$$\langle S_i^\alpha(\tau)\rangle = M_i^\alpha(\tau) + O(\tau^2). \tag{A.29}$$

After time τ, we initialize our states again to Bloch states in agreement with the expectation values $\langle S_i^\alpha(\tau)\rangle = M_i^\alpha(\tau) + O(\tau^2)$. Therefore, after time τ, the state is initialized to a product Bloch state agreeing with the classical equations of motion up to an error τ^2. We can then iterate the argument: We time evolve the reinitialized product Bloch state at time τ till time 2τ, which yields another error of order τ^2. Hence, for a time evolution of time t, we expect an error of order $t/\tau \times \tau^2 = t\tau$, which we also found numerically in Fig. 2.16. In principle, this analysis is also expected to hold for quadrupolar states for $t \to 0, \tau \to 0$. The result for quadrupolar presented in Fig. 2.17 may converge to this scaling for $t \to 0$ and $\tau \to 0$ or follow from numerical errors, as discussed in the next chapter.

A.4 Stability

As pointed out in the main text, we find the projection protocol to be unstable for quadrupolar states. Hence, we do not present averaged data in the main text, rather than an exemplary case. In Fig. A.1, we present the numerical results for the same case studied in the main text. Instead of the deviations, we show the values of the classical equations of motions and compare them to the results obtained via the projection protocol for the operators $S_i^\alpha S_i^\alpha$. The classical trajectories agree for a long time with the projected ones, however, at around $t = 1$ the values for the right spin get close to 1 or 0. Solving Eq. (A.23) for θ and ϕ using such values may yield instabilities, and could return the wrong values for θ, ϕ yielding a deviation of the trajectories.

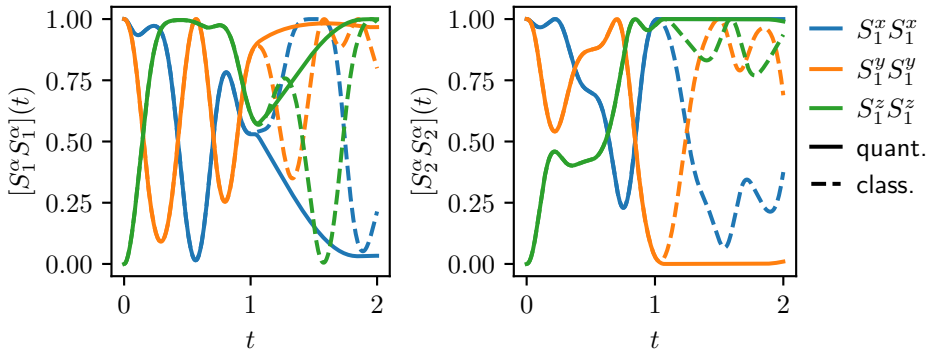

Figure A.1: *The same setup like in Fig. 2.17 but instead of deviations, we compare the classical trajectories (dashed) to the results of the projection protocol (solid). This reveals a numerical instability at around $t \sim 1$, after which the right spin does not evolve anymore in the projection protocol.*

A.5 Characterization of the Random Hamiltonians

A.5.1 The Level-Spacing Statistics

A well known method of characterization of RMTs is via their level-spacing statistics [285, 286] given by the distribution of of the (folded) ratio of successive level-spacing, r_n, defined as

$$r_n = \text{Min}\left(\frac{s_n}{s_{n-1}}, \frac{s_{n-1}}{s_n}\right), \tag{A.30}$$

where $s_n = E_{n+1} - E_n$ is the difference of successive Eigenvalues of the RMT arranged in ascending order. These distributions are shown in Fig. A.2. It is clear from the level-spacing statistics that with increasing S, the level-spacing statistics approaches the GOE (GUE) on increasing the rank of the operators present in the two-spin Hamiltonian in presence (absence) of time-reversal breaking terms. Since we have mostly considered $\mathcal{H}^{(1)}$, Eq. (2.18), in the main text, we show the level spacing statistics for $\mathcal{H}^{(1)}$. For this Hamiltonian we find that with increasing S, the results start deviating from GUE/GOE limit for spin-3/2 onwards which allow for even higher rank operators.

This is further emphasized in Fig. A.3 where we plot the average level spacing ratio, $\langle r_n \rangle$, with spin size. It is clear that for $S = 1/2$ the level spacing ratio for $\mathcal{H}^{(1)}$ without (with) Zeeman field is in agreement with GOE (GUE). However for higher spins the deviation as referred to above becomes manifest.

The same holds true for other quantities, such as the distribution of eigenvalues E, i.e., the density of states. In Fig. 2.4 we showed that it does not

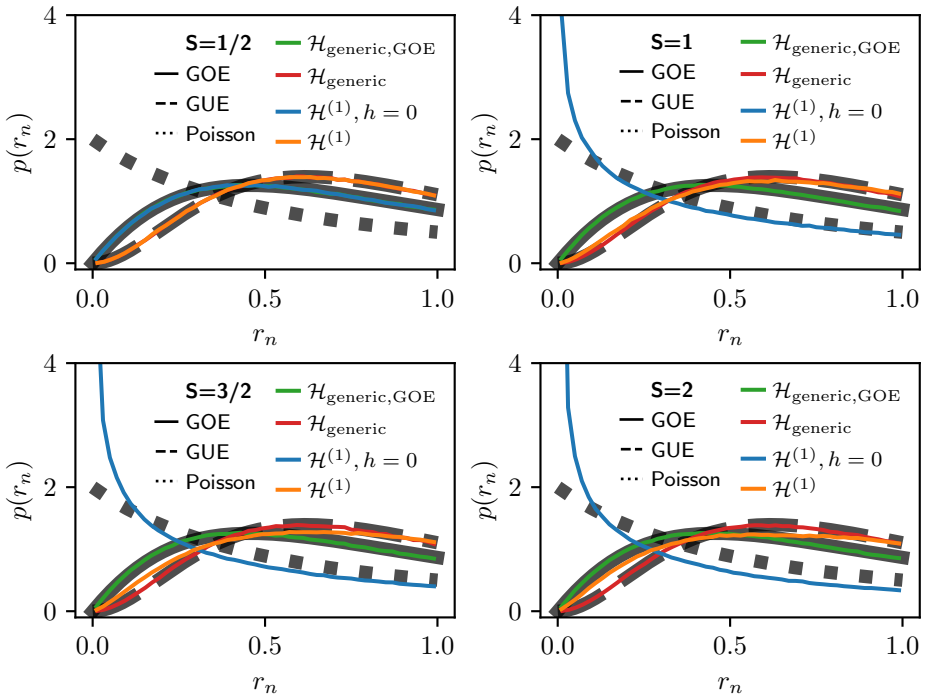

Figure A.2: *The distribution of (folded) level-spacing ratio, r_n (Eq. A.30) for $S = 1/2, 1, 3/2, 2$ for random spin Hamiltonians $\mathcal{H}^{(1)}$ (Eq. (2.18) with and without random Zeeman field), the full Hamiltonian $\mathcal{H}_{\text{generic}}$ from Eq. (2.18) and the full Hamiltonian restricted to $k_1 + k_2$ being even $\mathcal{H}_{\text{generic,GOE}}$ (similarly one could generate the GOE ensemble by only keeping $\mathcal{O}^{(k_1)}_{1,\alpha}\mathcal{O}^{(k_1)}_{1,\alpha} \in \mathbb{R}^{(2S+1)^2\times(2S+1)^2}$. They are compared with GOE, GUE and Poisson distributions [286]. The data is obtained from $10^6, 3\cdot 10^5, 15\cdot 10^4, 10^5$ instances for $S = 1/2, 1, 3/2, 2$, respectively, and all random numbers are generated from Normal Gaussian distributions $J^{(k_1k_2)}_{\alpha\beta} \sim \mathcal{N}(0, 1/|\mathcal{O}^{(k_1)}_{1,\alpha}|/|\mathcal{O}^{(k_1)}_{1,\alpha}|)$, where $|\mathcal{O}^{(k_1)}_{i,\alpha}|$ is the trace norm.*

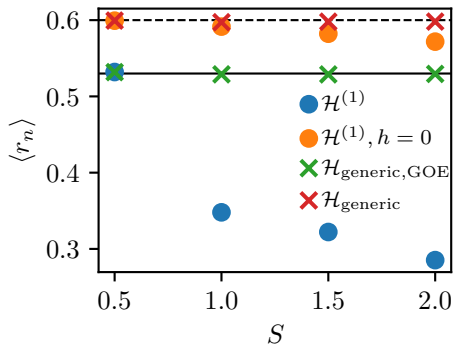

Figure A.3: *The average level spacing ratio, $\langle r_n \rangle$ (Eq. A.30) as a function of spin size, S. For GOE and GUE the average are given by 0.53 and 0.6 respectively [286].*

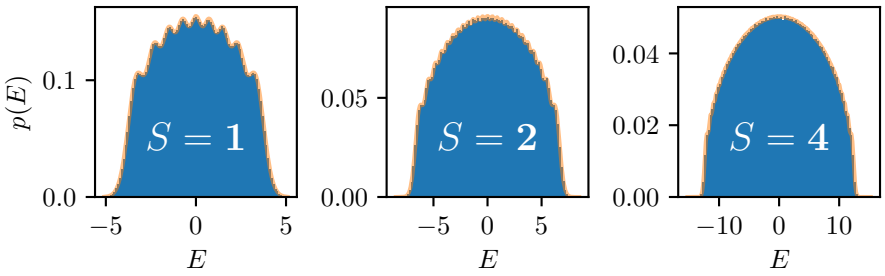

Figure A.4: *Density of states $p(E)$ for $\mathcal{H}_{\text{generic}}$ for different spin sizes. The results are compared to the RMT prediction (orange), as specified in the main text.*

agree with the random matrix prediction for large S for the Hamiltonians $\mathcal{H}^{(1)}$ with $h = 0$. In Fig. A.4 we show that for $\mathcal{H}_{\text{generic}}$ from Eq. (2.14) with $J_{\alpha\beta}^{(k_1k_2)} \sim \mathcal{N}(0, 1/|\mathcal{O}_{1,\alpha}^{(k_1)}|/|\mathcal{O}_{1,\alpha}^{(k_1)}|)$, the spectral density coincides with RMT, as expected.

The RMT result for the density of states for random matrices of finite sizes N can be found in Ref. [287, Eq. (16),(35)]. It reads for the GUE

$$R_1(E) = K_N(E,E) = \left\langle \sum_k \delta(E - E_k) \right\rangle \overset{N\to\infty}{\to} \frac{1}{2\pi}\sqrt{4N - E^2}. \tag{A.31}$$

Hence, the density of states is $p(E) = R_1(E)/Z$, where Z is the norm $Z = \int R_1(E)\mathrm{d}E = N$.

A.6 Evolution of the Weights of the Bloch States under the Ferromagnetic Heisenberg Hamiltonian

In section 2.5.1, we studied the growth of the entanglement entropy of Bloch states. Here we plot the weights of the wave function with time. This is shown in Fig. A.5 for $S = 15$ and initial product Bloch state $|\phi = \pi, \theta = 0\rangle|\phi = \pi, \theta = \pi\rangle$.

A.7 Classical and Quantum Dynamics of Local Observables

Consider the generic Hamiltonian from Eq. (2.14).

$$H = \sum_{k_1,k_2=0}^{2S} \sum_{m_1=-k_1}^{k_1} \sum_{m_2=-k_2}^{k_2} J_{m_1m_2}^{k_1k_2} \mathcal{O}_m^{k_1} \mathcal{O}_n^{k_2}. \tag{A.32}$$

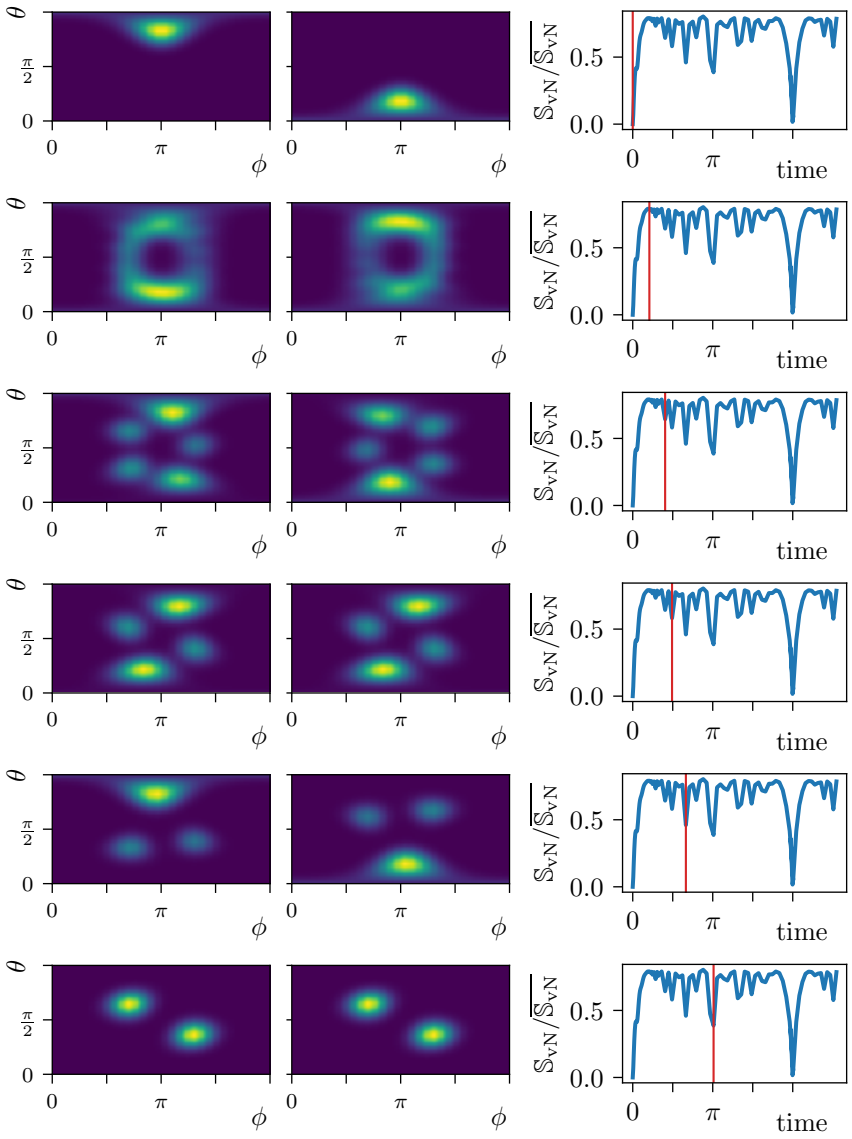

Figure A.5: *Results for the Husimi Q function $Q(\theta, \phi) = \langle \theta, \phi | \rho_{1,2} | \theta, \phi \rangle$ for the reduced density matrices of the two spins ρ_1 (left) and ρ_2 (center), where $|\theta, \phi\rangle$ are Bloch states. Different rows corresppond to different times, marked with the red line in the right panel. We show the results alongside the entanglement (right). The two spins with $S = 15$ are initialized to Bloch states with an included angle of $2\pi/3$ and time evolved with an antiferromagnetic Heisenberg Hamiltonian. This shows how the dips in entanglement can be related to highly non-uniform spin configurations with clusters.*

The Heisenberg equations of motion are given by (let us concentrate on site 1)

$$i\frac{d\mathcal{O}_{1,\alpha}^{(\tilde{k}_1)}}{dt} = \left[\mathcal{O}_{1,\alpha}^{(\tilde{k}_1)}, H\right] = \sum_{k_1,k_2=0}^{2S}\sum_{\beta=-k_1}^{k_1}\sum_{\gamma=-k_2}^{k_2}\mathcal{J}_{\beta\gamma}^{(k_1k_2)}\mathcal{O}_{2,\gamma}^{(k_2)}\left[\mathcal{O}_{1,\beta}^{(k_1)}, \mathcal{O}_{1,\alpha}^{(\tilde{k}_1)}\right] \quad \text{(A.33)}$$

$$= \sum_{k_1,k_2=0}^{2S}\sum_{p_1=|k_1-\tilde{k}_1|}^{(k_1+\tilde{k}_1)(\text{mod } 2S)}\sum_{\beta=-k_1}^{k_1}\sum_{q_1=-p_1}^{p_1}\sum_{\gamma=-k_2}^{k_2}\mathcal{J}_{\beta\gamma}^{(k_1k_2)}f_{q_1;\beta\alpha}^{p_1;k_1,\tilde{k}_1}\mathcal{O}_{1,q_1}^{(p_1)}\mathcal{O}_{2,\gamma}^{(k_2)} \quad \text{(A.34)}$$

where $f_{q_1;\beta\alpha}^{k_3;k_1,\tilde{k}_1}$ are structure constants that can be obtained from the Clebsch-Gordon coefficients of SU(2) algebra. The evolution of the expectation values is then given by the generalized Ehrenfest equation of the form

$$i\frac{d\langle\mathcal{O}_{1,\alpha}^{(\tilde{k}_1)}\rangle}{dt} = \sum_{k_1,k_2=0}^{2S}\sum_{p_1=|k_1-\tilde{k}_1|}^{(k_1+\tilde{k}_1)(\text{mod } 2S)}\sum_{\beta=-k_1}^{k_1}\sum_{q_1=-p_1}^{p_1}\sum_{\gamma=-k_2}^{k_2}\mathcal{J}_{\beta\gamma}^{(k_1k_2)}f_{q_1;\beta\alpha}^{p_1;k_1,\tilde{k}_1}\langle\mathcal{O}_{1,q_1}^{(p_1)}\mathcal{O}_{2,\gamma}^{(k_2)}\rangle$$

$$= \sum_{k_1,k_2=0}^{2S}\sum_{p_1=|k_1-\tilde{k}_1|}^{(k_1+\tilde{k}_1)(\text{mod } 2S)}\sum_{\beta=-k_1}^{k_1}\sum_{q_1=-p_1}^{p_1}\sum_{\gamma=-k_2}^{k_2}$$
$$\mathcal{J}_{\beta\gamma}^{(k_1k_2)}f_{q_1;\beta\alpha}^{p_1;k_1,\tilde{k}_1}\left[\langle\mathcal{O}_{1,q_1}^{(p_1)}\rangle\langle\mathcal{O}_{2,\gamma}^{(k_2)}\rangle + \left(\langle\mathcal{O}_{1,q_1}^{(p_1)}\mathcal{O}_{2,\gamma}^{(k_2)}\rangle - \langle\mathcal{O}_{1,q_1}^{(p_1)}\rangle\langle\mathcal{O}_{2,\gamma}^{(k_2)}\rangle\right)\right]. \quad \text{(A.35)}$$

The second term in the bracket on the RHS of the final expression follows from the deviation of the (time-evolved) state from the product state. On ignoring this term, we obtain the *classical* equation of motion which is given by

$$i\frac{d\langle\mathcal{O}_{n_1}^{\tilde{k}_1}\rangle}{dt} = = \sum_{k_1,k_2=0}^{2S}\sum_{p_1=|k_1-\tilde{k}_1|}^{(k_1+\tilde{k}_1)(mod\ 2S)}\sum_{m_1=-k_1}^{k_1}\sum_{q_1=-p_1}^{p_1}\sum_{m_2-k_2}^{k_2}J_{m_1m_2}^{k_1k_2}f_{q_1;m_1n_1}^{k_3;k_1,\tilde{k}_1}\langle\mathcal{O}_{q_1}^{p_1}\rangle\langle\mathcal{O}_{m_2}^{k_2}\rangle. \quad \text{(A.36)}$$

B Krylov Complexity

B.1 Dual-Unitary Operators

In this section we state briefly the construction of a dual-unitary circuit for $q = 2$, following [63]. The circuit unitary U is created by applying dual-unitary two qubit gates $U_{2j-1,2j}$ in a brickwork pattern. Each gate is drawn from the ensemble of gates

$$V_{j,j'} = e^{i\pi(\sigma_j^x\sigma_{j'}^x+\sigma_j^y\sigma_{j'}^y)/4+iJ\sigma_j^x\sigma_{j'}^x} \tag{B.1}$$

$$U_{j,j'} = u_j v_{j'} V_{j,j'} u'_j v'_{j'} \tag{B.2}$$

with J uniformly distributed in $[0, 2\pi)$ and u, v, u', v' being Haar random single qubit gates. An explicit form for dual-unitary gates for larger q is not required in this work.

B.2 Unitary Superoperator Structure

In this appendix we derive the structure of unitary superoperator $\mathcal{U}$ as stated in the main text [Eq. (3.14)],

$$\mathcal{U}_{mn} = (\mathcal{O}_m|\mathcal{U}|\mathcal{O}_n) = \begin{cases} 0 & \text{if} \quad m > n+1\,, \\ b_m & \text{if} \quad m = n+1\,, \\ a_m\, c_n/c_m & \text{if} \quad m < n+1\,, \end{cases}$$

with

$$a_n = (\mathcal{O}_n|\mathcal{U}|\mathcal{O}_n), \tag{B.3}$$

$$b_n = (\mathcal{O}_n|\mathcal{U}|\mathcal{O}_{n-1}), \tag{B.4}$$

$$c_n = (\mathcal{O}_0|\mathcal{U}|\mathcal{O}_n). \tag{B.5}$$

We start by showing that Gram-Schmidt orthonormalization yields $(O_t|\mathcal{O}_n) = 0$ for each $t < n$. In Eq. (3.12) we define the lower triangular matrix α with elements α_{nt}. As all $|\mathcal{O}_n)$ have to be linear independent, we need $\alpha_{nn} \neq 0$. Hence, the inverse matrix $\beta = \alpha^{-1}$ exists and is also a lower triangular matrix. We can write

$$|O_t) = \sum_{n=0}^{t} \beta_{t,n}|\mathcal{O}_n)\,, \tag{B.6}$$

as stated in Eq. (3.13) in the main text. Using the orthonormality of $|\mathcal{O}_n)$, the statement $(O_t|\mathcal{O}_n) = 0$ for $t < n$ follows immediately, since $|O_n)$ can be

written as a linear combination of $|\mathcal{O}_{m\leq n})$. Note that β is recursively the inverse of α: The $l \times l$ reduced matrix β is the inverse of the $l \times l$ reduced matrix α.

We hence find that $\mathcal{U}_{mn}$ is upper triangular, since for $m > n+1$,

$$\mathcal{U}_{mn} = (\mathcal{O}_m|\mathcal{U}|\mathcal{O}_n) = \sum_{t=0}^{n} \alpha_{n,t}(\mathcal{O}_m|O_{t+1}) = 0\,, \tag{B.7}$$

using that $(\mathcal{O}_m|O_{t+1}) = 0$ since $t+1 \leq n+1 < m$.

For $m \leq n$ we can write

$$\begin{aligned}
\mathcal{U}_{mn} = (\mathcal{O}_m|\mathcal{U}|\mathcal{O}_n) &= \sum_{t=0}^{m} \alpha^*_{m,t}(O_t|\mathcal{U}|\mathcal{O}_n) \\
&= \alpha^*_{m,0}(O_0|\mathcal{U}|\mathcal{O}_n) + \sum_{t=1}^{m} \alpha^*_{m,t}(O_t|\mathcal{U}|\mathcal{O}_n) \\
&= \alpha^*_{m,0}\mathcal{U}_{0n} + \sum_{t=1}^{m} \alpha^*_{m,t}(O_{t-1}|\mathcal{O}_n) \\
&= \alpha^*_{m,0}\mathcal{U}_{0n}
\end{aligned} \tag{B.8}$$

using the orthonormality $(O_{t-1}|\mathcal{O}_n) = 0$ for $1 \leq t \leq n$ and that $|\mathcal{O}_0) = |O_0)$. As such, all matrix elements for $m \leq n$ factorize, where we can already identify $c_n = \mathcal{U}_{0n}$. For the remaining factor we can write $a_m = \mathcal{U}_{mm} = \alpha^*_{m,0}\mathcal{U}_{0m} = \alpha^*_{m,0}c_m$, resulting in the presented expression $\mathcal{U}_{mn} = a_m c_n / c_m$.

The remaining nontrivial matrix elements are those with $m = n+1$, which can not be simplified and which we denote as $b_n = \mathcal{U}_{n+1,n}$.

Due to the unitarity these sequences fulfill

$$1 = \sum_{m=0}^{n+1} |\mathcal{U}_{m,n}|^2 = |b_n|^2 + |c_n|^2 \sum_{m=0}^{n} |a_m/c_m|^2 \tag{B.9}$$

for all n, which we can rewrite as

$$1 - |b_n|^2 = |c_n|^2 \sum_{m=0}^{n} |a_m/c_m|^2\,, \tag{B.10}$$

indicating how the lower diagonal elements are bounded by the remaining matrix elements.

B.3 Orthonormal Polynomials on the Unit Circle

In this appendix we review some properties of orthonormal polynomials on the unit circle that will serve to highlight the connection between the Krylov operators and the Fourier modes of the spectral function. Following Eq. (3.24), there is a direct correspondence between the Krylov operators and polynomials on the unit circle $p_n(\omega)$, defined as

$$p_n(\omega) = \sum_{k=0}^{n} \alpha_{n,k}\, e^{ik\omega}\,, \tag{B.11}$$

with the corresponding Krylov operator constructed as $|\mathcal{O}_n) = \sum_{k=0}^{n} \alpha_{n,k}|O_k)$. The orthonormality of the Krylov operators translates to the orthonormality of these functions provided we use the spectral function as weight function,

$$\int_0^{2\pi} \mathrm{d}\omega\, |f_O(\omega)|^2 p_n(\omega) p_m^*(\omega) = \delta_{mn}\,. \tag{B.12}$$

While in the main text the Krylov operators were constructed through a Gram-Schmidt procedure, an explicit expression for these polynomials can also be obtained following standard results from, e.g., Ref. [133]. A similar approach for Krylov operators constructed from a Liouvillian was presented in Ref. [132]. Again writing the Fourier modes of the spectral function as

$$S_n = \int_0^{2\pi} \mathrm{d}\omega\, |f_O(\omega)|^2 e^{in\omega}\,, \tag{B.13}$$

we consider Toeplitz matrices of the form

$$T_n = \begin{pmatrix} S_0 & S_1 & S_2 & \cdots & S_n \\ S_{-1} & S_0 & S_1 & \cdots & S_{n-1} \\ S_{-2} & S_{-1} & S_0 & \cdots & S_{n-2} \\ \vdots & \vdots & \vdots & \ddots & \vdots \\ S_{-n+1} & S_{-n+2} & S_{-n+3} & \cdots & S_1 \\ S_{-n} & S_{-n+1} & S_{-n+2} & \cdots & S_0 \end{pmatrix}, \tag{B.14}$$

where $(T_n)_{i,j} = S_{j-i}$. Since the spectral function has even parity we could also write $S_n = S_{-n}$, but the following results are more transparent by keeping the distinction between S_n and S_{-n}. The orthonormal polynomials can then

be directly expressed in determinant form as

$$p_n(\omega) = \frac{1}{\sqrt{|T_n T_{n-1}|}} \begin{vmatrix} S_0 & S_1 & S_2 & \dots & S_n \\ S_{-1} & S_0 & S_1 & \dots & S_{n-1} \\ S_{-2} & S_{-1} & S_0 & \dots & S_{n-2} \\ \vdots & \vdots & \vdots & \ddots & \vdots \\ S_{-n+1} & S_{-n+2} & S_{-n+3} & \dots & S_1 \\ 1 & e^{i\omega} & e^{2i\omega} & \dots & e^{in\omega} \end{vmatrix} . \tag{B.15}$$

This expression is to be contrasted with the Krylov operators for Liouvillian dynamics, where the corresponding matrices are Hankel matrices composed out of the different moments of the spectral functions [132].

As such, all orthonormal polynomials can be expressed through Toeplitz matrices, and the expansion coefficients $\alpha_{n,k}$ can be analytically obtained as the corresponding minor from these matrices. The inverse transformation, writing

$$e^{ik\omega} = \sum_{n=0}^{k} \beta_{k,n} p_n(\omega) \,, \tag{B.16}$$

can also be obtained from a factorization of the Toeplitz matrices. Writing

$$\begin{aligned} (T_n)_{k,\ell} = S_{\ell-k} &= \int_0^{2\pi} \mathrm{d}\omega \, |f_O(\omega)|^2 e^{i(\ell-k)\omega} \\ &= \int_0^{2\pi} \mathrm{d}\omega \, |f_O(\omega)|^2 \left(\sum_{m=0}^{k} \beta^*_{k,m} p^*_m(\omega) \right) \left(\sum_{n=0}^{\ell} \beta_{\ell,n} p_n(\omega) \right) \\ &= \sum_{m=0}^{\min(k,\ell)} \beta^*_{k,m} \beta_{\ell,m} \,, \end{aligned} \tag{B.17}$$

we can factorize the Toeplitz matrices as $T_n = B_n^\dagger B_n$, with B_n an upper-triangular matrix defined as $(B_n)_{k,\ell} = \beta_{\ell,k}$ if $k \leq \ell$ and 0 otherwise.

Finally, we observe that the upper Hessenberg structure of the unitary superoperator also appears in the literature on orthonormal polynomials on the unit circle [133].

B.4 Clifford Circuits

In this appendix we consider operator dynamics generated by Clifford circuits where the initial operator is a Pauli operator. Clifford circuits have the property that they transform (direct) products of Pauli matrices to direct

products of Pauli matrices. Since the product of Pauli matrices presents an orthonormal operator basis, for $|O_0)$ a Pauli matrix and Clifford dynamics it hence holds that $(O_s|O_t) = 0$ unless $O_s = O_t$.

We illustrate the Krylov dynamics for a Clifford circuit in Fig. B.1. Each operator $U_{j,j+1}$ is randomly drawn from the set of all two-site Clifford unitaries [288, 289]. Every new generated operator O_t is linear independent to all previous operators until the sequence repeats. The repetition is a consequence of the Floquet dynamics, using the same unitaries in each step: By drawing a random set of two-site Clifford gates, for some site j $U_{j,j+1}$ commutes with all O_t, effectively reducing the space of accessible operators through localisation [290]. Hence, for these cases, the Krylov complexity has a sawtooth shape, as shown in Fig. B.1 for a typical example picked at random. The Krylov complexity initially grows with the maximal possible rate, until a revival occurs when the initial operator is recovered. The Krylov complexity then starts periodically repeating since the dynamics cycles through the different direct products of Pauli matrices generated by the Clifford circuit, which are exactly the orthonormal Krylov operators. This example also highlights how the dimension of the Krylov basis does not necessarily attain the maximal possible value, since the dimension is here set by the periodicity of the operator dynamics.

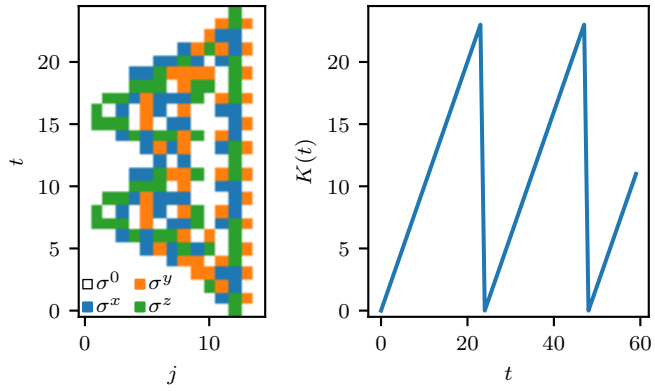

Figure B.1: *Clifford brickwork evolution for the initial operator σ^z (left) and the corresponding Krylov complexity $K(t)$ (right). The circuit is generated by drawing $U_{j,j+1}$ at random from the set of all two-site Clifford unitaries.*

B.5 Scaling Collapse

In this appendix, we report on the details of the function $(\Delta t)^g$ used to obtain a scaling collapse in the main text. To be as general as possible, we allow g to be Δt dependent. Then we obtain the function $(\Delta t)^g$ by interpolating the

functions a_n, b_n for different Δt yielding $a(\Delta t, n)$ and $b(\Delta t, n)$ with $n \in \mathbb{R}$. In the next step, we iteratively compare $a(\Delta t, n)$ [or $b(\Delta t, n)$] at consecutive Δt. We start at the smallest $\Delta t = 10^{-2}$ and compare to the values at the next smallest $\Delta t = 10^{-1.9}$. We then obtain g for this value of Δt by minimizing

$$\int \mathrm{d}n \, |a(\Delta t, n) - a(\Delta t', n(\Delta t')^g)|^2, \tag{B.18}$$

where we integrate over n by interpolating the $a(\Delta t, n)$, or in the same manner for $b(\Delta t, n)$. This yields g as a function of Δt. By extrapolation, we obtain g for $\Delta t = 10^{-2}$ [GUE: $g(\Delta t = 10^{-2}) = 1.43$, XXZ: $g(\Delta t = 10^{-2}) = 2.1$]. This yields the results for $(\Delta t)^g$ depicted in Fig. B.2. For small $\Delta t \to 0$, the

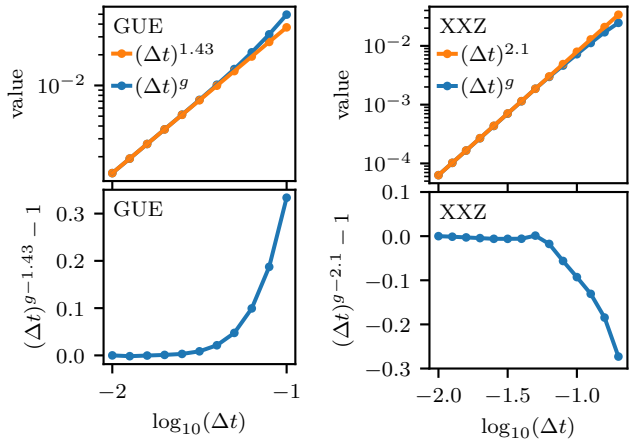

Figure B.2: *Rescaling factor g for the rescaling function $(\Delta t)^g$ for the GUE system (left) and XXZ system (right), see Fig. 3.3 and Fig. 3.6, and comparison to $(\Delta t)^{1.43}$ and $(\Delta t)^{2.1}$, respectively.*

scaling function seems to converge justifying the extrapolation to $\Delta t = 10^{-2}$, while deviations occur for large Δt. This may be expected, considering the operator spreading to converge for small Δt (see Fig. 3.4), while it deviates for larger Δt.

B.6 Convergence to the Maximally Ergodic Krylov Regime

In this appendix we consider the opposite limit, of large Δt and n, highlighting how $\mathcal{U}$ approaches $\mathcal{U}_{n+1,n} = 1$ exponentially. This convergence is shown in Fig. B.3 for the chaotic system with the Hamiltonian drawn from the GUE ensemble. We note that for dual-unitary circuits and the XXZ Hamiltonian a similar exponential decay can be observed.

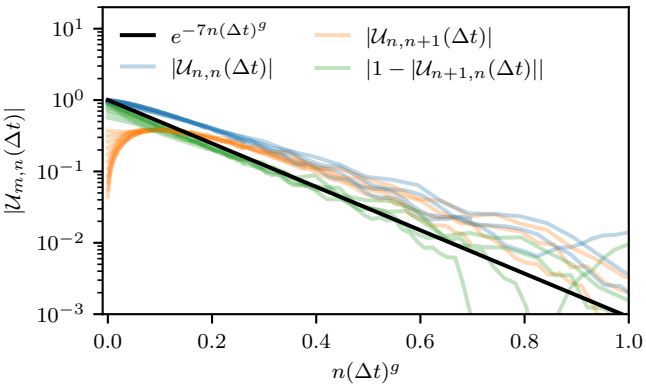

Figure B.3: *Convergence of the tridiagonal part of $\mathcal{U}$ to $\mathcal{U}_{n+1,n} = 1, \mathcal{U}_{n,m} = 0$ otherwise, with $U_{j,j+1} = \exp(-iH\Delta t)$ for a typical example of a Hamiltonian drawn from the GUE, the same as used in Fig. 3.3. The results were obtained using a system of size 70 and TEBD with an MPS bond dimension of 1024 while varying Δt from 10^{-2} to $10^{-1.2}$.*

B.7 Operator Growth

In this appendix we consider the operator growth of the Krylov operators $\mathcal{O}_n$. The operator growth is quantified through the OTOC

$$\mathrm{OTOC}(n,j) = \left\langle \mathrm{Tr}\left[\mathcal{O}_n^\dagger \sigma_j^\gamma \mathcal{O}_n \sigma_j^\gamma\right]/\mathcal{D}\right\rangle_\gamma , \tag{B.19}$$

where we averaged here over $\gamma \in \{x, y, z\}$, which we fit to an error function of the form

$$f_{a,\ell,D}(j) = a + (1-a)\{\mathrm{erf}[(j-\ell)/D] + 1\}/2 . \tag{B.20}$$

The fitting results for exemplary $\Delta t, n$ are shown in Fig. B.4. We allowed the error function to deviate from 0 by a value a at $j = 0$ to accommodate the observation that the OTOC is slightly negative at $j = 0$. This signals that σ_0^γ anticommutes rather than commute with $\mathcal{O}_n$. This may be a finite-time effect, and removing the fitting parameter a does not change the results qualitatively: We still observe the $n^{0.65}$ growth as stated in the main text.

B.8 Convergence to the Hamiltonian Regime

In this appendix we report on the results for the convergence of the superoperator $\mathcal{U}$ towards the Liouvillian $\mathcal{L}$ in the limit $\Delta t \to 0$ for the cases where a chaotic Hamiltonian is drawn from the GUE and for the XXZ Hamiltonian. We consider the convergence of the diagonal elements $\mathcal{U}_{nn} = a_n$ towards

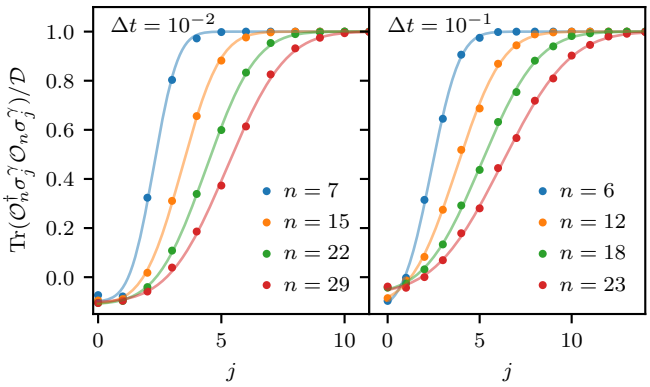

Figure B.4: *Fits (lines) to the OTOC data, (dots) Eq.* (B.19)*, using Eq. B.20. The OTOC data were generated using the Hamiltonian $H_{i,i+1}$ and the circuit structure also used for Fig. 3.3 as well as the same numerical simulation settings.*

1 and of the next-diagonal elements $\mathcal{U}_{n+1,n} = b_n$ towards the negative of $\mathcal{L}_{n+1,n} = \tilde{b}_n$, as expected in the limit $\Delta t \to 0$ from lowest order perturbation theory.

For the GUE case, the convergence is shown in Fig. B.5. Based on these results we expect $\mathcal{U}$ and $\mathcal{L}$ to return the same Krylov growth up to $n \sim 1/\Delta t$.

For the XXZ Hamiltonian, results are shown in Fig. B.6. It is interesting to note that for the XXZ Hamiltonian the scaling of the difference to $\mathcal{L}$ is different in comparison to the GUE example. Here, we observe the difference to grow as $\sim n^{1.4}\delta t^2$. Hence, for the XXZ circuit the superoperator $\mathcal{U}$ coincides with $\mathcal{L}$ up to $n \sim \Delta t^{-2/1.4}$, which is parametrically longer than for the GUE.

B.9 Detailed Derivation for the Integrable System

In the following we provide a detailed derivation for the exact solution of the integrable Trotterized XX model.

We transform the XX Hamiltonian using the Jordan-Wigner transformation to obtain a description in terms of the fermionic operators $c_j, c_j^\dagger$ defined

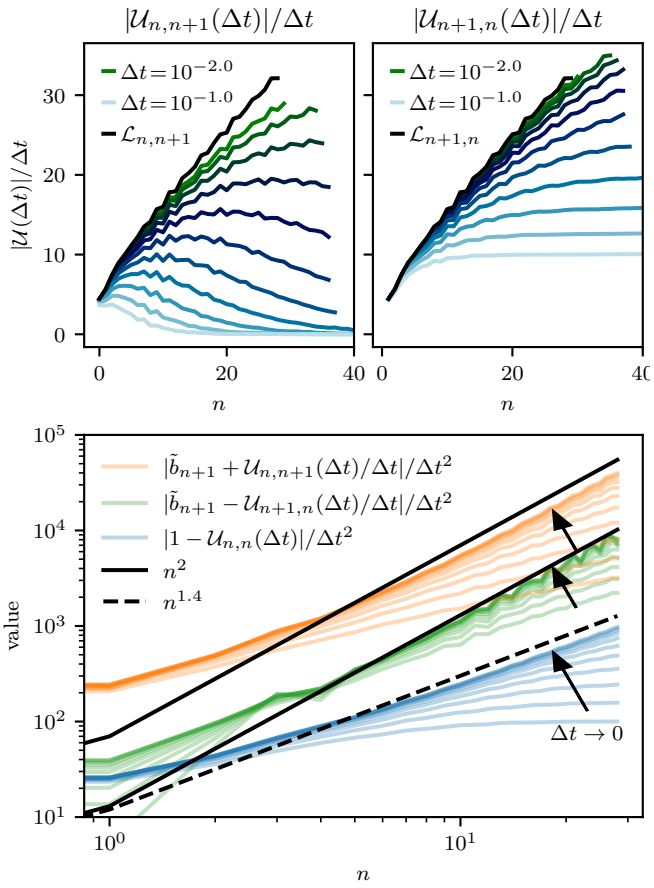

Figure B.5: *Convergence of the tridiagonal part of $\mathcal{U}$ to $\mathcal{L}$ with $U_{j,j+1} = \exp(-iH\Delta t)$ for a typical example of a Hamiltonian drawn from the GUE, the same used in Fig. 3.3. The results were obtained using a system of size 70 and TEBD with an MPS bond dimension of 1024 while varying Δt from 10^{-2} to 10^{-1}. Only numerically stable results are shown, determined by comparing to results obtained with a bond dimension of 512.*

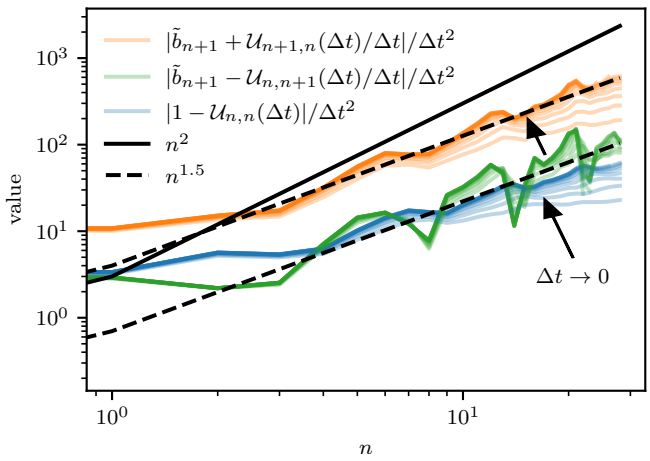

Figure B.6: *Convergence of the tridiagonal part of $\mathcal{U}$ to $\mathcal{L}$ for the interacting integrable XXZ Hamiltonian with $\Delta = 3$. The results were obtained using a system of size 70 and TEBD with an MPS bond dimension of 1024 while varying Δt from 10^{-2} to $10^{-0.7}$. Results for different Δt are shown using opaque lines which converge for $\Delta t \to 0$ from below. Only numerically stable results are shown, determined by comparing to results obtained with a bond dimension of 512.*

as

$$\sigma_j^z = 1 - 2c_j^\dagger c_j, \tag{B.21}$$

$$\sigma_j^x = \prod_{l<j}(1 - 2c_l^\dagger c_l)(c_j^\dagger + c_j), \tag{B.22}$$

$$\sigma_j^y = i\sigma_j^x\sigma_j^z = i\prod_{l<j}(1 - 2c_l^\dagger c_l)(c_j^\dagger - c_j). \tag{B.23}$$

The Hamiltonian can hence be rewritten as

$$\begin{aligned} H_{j,j+1} &= \sigma_j^x\sigma_{j+1}^x + \sigma_j^y\sigma_{j+1}^y \\ &= (c_j^\dagger - c_j)(c_{j+1}^\dagger + c_{j+1}) - (c_j^\dagger + c_j)(c_{j+1}^\dagger - c_{j+1}) \\ &= 2(c_j^\dagger c_{j+1} + c_{j+1}^\dagger c_j). \end{aligned} \tag{B.24}$$

The unitary evolution operator is given by $U = e^{-iH_2\Delta t}e^{-iH_1\Delta t}$, where for the two layers of the time evolution we use

$$H_1 = \sum_j H_{2j,2j+1} \tag{B.25}$$

$$H_2 = \sum_j H_{2j+1,2j+2}. \tag{B.26}$$

Both Hamiltonians preserve the momentum using a unit cell of size 2, allowing us to introduce fermionic operators with fixed momentum as

$$c_{k+} = \frac{1}{\sqrt{N}} \sum_{j=0}^{N-1} e^{ikj} c_{2j}, \tag{B.27}$$

$$c_{k-} = \frac{1}{\sqrt{N}} \sum_{j=0}^{N-1} e^{ikj} c_{2j+1}, \tag{B.28}$$

where we consider a finite system with N lattice sites, so that

$$H_1 = 2 \sum_k c_{k+}^\dagger c_{k-} + c_{k-}^\dagger c_{k+}, \tag{B.29}$$

$$H_2 = 2 \sum_k e^{-ik} c_{k+}^\dagger c_{k-} + e^{ik} c_{k-}^\dagger c_{k+} \,. \tag{B.30}$$

Now we can use that

$$[H_1, c_{k+}] = -2c_{k-}(c_{k+}^\dagger c_{k+} + c_{k+} c_{k+}^\dagger) = -2c_{k-} \,, \tag{B.31}$$

$$[H_1, c_{k+}^\dagger] = 2c_{k-}^\dagger(c_{k+} c_{k+}^\dagger + c_{k+}^\dagger c_{k+}) = 2c_{k-}^\dagger \,, \tag{B.32}$$

and similarly

$$[H_1, c_{k-}] = -2c_{k+}, \qquad [H_1, c_{k-}^\dagger] = 2c_{k+}^\dagger, \tag{B.33}$$

$$[H_2, c_{k+}] = -2c_{k-} e^{-ik}, \qquad [H_2, c_{k+}^\dagger] = 2c_{k-}^\dagger e^{ik}, \tag{B.34}$$

$$[H_2, c_{k-}] = -2c_{k+} e^{ik}, \qquad [H_2, c_{k-}^\dagger] = 2c_{k+}^\dagger e^{-ik}. \tag{B.35}$$

The time evolution for H_1 now follows from

$$\frac{\mathrm{d}}{\mathrm{d}t} e^{iH_1 t} \begin{pmatrix} c_{k+} \\ c_{k-} \end{pmatrix} e^{-iH_1 t} = -i \begin{pmatrix} 0 & 2 \\ 2 & 0 \end{pmatrix} e^{iH_1 t} \begin{pmatrix} c_{k+} \\ c_{k-} \end{pmatrix} e^{-iH_1 t} \tag{B.36}$$

so that we can write

$$e^{iH_1 \Delta t} \begin{pmatrix} c_{k+} \\ c_{k-} \end{pmatrix} e^{-iH_1 \Delta t} = \begin{pmatrix} \cos(2\Delta t) & -i\sin(2\Delta t) \\ -i\sin(2\Delta t) & \cos(2\Delta t) \end{pmatrix} \begin{pmatrix} c_{k+} \\ c_{k-} \end{pmatrix}. \tag{B.37}$$

For H_2 we similarly find

$$\frac{\mathrm{d}}{\mathrm{d}t} e^{iH_2 t} \begin{pmatrix} c_{k+} \\ c_{k-} \end{pmatrix} e^{-iH_2 t} = -i \begin{pmatrix} 0 & 2e^{-ik} \\ 2e^{ik} & 0 \end{pmatrix} e^{iH_1 t} \begin{pmatrix} c_{k+} \\ c_{k-} \end{pmatrix} e^{-iH_1 t} \,. \tag{B.38}$$

Using the eigenvectors $(1, e^{ik})^T/\sqrt{2}$, $(-e^{-ik}, 1)^T/\sqrt{2}$ with eigenvalues $2, -2$, we get

$$e^{iH_2\Delta t}\begin{pmatrix} c_{k+} \\ c_{k-}\end{pmatrix} e^{-iH_2\Delta t} = \frac{1}{2}\left[\begin{pmatrix} 1 & e^{-ik} \\ e^{ik} & 1\end{pmatrix} e^{-2i\Delta t} + \begin{pmatrix} 1 & -e^{-ik} \\ -e^{ik} & 1\end{pmatrix} e^{2i\Delta t}\right]\begin{pmatrix} c_{k+} \\ c_{k-}\end{pmatrix}$$
$$= \begin{pmatrix} \cos(2\Delta t) & -i\sin(2\Delta t)e^{-ik} \\ -i\sin(2\Delta t)e^{ik} & \cos(2\Delta t)\end{pmatrix}\begin{pmatrix} c_{k+} \\ c_{k-}\end{pmatrix}. \quad \text{(B.39)}$$

We have to multiply the matrix representations of the two layers to obtain

$$\mathcal{U}_k = \begin{pmatrix} \cos(2\Delta t) & -i\sin(2\Delta t)e^{-ik} \\ -i\sin(2\Delta t)e^{ik} & \cos(2\Delta t)\end{pmatrix}\begin{pmatrix} \cos(2\Delta t) & -i\sin(2\Delta t) \\ -i\sin(2\Delta t) & \cos(2\Delta t)\end{pmatrix} \quad \text{(B.40)}$$
$$= \begin{pmatrix} 1-\sin(2\Delta t)^2(1+e^{-ik}) & -i\cos(2\Delta t)\sin(2\Delta t)(1+e^{-ik}) \\ -i\cos(2\Delta t)\sin(2\Delta t)(1+e^{ik}) & 1-\sin(2\Delta t)^2(1+e^{ik})\end{pmatrix}. \quad \text{(B.41)}$$

This returns the expression from the main text. The matrix can be directly diagonalized to return eigenvalues $e^{\pm i\omega_k}$, with

$$\cos(\omega_k) = 1 - 2\sin^2(2\Delta t)\cos^2(k/2)\,. \quad \text{(B.42)}$$

The expressions for the autocorrelation function (3.72) then follow by making use of the fact that

$$(O_0|k+) = 1, \qquad (O_0|k-) = 0\,, \quad \text{(B.43)}$$

and expressing $|O_0)$ in the eigenbasis of Eq. (B.40).

C Information Relocalization

C.1 Gaussian State Formulation

In the following, we derive the Gaussian (BCS) formulation of the two states $e^{-iHt}|\uparrow^N\rangle$ and $\sigma_0^z(t)|\uparrow^N\rangle$.

C.1.1 Formalism

We start with a complete set of fermionic operators $c_{j'}$ with pairwise anti-commutation relations (ACRs) and their vacuum state with $c_{j'}|0\rangle = 0$. Let

$|\Phi\rangle$ be defined as the vacuum of another complete set of fermionic operators with ACRs and $d_{j'}|\Phi\rangle = 0$. Additionally we require the relation

$$d_{j'} = \sum_{l'} A_{j'l'} c_{l'} + B_{j'l'} c_{l'}^\dagger. \tag{C.1}$$

Then, $|\Phi\rangle$ can be written in Gaussian or BCS type form

$$|\Phi\rangle \propto \prod_{j'l'} \left(1 + X_{j'l'} c_{j'}^\dagger c_{l'}^\dagger\right) |0\rangle, \tag{C.2}$$

with $2X = -A^{-1}B$ [216, chapter 5.3].

C.1.2 Numerical Results for Gaussian States

In this chapter, we will provide numerical results supporting the domain wall relocalization picture presented in the main text for the case of quenched states.

In a standard picture, the vanishing of $M_{\uparrow^N}$ arises due to freely propagating domain walls at finite density [223, 291]. This perspective can usefully be extended to explaining the behavior of the OTOC starting from the fully polarized state.

As stated in the previous and also next chapters, see Eqs. (C.7), (C.1) and (C.2), conceptually (and pictorially), for O_p consisting of σ^z operators, one can encode the domain wall dynamics by following the (out-of-time) evolution via a "BCS" pairing function $X_{j'l'}$

$$U_{-t_b} O_\mathrm{p} U_{t_f} |\uparrow^N\rangle \propto \prod_{j'l'} \left(1 + X_{j'l'}(t_f, t_b) c_{j'}^\dagger c_{l'}^\dagger\right) |\uparrow^N\rangle \tag{C.3}$$

in terms of fermionic domain wall creation/annihilation operators with $U_t = \exp(-iHt)$, extending [216]. Note that this only applies to $g < J$, otherwise A, Eq. (C.2), is singular. The structure of the matrix $X_{j'l'}$ can be understood by noting that the operators $c_{j'}^\dagger c_{l'}^\dagger$ flip all spins between j' and l' if applied to the fully polarized state, e.g.

$$c_{j'}^\dagger c_{l'}^\dagger |\uparrow_1 \cdots \uparrow_N\rangle = |\uparrow_1 \cdots \uparrow_{j-1} \underbrace{\downarrow_j \cdots \downarrow_{l-1}}_{j'} \underbrace{\uparrow_l}_{l'} \cdots\rangle. \tag{C.4}$$

Our discussion is based on the snapshots of $X_{j'l'}$ in Fig. C.1: $X_{j'l'}(t, 0)$ after a single forward time evolution (left), after half of the back evolution $X_{j'l'}(t, t/2)$ (center) and after full back evolution $X_{j'l'}(t, t)$ (right). The initial state $|\uparrow^N\rangle$ has no domain walls. The domain walls, created in pairs,

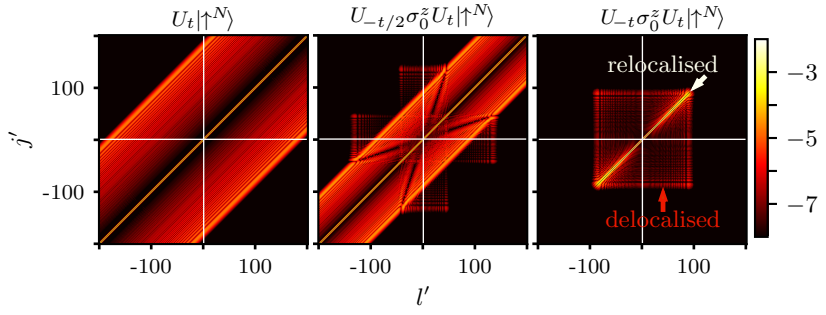

Figure C.1: *Domain wall pairing, encoded by* $\log|X_{j'l'}|$ *(Eqs.* (C.7), (C.1) *and* (C.2)*), for three different stages of the OTOC protocol: after the forward evolution to time* t*, as well during and after the backward evolution. The white lines indicate site* 0*, where the perturbation* σ_0^z *is applied. For the simulation we used* $N = 600, t = 300, J = 1, g = 0.3$ *and show the bulk effects by setting* $-200 \leq j', l' < 200$*.*

spread essentially independently, either in the same direction, so that $X_{j'l'}(t,0)$ close to the diagonal is nonzero or in opposite directions, yielding a wave front where $X_{j'l'}(t,0)$ is nonzero for $|j'-l'| \approx 2v_{\mathrm{wf}}t$ with the wavefront velocity v_{wf}, see Fig. C.1 (left). The following perturbation σ_j^z flips all signs $\sigma_j^z c_{l'}^{(\dagger)}\sigma_j^z = \mathrm{sign}(l'-j)c_{l'}^{(\dagger)}$ [7]. The late-time OTOC signal can then be assigned to arise from the two mechanisms, relocalization and delocalization. Relocalization is the (imperfect) back evolution of domain walls within the region $2v_{\mathrm{wf}}t$, yielding large values for $|X_{j'l'}(t,t)|$ close to the diagonal $j'=l'$, decaying exponentially with $|j'-l'|$. The delocalization mechanism is a perturbation of all 'wave fronts' close to the site of the perturbation σ_0^z yielding additional pairs of delocalized domain walls in $\sigma_0^z(t)|\uparrow^N\rangle$.

As explained in the main text, relocalization is absent for even n_V. This is supported numerically in Fig. C.2: The resulting time evolution of the X-matrix therefore shows only a delocalized signal.

In the following Chapters C.1.3 to C.1.5 , we will provide analytical calculations and definitions for the re- and delocalization mechanisms. We will show how the relocalization mechanism can be introduced as an approximation, which predicts $\sigma_0^z(t)|\uparrow^N\rangle$ to be a product state of rotated spins. This approach also elegantly provides a handle on the delocalized part, which can be identified here as the difference between the exact result and our approximation: $X^d = X - X^r$ is largely featureless and spreads out linearly with

[7] Here we use open boundary conditions or a infinitely larger system, see App. C.3

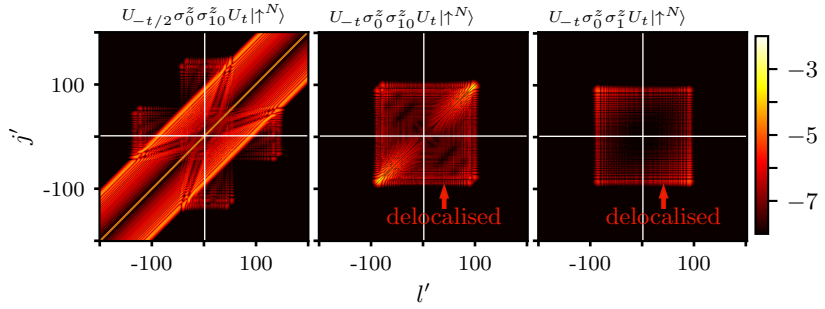

Figure C.2: *The results for the X-matrix are shown for delocalized domain walls with the same configuration as used in Fig. C.1. The difference to the results shown in Fig. C.1 is to apply $\sigma_0^z\sigma_{10}^z$ (left, center) and $\sigma_0^z\sigma_1^z$ (right) on the state shown in the left panel. The left panel shows the X-matrix for the state after half back evolution and the center and right panel after full back evolution.*

time as shown in Fig. C.3.

C.1.3 Domain Wall Relocalization for Quenched States

For ordinary time evolution, $e^{-iH_{\mathrm{TFI}'}t}|\uparrow^N\rangle$ is the vacuum of

$$d_{1,j'}(t) = e^{-iH_{\mathrm{TFI}'}t}c_{j'}e^{iH_{\mathrm{TFI}'}t} = c_{j'}(-t), \tag{C.5}$$

where we add the index 1 at $d_{1,j'}$ to distinguish it from different sets of fermionic operators introduced later. For this case, the calculation of A_1, B_1 in Eq. (C.1) can be performed either for open boundary conditions [217] or for periodic boundary conditions using the analytical solution of $H_{\mathrm{TFI}'}$ [186, 219]. Note that due to inversion symmetry $\mathcal{I}c_{l'}\mathcal{I}^{-1} = ic_{-l'}$ of the Hamiltonian, we have with Eqs. (C.1) and (C.5)

$$A_{1,j'l'} = A_{1,(-j')(-l')},\ B_{1,j'l'} = -B_{1,(-j')(-l')} \tag{C.6}$$

for $d_{1,j'}(t) = c_{j'}(-t)$.

For the OTOC, the state $O_{\mathrm{p}}(t)|\uparrow^N\rangle$ is the vacuum of

$$d_{2,j'}(t) = O_{\mathrm{p}}(t)c_{j'}O_{\mathrm{p}}(t). \tag{C.7}$$

This can also be written in the form of Eq. (C.1), as the system is integrable, i.e., an evolved single particle operator remains a single particle operator as can be confirmed by calculating $[c_{j'}, H_{\mathrm{TFI}'}]$ and $[c_{j'}, O_{\mathrm{p}}]$ using (4.6). In the following we calculate analytical expressions for $A_{2,j'l'}$ and $B_{2,j'l'}$. We present

the calculation in detail below; a rough and simple cartoon of it is provided by the following picture. During the forward evolution part, the domain wall c_0 spreads in opposite directions inversion symmetrically, yielding

$$c_0(-t) \approx \alpha(t)(c_{-vt} + c_{vt}) + \beta(t)(-c^\dagger_{-vt} + c^\dagger_{vt}). \tag{C.8}$$

Now, the perturbation $O_\mathrm{p} = \sigma^z_0$ yields

$$\sigma^z_0 c_0(-t)\sigma^z_0 \approx \alpha(t)(-c_{-vt} + c_{vt}) + \beta(t)(c^\dagger_{-vt} + c^\dagger_{vt}). \tag{C.9}$$

The back evolution in time preserves the inversion symmetry of the above equation, so that we find to lowest order

$$\sigma^z_0(t)c_0\sigma^z_0(t) \approx \alpha(c_1 - c_{-1}) + \beta c^\dagger_0 \tag{C.10}$$

with some prefactors, $\alpha \approx \sqrt{(1-g^2/J^2)/2}, \beta \approx g$. Note that here we use the index 0 to refer to a site in the center of the system.

The analytical calculation now proceeds as follows. We calculate $d_{2,j'}(t) = \sigma^z_0(t)c_{j'}\sigma^z_0(t)$ using the known solutions for periodic boundary conditions and the formulation for σ^z_0, Eq. (4.6), in the limit $N \to \infty, t \to \infty$. We comment in Supplemental Material C.3 on calculating Ising odd operators with periodic boundary conditions.

The Hamiltonian can be diagonalized using a Fourier transformation $c_{j'} = \sum_{k'} e^{ik'j'}/\sqrt{N}$ followed by a Bogoliubov transformation with angle $\tan(\theta_{k'}) = \sin(k')/(g^{-1} + \cos(k'))$, so that $H = \sum \epsilon_{k'}\gamma^\dagger_{k'}\gamma_{k'}$ up to a constant with $\epsilon_{k'} = 2\sqrt{g^2 + J^2 + 2gJ\cos k'}$ and $\gamma^\dagger_k = \cos(\theta_k/2)c^\dagger_{k'} - i\sin(\theta_k/2)c_{-k'}$ [186, 219]. From this follows that the Hamiltonian acts as a 2×2 subspace spanned by $\gamma^\dagger_{k'}\gamma_{k'}$ being 0 or 1 within each momentum subspace.

Hence, a single propagated domain wall operator is

$$\begin{aligned} c_{j'}(-t) = \frac{1}{\sqrt{N}}\sum_{k'} &\cos(\theta_{k'}/2)e^{ik'j'}e^{i\epsilon_{k'}t}\gamma_{k'} \\ &- i\sin(\theta_{k'}/2)e^{ik'j'}e^{-i\epsilon_{k'}t}\gamma^\dagger_{-k'}. \end{aligned} \tag{C.11}$$

Now we apply the approximation as discussed in the main text. Due to the sign of the group velocity $\mathrm{sign}(v_g(k')) = \mathrm{sign}(\partial_{k'}\epsilon_{k'}) = -\mathrm{sign}(k')$, all modes k' separate in space for $t \to \infty$ according to $\mathrm{sign}(k')$.

For the choice of σ^z_0 discussed above, we have $\sigma^z_0 c_{l'}\sigma^z_0 = \mathrm{sign}(l')c_{l'}$ and, hence, can approximate

$$\begin{aligned} &\sigma^z_0 c_{j'}(-t)\sigma^z_0 \approx \\ &\frac{-1}{\sqrt{N}}\sum_{k'} \mathrm{sign}(k')\cos(\theta_{k'}/2)e^{ik'j'+i\epsilon_{k'}t}\gamma_{k'} \\ &\qquad +\mathrm{sign}(k')i\sin(\theta_{k'}/2)e^{ik'j'-i\epsilon_{k'}t}\gamma^\dagger_{-k'} \end{aligned} \tag{C.12}$$

which becomes exact for $t \to \infty$. The relative minus sign stems from the fact that $\gamma_{k'}$ and $\gamma^\dagger_{-k'}$ have opposite group velocities.

Performing the second time evolution on $\sigma^z_0 c_{j'}(-t)\sigma^z_0$ one obtains $d_{2,j'} = \sigma^z_0(t)c_{j'}\sigma^z_0(t)$ with the relation

$$A_{j'l'} = \frac{-1}{N}\sum_{k'} e^{ik'(j'-l')}\mathrm{sign}(k')\cos(\theta_{k'}) \tag{C.13}$$

$$B_{j'l'} = \frac{-i}{N}\sum_{k'} e^{ik'(j'-l')}\mathrm{sign}(k')\sin(\theta_{k'}). \tag{C.14}$$

Calculating $X_{j'l'}$ can be achieved in momentum space

$$\begin{aligned} 2X_{j'l'} &= -\sum_{m'}(A^{-1})_{j'm'}B_{m'l'} \\ &= -i\sum_{k'} e^{ik'(j'-l')}\sin(\theta_{k'})/\cos(\theta_{k'}). \end{aligned} \tag{C.15}$$

Integrating via the residue theorem yields

$$\begin{aligned} &\frac{-i}{2\pi}\int_{-\pi}^{\pi} \mathrm{d}k' \frac{\sin(k')}{(Jg^{-1}+\cos(k'))} e^{i(j'-l')k'} \\ &= -\mathrm{sign}(j'-l')p^{-|j'-l'|} \end{aligned} \tag{C.16}$$

using that $p^{-1} = e^{ik'_r}$ with $Jg^{-1} + \cos k'_r = 0$, and hence, $p^{-1} = -Jg^{-1} + \sqrt{J^2g^{-2}-1}$. The integration contour is a rectangle, where the integration paths along $-\pi + i\mathrm{Im}(k')$ and $+\pi + i\mathrm{Im}(k')$ cancel as the integrand is 2π periodic and the integration direction is opposite along the rectangular integration contour. The contributions at $\mathrm{Im}(k') \to \infty$ $(-\infty)$ vanish as the integrand is exponentially suppressed for $j'-l' > 0$ $(j'-l' < 0)$.

Finally, this exponential decaying X matrix yields a product state as shown in Appendix C.1.4.

C.1.4 A Relocalized X-matrix Yields a Product State

First, we use that the state is given as

$$\prod_{i'<j'}(1 + 2X_{i'j'}c^\dagger_{i'}c^\dagger_{j'})|0\rangle, X_{i'j'} = p^{-|i'-j'|}/2 \tag{C.17}$$

In this state the product generates all possible combinations of products of $O_{i'j'} = c^\dagger_{i'}c^\dagger_{j'}$. For each of these products of pairs of raising operators, the following holds.

(A) In each operator product

$$(c^\dagger_{i'_1} c^\dagger_{j'_1})(c^\dagger_{i'_2} c^\dagger_{j'_2}) \cdots \tag{C.18}$$

each index only occurs once, as operators containing two identical raising operators vanish.

(B) All pairs of raising operators $c^\dagger_{i'_1} c^\dagger_{j'_1}, \ldots$ commute with all other pairs. This allows us to resort the product of pairs.

(C) Only those operator products remain where there is no overlap between pairs, i.e., given an operator pair i'_l, j'_l in a product of pairs, all other pairs i'_m, j'_m fulfill either

$$i'_l < j'_l < i'_m < j'_m \text{ or } i'_m < j'_m < i'_l < j'_l. \tag{C.19}$$

This holds because, for each operator product where pairs have overlap, there is another operator product generating the same state when applied to $|0\rangle$ with opposite sign. By exchanging for two pairs i'_1, i'_2, we get $c^\dagger_{i'_1} c^\dagger_{i'_2} = -c^\dagger_{i'_2} c^\dagger_{i'_1}$ with the same prefactors $X_{i'_1 j'_1} X_{i'_2 j'_2}$ and $X_{i'_2 j'_1} X_{i'_1 j'_2}$ as follows from

$$\Leftrightarrow \quad X_{i'_1 j'_1} X_{i'_2 j'_2} \overset{!}{=} X_{i'_2 j'_1} X_{i'_1 j'_2} \tag{C.20}$$

$$\Leftrightarrow \quad p^{-|j'_1 - i'_1|} p^{-|j'_2 - i'_2|} \overset{!}{=} p^{-|j'_1 - i'_2|} p^{-|j'_2 - i'_1|} \tag{C.21}$$

$$\Leftrightarrow \quad p^{-j'_1 + i'_1 - j'_2 + i'_2} \overset{!}{=} p^{-|j'_1 - i'_2| - |j'_2 - i'_1|} \tag{C.22}$$

$$\Leftrightarrow \quad j'_1 - i'_1 + j'_2 - i'_2 \overset{!}{=} |j'_1 - i'_2| + |j'_2 - i'_1| \tag{C.23}$$

Now, two pairs having overlap means that $i'_1 < j'_2$ and $i'_2 < j'_1$, which implies with Eq. (C.17) that j'_1, j'_2 are both larger than i'_1 and i'_2. In this case, Eq. (C.23) is fulfilled. Hence, the two operator products have the same prefactor $X_{j'_1 i'_1} X_{j'_2 i'_2} = X_{j'_1 i'_2} X_{j'_2 i'_1}$. As a result, if two pairs overlap, there is always another operator product in Eq. (C.17) with the two operators $c^\dagger_{i'_1}, c^\dagger_{i'_2}$ exchanged which yields a -1 sign and these two operator products cancel.

Hence, all operator products generated in Eq. (C.17) cancel which contain two pairs, i'_1, j'_1 and i'_2, j'_2, fulfilling

$$i'_1 < j'_2 \text{ and } i'_2 < j'_1. \tag{C.24}$$

Therefore, only those operator products remain for which Eq. (C.24) is not fulfilled for all pairs in the operator product yielding $i'_1 > j'_2$ or $i'_2 > j'_1$ for all pairs. With $j'_1 > i'_1, j'_2 > i'_2$ from Eq. (C.17), it implies

$$j'_1 > i'_1 > j'_2 > i'_2 \text{ or } j'_2 > i'_2 > j'_1 > i'_1, \tag{C.25}$$

for all pairs, which means that there is no overlap between pairs. We can verify that those operator products do not cancel, as they have different prefactors: Eqs. (C.25) and (C.23) yield

$$\Rightarrow \quad j_1' - i_1' + j_2' - i_2' \stackrel{!}{=} j_1' - i_2' + i_1' - j_2' \Rightarrow i_1' = j_2' \tag{C.26}$$

$$(\Rightarrow \quad j_1' - i_1' + j_2' - i_2' \stackrel{!}{=} -j_1' + i_2' - i_1' + j_2' \Rightarrow j_1' = i_2') \tag{C.27}$$

contradicting (A). This means that in the case that there is no overlap between two pairs, the operator products related by flipping two operators i_1', i_2' have prefactors which differ in magnitude, so that the operator products do not cancel.

A unique way of pairing these operator products to cancel respectively is to choose those two overlapping pairs $(j_1', i_1'), (j_2', i_2')$ out of the operator product of which i_1' and i_2' are closest to $N/2$ and in case there is ambiguity, choose that pair with $i' > N/2$ (note that each index can only occur once). Swapping $i_1' \leftrightarrow i_2'$ leaves this choice invariant. Hence, we found, for each operator product with overlapping pairs, a unique second operator product with the opposite prefactor.

Using these properties, we can verify order by order in p^{-1} that the above state coincides with the product state

$$\prod_i (1 + p^{-1}\sigma_i^x)|\uparrow^N\rangle. \tag{C.28}$$

For that, note that

$$4c_{i'}^\dagger c_{j'}^\dagger = \tau_{i'}^z \tau_{j'}^z (\mathbb{1}_{i'} + \tau_{i'}^x)\tau_{i'+1}^x \cdots \tau_{j'-1}^x (\mathbb{1}_{j'} + \tau_{j'}^x). \tag{C.29}$$

This can be transformed using the duality transformation $\tau_{i'}^z \tau_{i'+1}^z = \sigma_{i'+1/2}^x$ and, hence,

$$\tau_{i'}^z \tau_{j'}^z = (\tau_{i'}^z \tau_{i'+1}^z)(\tau_{i'+1}^z \tau_{i'+2}^z)\tau_{i'+2}^z \tau_{j'}^z = \sigma_{i'+1/2}^x \cdots \sigma_{j'-1/2}^x \ . \tag{C.30}$$

Similarly, the product of τ^x's can be transformed into a pair of σ^z's yielding

$$\begin{aligned} 4c_{i'}^\dagger c_{j'}^\dagger =& \sigma_{i'+1/2}^x \cdots \sigma_{j'-1/2}^x \\ & \times (\sigma_{i'+1/2}^z + \sigma_{i'-1/2}^z)(\sigma_{j'-1/2}^z + \sigma_{j'+1/2}^z). \end{aligned} \tag{C.31}$$

We can now use the properties (A)-(C) when plugging this formula into Eq. (C.17), especially statement (C), where in the expanded form of the product, there are no terms where the σ^x parts of the operators in Eq. (C.31) overlap or even touch. Hence, for all nonvanishing products, $(\sigma_{i'+1/2}^z + \sigma_{i'-1/2}^z)(\sigma_{j'-1/2}^z + \sigma_{j'+1/2}^z) = 4$, so that we can use

$$(1+2X_{i'j'}c_{i'}^\dagger c_{j'}^\dagger)|0\rangle = (1+p^{-|i'-j'|}\sigma^x_{i'+1/2}\cdots\sigma^x_{j'-1/2})|0\rangle. \tag{C.32}$$

Hence, we create all possible states where the prefactor of each state is given by the product of consecutive spin flips $p^{-|i'-j'|}$. This is the same for the product state

$$\prod_i (1+p^{-1}\sigma_i^x)|0\rangle. \tag{C.33}$$

C.1.5 Delocalization

The analytical result for the relocalization effect allows for computing the delocalization as the remaining difference

$$X^{\mathrm{d}} := X - X^{\mathrm{r}}, \tag{C.34}$$

with X^{r} given in Eq. (C.15) and X being the full state as obtained from solving Eq. (C.7) and inserting into (C.2). Numerical results are shown in Fig. C.3. This yields the remaining part of the picture presented in the main text: Delocalization following from the wavefunction being not perfectly separated at the moment of applying O_{p} as used for the calculation of X^{r} in Eq. (C.12). This delocalized part then spreads ballistically in time with a constant shape, as shown in the inset. This is what is shown schematically in Fig. 4.2.

C.2 Analytical Calculation of Domain Wall Densities

The calculation of

$$n_{\mathrm{DW}} = \lim_{T\to\infty}\frac{1}{2T}\int_{-T}^{T}\mathrm{d}t\,\frac{1}{N}\sum_{j'}\langle\uparrow^N|e^{iH_{\mathrm{TFI}'}t}c_{j'}^\dagger c_{j'}e^{-iH_{\mathrm{TFI}'}t}|\uparrow^N\rangle \tag{C.35}$$

can be done by using the known transformation in the eigenbasis of $H_{\mathrm{TFI}'}$ and its inverse. Hence, one obtains in the limit $N\to\infty$

$$n_{\mathrm{DW}} = \frac{1}{4\pi}\int_{-\pi}^{\pi}\mathrm{d}k'\,\sin^2(\theta_{k'}) \tag{C.36}$$

$$= \frac{1}{4\pi}\int_{-\pi}^{\pi}\mathrm{d}k'\,\frac{\sin^2(k')}{(g^{-1}+\cos(k'))^2+\sin^2(k')} \tag{C.37}$$

$$= \begin{cases} g^2/4 & g\le 1 \\ 1/4 & g>1 \end{cases}, \tag{C.38}$$

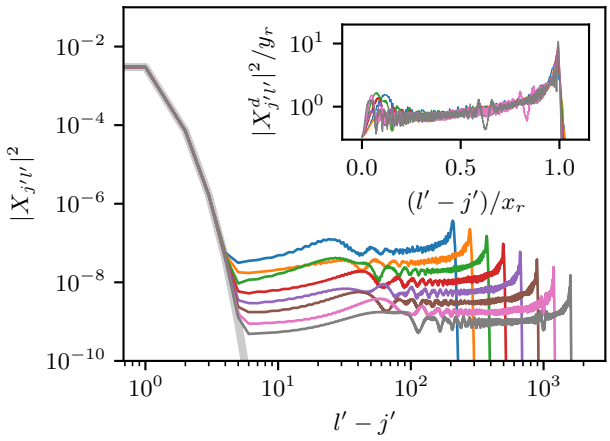

Figure C.3: *Central row of $|X_{j'l'}|^2$, with $J = 1, g = 0.3, N = 4000$ and times $700 < t < 5300$. The wide gray line indicates the exponential decay due to the relocalized domain wall pairs, X^r (Eq. (C.15)). The inset shows its deviation, $|X^d_{j'l'}|^2 = |X_{j'l'} - X^r_{j'l'}|^2$; these curves collapse upon rescaling the axes with $x_r = v_{\mathrm{wf}}t \approx 0.3t$ and $y_r = 0.04/t^2$, respectively. The data is averaged over ten adjacent j' and two l'.*

where we used the Weierstrass substitution in the last step to solve the integral.

Using the known relation of $d_{2,j'}$ as given in Eq. (C.14), we can derive, see also Eq. (4.17),

$$n_{\mathrm{DW,OTOC}} = \lim_{t\to\infty} \frac{1}{N} \sum_{j'} \langle\uparrow^N|\sigma^z_0(t)c^\dagger_{j'}c_{j'}\sigma^z_0(t)|\uparrow^N\rangle \tag{C.39}$$

$$= \lim_{t\to\infty} \frac{1}{N} \sum_{j'} \langle\uparrow^N|\sigma^z_0(t)c^\dagger_{j'}\sigma^z_0(t)\sigma^z_0(t)c_{j'}\sigma^z_0(t)|\uparrow^N\rangle \tag{C.40}$$

$$= \lim_{t\to\infty} \frac{1}{N} \sum_{j',l'} B^*_{j'l'}B_{j'l'} = \frac{1}{2\pi}\int_{-\pi}^{\pi} \mathrm{d}k' \, \sin^2(\theta_{k'}) \tag{C.41}$$

$$= 2n_{\mathrm{DW}} \tag{C.42}$$

This shows that the physics determining the nonanalytic behavior in n_{DW} as also discussed in Ref. [227] and the nonanalytic behavior of the OTOC $n_{\mathrm{DW,OTOC}}$ are the same.

C.3 Ising Odd Operators and Periodic Boundary Conditions

To proceed with the analytical calculation of A, B in Appendix C.1.3 we must use periodic boundary conditions, see Refs. [186, 219]. In contrast with the case with open boundary conditions, the special role of the domain wall at site $\frac{1}{2}$ does not play a special role; its presence/absence does not fix the spin at site 1. Hence, we cannot translate a single σ_j^z or, more generally, an Ising odd O_p into the fermionic domain wall formulation. Instead, we must use $\sigma_j^z\sigma_{j+\lfloor N/2\rfloor}^z$, which becomes $\tau_{j+1/2}^x\tau_{j+3/2}^x\cdots\tau_{j+\lfloor N/2\rfloor-1/2}^x$. However, in the TDL, taking first $N\to\infty$, no domain wall will be influenced within finite times by both, σ_j^z and $\sigma_{j+\lfloor N/2\rfloor}^z$, so that we will only consider one part of the system and use, e.g., $\sigma_{j+\lfloor N/2\rfloor}^z\to\cdots\tau_{j+\lfloor N/2\rfloor-3/2}^x\tau_{j+\lfloor N/2\rfloor-1/2}^x$.

C.4 OTOC Values in the ANNNI Model

C.4.1 Quenched OTOCs

In this section, we provide the numerical results used to generate Fig. 4.8. We simulate the time evolution of the ANNNI model as specified in the main text up to a size of 24 qubits, see Fig. C.4. By comparing the results for $N = 22$ and 24, we select a window of large times for which boundary effects can still be neglected. We average the OTOC over these times, which yields the data shown in Fig. 4.8.

C.4.2 Thermal OTOC Expectation Values in the ANNNI Model

In this section, we discuss the results for the thermal expectation value for the ANNNI model, taking $\langle\uparrow^N|\sigma_0^x\sigma_0^z(t)\sigma_0^x\sigma_0^z(t)|\uparrow^N\rangle$ as a numerically more feasible example. The analytical calculation equivalent to the one outlined in the previous sections yields

$$\mathrm{Tr}\left[\sigma_0^x\sigma_0^z(t)\sigma_0^x\sigma_0^z(t)\right]\overset{t\to\infty}{\to}\frac{-4}{\pi^2}\begin{cases}1 & 1>g\\ \frac{1}{g^2} & 1\le g\end{cases}. \tag{C.43}$$

for the integrable TFIM for this correlator, yielding a comparable non-analyticity to $\mathrm{Tr}\left[\sigma_0^x\sigma_0^z(t)\sigma_0^x\sigma_0^z(t)\right]$. The numerical results for the ANNNI model are shown in Fig. C.5. Particularly insightful are the results for $g = 1.5, \Delta = 0.05$. For this parameter set, the largest bond dimension appears to be sufficient to reliably calculate the signal up to $t\approx 50$ until which the signal has leveled out. This confirms that, also with weak integrability-breaking perturbations, a stable signal at least for intermediate

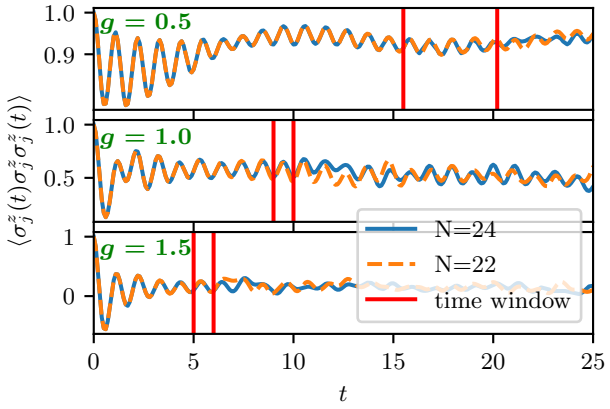

Figure C.4: *Numerical simulation results for the ANNNI model for $N = 22$ (orange) and $N = 24$ (blue) for three different exemplary values of g, as indicated in green, while $J = 1$ and $\Delta = 0.5$. The results were obtained using Krylov time evolution. The red lines indicate the manually selected time window over which the OTOC has been averaged, yielding the results shown in Fig. 4.8.*

times is observable. The expected long-time decay of the signal due to the quasiparticle interactions cannot be studied reliably due to computational limitations. In general, we observe the required bond dimension to grow rapidly once the OTOC signal decays. For example, for $g = 0.5$ or 1.5 with $\Delta = 0.2, \Delta = 0.5$ a decay of the signal is clearly visible, but the results are not converged.

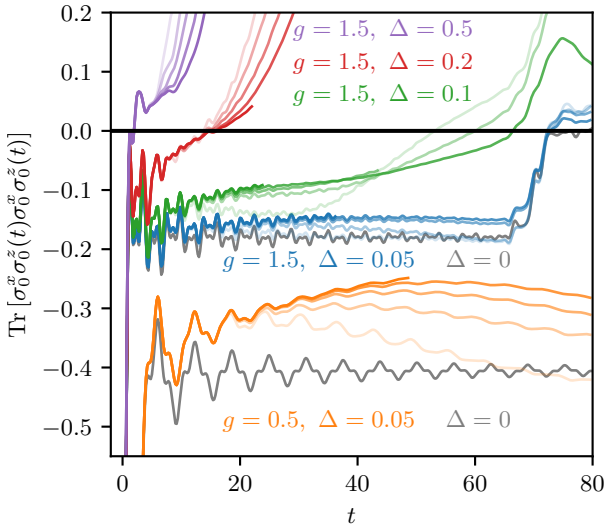

Figure C.5: *Results for* $\mathrm{Tr}\,[\sigma_0^x \sigma_0^z(t) \sigma_0^x \sigma_0^z(t)]$ *for the ANNNI model with* 70 *sites and different* Δ *and* g*. The simulation was performed using TEBD and second-order trotterization with a step size of* $\mathrm{d}t = 0.2$*. The bond dimension was varied from* 64 *(opaque) to* 1024 *(solid). For times for which the simulations coincide for different bond dimensions, they also coincide when choosing a smaller* $\mathrm{d}t$*. The decay of the results for* $g = 1.5$ *at* $t \approx 60$ *are finite-size effects.*

D Dephasing and Information Scrambling

D.1 Stochastic Independence of Parts

In order to evaluate the phase flip sensitivity for an expectation value with observable O, we truncate the sum in Eq. (5.14) to $d \leq D$. We compute the difference in the expectation value compared to the exact result. We average the difference by integrating the unitaries $\mathcal{U}_t$ over the group G. In the following, the phase flip channel is a subgroup of G. We use the previous definition for the summed Hamming distance $d(X) = \sum_{t,l} X_{t,l}$.

$$\mathrm{MSE}(T) = \int_G \mathrm{d}\mathcal{U}_T \cdots \int_G \mathrm{d}\mathcal{U}_1 \mathrm{Tr}\left[O\left(\sum_d \rho_d(T) - \sum_d^D \rho_d(T)\right)\right]^2 \tag{D.1}$$

$$= \int_G \mathrm{d}\mathcal{U}_T \cdots \int_G \mathrm{d}\mathcal{U}_1 \left(\sum_{d>D} \mathrm{Tr}\left[O\rho_d(T)\right]\right)^2 \tag{D.2}$$

$$= \sum_{X \text{ with } d(X)>D} \int_G \mathrm{d}\mathcal{U}_T \cdots \int_G \mathrm{d}\mathcal{U}_1 \mathrm{Tr}\left(\left[O\rho_X(T)\right]\right)^2. \tag{D.3}$$

Here the last step follows from the stochastic independence of different $\rho_X(t)$ which can be seen in two steps. First, we have for the group G' of the unitary U that $\sigma^z G' = G'$ so that

$$\int_G \mathrm{d}\mathcal{U}\,(\mathcal{P}_\alpha \circ \mathcal{U}) \otimes \mathcal{U} \tag{D.4}$$

$$= \frac{1}{2}\int_{G'} \mathrm{d}U\,(U \otimes U^\dagger + (-1)^\alpha \sigma^z U \otimes U^\dagger \sigma^z) \otimes U \otimes U^\dagger \tag{D.5}$$

$$= \int_{G'} \mathrm{d}U\, U \otimes U^\dagger \otimes U \otimes U^\dagger + (-1)^\alpha \int_{G'} \mathrm{d}U\, \sigma^z U \otimes U^\dagger \sigma^z \otimes U \otimes U^\dagger \tag{D.6}$$

$$= \int_{G'} \mathrm{d}U\, U \otimes U^\dagger \otimes U \otimes U^\dagger + (-1)^\alpha \int_{\sigma^z G'} \mathrm{d}U\, U \otimes U^\dagger \otimes \sigma^z U \otimes U^\dagger \sigma^z \tag{D.7}$$

$$= \int_{G'} \mathrm{d}U\, U \otimes U^\dagger \otimes U \otimes U^\dagger + (-1)^\alpha \int_{G'} \mathrm{d}U\, U \otimes U^\dagger \otimes \sigma^z U \otimes U^\dagger \sigma^z \tag{D.8}$$

$$= \int_{G'} \mathrm{d}U\, U \otimes U^\dagger \otimes \left(U \otimes U^\dagger + (-1)^\alpha \sigma^z U \otimes U^\dagger \sigma^z\right) \tag{D.9}$$

$$= \int_G \mathrm{d}\mathcal{U}\, \mathcal{U} \otimes (\mathcal{P}_\alpha \circ \mathcal{U}). \tag{D.10}$$

Using this property, we can follow

$$\int_G \mathrm{d}\mathcal{U}_t \left(\mathcal{P}_\alpha \circ \mathcal{U}_t\right)[\rho(t-1)] \otimes \left(\mathcal{P}_\beta \circ \mathcal{U}_t\right)[\rho(t-1)] \tag{D.11}$$

$$= \int_G \mathrm{d}\mathcal{U}_t\, \mathcal{U}_t[\rho(t-1)] \otimes \left(\mathcal{P}_\beta \circ \mathcal{P}_\alpha \circ \mathcal{U}_t\right)[\rho(t-1)] \tag{D.12}$$

$$= \int_G \mathrm{d}\mathcal{U}_t\, \mathcal{U}_t[\rho(t-1)] \otimes \left(\mathcal{P}_\alpha \circ \mathcal{U}_t\right)[\rho(t-1)]\delta_{\alpha,\beta} \tag{D.13}$$

$$= \int_G \mathrm{d}\mathcal{U}_t \left(\mathcal{P}_\alpha \circ \mathcal{U}_t\right)[\rho(t-1)] \otimes \left(\mathcal{P}_\alpha \circ \mathcal{U}_t\right)[\rho(t-1)]\delta_{\alpha,\beta}, \tag{D.14}$$

using $\mathcal{P}_\alpha \circ \mathcal{P}_\beta = \mathcal{P}_\alpha \delta_{\alpha,\beta}$ in the two last steps, respectively.

Applying this relation for every unitary and projector we obtain

$$\overline{\rho_{X_1} \otimes \rho_{X_2}} = \int_G \mathrm{d}\mathcal{U}_T \cdots \int_G \mathrm{d}\mathcal{U}_1 \rho_{X_1} \otimes \rho_{X_2} \tag{D.15}$$

$$= \int_G \mathrm{d}\mathcal{U}_T \cdots \int_G \mathrm{d}\mathcal{U}_1 \rho_{X_1} \otimes \rho_{X_1} \delta_{X_1,X_2} = \delta_{X_1,X_2} \overline{\rho_{X_1} \otimes \rho_{X_1}} \tag{D.16}$$

from which the above stated properties follow.

Note that this property holds for any channel as long as the group we average over is invariant under the application of the channel.

D.2 Haar-Random Circuits

In the following, we want to investigate the role of decoherence in the form of the phase flip channel for correlators $\mathrm{Tr}[U\sigma_0^z U^\dagger \sigma_0^z]$ in Haar-random circuits without conservation laws. They serve as an example for a typical circuit without any further constraints.

D.2.1 Weingarten Calculus for Haar-Random Circuits

We begin with a short review of Weingarten Calculus adapted to our use case, for a more general explanation, see [292] or its application in operator spreading [56]. As also discussed in the main text, Eq. (5.24), we can rewrite the calculation of the second moments to an expectation value in a double Hilbert space

$$\overline{\mathrm{Tr}[\sigma_0^z(T)\sigma_0^z]\mathrm{Tr}[\sigma_0^z(T)\sigma_0^z]} = \mathrm{Tr}\left[\overline{[\sigma_0^z \otimes \sigma_0^z](T)}\sigma_0^z \otimes \sigma_0^z\right], \tag{D.17}$$

where the overline denotes the ensemble average, which here amounts to integrating all gates over the group of Haar-random gates.

Now the whole circuit, and, hence, individual gates $V_{j,j+1}$ appear four times in the expression Eq. (D.17), so that the ensemble average involves integrals of the two-site gates $V_{j,j+1}$ over the Haar-random group $G_{\text{Haar rd}}$ of the form

$$P_{j,j+1} = \int_{G_{\text{Haar rd}}} \mathrm{d}V_{j,j+1} \, (V_{j,j+1} \otimes V_{j,j+1}^\dagger \otimes V_{j,j+1} \otimes V_{j,j+1}^\dagger). \tag{D.18}$$

From the Schur-Weyl duality [293] we know that we can write

$$P_{j,j+1} = \sum_{\alpha,\beta} W_{\alpha,\beta} \left(|\Pi_\alpha\rangle\langle\Pi_\beta| \right)_{j,j+1}, \tag{D.19}$$

where

$$|\Pi_\alpha\rangle \in \Bigg\{ |II\rangle = \frac{1}{q^2} \sum_{a_j,a_{j+1},b_j,b_{j+1}} |a_j a_{j+1}\rangle \otimes |a_j a_{j+1}\rangle \otimes |b_j b_{j+1}\rangle \otimes |b_j b_{j+1}\rangle, \tag{D.20}$$

$$|SS\rangle = \frac{1}{q^2} \sum_{a_j,a_{j+1},b_j,b_{j+1}} |a_j a_{j+1}\rangle \otimes |b_j b_{j+1}\rangle \otimes |b_j b_{j+1}\rangle \otimes |a_j a_{j+1}\rangle \Bigg\}, \tag{D.21}$$

$$|I\rangle = \frac{1}{q} \sum_{a,b} |a\rangle \otimes |a\rangle \otimes |b\rangle \otimes |b\rangle, \tag{D.22}$$

$$|S\rangle = \frac{1}{q} \sum_{a,b} |a\rangle \otimes |b\rangle \otimes |b\rangle \otimes |a\rangle. \tag{D.23}$$

with q being the local Hilbert space dimension, which is $q = 2$ for qubits. From Eq. (D.18) and the properties of the Haar-random group it follows that P is a projector, and defining $D_{\alpha,\beta} = \langle\Pi_\alpha|\Pi_\beta\rangle$ we can find the Weingarten matrix W to fulfill

$$P^2 = P \Rightarrow WDW = W \Rightarrow W = D^{-1} = \begin{pmatrix} 1 & q^{-2} \\ q^{-2} & 1 \end{pmatrix}^{-1} = \frac{q^2}{q^4-1} \begin{pmatrix} q^2 & -1 \\ -1 & q^2 \end{pmatrix}. \tag{D.24}$$

Now we can just simulate the dynamics of Eq. (D.17) in the space spanned by $|I\rangle$ and $|S\rangle$. In this folded space, the initial operator $\sigma_0^z \otimes \sigma_0^z$ becomes on site 0

$$|\rho_{\text{init}}\rangle_0 = \sum_{a,b} (-1)^a (-1)^b |a\rangle \otimes |a\rangle \otimes |b\rangle \otimes |b\rangle, \qquad |\rho_{\text{init}}\rangle_{j\neq 0} = |I\rangle_j. \tag{D.25}$$

The application of the first gate projects into the $|S\rangle, |I\rangle$ subspace, in which

$$\langle I|\rho_{\text{init}}\rangle_0 = 0, \langle S|\rho_{\text{init}}\rangle_0 = 1 \quad \text{and} \quad \langle I|\rho_{\text{init}}\rangle_{j\neq 0} = q^2, \langle S|\rho_{\text{init}}\rangle_{j\neq 0} = 1. \tag{D.26}$$

The same holds for the final state as $O = \rho_{\text{init}}$. Hence, the simulation of Eq. (D.17) corresponds to simulating the evolution of the initial state $|\cdots I_{-1}S_0I_1\cdots\rangle$ under the evolution of Eq. (D.24) and calculating the overlap with the final state $|\cdots I_{-1}S_0I_1\cdots\rangle$. For example, we find

$$\begin{aligned} P_{0,1}|SI\rangle &= \frac{q^2}{q^4-1}\left(q^2|SS\rangle\langle SS| - |SS\rangle\langle II| - |II\rangle\langle SS| + q^2|II\rangle\langle II|\right)|SI\rangle \\ &= \frac{q}{q^2+1}\left(|SS\rangle + |II\rangle\right). \end{aligned} \tag{D.27}$$

For a TEBD simulation we use $|S'\rangle = q|S\rangle$ as a basis, making the simulation more stable, so that all necessary evolution rules are

$$P|S'I\rangle = \frac{1}{q^2+1}|S'S'\rangle + \frac{q^2}{q^2+1}|II\rangle, \quad P|S'S'\rangle = |S'S'\rangle \quad P|I'I'\rangle = |I'I'\rangle. \tag{D.28}$$

In order to evaluate the Hamming distance contributions, we insert $\mathcal{P}_0 + \mathcal{P}_1 e^{i\omega}$, Eq. (5.7), everywhere and Fourier transforming the result in ω. In this basis, their respective action can be calculated to be

$$\mathcal{P}_0|I\rangle = |I\rangle, \qquad \mathcal{P}_0|S'\rangle = \frac{q}{q+1}|I\rangle + \frac{1}{q+1}|S'\rangle, \tag{D.29}$$

$$\mathcal{P}_1|I\rangle = 0, \qquad \mathcal{P}_1|S'\rangle = \frac{-q}{q+1}|I\rangle + \frac{q}{q+1}|S'\rangle. \tag{D.30}$$

D.2.2 Numerical Results

For Haar-random circuits, fluctuations of correlation values decay exponentially. In order to analyze the Hamming distance d dependence, we again compute the variance contribution of all parts with Hamming distance d

$$\text{Var}\langle O\rangle_{\rho_d(T)} = \sum_{X \text{ with } d(X)=d} \overline{\langle O\rangle^2_{\rho_X(T)}}. \tag{D.31}$$

This corresponds to all possibilities of applying the projector $\mathcal{P}_0$ everywhere except for d-spacetime points where we apply the complementary projector $\mathcal{P}_1$. The results are shown in Fig. D.1 and Fig. D.2. For large times, the distribution appears to converge when rescaling the Hamming distance with

$t^{1.55}$ being maximal around $d/t^{1.55} \sim 0.3$. Hence, for these circuits the Hamming distance d of the parts with the largest contribution to the fluctuations is growing with time as $t^{1.55}$. This means that the number of largest contributions to the signal stems from those parts, which are off-diagonal at a macroscopic fraction of time points. In this sense, we can understand the signal as quantum: The contribution of the purely classical part ρ_0 vanishes; the amount of Hamming distance we have to keep for a faithful approximation to the expectation value scales roughly linear with the size of the butterfly cone.

The diffusive growth observed here may appear surprising given that information spreading measured by out-of-time ordered correlators is linear. This may be explained by us calculating $\mathrm{Tr}[\sigma_0^z(t)\sigma_0^z]$, the linear spreading information is projected out, leaving the part contributing to the signal to grow diffusively.

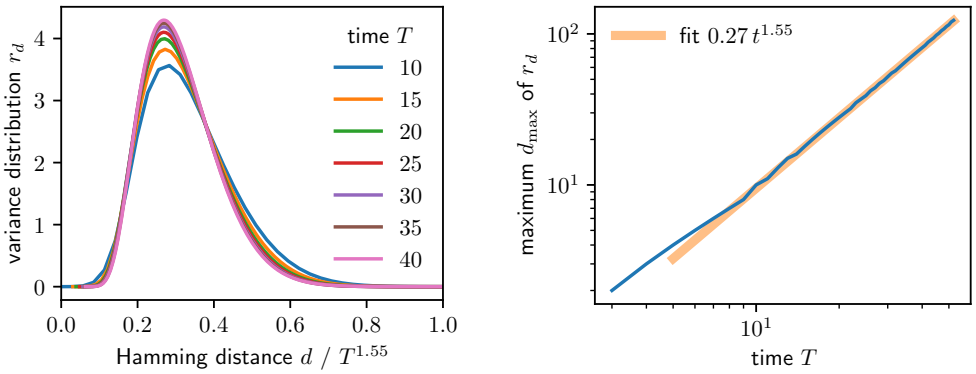

Figure D.1: *Left: Hamming distance d4 resolved variance distribution r_d for Haar-random circuits at different times with local Hilbert space dimension $q = 2$. The Hamming distance d resolved variance $\mathrm{Var}\langle O\rangle_{\rho_d}$ is divided by the full variance $\mathrm{Var}\langle O\rangle_{\rho}$ at every given timestep, the Hamming distance is rescaled with $t^{1.55}$, the scaling of the position of the coherence-maximum, see right panel. Right: Hamming distance $d_{\max}$ for which r_d is maximal as a function of time (blue) and the fit (orange) indicating a scaling of $\sim t^{1.55}$. Results are obtained using state-vector simulations with system size $N = 26$.*

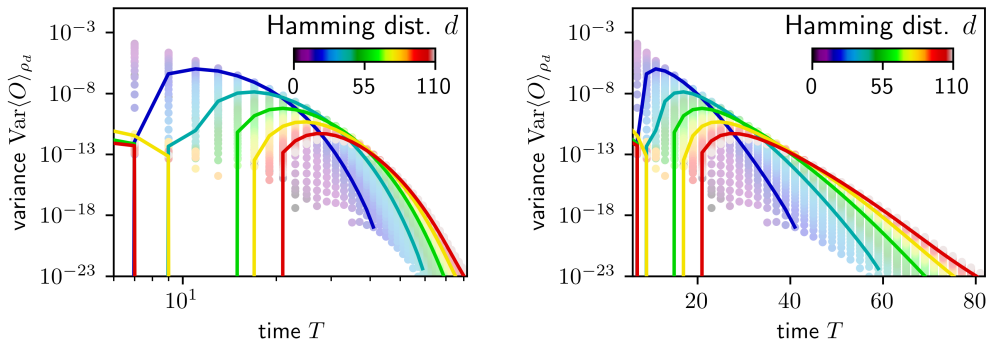

Figure D.2: *Variance of correlation values per Hamming distance* $\mathrm{Var}\langle O\rangle_{\rho_d}$ *for Haar-random circuits on log scale (left) and linear scale (right), the same data as in Fig. D.1. In contrast to Haar-random circuits with a* $U(1)$ *conservation law, the is no long-time polynomial decay,* $\mathrm{Var}\langle O\rangle_{\rho_d}$ *appears to decay over exponentially fast with time.*

D.3 Free Fermionic Circuits

Another instructive set of circuits to study are free fermionic U(1) Haar-random circuits, obtained by removing the interaction term $e^{i\alpha\sigma_j^z\sigma_{j+1}^z}$ from U(1) Haar-random circuits. Here, we find the most significant contribution to the variance to come from those terms with a coherence scaling linear in time, see Fig. D.3.

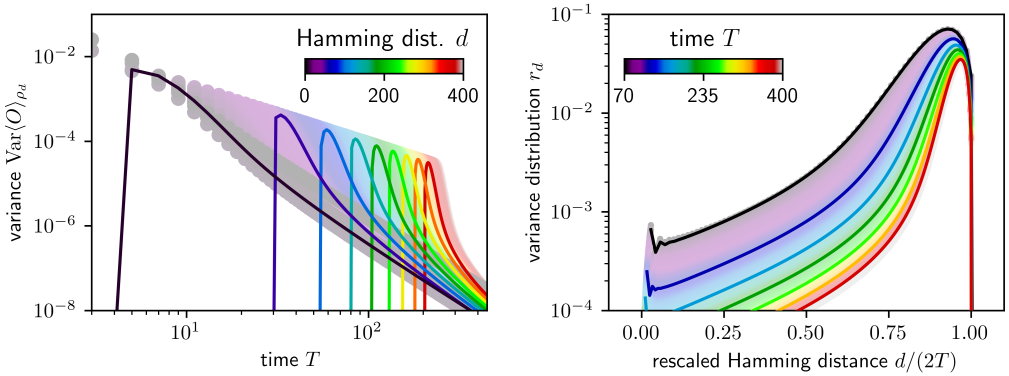

Figure D.3: *Similar to Fig. 5.3 and D.2 we show left the Hamming distance resolved variance* $\mathrm{Var}\langle O\rangle_{\rho_d}$ *for the correlator with* $\rho_{\text{init}} = O = \sigma_0^z$ *and right the distribution of variance for different times. The lines are added as guide to the eyes for every* 50*th Hamming distance starting at* $d = 8$*. We find all* $\mathrm{Var}\langle O\rangle_{\rho_d}$ *to decay as* $T^{-2.5}$ *for large times, while their sum decays as* $\mathrm{Var}\langle O\rangle_{\rho} \propto T^{-1.5}$

A pictorial explanation based on the analytical perturbative calculation, App. D.4.5, can be devised as follows, analyzing

$$\mathrm{Var}\langle O\rangle_\rho = \overline{\mathrm{Tr}\left[\sigma_0^z(t)\sigma_0^z \otimes \sigma_0^z(t)\sigma_0^z\right]} - \overline{\mathrm{Tr}\left[\sigma_0^z(t)\sigma_0^z\right]}^2. \tag{D.32}$$

The rules are almost the same as stated for Haar-random circuits with $U(1)$ conservation, the only rules which change are Eq. (D.59) and Eq. (D.60), which are replaced by

$$\begin{matrix}\sigma^+ I \\ \sigma^- I\end{matrix} \mapsto \frac{1}{2}\begin{pmatrix}\sigma^+ I + Z\sigma^+ \\ \sigma^- I + Z\sigma^-\end{pmatrix}, \tag{D.33}$$

$$\begin{matrix}\sigma^+ Z \\ \sigma^- Z\end{matrix} \mapsto \frac{1}{2}\begin{pmatrix}\sigma^+ Z + I\sigma^+ \\ \sigma^- Z + I\sigma^-\end{pmatrix}. \tag{D.34}$$

This is easy to understand: in the free fermionic case, the particles are connected via a Jordan-Wigner string rather than creating additional σ^z random walkers. This enhances the quantum correction to the variance as since only the two quantum random walkers have to annihilate again compared to the interacting case, where many particles are created and have all to be annihilated again to yield a non-vanishing contribution to the variance.

In detail, the dynamics can again be understood in terms of the probability distribution describing the position of the two σ^z's in $\sigma_0^z(t) \otimes \sigma_0^z(t)$. Initially, we start with two Z-random walkers on the same site $\sigma_0^z \otimes \sigma_0^z$, which position is correlated. To lowest order, these walkers spread independently, yielding a decay of $\overline{\mathrm{Tr}\left[\sigma_0^z(t)\sigma_0^z \otimes \sigma_0^z(t)\sigma_0^z\right]}$. This initial correlation and its decay is the same as that of the term $\overline{\mathrm{Tr}\left[\sigma_0^z(t)\sigma_0^z\right]}$ and this way subtracted away.

Now we can have two different interaction processes yielding a non-vanishing variance: one which we call "classical" as it is invariant under phase flip noise and one which we call "quantum" which is destroyed by phase flip noise, as discussed in Appendix D.4.5 Eq. (D.50) to (D.62).

The "classical" interaction process occurs when the two random walkers meet yielding correction terms to their independent spreading. This interaction is suppressed by a factor $1/12$, allowing for a perturbative treatment, as discussed in Eq. (D.58), yielding these classical interaction variance contributions scale as $T^{-2.5}$.

We can now compare this "classical" variance to the "quantum" variance. This is formed by the two σ^z-random walkers fusing to two $\sigma^\pm, \sigma^\mp$-random walkers, see Eqs. (D.58) and (D.56). These are susceptible to phase flip noise and mapped to 0 under action of $\mathcal{P}_0$. The "quantum" random walkers preserve the initial fusion information as a sign, compare Eq. D.58 and (D.56),

over time, so that when interacting at a later time, they can decouple again into two random Z-random walkers biasing the configuration which yield to their creation. This then contribute to the variance. This allows the "quantum" random walker to propagate the fusion information over long periods of time and that way, stabilizing the variance over long periods of time. This can also be seen in Fig. D.3 (right): at any time, most of the variance is created by the parts with Hamming distance d close to $2T$, where $2T$ is the maximum Hamming distance created by the quantum walkers being created at time $t = 0$ for the whole duration of the process. Hence, most of the variances comes from parts where the quantum walkers live for most of the time.

A possible explanation for these processes to be dominant follows again from the evolution equations, Eq. (D.50) to (D.62). While the classical contributions to the variance scale as $T^{-2.5}$ due to the propagators being effectively $\partial_a G$, Eq. (D.72), the free fermionic quantum walkers perform a random walk which may yield a slower decay of the variance as $T^{-1.5}$.

D.4 Details for Haar-Random Circuits with U(1) Conservation

D.4.1 Maximum

In this chapter, we provide the numerical results for the position of the maximum $t_{\max}$ for a given Hamming distance part ρ_d for the correlation values for U(1) Haar-random circuits. They are shown in Fig. D.4.

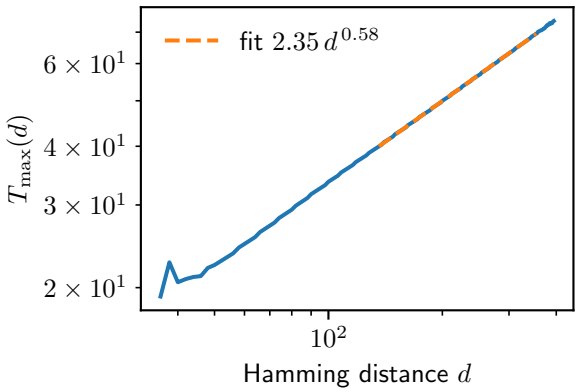

Figure D.4: *Position of the maximum $T_{\max}$ of $\mathrm{Var}\langle O\rangle_{\rho_d}$ for a given Hamming distance d for the results shown in Fig. 5.3 (top). The maximum is found by fitting a parabola to the peak. Then, the center of the fitted parabola is used as $T_{\max}(d)$.*

D.4.2 Additional Figure

For completeness, we show the required Hamming distance as a function of time given a relative error ϵ_r in this section.

For short and intermediate times, the behavior of the relative error is quite different and shown in Fig. D.5. Here we find that to achieve a certain accuracy, the required Hamming distance cutoff D, Eq. (5.17), increases at first, then reaches a peak, and finally decreasing and levels off, converging to the discussed long-time value. This comes from an enhancement of the variance for intermediate times before it approaches the long-time behavior, see also Section 5.4. It highlights the long-time-limit suppressing the intricate intermediate time behavior and being, that way, simpler.

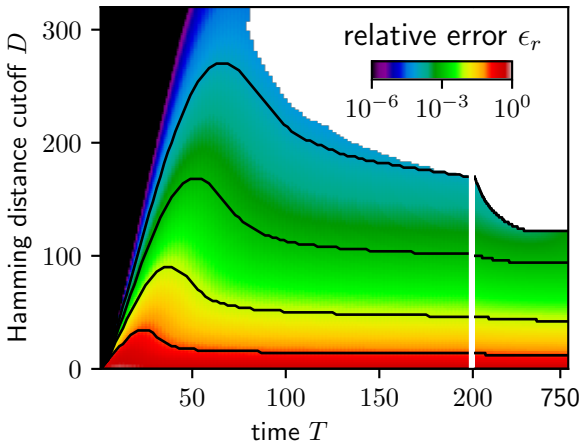

Figure D.5: *Needed Hamming distance cutoff D as a function of time for different relative errors ϵ_r, Eq. (5.17), i.e., the root-MSE over the standard deviation of $\langle O \rangle_\rho = \mathrm{Tr}[\sigma_0^z(t)\sigma_0^z]$ over the circuit ensemble. The black lines mark the results for the relative error in steps of 10^{-1}, the right site of the Figure is plotted on a different linear scale, separated by the white line from the left part.*

D.4.3 Classical Contribution to the Variance

In this chapter we show the evidence for the classical variance contributing at least about 90% of the total variance. The numerical results are shown in Fig. D.6

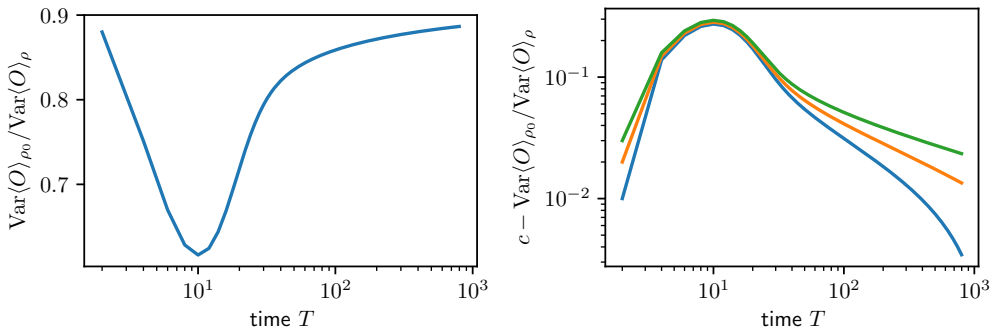

Figure D.6: *Ratio of the classical variance* $\mathrm{Var}\langle O\rangle_{\rho_0}$*, main text Eq.* (5.14)*, and the full variance* $\mathrm{Var}\langle O\rangle_\rho$ *(top). Assuming a polynomial convergence towards the long-time-limit, the long-time-limit has to be larger than about* 0.89*, as can be deduced by the curves in the lower panel not showing a polynomial decay when subtracting* 0.89*.*

D.4.4 Expectation Values

In this chapter we present the results when calculating expectation values rather analogous to the analysis of correlators provided in the main text.

In particular, we consider the expectation value

$$\langle\Psi|U^\dagger(T)\sigma_0^z U(T)|\Psi\rangle, \tag{D.35}$$

where $|\Psi\rangle$ is a domain wall state

$$|\Psi\rangle = |\uparrow\rangle_{-L/2+1}\otimes\cdots\otimes|\uparrow\rangle_0\otimes|\downarrow\rangle_1\otimes\cdots|\downarrow\rangle_{L/2} \tag{D.36}$$

and U is a charge-conserving brickwall circuit as introduced in the main text.

Again, we decompose the circuit-to-circuit variance of the expectation values according to the phase flip noise sensitivity in terms of the Hamming distance d, for which we show the results in Fig. D.7.

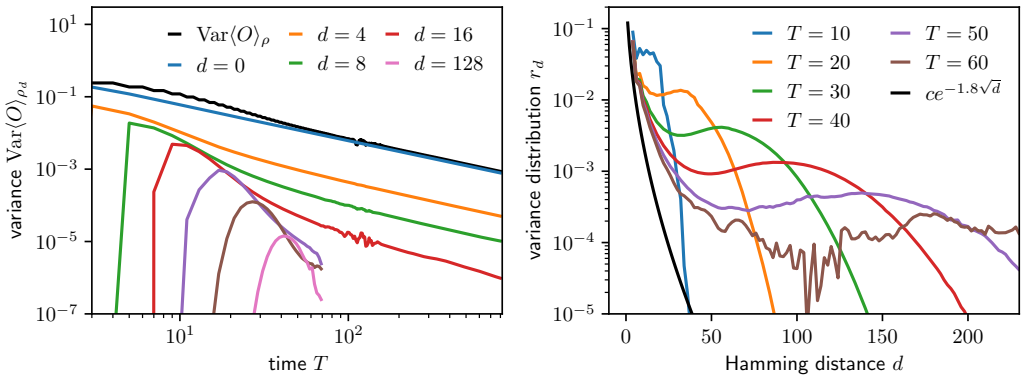

Figure D.7: *Results for the Hamming distance d resolved circuit-to-circuit variance for expectation values, see D.35. These figures are analogous to the figure in the main text for correlators, see Fig. 5.3. Again, we resolve the variance according to the Hamming distance d by calculating the variance contribution of the density matrix $\rho_d(T)$, Eq. (5.14). Left: variance as a function of time T for different d. Black shows the full variance, i.e., the sum over d. Right: variance distribution r_d as a function of Hamming distance d for different times. Note that the normalization yields the sum over every curve to be 1. Black shows for comparison the long-time-limit approached by the variance distribution for the correlators, taken from Fig. 5.3. The results were obtained the same way like in Fig. 5.3, with a system of size 200 with the precision of itensor set to 10^{-20} and by simulating the average gate dynamics. Numerical approximation errors are clearly visible (fast oscillation around time 100 in the left panel, large fluctuations for Hamming distance larger than 50 in the right panel. Hence, we limit the shown results.*

First, we note that the numerical approximation through TEBD affect the results far more severely, preventing a large time analysis as done in the main text. Restricting ourselves to the faithful results, we find similar results like in the main text for correlators. The "classical" part of the variance dominates for large times, again yielding around 90% of the full variance, see Fig. D.7 (left). Hence, one can reasonably approximate the real expectation value for an individual circuit using this classical approximation. Similarly to the results in the main text, the variance contributions decay quickly with an increasing amount of coherence, see Fig. D.7 (right). However, due to the numerical limitations, we cannot make any statements about the long-time scaling. Different to correlators, for finite times, we also observe a finite fraction of the variance to come from parts ρ_X with a large amount of Hamming distance $d(X)$, scaling faster than linear with time. This is again reminiscent of the Haar-random case and cannot be captured efficiently through an expansion in terms of the coherence. However, the fraction of these variance contributions decay so that they become irrelevant for large

times.

The performance of the Monte Carlo sampling algorithm is shown in Fig. D.8. Again, numerical inaccuracies prevent us from making statements about the scaling. Similar to correlators, the relative error decays quickly with increasing τ. At finite times, it saturates, as can be expected from the analyzes of Fig. D.7: there are large coherence contributions which require a large τ to be captured, but their overall contribution vanishes in time. As a result, using a fixed τ, the relative error decreases in time. Hence, we expect a similar scaling like for correlators.

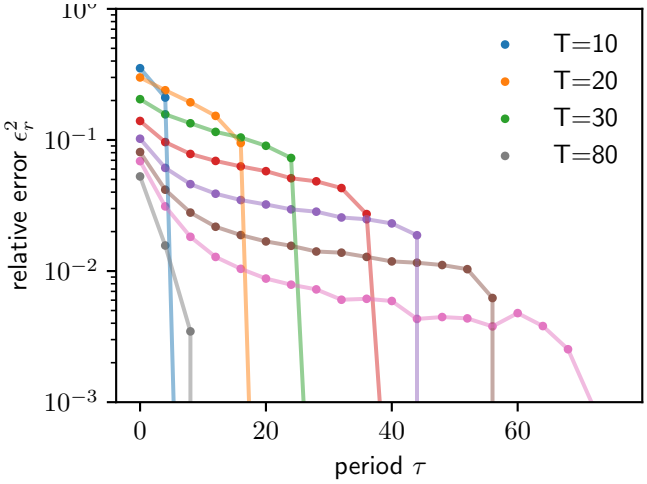

Figure D.8: *Performance of the Hamming distance based approximation algorithm for expecation values $\langle\Psi|\sigma_0^z(T)|\Psi\rangle$ taking four different diamond shaped collections, analogous to Fig. 5.6. We show the relative error squared, i.e., the MSE divided by the full variance for different times.*

D.4.5 Analytical Considerations

In this section we discuss the analytical calculation in detail. We start with the ensemble mean and then calculate the variance approximately.

Ensemble Averaged Correlator We aim to calculate

$$\overline{C} = \overline{\mathrm{Tr}[U\sigma_0^z U^\dagger \sigma_0^z]}/2^L, \tag{D.37}$$

where U is a brickwall circuit of depth T, σ_0^z is a Pauli matrix and the overline denotes integrating every two-qubit gate $V_{j,j+1}$ over the Haar-random ensemble with $U(1)$ conservation, i.e., the ensemble average, Appendix 5.3.1.

Taking the average commutes with the trace so that we can write

$$\overline{C} = \mathrm{Tr}[\overline{U\sigma_0^z U^\dagger}\sigma_0^z]/2^L. \tag{D.38}$$

This can be solved iteratively. For the first time evolution, it holds

$$\overline{V_{0,1}\sigma_0^z V_{0,1}^\dagger} = \int \mathrm{d}V_{0,1}\,(V_{0,1}\sigma_0^z V_{0,1}^\dagger) = \sigma_0^z/2 + \sigma_1^z/2, \tag{D.39}$$

where the integral denotes integrating $V_{0,1}$ over the Haar-random ensemble with $U(1)$ conservation, Appendix 5.3.1.

Hence under the evolution, the σ^z is just mapped to a superposition of σ^zs, the σ^z just performs a random walk and it holds for any time

$$\overline{U\sigma_0^z U^\dagger} = \sum_j p(j,T)\sigma_j^z. \tag{D.40}$$

The time evolution of $p(j,T)$ can then be written as

$$p(j,T+1) = \begin{cases} \frac{p(j,T)+p(j+(-1)^j,T)}{2} & T \text{ even} \\ \frac{p(j,T)+p(j-(-1)^j,T)}{2} & T \text{ odd} \end{cases}. \tag{D.41}$$

In order to arrive at a closed set of iteration equations, we coarse grain in space and time. We introduce $q(j,T) = p(j,T)/2 + p(j+1,T)/2$ and obtain for j and T even

$$q(j,T+2) = \frac{q(j-2,T) + 2q(j,T) + q(j+2,T)}{4}, \tag{D.42}$$

which is a closed set of equations for the whole (coarse grained) time evolution. Hence, we apply the continuum limit and use

$$q(j,T+2) \approx q(j,T) + 2\partial_T q(j,T) \tag{D.43}$$
$$q(j\pm 2,T) \approx q(j,T) \pm 2\partial_j q(j,T) + 2\partial_T^2 q(j,T). \tag{D.44}$$

This yields the diffusion equation

$$\partial_T q(j,T) = \frac{1}{2}\partial_j^2 q(j,T). \tag{D.45}$$

It has the well known solution

$$q(j,T) = \frac{1}{\sqrt{2\pi T}} e^{\frac{j^2}{2T}}, \tag{D.46}$$

and required $\sum_j q(j,T) = 1$.

Hence, for large times we expect the continuum limit to be a valid approximation and obtain

$$\overline{C} = \mathrm{Tr}[\overline{U\sigma_0^z U^\dagger}\sigma_0^z]/2^L = p(0,T) \approx q(0,T) = \frac{1}{\sqrt{2\pi T}} \tag{D.47}$$

and the propagator reported in the main text

$$G(T, i-j) = \mathrm{Tr}[\overline{U\sigma_i^z U^\dagger}\sigma_j^z]/2^L = p(i-j,T) \approx q(i-j,T) = \frac{e^{-(i-j)^2/2T}}{\sqrt{2\pi T}}. \tag{D.48}$$

Variance of the Correlator We proceed with calculating

$$\overline{C^2} = \overline{\mathrm{Tr}[U\sigma_0^z U^\dagger \sigma_0^z]^2} = \mathrm{Tr}[\overline{U\sigma_0^z U^\dagger \otimes U\sigma_0^z U^\dagger}\sigma_0^z \otimes \sigma_0^z], \tag{D.49}$$

where we doubled the size of the Hilbert space so that we have two copies, denoted with $\otimes$.

Similar to the mean, we start with calculating the update rules. We start with the initial condition

$$\int \mathrm{d}V_{0,1}\, (V_{0,1} i\sigma_0^z V_{0,1}^\dagger) \otimes (V_{0,1}\sigma_0^z V_{0,1}^\dagger) \tag{D.50}$$

$$= \frac{\sigma_0^z + \sigma_1^z}{2} \otimes \frac{\sigma_0^z + \sigma_1^z}{2} \tag{D.51}$$

$$+ \frac{1}{12}(\sigma_0^z \otimes \sigma_0^z + \sigma_1^z \otimes \sigma_1^z) - \frac{1}{12}(\sigma_0^z \otimes \sigma_1^z + \sigma_1^z \otimes \sigma_0^z) \tag{D.52}$$

$$+ \frac{2}{3}(\sigma_0^+\sigma_1^- \otimes \sigma_0^-\sigma_1^+ + \sigma_0^-\sigma_1^+ \otimes \sigma_0^+\sigma_1^-). \tag{D.53}$$

The first line is the "non-interaction" diffusion and corresponds to the dynamics of $\overline{C}^2$. The second line is a classical "interaction" correction - it is phase flip insensitive. The third line is a quantum "interaction" and creates the $\sigma_j^q = \sigma_j^+ \otimes \sigma_j^-$ walkers. These are phase flip sensitive and projected out by $\mathcal{P}_1[\sigma^\pm] = 0$. In order to fully calculate the second moment, we need the full set of evolution rules, which we provide in a shortened notation. We write everything in blocks of four: the first row is the first copy of the Hilbert space, the second row is the second copy of the Hilbert space, the left column corresponds to site j and the right column to site $j+1$.

$$\begin{matrix} A & B \\ C & D \end{matrix} \equiv A_j B_{j+1} \otimes C_j C_{j+1}. \tag{D.54}$$

Furthermore, we use $Z \equiv \sigma^z$ and for the identity I and the arrow $\mapsto$ represents the evolution under the averaged two-qubit gate.

In this formulation, Eq. D.50 reads

$$\begin{matrix} ZI \\ ZI \end{matrix} \mapsto \frac{1}{4}\left(\begin{matrix} ZI \\ ZI \end{matrix} + \begin{matrix} IZ \\ ZI \end{matrix} + \begin{matrix} ZI \\ IZ \end{matrix} + \begin{matrix} IZ \\ IZ \end{matrix}\right) \tag{D.55}$$

$$+ \frac{1}{12}\left(\begin{matrix} ZI \\ ZI \end{matrix} + \begin{matrix} IZ \\ IZ \end{matrix}\right) - \frac{1}{12}\left(\begin{matrix} ZI \\ IZ \end{matrix} + \begin{matrix} ZI \\ IZ \end{matrix}\right) + \frac{2}{3}\left(\begin{matrix} \sigma^+\sigma^- \\ \sigma^-\sigma^+ \end{matrix} + \begin{matrix} \sigma^-\sigma^+ \\ \sigma^+\sigma^- \end{matrix}\right). \tag{D.56}$$

All other needed evolution rules are

$$\begin{matrix} IZ \\ II \end{matrix} \mapsto \frac{1}{2}\left(\begin{matrix} ZI \\ II \end{matrix} + \begin{matrix} IZ \\ II \end{matrix}\right), \tag{D.57}$$

$$\begin{matrix} IZ \\ ZI \end{matrix} \mapsto \frac{1}{4}\left(\begin{matrix} ZI \\ ZI \end{matrix} + \begin{matrix} IZ \\ ZI \end{matrix} + \begin{matrix} ZI \\ IZ \end{matrix} + \begin{matrix} IZ \\ IZ \end{matrix}\right) - \frac{1}{12}\left(\begin{matrix} ZI \\ ZI \end{matrix} + \begin{matrix} IZ \\ IZ \end{matrix}\right) + \frac{1}{12}\left(\begin{matrix} ZI \\ IZ \end{matrix} + \begin{matrix} ZI \\ IZ \end{matrix}\right)$$

$$- \frac{2}{3}\left(\begin{matrix} \sigma^+\sigma^- \\ \sigma^-\sigma^+ \end{matrix} + \begin{matrix} \sigma^-\sigma^+ \\ \sigma^+\sigma^- \end{matrix}\right), \tag{D.58}$$

$$\begin{matrix} \sigma^+I \\ \sigma^-I \end{matrix} \mapsto \frac{1}{4}\left(\begin{matrix} \sigma^+I \\ \sigma^-I \end{matrix} + \begin{matrix} \sigma^+Z \\ \sigma^-Z \end{matrix} + \begin{matrix} I\sigma^+ \\ I\sigma^- \end{matrix} + \begin{matrix} Z\sigma^+ \\ Z\sigma^- \end{matrix}\right), \tag{D.59}$$

$$\begin{matrix} \sigma^+Z \\ \sigma^-Z \end{matrix} \mapsto \frac{1}{4}\left(\begin{matrix} \sigma^+I \\ \sigma^-I \end{matrix} + \begin{matrix} \sigma^+Z \\ \sigma^-Z \end{matrix} + \begin{matrix} I\sigma^+ \\ I\sigma^- \end{matrix} + \begin{matrix} Z\sigma^+ \\ Z\sigma^- \end{matrix}\right), \tag{D.60}$$

$$\begin{matrix} \sigma^+\sigma^+ \\ \sigma^-\sigma^- \end{matrix} \mapsto \begin{matrix} \sigma^+\sigma^+ \\ \sigma^-\sigma^- \end{matrix}, \tag{D.61}$$

$$\begin{matrix} \sigma^+\sigma^- \\ \sigma^-\sigma^+ \end{matrix} \mapsto + \frac{1}{24}\left(\begin{matrix} ZI \\ ZI \end{matrix} + \begin{matrix} IZ \\ IZ \end{matrix}\right) - \frac{1}{24}\left(\begin{matrix} ZI \\ IZ \end{matrix} + \begin{matrix} ZI \\ IZ \end{matrix}\right) + \frac{1}{3}\left(\begin{matrix} \sigma^+\sigma^- \\ \sigma^-\sigma^+ \end{matrix} + \begin{matrix} \sigma^-\sigma^+ \\ \sigma^+\sigma^- \end{matrix}\right). \tag{D.62}$$

All other needed evolution rules follow by the symmetry of swapping the left and right column, the top and bottom row or multiplying the rules with the invariant $\begin{matrix} ZZ \\ ZZ \end{matrix}$.

These rules are the ones used in the main text to obtain the second moment of the correlator and the expectation value via numerical simulation with TEBD presented in Fig. 5.3.

These rules also yield the statements made in the main text: We have classical and quantum "interactions", the quantum interactions yield quantum particles $\sigma_j^q = \sigma_j^+ \otimes \sigma_j^-$, sensitive to phase flips. Due to the brickwall structure, the quantum particles are created in pairs and live for at least two time steps, hence, the minimal amount of Hamming distance is 4. These quantum particles then perform a random walk while emitting or absorbing

Z random walkers, Eq. (D.59) and (D.60). This random walkers can then fuse again, yielding a similar correction to the non-interacting Z-walkers like the classical one, compare Eq. (D.58) the terms with prefactor 1/12 and Eq. (D.62) with prefactor 1/24. Classical corrections are on the order of 1/12, quantum interactions are further suppressed by the prefactors 2/3 and 1/24 as well as the 1/4 in the random walk. Furthermore, the quantum processes generate many-body dynamics, since the σ_j^q emit and absorb Z-random walkers. Since the final probe in the correlator only permits one Z random walker per Hilbert space, all of these emitted random walkers during a quantum process have to be absorbed again.

Now, we can perform an analytical calculation of the second moment using the above set of rules and the propagator q from the previous chapter. As an approximation, we just consider processes with a single classical interaction at site a at time t so that we split up the circuit whole time evolution T into three parts: the circuit up to t, the layer $\mathcal{U}_t$ generating the interaction and finally all the layers after t till T. We approximate the time evolution of the first and last part as random walks for which we derived the propagator G, Eq. (D.48).

Single Interaction. It yields for the process $\sigma_a^z \otimes \sigma_a^z \to \sigma_a^z \otimes \sigma_a^z/12$ of a single classical interaction

$$\begin{aligned}\overline{C^2}\Big|_{\sigma_a^z\otimes\sigma_a^z\to\sigma_a^z\otimes\sigma_a^z/12 \text{ at } t} &= \mathrm{Tr}[\sigma_0^z(t)\sigma_a^z]\mathrm{Tr}[\sigma_0^z(t)\sigma_a^z] \\ &\quad\times \frac{1}{12}\mathrm{Tr}[\sigma_a^z(T-t-1)\sigma_0^z]\mathrm{Tr}[\sigma_a^z(T-t-1)\sigma_0^z]/2^{4L} \\ &\approx G(t,a)^2 G(T-t-1,a)^2/12. \end{aligned} \tag{D.63}$$

All possible classical processes from Eq. (D.58) for a two-qubit gate acting on sites a and $a+1$ at time t are

$$Z_a \otimes Z_a \to \frac{1}{12}\left(Z_a \otimes Z_a - Z_a \otimes Z_{a+1} - Z_{a+1} \otimes Z_a + Z_{a+1} \otimes Z_{a+1}\right) \tag{D.64}$$

$$Z_{a+1} \otimes Z_a \to \frac{-1}{12}\left(Z_a \otimes Z_a - Z_a \otimes Z_{a+1} - Z_{a+1} \otimes Z_a + Z_{a+1} \otimes Z_{a+1}\right) \tag{D.65}$$

$$Z_a \otimes Z_{a+1} \to \frac{-1}{12}\left(Z_a \otimes Z_a - Z_a \otimes Z_{a+1} - Z_{a+1} \otimes Z_a + Z_{a+1} \otimes Z_{a+1}\right) \tag{D.66}$$

$$Z_{a+1} \otimes Z_{a+1} \to \frac{-1}{12}\left(Z_a \otimes Z_a - Z_a \otimes Z_{a+1} - Z_{a+1} \otimes Z_a + Z_{a+1} \otimes Z_{a+1}\right), \tag{D.67}$$

which sum up to

$$(Z_a - Z_{a+1}) \otimes (Z_a - Z_{a+1}) \to \frac{1}{12}(Z_a - Z_{a+1}) \otimes (Z_a - Z_{a+1}). \tag{D.68}$$

This yields in terms of the propagators and approximating $T-t-1 \approx T-t$

$$\overline{C^2}\Big|_{\text{classical interaction at } t,a} \approx \frac{1}{12}\left[G(t,a) - G(t,a+1)\right]^2 \tag{D.69}$$

$$\times \left[G(T-t-1,a) - G(T-t-1,a+1)\right]^2 \tag{D.70}$$

$$\approx \frac{1}{12}\left[\partial_a G(t,a)\right]^2 \left[\partial_a G(T-t-1,a)\right]^2. \tag{D.71}$$

Now we sum over all t and all even or odd a and approximation $T-t-1 \approx T-t$

$$\overline{C^2}\Big|_{\text{single classical interaction}} \approx \frac{1}{12}\int \mathrm{d}t \int \frac{\mathrm{d}a}{2}\, \left[\partial_a G(t,a)\right]^2 \left[\partial_a G(T-t,a)\right]^2. \tag{D.72}$$

Defining the variables $\tilde{t} = t/T$ and $\tilde{a} = a/\sqrt{T}$ yields the desired scaling $T^{-5/2}$ and a T independent integral. We may proceed with the analytical calculation as

$$\overline{C^2}\Big|_{\text{single classical interaction}} = \frac{1}{24}\frac{1}{4\pi^2}\int \mathrm{d}t \int \mathrm{d}a \frac{a^4}{t^3(T-t)^3} e^{\frac{-a^2}{2t}\frac{-a^2}{2(T-t)}} \tag{D.73}$$

$$= \frac{1}{24}\frac{1}{4\pi^2}\int \mathrm{d}t \int \mathrm{d}a \frac{a^4}{t^3(T-t)^3} e^{\frac{-a^2}{2t}\frac{-a^2}{2(T-t)}}. \tag{D.74}$$

Defining $\sigma^2 = \frac{t(T-t)}{T}$ we use

$$\int \mathrm{d}a\, a^4 e^{-\frac{a^2}{2\sigma^2}} = \sqrt{2\pi\sigma^2}3\sigma^4 \tag{D.75}$$

and get

$$\overline{C^2}\Big|_{\text{single classical interaction}} = \frac{1}{8}\frac{1}{(2\pi)^{3/2}}\frac{1}{T^{5/2}}\int_0^T \mathrm{d}t \frac{1}{\sqrt{t(T-t)}} \tag{D.76}$$

$$\overset{r=t/T}{=} \frac{1}{8}\frac{1}{(2\pi)^{3/2}}\frac{1}{T^{5/2}}\int_0^1 \mathrm{d}r \frac{1}{\sqrt{r(1-r)}} \tag{D.77}$$

$$= \frac{1}{16\sqrt{2\pi}}\frac{1}{T^{5/2}}, \tag{D.78}$$

where we used the known solution π for the integral over r. The prefactor does not agree with the numerical solution, which we attribute to the approximation of taking the continuum limit.

Multiple Interactions. We can now consider the case of two interactions. For that, we have to consider all processes starting at site 0 going to sites $a, a+1$ and then to sites $b, b+1$ and finally back to 0

$$Z_0 \otimes Z_0 \tag{D.79}$$
$$\overset{\text{evolution } t_1}{\to} (Z_a - Z_{a+1}) \otimes (Z_a - Z_{a+1}) \tag{D.80}$$
$$\overset{\text{interaction}}{\to} (Z_a - Z_{a+1}) \otimes (Z_a - Z_{a+1}) \overset{\text{evolution } t_2}{\to} (Z_b - Z_{b+1}) \otimes (Z_b - Z_{b+1}) \tag{D.81}$$
$$\overset{\text{interaction}}{\to} (Z_b - Z_{b+1}) \otimes (Z_b - Z_{b+1}) \tag{D.82}$$
$$\overset{\text{evolution } T-t_1-t_2}{\to} Z_0 \otimes Z_0. \tag{D.83}$$

$$\overline{C^2}\Big|_{\text{two separate classical interactions}} \tag{D.84}$$
$$\approx \frac{1}{12} \int \mathrm{d}t_1 \int \frac{\mathrm{d}a}{2} \int \mathrm{d}t_2 \int \frac{\mathrm{d}b}{2} \left[\partial_a G(t_1, a)\right]^2 \left[\partial_a^2 G(t_2, a-b)\right]^2 \left[\partial_b G(T - t_1 - t_2, b)\right]^2$$
$$\propto \frac{1}{T^4}, \tag{D.85}$$

where the scaling in the last step follows from pulling T out of the integral by defining the dimensionless integration variables $\tilde{t}_1 = t_1/T$, $\tilde{t}_2 = t_2/T$ and $\tilde{a} = a/\sqrt{T}$, $\tilde{b} = b/\sqrt{T}$. Iterating this argument shows that higher order interaction processes with k interactions, where all interaction a separated in time by $\mathcal{O}(T)$, are suppressed as $T^{-1-3k/2}$. Hence, in the long-time-limit those processes are dominant where the interactions occur in vicinity to each other. We show the classical part of the variance resolved according to the number of interactions in Fig. D.9. We observe an exponential decay, which justifies the perturbative treatment in the number of interactions and focusing on the single interaction contribution as the dominant contribution.

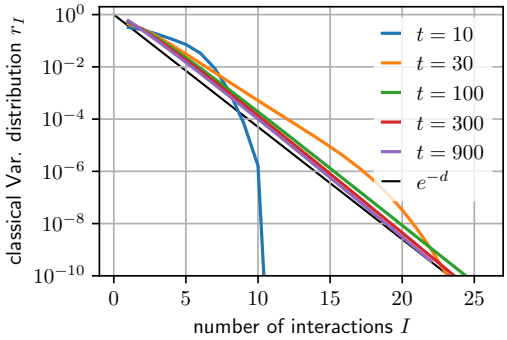

Figure D.9: *Distribution of the classical variance* $r_I = \mathrm{Var}\langle\sigma_0^z(T)\rangle_{\rho_I}/\mathrm{Var}\langle\sigma_0^z(T)\rangle_\rho$ *as calculated from the first two parts Eqs.* (D.50) *and* (D.52) *over the number of interactions, i.e., number of corrections Eq.* (D.52) *considered. The results were obtained through direct simulation of Eq.* (D.50) *and multiplying the term in Eq.* (D.52) *with* $e^{i\omega}$ *and, then, performing a Fourier transformation in* ω *to obtain the variance resolved by the number of interactions* I*. We can see a clear exponential decay, justifying the expansion in the number of interactions or corrections.*

Single interaction at the boundary. When the interaction occurs at the boundary, i.e., within the first or last time steps, the summation over processes does not scale with T, and the first propagator is T independent. We hence get via dimensional analysis

$$\overline{C^2}\Big|_{\text{single classical boundary interaction}} \approx \frac{1}{12}\sum_{(t,a)\ll T}\left[\partial_a G(t,a)\right]^2\left[\partial_a G(T-t,a)\right]^2 \propto \frac{1}{T^3}, \tag{D.86}$$

where we used $\partial_a G(T-t,a) \propto T^{-3/2}$. Hence, the correction T^{-3} to the $T^{-5/2}$ decay originates from boundary effects.

D.5 Sampling Algorithm

D.5.1 Stochastic Independence of Partitions

In this section we discuss the linear dependence of partitions. We omit the time dependence on T in the following. A partition Y of a circuit refers to inserting at every space time location a projector, either $\mathcal{P}_0$ or $\mathcal{P}_2$. Note that for a part ρ_X we inserted either $\mathcal{P}_0$ or $\mathcal{P}_1$. A partition Y can be written as a sum over all parts it contains as

$$\rho_Y = \sum_{\{X_{t,l} \text{ so that } Y_{t,l}=2\}} \rho_X, \tag{D.87}$$

which essentially encodes the constraint that a partition imposes on all parts it contains: if a partition has the projector $\mathcal{P}_0$ at some point (t,l), i.e., $Y_{t,l}=0$, all parts contained in that collection also have to have $\mathcal{P}_0$ at (t,l), i.e., $X_{t,l}=0$ for all (t,l) for which $Y_{t,l}=0$, and otherwise we sum over $X_{t,l}\in\{0,1\}$.

We have shown before that different parts are stochastically independent. Using the decomposition of partitions into parts yields the stochastic dependence of partitions

$$\overline{\rho_{Y_1}\rho_{Y_2}} = \sum_{\{X_{1,t,l} \text{ so that } Y_{1,t,l}=2\}} \sum_{\{X_{2,t,l} \text{ so that } Y_{2,t,l}=2\}} \overline{\rho_{X_1}\rho_{X_2}} \tag{D.88}$$

$$= \sum_{\{X_{1,t,l} \text{ so that } Y_{1,t,l}=2\}} \sum_{\{X_{2,t,l} \text{ so that } Y_{2,t,l}=2\}} \delta_{X_1,X_2}\overline{\rho_{X_1}\rho_{X_1}} \tag{D.89}$$

$$= \sum_{\{X_{1,t,l} \text{ so that } Y_{1,t,l}=2 \text{ and } Y_{1,t,l}=2\}} \overline{\rho_{X_1}\rho_{X_1}} \tag{D.90}$$

We can rewrite the condition $Y_{1,t,l}=2$ and $Y_{1,t,l}=2$ by defining

$$(Y_1\odot Y_2)_{t,l} = Y_{1,t,l}\,Y_{2,t,l}/2. \tag{D.91}$$

Note that $Y_1\odot Y_2$ is again a partition. So that we can write

$$\sum_{\{X_{1,t,l} \text{ so that } Y_{1,t,l}=2 \text{ and } Y_{1,t,l}=2\}} \rho_{X_1} = \rho_{Y_1\odot Y_2}. \tag{D.92}$$

Together with Eq. (D.94) it follows that $\rho_{Y_1\odot Y_2}$ are all paths which are both, in Y_1 and Y_2 so that $\rho_{Y_2}-\rho_{Y_1\odot Y_2}$ are all paths which are solely in Y_2. Hence, ρ_{Y_1} and

$$\rho'_{Y_2} = \rho_{Y_2} - \rho_{Y_1\odot Y_2} \tag{D.93}$$

are stochastically independent

$$\overline{\rho_{Y_1}\otimes\rho_{Y_2'}} = 0. \tag{D.94}$$

Hence, they can be added to reduce the MSE reliably

$$\overline{(\langle O\rangle_\rho - \langle O\rangle_{\rho_{Y_1}+\rho'_{Y_2}})^2} = \overline{(\langle O\rangle_\rho - \langle O\rangle_{\rho_{Y_1}} - \langle O\rangle_{\rho'_{Y_2}})^2} \tag{D.95}$$

$$= \overline{\langle O\rangle_\rho^2} - \overline{\langle O\rangle_{\rho_{Y_1}}^2} - \overline{\langle O\rangle_{\rho_{Y_2'}}^2} \leq \overline{(\langle O\rangle_\rho - \langle O\rangle_{\rho_{Y_1}})^2} \tag{D.96}$$

where we used

$$\overline{\rho\otimes\rho_Y} = \overline{\rho_Y\otimes\rho_Y}. \tag{D.97}$$

D.5.2 Detailed Explanation Sampling for Partitions

In this section we discuss the details of the Monte Carlo sampling algorithm for partitions. For that, we consider the diamond-shaped partitions presented in the main text, Fig. 5.4. The procedure is shown in Fig. D.10.

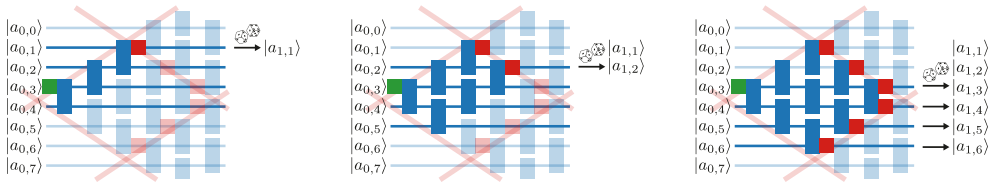

Figure D.10: *Initial iterative sampling procedure for getting Monte Carlo sampling estimates for partitioned circuits yielding ρ_{Y_1}, see Fig. 5.4. Right: we start with a random product state $|a_{0,j}\rangle$ and apply the first three gates (blue, solid). Then, the first projector $\mathcal{P}_0$ (red, solid) is equivalent to a marginal sampling using the probabilities $p_{a_{1,1}} = \langle a_0|a_{1,1}\rangle\langle a_{1,1},|a_0\rangle$. Note that this operation only involves 4 sites and in general $\tau/2+1$ sites. Center: We iterate the procedure, again applying three more gates to the tensor $\langle a_{a,a}|a_0\rangle$ obtained from the previous iteration. Again, we use the equivalence of the $\mathcal{P}_0$ projection to sample, calculating the probabilities via a tensor network contraction, again involving only 4 sites. Right: Final step, where the last set of gates is applied and all remaining sites are sampled. We end again with a product state. Note that previously, the operations depicted were meant to be superoperators. Here, these superoperators act on states of the form $|a\rangle\langle a|$, so that we can treat them as ordinary operators acting on $|a\rangle$.*

For the correlators, for every sample, we start by inserting a random product state $|a_0\rangle$ next to ρ_{init}. This yields a $s_{\text{init}} = \pm 1$ sign. In the first iteration, we apply the first set of gates, as shown in Fig. D.10 (left). This involves $\tau/2+1$ sites and yields a statevector for $\tau/2+1$ sites, for now, we ignore all sites no gates are applied to. Using that the action $\mathcal{P}_0$ on site 1 can be written as

$$\mathcal{P}_{0,1}[\rho] = \sum_{a_{1,1}} |a_{1,1}\rangle\langle a_{1,1}|\text{Tr}[\rho|a_{1,1}\rangle\langle a_{1,1}|], \tag{D.98}$$

we use $\text{Tr}[\rho|a_{1,1}\rangle\langle a_{1,1}|] = p_{a_{1,1}}$ as probabilities to select one element of the sum in Eq. (D.98) and sample. We apply the selected state $|a_{1,1}\rangle$ to the statevector. In this example with qubits, this yields a tensor with 3 "open" legs, i.e., a vector of size 2^3 corresponding to the sites $2, 3$ and 4. Then, we can apply the next set of gates, Fig. D.10 (center). This can be done via tensor network contraction. Again, we are left with a vector v of size 2^4 from 4 open legs corresponding to the sites $2, 3, 4$ and 5. We use the equivalence

of the projector $\mathcal{P}_0$ on site 2 as in Eq. (D.98) and use the absolute values squared $|v_i|^2$ as probabilities to calculate the marginal probabilities $p_{a_{1,2}}$. Again, we select one $a_{1,2}$ via sampling and apply the state to the tensor network, yielding a vector of size 2^3 for the three remaining open sites $3, 4$ and 5. In the last step, we apply the remaining gates and select the states for the remaining sites by sampling. Hence, we again have a product state on all sites and can repeat the procedure with the next group of gates. After having applied the final group of gates, we obtain the product state $|a_T\rangle$. Then, we calculate the expectation value of σ_0^z for this product state yielding a final sign $s_{\text{final}} = \pm 1$. Repeating the sampling M times and getting M values $s_{\text{init},m}, s_{\text{final},m}$), we estimate calculate

$$\text{Tr}[\rho_{Y_1}\sigma_0^z] \approx \frac{1}{M}\sum_m s_{\text{init},m}s_{\text{final},m}. \tag{D.99}$$

When combining different partitions, we use this scheme to get estimates for all required values $\text{Tr}[\rho_{Y_1}\sigma_0^z]$ and combine these estimates via Eq. (5.34).

D.5.3 Detailed Performance of the Addition Algorithm with Four Partitions

In this chapter we discuss the details of the performance of the addition algorithm when using four partitions instead of $\tau/2$. The main result is, that even with four partitions, we get most of the variance contributions up to Hamming distance $d \sim \tau$.

For that, consider Fig. D.11. Here, we show as a function of the Hamming distance $d(X)$, the fraction of the variance

$$f_{Y_a,d} = \frac{\text{Var}\langle O\rangle_{\rho_{Y_a,d}}}{\text{Var}\langle O\rangle_{\rho_d}} \tag{D.100}$$

captured by the algorithm, where

$$\rho_{Y_a} = \rho_{Y_1\cup Y_2\cup Y_3\cup Y_4} \tag{D.101}$$

and $\rho_{Y_a,d}$ is the Hamming distance decomposed ρ_{Y_a}, see Eq. (5.14).

This confirms the expectation of the Hamming distance coming from small regions. If the Hamming distance would be dispersed across the whole part, with a low local Hamming distance density, we would expect an failure of the algorithm and an exponential decay of the captured relative variance of the form $f_{Y_a,d} \sim e^{-\mu d(X)/\tau}$ with some μ. The reason being, that the algorithm misses parts where the Hamming distance terms are on two lines

with distance of at least τ to each other, see Fig 5.5. Now, increasing the Hamming distance in a low-Hamming-distance density setting would yield the probability to not hit any of those lines with a $\mathcal{P}_1$ to decay exponentially, the probability for an individual hit scales with the fraction of space-time locations where Y_a has a $\mathcal{P}_0$, which scale as $\sim \mu/\tau$ with τ, so that the amount of space-time locations without $\mathcal{P}_0$ in Y_a scale as $(1-\mu/\tau) \approx e^{-\mu/\tau}$. Now, inserting d projectors $\mathcal{P}_1$, we get a probability of $e^{-\mu d/\tau}$ that none of the $\mathcal{P}_1$ and $\mathcal{P}_0$ coincide, yielding an expected exponential decay of $f_{Y_a,d}$. Instead, we find in Fig. D.11 that the algorithm captures most of the variance for parts with a Hamming distance d up to very roughly $d(X) \sim \tau^{1.75}$ (the three different τ analyzed are insufficient to make precise statements about the exponent).

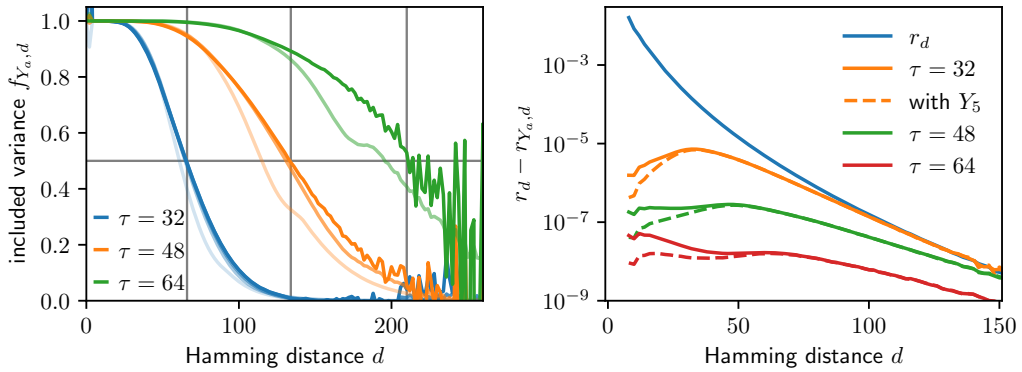

Figure D.11: *Left: fraction of the variance $f_{Y_a,d}$, Eq. (D.100), captured by the addition algorithm with four partitions, see Fig. 5.4 for different times up to about $T = 150$, T being a multiple of τ, and different periods τ of the partition pattern. Right: Residual variance distribution $r_d - r_{Y_a,d} = (\mathrm{Var}\langle O\rangle_{\rho_d} - \mathrm{Var}\langle O\rangle_{\rho_{Y_a,d}})/\mathrm{Var}\langle O\rangle_\rho$ not captured by the algorithm for different τ (orange, green and red) for large times $T \approx 200$. For reference, the full variance distribution r_d (blue) is also shown. For the dotted lines, we added one more partition Y_5 as explained in the main text, Fig. 5.6, in order to capture low-coherence paths more efficiently.*

This further indicates that the Hamming distance does not only accumulate in space and time, it also forms regions with a smaller surface than volume. If the volume would scale with the surface, as if the regions forms lines, we would expect to not being able to capture any parts with coherence larger than $d(X) \sim \tau$. However, it seems like we capture most of the coherence up to $d(X) \sim \tau^{1.75}$. Based on the underlying dynamics being diffusive, this may not be too surprising.

In any way, the Hamming distance forming regions, i.e., the $\mathcal{P}_1$ typically

accumulating in a single region, is a behavior making the simulation easier, it condenses the Hamming distance in space and time, allowing it to be captured by the algorithm more efficiently in practice compared to the more rigorous scaling analysis yielding Eq. 5.36.

Last, one may then ask what parts are the most important ones left out by the algorithm. For that, we show the residual variance distribution $r_d - r_{Y_a,d} = (\mathrm{Var}\langle O\rangle_{\rho_d} - \mathrm{Var}\langle O\rangle_{\rho_{Y_a,d}})/\mathrm{Var}\langle O\rangle_{\rho}$ in Fig. D.11 (right).

For small $\tau = 32$ we observe that the most residual variance comes from parts with coherence $d(X) \sim \tau$. For larger τ, more variance is captured, the residual variance decreases. However, the lower Hamming distance parts now start to dominate the residual variance. This is the trade-off one may want to optimize: By increasing the number of partitions these small Hamming distance parts can be captured at the cost of increasing the computational complexity, making the scaling for large desired accuracies slightly worse than stated in Eq. (5.37). This is shown with the dashed lines in Fig. D.11 (right), where we added one more partition Y_5 to Y_a, capturing a larger fraction of the low-Hamming distance parts.

However, adding Y_5 does not help capturing any more of the large-Hamming distance parts. In particular, the maximum of the residual coherence at $d(X) = \tau$ is unchanged. This suggests that most of the residual variance originates from parts of the form that $d(X) = 2$ for a duration of $\tau/2$, the minimal distance between the edges of the diamonds Fig. 5.4, and $d(X) = 0$ otherwise. These can only be captured by increasing τ and not by adding more partitions with the same or smaller τ.

References

[1] Z. Qi, T. Scaffidi, and X. Cao, Phys. Rev. B **108**, 054301 (2023), arXiv:2304.11138 [quant-ph] .

[2] M. Kues, C. Reimer, P. Roztocki, L. R. Cortés, S. Sciara, B. Wetzel, Y. Zhang, A. Cino, S. T. Chu, B. E. Little, *et al.*, Nature **546**, 622 (2017).

[3] M. Ringbauer, M. Meth, L. Postler, R. Stricker, R. Blatt, P. Schindler, and T. Monz, Nat. Phys. **18**, 1053 (2022).

[4] P. B. Nisbet-Jones, J. Dilley, A. Holleczek, O. Barter, and A. Kuhn, New J. Phys. **15**, 053007 (2013).

[5] N. Goss, A. Morvan, B. Marinelli, B. K. Mitchell, L. B. Nguyen, R. K. Naik, L. Chen, C. Jünger, J. M. Kreikebaum, D. I. Santiago, *et al.*, Nat. Commun. **13**, 7481 (2022).

[6] F. Graffitti, V. D'Ambrosio, M. Proietti, J. Ho, B. Piccirillo, C. de Lisio, L. Marrucci, and A. Fedrizzi, Phys. Rev. Res. **2**, 043350 (2020).

[7] B. P. Lanyon, M. Barbieri, M. P. Almeida, T. Jennewein, T. C. Ralph, K. J. Resch, G. J. Pryde, J. L. O'brien, A. Gilchrist, and A. G. White, Nat. Phys. **5**, 134 (2009).

[8] Y. Wang, Z. Hu, B. C. Sanders, and S. Kais, Aip. Conf. Proc. **8**, 589504 (2020).

[9] M. Erhard, R. Fickler, M. Krenn, and A. Zeilinger, Light: Sci. Appl. **7**, 17146 (2018).

[10] I. Nape, B. Sephton, P. Ornelas, C. Moodley, and A. Forbes, APL Photonics **8** (2023).

[11] S. Ecker, F. Bouchard, L. Bulla, F. Brandt, O. Kohout, F. Steinlechner, R. Fickler, M. Malik, Y. Guryanova, R. Ursin, and M. Huber, Phys. Rev. X **9**, 041042 (2019).

[12] P. Colciaghi, Y. Li, P. Treutlein, and T. Zibold, Phys. Rev. X **13**, 021031 (2023).

[13] M. Albiez, R. Gati, J. Fölling, S. Hunsmann, M. Cristiani, and M. K. Oberthaler, Phys. Rev. Lett. **95**, 010402 (2005).

[14] A. MacDonald, r. P. Schiffer, and h. N. Samarth, Nat. Mater. **4**, 195 (2005).

[15] T. Jungwirth, J. Sinova, J. Mašek, J. Kučera, and A. H. MacDonald, Rev. Mod. Phys. **78**, 809 (2006).

[16] M. R. Atkin and S. Zohren, Phys. Rev. A **92**, 012331 (2015).

[17] D. Collins, N. Gisin, N. Linden, S. Massar, and S. Popescu, Phys. Rev. Lett. **88**, 040404 (2002).

[18] E. Schrödinger, Math. Proc. Cambridge Philos. Soc. **31**, 555–563 (1935).

[19] B. Collins, I. Nechita, and K. Życzkowski, J. Phys. Math. Theor. **43**, 275303 (2010).

[20] K. Życzkowski, K. A. Penson, I. Nechita, and B. Collins, J. Math. Phys. **52** (2011).

[21] D. N. Page, Phys. Rev. Lett. **71**, 1291 (1993).

[22] S. K. Foong and S. Kanno, Phys. Rev. Lett. **72**, 1148 (1994).

[23] J. Sánchez-Ruiz, Phys. Rev. E **52**, 5653 (1995).

[24] S. Sen, Phys. Rev. Lett. **77**, 1 (1996).

[25] H.-J. Sommers and K. Życzkowski, J. Phys. A **37**, 8457 (2004).

[26] C. Nadal, S. N. Majumdar, and M. Vergassola, Phys. Rev. Lett. **104**, 110501 (2010).

[27] C. Nadal, S. N. Majumdar, and M. Vergassola, J. Stat. Phys. **142**, 403 (2011).

[28] D. Dahlbom, H. Zhang, Z. Laraib, D. M. Pajerowski, K. Barros, and C. Batista, (2023), 10.48550/ARXIV.2304.03874, arXiv:2304.03874 [cond-mat.str-el] .

[29] A. M. Kaufman and K.-K. Ni, Nat. Phys. **17**, 1324 (2021).

[30] A. M. Kaufman, M. E. Tai, A. Lukin, M. Rispoli, R. Schittko, P. M. Preiss, and M. Greiner, Science **353**, 794 (2016).

[31] T. Mori, Phys. Rev. B **98**, 104303 (2018).

[32] J. Sakurai and J. Napolitano, *Modern Quantum Mechanics* (Cambridge University Press, 2020).

[33] G. Livan, M. Novaes, and P. Vivo, Monograph Award **63**, 54 (2018).

[34] R. M. Angelo and K. Furuya, Phys. Rev. A **71**, 042321 (2005).

[35] J. Fröhlich, A. Knowles, and E. Lenzmann, Lett. Math. Phys. **82**, 275 (2007).

[36] A. C. Potter and R. Vasseur, "Entanglement dynamics in hybrid quantum circuits," in *Entanglement in Spin Chains* (Springer International Publishing, 2022) p. 211–249.

[37] P. Suchsland, R. Moessner, and P. W. Claeys, Phys. Rev. B **111**, 014309 (2025).

[38] B. Bertini, P. Kos, and T. Prosen, SciPost Physics **8** (2020), 10.21468/scipostphys.8.4.067.

[39] D. E. Parker, X. Cao, A. Avdoshkin, T. Scaffidi, and E. Altman, Phys. Rev. X **9**, 041017 (2019).

[40] V. Balasubramanian, P. Caputa, J. M. Magan, and Q. Wu, Physical Review D **106** (2022), 10.1103/physrevd.106.046007.

[41] V. Viswanath and G. Mueller, *The recursion method Application to many-body dynamics* (Springer, Germany, 1994).

[42] A. Dymarsky and A. Gorsky, Phys. Rev. B **102**, 085137 (2020).

[43] E. Rabinovici, A. Sánchez-Garrido, R. Shir, and J. Sonner, J. High Energ. Phys. **2022**, 151 (2022).

[44] E. Rabinovici, A. Sánchez-Garrido, R. Shir, and J. Sonner, J. High Energ. Phys. **2022**, 211 (2022).

[45] M. Bukov, L. D'Alessio, and A. Polkovnikov, Adv. Phys. **64**, 139 (2015).

[46] M. P. Fisher, V. Khemani, A. Nahum, and S. Vijay, Annu. Rev. Conden. Ma. P. **14**, 335 (2023).

[47] D. J. Yates and A. Mitra, Phys. Rev. B **104**, 195121 (2021).

[48] D. J. Yates, A. G. Abanov, and A. Mitra, Commun. Phys. **5**, 43 (2022).

[49] H. F. Trotter, Proc. Amer. Math. Soc. **10**, 545 (1959).

[50] M. Suzuki, Prog. Theor. Phys. **56**, 1454 (1976).

[51] G. Vidal, Phys. Rev. Lett. **98**, 070201 (2007).

[52] G. Vidal, Phys. Rev. Lett. **93**, 040502 (2004).

[53] S. R. White and A. E. Feiguin, Phys. Rev. Lett. **93** (2004), 10.1103/physrevlett.93.076401.

[54] M. Fishman, S. R. White, and E. M. Stoudenmire, SciPost Phys. Codebases , 4 (2022).

[55] S. Lloyd, Science **273**, 1073 (1996).

[56] A. Nahum, S. Vijay, and J. Haah, Phys. Rev. X **8**, 021014 (2018).

[57] C. W. von Keyserlingk, T. Rakovszky, F. Pollmann, and S. L. Sondhi, Phys. Rev. X **8**, 021013 (2018).

[58] V. Khemani, A. Vishwanath, and D. A. Huse, Phys. Rev. X **8**, 031057 (2018).

[59] A. Chan, A. De Luca, and J. T. Chalker, Phys. Rev. X **8**, 041019 (2018).

[60] T. Zhou and A. Nahum, Phys. Rev. X **10**, 031066 (2020).

[61] S. J. Garratt and J. T. Chalker, Phys. Rev. X **11**, 021051 (2021).

[62] B. Bertini, P. Kos, and T. Prosen, Phys. Rev. Lett. **121**, 264101 (2018).

[63] B. Bertini, P. Kos, and T. Prosen, Phys. Rev. Lett. **123**, 210601 (2019).

[64] L. Piroli, B. Bertini, J. I. Cirac, and T. Prosen, Phys. Rev. B **101**, 094304 (2020).

[65] P. W. Claeys and A. Lamacraft, Phys. Rev. Res. **2**, 033032 (2020).

[66] P. W. Claeys and A. Lamacraft, Phys. Rev. Lett. **126**, 100603 (2021).

[67] S. Aravinda, S. A. Rather, and A. Lakshminarayan, Phys. Rev. Res. **3**, 043034 (2021).

[68] W. W. Ho and S. Choi, Phys. Rev. Lett. **128**, 060601 (2022).

[69] M. Borsi and B. Pozsgay, Phys. Rev. B **106**, 014302 (2022).

[70] P. W. Claeys and A. Lamacraft, Quantum **6**, 738 (2022).

[71] S. A. Rather, S. Aravinda, and A. Lakshminarayan, PRX Quantum **3**, 040331 (2022).

[72] M. A. Rampp, R. Moessner, and P. W. Claeys, Phys. Rev. Lett. **130**, 130402 (2023).

[73] M. Vanicat, L. Zadnik, and T. Prosen, Phys. Rev. Lett. **121**, 030606 (2018).

[74] M. Ljubotina, L. Zadnik, and T. Prosen, Phys. Rev. Lett. **122**, 150605 (2019).

[75] A. J. Friedman, A. Chan, A. De Luca, and J. T. Chalker, Phys. Rev. Lett. **123**, 210603 (2019).

[76] T. Gombor and B. Pozsgay, Phys. Rev. E **104**, 054123 (2021).

[77] L. Sá, P. Ribeiro, and T. Prosen, Phys. Rev. B **103**, 115132 (2021).

[78] A. Sopena, M. H. Gordon, D. García-Martín, G. Sierra, and E. López, Quantum **6**, 796 (2022).

[79] G. Giudice, G. Giudici, M. Sonner, J. Thoenniss, A. Lerose, D. A. Abanin, and L. Piroli, Phys. Rev. Lett. **128**, 220401 (2022).

[80] P. W. Claeys, J. Herzog-Arbeitman, and A. Lamacraft, SciPost Phys. **12**, 007 (2022).

[81] Y. Miao, V. Gritsev, and D. V. Kurlov, SciPost Phys. **16** (2022), 10.21468/scipostphys.16.3.078.

[82] E. Vernier, B. Bertini, G. Giudici, and L. Piroli, Phys. Rev. Lett. **130** (2022), 10.1103/physrevlett.130.260401.

[83] Y. Miao and E. Vernier, Quantum **7**, 1160 (2023).

[84] E. Ott, *Chaos in Dynamical Systems*, 2nd ed. (Cambridge University Press, Cambridge, 2002).

[85] L. E. Fischer, M. Leahy, A. Eddins, N. Keenan, D. Ferracin, M. A. C. Rossi, Y. Kim, A. He, F. Pietracaprina, B. Sokolov, S. Dooley, Z. Zimborás, F. Tacchino, S. Maniscalco, J. Goold, G. García-Pérez, I. Tavernelli, A. Kandala, and S. N. Filippov, "Dynamical simulations of many-body quantum chaos on a quantum computer," (2024), arXiv:2411.00765 [quant-ph] .

[86] A. Foligno, P. Kos, and B. Bertini, Physical Review Letters **132** (2024), 10.1103/physrevlett.132.250402.

[87] S. Gopalakrishnan and A. Lamacraft, Phys. Rev. B **100**, 064309 (2019).

[88] W. E. Arnoldi, Quart. Appl. Math. **9**, 17 (1951).

[89] J. D. Noh, Phys. Rev. E **104**, 034112 (2021).

[90] F. Ballar Trigueros and C.-J. Lin, SciPost Phys. **13**, 037 (2022).

[91] R. Heveling, J. Wang, and J. Gemmer, Phys. Rev. E **106**, 014152 (2022).

[92] B. Bhattacharjee, X. Cao, P. Nandy, and T. Pathak, J. High Energ. Phys. **2022** (2022), 10.1007/jhep05(2022)174.

[93] Z. Qi, T. Scaffidi, and X. Cao, Phys. Rev. B **108** (2023), 10.1103/physrevb.108.054301.

[94] H.-C. Yeh, G. Cardoso, L. Korneev, D. Sels, A. G. Abanov, and A. Mitra, Phys. Rev. B **108** (2023), 10.1103/physrevb.108.165143.

[95] E. Rabinovici, A. Sánchez-Garrido, R. Shir, and J. Sonner, J. High Energ. Phys. **2021**, 62 (2021).

[96] S. Baek, arXiv:2210.06815 [hep-th, physics:nlin, physics:quant-ph] (2022).

[97] D. Patramanis, Progress of Theoretical and Experimental Physics **2022**, 063A01 (2022), https://academic.oup.com/ptep/article-pdf/2022/6/063A01/44062693/ptac081.pdf .

[98] A. Chapman, S. J. Elman, and R. L. Mann, arXiv:2305.15625 [cond-mat, physics:quant-ph] (2023).

[99] N. Iizuka and M. Nishida, J. High Energy Phys. **2023** (2023), 10.1007/jhep11(2023)065.

[100] S. Moudgalya and O. I. Motrunich, Phys. Rev. X **12**, 011050 (2022).

[101] S. Moudgalya and O. I. Motrunich, Annals of Physics, Volume 455, August 2023, 169384 **455**, 169384 (2022), arXiv:2209.03370 [cond-mat.str-el] .

[102] B. Bhattacharjee, S. Sur, and P. Nandy, Phys. Rev. B **106**, 205150 (2022).

[103] J. Kim, J. Murugan, J. Olle, and D. Rosa, Phys. Rev. A **105**, L010201 (2022).

[104] S.-K. Jian, B. Swingle, and Z.-Y. Xian, J. High Energ. Phys. **2021**, 14 (2021).

[105] P. Caputa and S. Datta, J. High Energ. Phys. **2021**, 188 (2021).

[106] A. Dymarsky and M. Smolkin, Phys. Rev. D **104**, L081702 (2021).

[107] K. Adhikari and S. Choudhury, Fortschr. Phys. **70**, 2200126 (2022).

[108] A. Kar, L. Lamprou, M. Rozali, and J. Sully, J. High Energ. Phys. **2022**, 16 (2022).

[109] A. Avdoshkin, A. Dymarsky, and M. Smolkin, J. High Energy Phys. **2024** (2022), 10.1007/jhep06(2024)066.

[110] A. Banerjee, A. Bhattacharyya, P. Drashni, and S. Pawar, Phys. Rev. D **106**, 126022 (2022).

[111] H. A. Camargo, V. Jahnke, K.-Y. Kim, and M. Nishida, J. High Energy Phys. **2023** (2022), 10.1007/jhep05(2023)226.

[112] D. P. Jatkar, S. Mahato, S. Mondkar, and P. Thalore, "Violation of universal operator growth hypothesis in w_3 conformal field theories," (2025), arXiv:2506.01957 [hep-th] .

[113] K. Hashimoto, K. Murata, N. Tanahashi, and R. Watanabe, J. High Energy Phys. **2023** (2023), 10.1007/jhep11(2023)040.

[114] P. Caputa, J. M. Magan, and D. Patramanis, Phys. Rev. Res. **4**, 013041 (2022).

[115] V. Balasubramanian, P. Caputa, J. M. Magan, and Q. Wu, Phys. Rev. D **106**, 046007 (2022).

[116] Z.-Y. Fan, J. High Energ. Phys. **2022**, 232 (2022).

[117] Z.-Y. Fan, Phys. Rev. A **105**, 062210 (2022).

[118] C. Lv, R. Zhang, and Q. Zhou, Phys. Rev. Res. **6** (2023), 10.1103/physrevresearch.6.l042001.

[119] K. Pal, K. Pal, A. Gill, and T. Sarkar, Phys. Rev. B **108** (2023), 10.1103/physrevb.108.104311.

[120] R. Zhang and H. Zhai, Quantum Frontiers **3** (2023), 10.1007/s44214-024-00054-4.

[121] N. Hörnedal, N. Carabba, K. Takahashi, and A. del Campo, Quantum **7**, 1055 (2023).

[122] P. W. Claeys, M. Pandey, D. Sels, and A. Polkovnikov, Phys. Rev. Lett. **123**, 090602 (2019).

[123] K. Takahashi and A. del Campo, Phys. Rev. X **14** (2023), 10.1103/physrevx.14.011032.

[124] B. Bhattacharjee, arXiv:2302.07228 [cond-mat, physics:hep-th, physics:quant-ph] (2023).

[125] A. Bhattacharya, P. Nandy, P. P. Nath, and H. Sahu, J. High Energ. Phys. **2022** (2022), 10.1007/jhep12(2022)081.

[126] L. D'Alessio, Y. Kafri, A. Polkovnikov, and M. Rigol, Adv. Phys. **65**, 239 (2016).

[127] L. D'Alessio and M. Rigol, Phys. Rev. X **4**, 041048 (2014).

[128] A. Lazarides, A. Das, and R. Moessner, Phys. Rev. E **90**, 012110 (2014).

[129] M. Pandey, P. W. Claeys, D. K. Campbell, A. Polkovnikov, and D. Sels, Phys. Rev. X **10**, 041017 (2020).

[130] M. Brenes, T. LeBlond, J. Goold, and M. Rigol, Phys. Rev. Lett. **125**, 070605 (2020).

[131] T. LeBlond, D. Sels, A. Polkovnikov, and M. Rigol, Phys. Rev. B **104**, L201117 (2021).

[132] W. Mück and Y. Yang, Nucl. Phys. B **984**, 115948 (2022).

[133] G. Szegő, *Orthogonal Polynomials* (American Mathematical Society, 1975) p. 297.

[134] P. Nevai, J. Approx. Theory **48**, 3 (1986), Theorem 4.5.10.

[135] F. Fritzsch and T. Prosen, Phys. Rev. E **103**, 062133 (2021).

[136] P. Sierant, A. Maksymov, M. Kuś, and J. Zakrzewski, Phys. Rev. E **99**, 050102 (2019).

[137] M. Kolodrubetz, D. Sels, P. Mehta, and A. Polkovnikov, Phys. Rep. **697**, 1 (2017).

[138] M. Brenes, J. Goold, and M. Rigol, Phys. Rev. B **102**, 075127 (2020).

[139] T. Ishii, T. Kuwahara, T. Mori, and N. Hatano, Phys. Rev. Lett. **120**, 220602 (2018).

[140] L. M. Sieberer, T. Olsacher, A. Elben, M. Heyl, P. Hauke, F. Haake, and P. Zoller, npj Quantum Inf. **5**, 1 (2019).

[141] M. Heyl, P. Hauke, and P. Zoller, Sci. Adv. (2019), 10.1126/sciadv.aau8342.

[142] C. Yi, Phys. Rev. A **104**, 052603 (2021).

[143] K. Chinni, M. H. Muñoz-Arias, I. H. Deutsch, and P. M. Poggi, PRX Quantum **3**, 010351 (2022).

[144] C. Kargi, J. P. Dehollain, L. M. Sieberer, F. Henriques, T. Olsacher, P. Hauke, M. Heyl, P. Zoller, and N. K. Langford, arXiv:2110.11113 [cond-mat, physics:quant-ph] (2023).

[145] H. Zhao, M. Bukov, M. Heyl, and R. Moessner, PRX Quantum **4** (2022), 10.1103/prxquantum.4.030319.

[146] C. Mc Keever and M. Lubasch, Phys. Rev. Res. **5**, 023146 (2023).

[147] L. K. Kovalsky, F. A. Calderon-Vargas, M. D. Grace, A. B. Magann, J. B. Larsen, A. D. Baczewski, and M. Sarovar, Phys. Rev. Lett. **131**, 060602 (2023).

[148] R. Orús, Ann. Phys. **349**, 117 (2014).

[149] V. Gritsev and A. Polkovnikov, SciPost Phys. **2**, 021 (2017).

[150] B. Bertini, P. Kos, and T. Prosen, SciPost Phys. **8**, 068 (2020).

[151] T. Prosen and E. Ilievski, Phys. Rev. Lett. **107**, 060403 (2011).

[152] A. Sen, S. Nandy, and K. Sengupta, Phys. Rev. B **94**, 214301 (2016).

[153] S. E. Tapias Arze, P. W. Claeys, I. Pérez Castillo, and J.-S. Caux, SciPost Physics Core **3**, 001 (2020).

[154] B. Buča, Phys. Rev. X **13**, 031013 (2023).

[155] A. Lerose, M. Sonner, and D. A. Abanin, Phys. Rev. X **11**, 021040 (2021), publisher: American Physical Society.

[156] T. Rakovszky, C. W. Von Keyserlingk, and F. Pollmann, Phys. Rev. B **105**, 075131 (2022).

[157] C. Von Keyserlingk, F. Pollmann, and T. Rakovszky, Phys. Rev. B **105**, 245101 (2022).

[158] S. Aditya, S. Samanta, A. Sen, K. Sengupta, and D. Sen, Phys. Rev. B **105**, 104303 (2022).

[159] P. Suchsland, B. Douçot, V. Khemani, and R. Moessner, Phys. Rev. B **112**, 014311 (2025).

[160] I. Bloch, J. Dalibard, and W. Zwerger, Rev. Mod. Phys. **80**, 885 (2008).

[161] I. Bloch, J. Dalibard, and S. Nascimbene, Nat. Phys. **8**, 267 (2012).

[162] R. Blatt and C. F. Roos, Nat. Phys. **8**, 277 (2012).

[163] I. M. Georgescu, S. Ashhab, and F. Nori, Rev. Mod. Phys. **86**, 153 (2014).

[164] M. Schreiber, S. S. Hodgman, P. Bordia, H. P. Lüschen, M. H. Fischer, R. Vosk, E. Altman, U. Schneider, and I. Bloch, Science **349**, 842 (2015).

[165] J. Smith, A. Lee, P. Richerme, B. Neyenhuis, P. W. Hess, P. Hauke, M. Heyl, D. A. Huse, and C. Monroe, Nat. Phys. **12**, 907 (2016).

[166] P. Bordia, H. P. Lüschen, S. S. Hodgman, M. Schreiber, I. Bloch, and U. Schneider, Phys. Rev. Lett. **116** (2016), 10.1103/physrevlett.116.140401.

[167] J. yoon Choi, S. Hild, J. Zeiher, P. Schauß, A. Rubio-Abadal, T. Yefsah, V. Khemani, D. A. Huse, I. Bloch, and C. Gross, Science **352**, 1547 (2016), https://www.science.org/doi/pdf/10.1126/science.aaf8834 .

[168] E. A. Martinez, C. A. Muschik, P. Schindler, D. Nigg, A. Erhard, M. Heyl, P. Hauke, M. Dalmonte, T. Monz, P. Zoller, and R. Blatt, Nature **534**, 516 (2016).

[169] N. Fläschner, D. Vogel, M. Tarnowski, B. S. Rem, D. S. Lühmann, M. Heyl, J. C. Budich, L. Mathey, K. Sengstock, and C. Weitenberg, Nat. Phys. **14**, 265 (2018).

[170] P. Jurcevic, H. Shen, P. Hauke, C. Maier, T. Brydges, C. Hempel, B. Lanyon, M. Heyl, R. Blatt, and C. Roos, Phys. Rev. Lett. **119** (2017), 10.1103/physrevlett.119.080501.

[171] J. Zhang, G. Pagano, P. W. Hess, A. Kyprianidis, P. Becker, H. Kaplan, A. V. Gorshkov, Z. X. Gong, and C. Monroe, Nature **551**, 601 (2017).

[172] J. Zhang, P. W. Hess, A. Kyprianidis, P. Becker, A. Lee, J. Smith, G. Pagano, I.-D. Potirniche, A. C. Potter, A. Vishwanath, N. Y. Yao, and C. Monroe, Nature **543**, 217 (2017).

[173] S. Choi, J. Choi, R. Landig, G. Kucsko, H. Zhou, J. Isoya, F. Jelezko, S. Onoda, H. Sumiya, V. Khemani, C. von Keyserlingk, N. Y. Yao, E. Demler, and M. D. Lukin, Nature **543**, 221 (2017).

[174] M. K. Joshi, A. Elben, B. Vermersch, T. Brydges, C. Maier, P. Zoller, R. Blatt, and C. F. Roos, Phys. Rev. Lett. **124**, 240505 (2020).

[175] R. J. Lewis-Swan, A. Safavi-Naini, A. M. Kaufman, and A. M. Rey, Nature Reviews Physics **1**, 627 (2019).

[176] Z. Lenarč ič, F. Lange, and A. Rosch, Phys. Rev. B **97** (2018), 10.1103/physrevb.97.024302.

[177] B. Swingle, Nat. Phys. **14**, 988 (2018).

[178] S. Xu and B. Swingle, PRX Quantum **5**, 010201 (2024).

[179] M. Srednicki, Phys. Rev. E **50**, 888–901 (1994).

[180] T. Yoshimura, S. J. Garratt, and J. T. Chalker, Phys. Rev. B **111**, 094316 (2025).

[181] H. Sahu and F. Iemini, Phys. Rev. B **111** (2025), 10.1103/physrevb.111.104302.

[182] M. A. Rampp, R. Moessner, and P. W. Claeys, Phys. Rev. Lett. **130**, 130402 (2023).

[183] Y. Gu, A. Kitaev, and P. Zhang, J. High Energy Phys. **2022** (2022), 10.1007/jhep03(2022)133.

[184] B. Kobrin, Z. Yang, G. D. Kahanamoku-Meyer, C. T. Olund, J. E. Moore, D. Stanford, and N. Y. Yao, Phys. Rev. Lett. **126** (2021), 10.1103/physrevlett.126.030602.

[185] B. Bertini and L. Piroli, Phys. Rev. B **102** (2020), 10.1103/physrevb.102.064305.

[186] C.-J. Lin and O. I. Motrunich, Phys. Rev. B **97** (2018), 10.1103/physrevb.97.144304.

[187] V. Khemani, A. Vishwanath, and D. A. Huse, Phys. Rev. X **8**, 031057 (2018).

[188] C. von Keyserlingk, T. Rakovszky, F. Pollmann, and S. Sondhi, Phys. Rev. X **8** (2018), 10.1103/physrevx.8.021013.

[189] T. Rakovszky, F. Pollmann, and C. von Keyserlingk, Phys. Rev. X **8** (2018), 10.1103/physrevx.8.031058.

[190] X. Mi *et al.*, Science **374**, 1479–1483 (2021).

[191] M. Heyl, F. Pollmann, and B. Dóra, Phys. Rev. Lett. **121** (2018), 10.1103/physrevlett.121.016801.

[192] C. B. Dağ, K. Sun, and L.-M. Duan, Phys. Rev. Lett. **123** (2019), 10.1103/physrevlett.123.140602.

[193] Q. Wang and F. Pérez-Bernal, Phys. Rev. A **100**, 062113 (2019).

[194] Z.-H. Sun, J.-Q. Cai, Q.-C. Tang, Y. Hu, and H. Fan, Ann. Phys. (Berl.) **532**, 1900270 (2020).

[195] H. Shen, P. Zhang, R. Fan, and H. Zhai, Phys. Rev. B **96**, 054503 (2017).

[196] X. Nie, B.-B. Wei, X. Chen, Z. Zhang, X. Zhao, C. Qiu, Y. Tian, Y. Ji, T. Xin, D. Lu, and J. Li, Phys. Rev. Lett. **124**, 250601 (2020).

[197] B. Chen, X. Hou, F. Zhou, P. Qian, H. Shen, and N. Xu, Appl. Phys. Lett. **116**, 194002 (2020).

[198] S. Zamani, R. Jafari, and A. Langari, Phys. Rev. B **105**, 094304 (2022).

[199] A. I. Larkin and Y. N. Ovchinnikov, Soviet Journal of Experimental and Theoretical Physics **28**, 1200 (1969).

[200] J. Li, R. Fan, H. Wang, B. Ye, B. Zeng, H. Zhai, X. Peng, and J. Du, Phys. Rev. X **7**, 031011 (2017).

[201] M. Gärttner, J. G. Bohnet, A. Safavi-Naini, M. L. Wall, J. J. Bollinger, and A. M. Rey, Nat. Phys. **13**, 781 (2017).

[202] N. Y. Yao, F. Grusdt, B. Swingle, M. D. Lukin, D. M. Stamper-Kurn, J. E. Moore, and E. A. Demler, "Interferometric approach to probing fast scrambling," (2016).

[203] B. Swingle, G. Bentsen, M. Schleier-Smith, and P. Hayden, Phys. Rev. A **94** (2016), 10.1103/physreva.94.040302.

[204] G. Zhu, M. Hafezi, and T. Grover, Phys. Rev. A **94** (2016), 10.1103/physreva.94.062329.

[205] M. Campisi and J. Goold, Phys. Rev. E **95** (2017), 10.1103/physreve.95.062127.

[206] I. L. Aleiner, L. Faoro, and L. B. Ioffe, Ann. Phys-new. York. **375**, 378 (2016).

[207] A. Bohrdt, C. B. Mendl, M. Endres, and M. Knap, New J. Phys. **19**, 063001 (2017).

[208] R. Fan, P. Zhang, H. Shen, and H. Zhai, Science Bulletin **62**, 707 (2017).

[209] Y. Huang, Y.-L. Zhang, and X. Chen, Ann. Phys. (Berl.) **529**, 1600318 (2016).

[210] J. Maldacena, S. H. Shenker, and D. Stanford, J. High Energy Phys. **2016** (2016), 10.1007/jhep08(2016)106.

[211] P. Hayden and J. Preskill, J. High Energy Phys. **2007**, 120 (2007).

[212] Y. Sekino and L. Susskind, J. High Energy Phys. **2008**, 065 (2008).

[213] P. Pfeuty, Ann. Phys-new. York. **57**, 79 (1970).

[214] M. Sigrist, AIP Conf. Proc. **789**, 165 (2005), https://pubs.aip.org/aip/acp/article-pdf/789/1/165/11444756/165_1_online.pdf .

[215] A.-G. Penner, H. Schmid, L. I. Glazman, and F. von Oppen, "Subharmonic spin correlations and spectral pairing in floquet time crystals," (2025), arXiv:2501.18760 [cond-mat.stat-mech] .

[216] Mbeng, Glen Bigan and Russomanno, Angelo and Santoro, Giuseppe E., "The quantum Ising chain for beginners," arXiv (2020).

[217] E. Lieb, T. Schultz, and D. Mattis, Ann. Phys-new. York. **16**, 407 (1961).

[218] M. Wimmer, ACM Transactions on Mathematical Software **38**, 1–17 (2012).

[219] P. Calabrese, F. H. L. Essler, and M. Fagotti, J. Stat. Mech: Theory Exp. **2012**, P07016 (2012).

[220] D. Rossini, S. Suzuki, G. Mussardo, G. E. Santoro, and A. Silva, Phys. Rev. B **82** (2010), 10.1103/physrevb.82.144302.

[221] M. Heyl, A. Polkovnikov, and S. Kehrein, Phys. Rev. Lett. **110** (2013), 10.1103/physrevlett.110.135704.

[222] M. Fagotti and F. H. L. Essler, Phys. Rev. B **87** (2013), 10.1103/physrevb.87.245107.

[223] F. H. L. Essler and M. Fagotti, J. Stat. Mech: Theory Exp. **2016**, 064002 (2016).

[224] M. P. A. Fisher, "Duality in low dimensional quantum field theories," in *Strong interactions in low dimensions*, edited by D. Baeriswyl and L. Degiorgi (Springer Netherlands, Dordrecht, 2004) pp. 419–438.

[225] W. P. Su, J. R. Schrieffer, and A. J. Heeger, Phys. Rev. Lett. **42**, 1698 (1979).

[226] J. K. Asbóth, L. Oroszlány, and A. Pályi, *A Short Course on Topological Insulators* (Springer International Publishing, 2016).

[227] P. Titum, J. T. Iosue, J. R. Garrison, A. V. Gorshkov, and Z.-X. Gong, Phys. Rev. Lett. **123**, 115701 (2019).

[228] D. Schubert, J. Richter, F. Jin, K. Michielsen, H. De Raedt, and R. Steinigeweg, Phys. Rev. B **104** (2021), 10.1103/physrevb.104.054415.

[229] T. Bilitewski, S. Bhattacharjee, and R. Moessner, Phys. Rev. B **103** (2021), 10.1103/physrevb.103.174302.

[230] C. Karrasch and D. Schuricht, Phys. Rev. B **87** (2013), 10.1103/physrevb.87.195104.

[231] D. A. Abanin *et al.*, "Constructive interference at the edge of quantum ergodic dynamics," (2025), arXiv:2506.10191 [quant-ph] .

[232] N. Lashkari, D. Stanford, M. Hastings, T. Osborne, and P. Hayden, J. High Energy Phys. **2013**, 22 (2013).

[233] R. Oliveira, O. C. O. Dahlsten, and M. B. Plenio, Phys. Rev. Lett. **98**, 130502 (2007).

[234] O. C. O. Dahlsten, R. Oliveira, and M. B. Plenio, J. Phys. Math. Theor. **40**, 8081–8108 (2007).

[235] M. Žnidarič, Phys. Rev. A **78**, 032324 (2008).

[236] F. G. S. L. Brandão, A. W. Harrow, and M. Horodecki, Commun. Math. Phys. **346**, 397–434 (2016).

[237] M. P. Fisher, V. Khemani, A. Nahum, and S. Vijay, Annu. Rev. Conden. Ma. P. **14**, 335–379 (2023).

[238] B. Bertini, K. Klobas, P. Kos, and D. Malz, Phys. Rev. X **15** (2025), 10.1103/physrevx.15.011015.

[239] A. C. Potter and R. Vasseur, "Entanglement dynamics in hybrid quantum circuits," in *Entanglement in Spin Chains: From Theory to Quantum Technology Applications*, edited by A. Bayat, S. Bose, and H. Johannesson (Springer International Publishing, Cham, 2022) pp. 211–249.

[240] W. Brown and O. Fawzi, "Scrambling speed of random quantum circuits," (2013), arXiv:1210.6644 [quant-ph] .

[241] J. Haferkamp, Quantum **6**, 795 (2022).

[242] F. Fritzsch and P. W. Claeys, "Free probability in a minimal quantum circuit model," (2025), arXiv:2506.11197 [quant-ph] .

[243] A. Nahum, S. Roy, S. Vijay, and T. Zhou, Phys. Rev. B **106** (2022), 10.1103/physrevb.106.224310.

[244] P. Hosur, X.-L. Qi, D. A. Roberts, and B. Yoshida, J. High Energy Phys. **2016** (2016), 10.1007/jhep02(2016)004.

[245] C. W. von Keyserlingk, T. Rakovszky, F. Pollmann, and S. L. Sondhi, Phys. Rev. X **8**, 021013 (2018).

[246] V. Khemani, A. Vishwanath, and D. A. Huse, Phys. Rev. X **8** (2018), 10.1103/physrevx.8.031057.

[247] A. Foligno, P. Calabrese, and B. Bertini, PRX Quantum **6**, 010324 (2025).

[248] C. von Keyserlingk, F. Pollmann, and T. Rakovszky, Phys. Rev. B **105** (2022), 10.1103/physrevb.105.245101.

[249] A. Nahum, S. Vijay, and J. Haah, Phys. Rev. X **8**, 021014 (2018).

[250] E. McCulloch, J. De Nardis, S. Gopalakrishnan, and R. Vasseur, Phys. Rev. Lett. **131**, 210402 (2023).

[251] R. Horodecki, P. Horodecki, M. Horodecki, and K. Horodecki, Rev. Mod. Phys. **81**, 865 (2009).

[252] B. Skinner, J. Ruhman, and A. Nahum, Phys. Rev. X **9** (2019), 10.1103/physrevx.9.031009.

[253] U. Schollwöck, Ann. Phys-new. York. **326**, 96–192 (2011).

[254] G. Vidal, Phys. Rev. Lett. **91**, 147902 (2003).

[255] D. Gottesman, "The heisenberg representation of quantum computers," (1998), arXiv:quant-ph/9807006 [quant-ph] .

[256] S. Aaronson and D. Gottesman, Phys. Rev. A **70**, 052328 (2004).

[257] S. Bravyi and A. Kitaev, Phys. Rev. A **71** (2005), 10.1103/physreva.71.022316.

[258] S. Bravyi and J. Haah, Phys. Rev. A **86** (2012), 10.1103/physreva.86.052329.

[259] S. Bravyi and D. Gosset, Phys. Rev. Lett. **116** (2016), 10.1103/physrevlett.116.250501.

[260] C. Gidney, N. Shutty, and C. Jones, "Magic state cultivation: growing t states as cheap as cnot gates," (2024), arXiv:2409.17595 [quant-ph] .

[261] G. González-García, J. I. Cirac, and R. Trivedi, Quantum **9**, 1730 (2025).

[262] A. Lerose, M. Sonner, and D. A. Abanin, Phys. Rev. X **11** (2021), 10.1103/physrevx.11.021040.

[263] M. Sonner, A. Lerose, and D. A. Abanin, Ann. Phys-new. York. **435**, 168677 (2021), special issue on Philip W. Anderson.

[264] T. Baumgratz, M. Cramer, and M. B. Plenio, Phys. Rev. Lett. **113** (2014), 10.1103/physrevlett.113.140401.

[265] A. Streltsov, G. Adesso, and M. B. Plenio, Rev. Mod. Phys. **89** (2017), 10.1103/revmodphys.89.041003.

[266] H. Thomas, P.-E. Emeriau, E. Kashefi, H. Ollivier, and U. Chabaud, "On the role of coherence for quantum computational advantage," (2024), arXiv:2410.07024 [quant-ph] .

[267] I. Frérot and T. Roscilde, Phys. Rev. B **94** (2016), 10.1103/physrevb.94.075121.

[268] H. F. Dowker and J. J. Halliwell, Phys. Rev. D **46**, 1580 (1992).

[269] D. Vorberg, W. Wustmann, R. Ketzmerick, and A. Eckardt, Phys. Rev. Lett. **111** (2013), 10.1103/physrevlett.111.240405.

[270] M. Schlosshauer, "The quantum-to-classical transition and decoherence," (2019), arXiv:1404.2635 [quant-ph] .

[271] T. Zhou and A. Nahum, Phys. Rev. X **10** (2020), 10.1103/physrevx.10.031066.

[272] A. Foligno, T. Zhou, and B. Bertini, Phys. Rev. X **13**, 041008 (2023).

[273] A. A. Michailidis, D. A. Abanin, and L. V. Delacrétaz, Phys. Rev. X **14**, 031020 (2024).

[274] P. O'Donovan, P. Strasberg, K. Modi, J. Goold, and M. T. Mitchison, "Quantum master equation from the eigenstate thermalization hypothesis," (2024), arXiv:2411.07706 [quant-ph] .

[275] S. J. Garratt and J. T. Chalker, Phys. Rev. X **11**, 021051 (2021).

[276] T. Rakovszky, C. W. von Keyserlingk, and F. Pollmann, "Dissipation-assisted operator evolution method for capturing hydrodynamic transport," (2020), arXiv:2004.05177 [cond-mat.str-el] .

[277] C. D. White, M. Zaletel, R. S. K. Mong, and G. Refael, Phys. Rev. B **97** (2018), 10.1103/physrevb.97.035127.

[278] T. Schuster, C. Yin, X. Gao, and N. Y. Yao, "A polynomial-time classical algorithm for noisy quantum circuits," (2024), arXiv:2407.12768 [quant-ph] .

[279] A. Angrisani, A. Schmidhuber, M. S. Rudolph, M. Cerezo, Z. Holmes, and H.-Y. Huang, "Classically estimating observables of noiseless quantum circuits," (2024), arXiv:2409.01706 [quant-ph] .

[280] K. Noh, L. Jiang, and B. Fefferman, Quantum **4**, 318 (2020).

[281] A. A. Mele, Quantum **8**, 1340 (2024).

[282] M. A. Nielsen and I. L. Chuang, *Quantum Computation and Quantum Information: 10th Anniversary Edition* (Cambridge University Press, 2010).

[283] A. Auerbach, *Interacting electrons and quantum magnetism* (Springer Science & Business Media, 2012).

[284] K. Penc and A. M. Läuchli, in *Introduction to frustrated magnetism: materials, experiments, theory* (Springer, 2010) pp. 331–362.

[285] V. Oganesyan and D. A. Huse, Phys. Rev. B **75**, 155111 (2007).

[286] Y. Y. Atas, E. Bogomolny, O. Giraud, and G. Roux, Phys. Rev. Lett. **110**, 084101 (2013).

[287] M. A. Stephanov, J. J. M. Verbaarschot, and T. Wettig, "Random matrices," (2005), arXiv:hep-ph/0509286 [hep-ph] .

[288] J. Richter, O. Lunt, and A. Pal, Phys. Rev. Res. **5**, L012031 (2023).

[289] A. D. Córcoles, J. M. Gambetta, J. M. Chow, J. A. Smolin, M. Ware, J. Strand, B. L. T. Plourde, and M. Steffen, Phys. Rev. A **87**, 030301 (2013).

[290] A. Chandran and C. R. Laumann, Phys. Rev. B **92**, 024301 (2015).

[291] H. Rieger and F. Iglói, Phys. Rev. B **84** (2011), 10.1103/physrevb.84.165117.

[292] B. Collins, S. Matsumoto, and J. Novak, Notices Amer. Math. Soc. **69**, 1 (2022).

[293] A. W. Harrow, "The church of the symmetric subspace," (2013), arXiv:1308.6595 [quant-ph] .

End

Versicherung

Hiermit versichere ich, dass ich die vorliegende Arbeit ohne unzulässige Hilfe Dritter und ohne Benutzung anderer als der angegebenen Hilfsmittel angefertigt habe; die aus fremden Quellen direkt oder indirekt übernommenen Gedanken sind als solche kenntlich gemacht. Die Arbeit wurde bisher weder im Inland noch im Ausland in gleicher oder ähnlicher Form einer anderen Prüfungsbehörde vorgelegt. Ferner erkenne ich die Promotionsordnung des Bereichs Mathematik und Naturwissenschaften der Technischen Universität Dresden vom 23. Februar 2011 an.
Diese Arbeit wurde am Max-Planck-Institut für Physik komplexer Systeme in Dresden unter der wissenschaftlichen Betreuung von Prof. Dr. Roderich Moessner verfasst.

Lucien Philippe Leonard Suchsland
18. August 2025, Dresden